Detection of trapped survivors in collapsed reinforced concrete buildings using structure-borne sound transmission

Thesis submitted in accordance with the requirements of the University

of Liverpool for the degree of Doctor of Philosophy

by

Marios Filippoupolitis

School of Architecture, University of Liverpool

August 2020

Abstract

Every few years an earthquake of high magnitude occurs around the globe resulting in collapsed structures with people trapped inside them. The seismic research method has the potential to detect physical movement or signals by measuring vibration due to structure – borne sound using seismic sensors. The placement and positioning of these sensors is critical for the successful detection of the survivors and prediction models could be developed and used as a tool to assist in the decision making of the rescue teams. This thesis investigates the potential to use Statistical Energy Analysis (SEA) to model the vibration transmission between structural members of a collapsed reinforced concrete building in order to find trapped survivors.

Experimental Modal Analysis (EMA) was carried out to validate finite element models of reinforced concrete beam junctions with surface-to-surface contact conditions which are used to investigate the normal contact stiffness between reinforced concrete beams. It is shown that the contact stiffness follows a lognormal distribution and that the mean value could be used as approximation of the contact stiffness in beam junctions.

An ensemble of 30 random beam junctions was generated for Monte Carlo simulations with Finite Element Method (FEM) that allowed Experimental Statistical Energy Analysis (ESEA) to be used to determine Coupling Loss Factors (CLFs) between the two beams. These were compared with CLFs calculated using an analytical model based on a lump spring connector (LSC). It was shown that close agreement (difference within 5 dB) was achieved only for bending waves or torsional waves between FEM ESEA and the analytical model up to the frequency where half the bending or torsional wavelength equalled the longest side of the contact area. When all wave types were combined, reasonable agreement (difference within 10 dB) can be achieved at frequencies below 900 Hz.

FEM, SEA path analysis and general SEA matrix solutions were used to estimate vibration transmission in piles of beams using both FEM ESEA CLFs and CLFs from an analytical model of a lump spring connector. It was shown that SEA is more accurate when the number of transmission paths increases and that reasonable agreement is achieved between SEA and FEM up to 700 Hz for the majority of the beams in the piles.

Additionally, an ensemble of 30 randomly damaged beam-to-column junctions was generated using a Monte Carlo simulation with FEM. This allows an assessment of ESEA with two or three subsystems to be used to determine the CLFs between the beam and the column considering either only bending modes or the combination of all modes. It is shown that the bending modes are dominating the dynamic response of the junctions over the combination of all the modes and that the uncertainty of predicting the CLFs using FEM ESEA is sufficiently low that it should be feasible to estimate the coupling even when the exact angle between the beam and the column is unknown. In addition, the use of two instead of three subsystems for the junction significantly decreases the number of negative coupling loss factors in FEM ESEA indicating that the two-subsystem model provides a reasonable basis on which to build an SEA model.

For the one who changed my perspective on life,

for Νεφέλη.

Acknowledgements

I would like to gratefully acknowledge the funding provided by the Institute for Risk and Uncertainty of the University of Liverpool and the Engineering and Physical Sciences Research Council (EPSRC).

I would like to thank my supervisor, Professor Carl Hopkins, for his support, advice, and guidance over the years of this PhD. Carl was always available to me for discussing any matter that concerned me.

I would like also to thank Dr Gary Seiffert for his help in the experimental work of this thesis and for his positive vibe and attitude.

I would like to gratefully acknowledge Prof. Barry M. Gibbs for our discussions regarding acoustics and life in general.

Special thanks to my colleagues in the Acoustics Research Unit, Xiaoxue Shen, Nazmiye Gulenay Yilmaz and especially Alessia Frescura for their support during the writing up of this thesis.

I would like to thank my family and especially my brother Avgoustinos Filippoupolitis who had my back during the last one and a half years.

Last but not least, I would like to gratefully acknowledge Dr. Eleni-Eva Toumbakari. Eleni was the supervisor of my undergraduate thesis and was the first person who believed in me and my research skills.

Contents

List of Symbols

$c_{\mathrm{B,b}}$	Phase velocity for the propagating bending waves on a solid beam (m/s)
$c_{\mathrm{L,b}}$	Phase velocity of a beam for quasi-longitudinal waves (m/s)
f	Frequency (Hz)
f_{ck}	Characteristic crushing strength of concrete (N/mm^2)
f_{ms}	Mass – spring resonant frequency (Hz)
f_{yk}	Characteristic yield strength of steel (N/mm^2)
h	Depth (m)
i	$\sqrt{}$-1, integer
j	Integer
k	Spring stiffness (N/m)
m	Mass (kg)
t	Time (s)
u	Displacement (m)
v	Velocity (m/s)
x	Coordinate position (cm)

y	Coordinate position (cm)

A	FEM data
C	Structural damping (Ns/m), contact area (cm^2)
E	Young's modulus (N/m^2), energy (J)
F	Force (N)
K	Stiffness (N/m)
L	Length (m)
$L_{C,max}$	Length of the longest side of the surface-to-surface contact area (m)
M	Mass (kg)
N	Mode count, number of nodes, positions, samples, etc.
S	Cross-sectional area of a beam (m^2)
W	Power (W)
X	Experimental data
$Y_{\mathrm{A,FEM}}$	FEM driving-point mobility for combination of bending, torsional and longitudinal modes (m/Ns)

$Y_{\mathrm{B,FEM}}$	FEM driving-point mobility for excitation of bending modes (m/Ns)
$Y_{\mathrm{B,Inf}}$	Driving-point mobility of a thin beam of infinite extent for excitation of bending waves in the central part of the beam (m/Ns)
Y_{c}	Mobility of a point spring connection (m/Ns)
Y_{dp}	Driving-point mobility (m/Ns)
YR	Spatial-average transfer mobility ratio (dB)
$Y_{\mathrm{T,FEM}}$	FEM driving-point mobility for excitation of torsional modes (m/Ns)

ζ	Damping ratio (-)
η_{ii}	Internal loss factor for subsystem i (-)
η_{ij}	Coupling loss factor from subsystem i to subsystem j (-)
θ	Rotation angle (degrees)
λ_{B}	Bending wavelength (m)
λ_{T}	Torsional wavelength (m)
v	Poisson’s ratio (-)

ρ	Density (kg/m^3)
ρ_s	Surface density (kg/m^2)
τ	Transmission coefficient (-)
φ_A	Translational degrees of freedom for the FEM mode shapes (m)
φ_X	Translational degrees of freedom for the experimental mode shapes (m)
ω	Angular frequency (radians/s)
Φ	Mode of vibration (-)

List of Abbreviations

B32	Abaqus quadratic linear beam element
C3D20R	Abaqus continuum three-dimensional quadratic element with 20 nodes and reduced integration
CLF	Coupling Loss Factor
DOF	Degrees of Freedom
EMA	Experimental Modal Analysis
ESEA	Experimental Statistical Energy Analysis
FEM	Finite Element Method
FFT	Fast Fourier Transform
LSC	Lump Spring Connector
MAC	Modal Assurance Criterion
NFPA	National Fire Protection Association (USA)
PMAC	Partial Modal Assurance Criterion
PMVR	Partial Modal Vector Ratio
SEA	Statistical Energy Analysis
SPRING1	Abaqus spring element between a node and ground, acting in a fixed direction

SPRING2	Abaqus spring element between two nodes, acting in a fixed direction
USAR	Urban Search and Rescue

List of Figures

List of Tables

1. Introduction

1.1 Background and motivation

Every few years an earthquake of high magnitude occurs around the globe resulting in collapsed structures with people trapped inside them. When victims are trapped inside a collapsed building, the challenge is to detect and locate survivors within a period of time that will allow them to be rescued. An uninjured healthy adult with a supply of fresh air has a high probability of survival if the rescue occurs within 72 hours of the entrapment [1]. After 72 hours the survival rate is decreasing and without access to water the victims are unlikely to survive for more than 5-6 days ([1], [2]). However, important variables affect the survivability including the structure type and void space formation, the cause of the structural collapse, the survival location in the building and the speed and sophistication of available urban search and rescue (USAR) capabilities [3].

In a canine search, up to three dogs use their sense of smell to search the entire site individually or in pairs to detect potential victims trapped inside rubble. This USAR technique is considered as the most effective and it is time efficient [4]. However, the main disadvantages are the limited availability and operational time of the canines as long as their stress-sensitivity [5]. Other USAR techniques include the use of optical sensors such as video, infrared and thermal cameras and/or acoustical sensors (e.g. microphones, probes) mounted on either a bendable cable or a telescopic rod or recently on robots. Although these techniques offer a direct communication between the rescuers and the trapped survivor, their efficiency depends on the existence of voids inside the rubble ([4], [6]).

Airborne sound from survivors tends to be highly attenuated by layers of rubble and requires the existence of air paths for propagation to the surface. For this reason, there is greater potential to detect physical movement or signals by measuring vibration due to structure-borne sound (i.e. seismic research method). In a seismic search, a small number of seismic sensors are moved over a regular grid so that the operators can be certain they have searched the entire site. The placement and positioning of these sensors is critical for the successful detection of the survivors. However, grid spacing and sensor placement are often decided simply by checking whether it is possible to detect transients generated by the operators in an adjacent grid area on the surface in places where the structure is safe to walk [4]. This can be misleading because horizontal propagation of vibration across the surface of a collapsed structure is not necessarily indicative of propagation into the depths of a collapsed structure. In addition, if the search area is not completely silent the seismic sensors will detect signals from other sources of vibration and not only from a trapped survivor. This will possibly make the operator to fail to detect or locate the survivor [4].

To address this problem, it is proposed that prediction models could be developed and used as a tool to assist in the decision making of the rescue teams. Deterministic models such as Finite Element Method (FEM) [7] are not efficient for modelling collapsed buildings which are complex systems with a high degree of uncertainty (e.g. the collapse pattern and the size, the distribution and the contact conditions between the debris). To predict vibration transmission in collapsed buildings, there is potential to develop models based on Statistical Energy Analysis (SEA) as these can account for the inherent uncertainty in describing modal features of component parts of a structure [8]. In addition, SEA models are much more efficient in terms of the computational time needed compared with FEM. Therefore, this thesis investigates whether SEA could be used to model vibration transmission between the structural members of a collapsed reinforced concrete building.

1.2 Literature review

This section reviews the literature related to the main topics in this thesis.

1.2.1 Collapse patterns in reinforced concrete buildings after earthquakes

According to NFPA 1670 [9], in buildings there are five main types of collapse patterns: (a) lean-to, (b) cantilever, (c) pancake, (d) V-shape and (e) A-frame collapse. In heavy floor structures such as the reinforced concrete buildings the most frequent earthquake collapse patterns that lead in trapped survivors are: (a) the pancake and (b) the lean-to collapse.

In a *complete* pancake collapse (see Figure 1-1a) the column-floor joints fail, the columns fracture and the floors are collapsing on top of each other. Specifically, a complete pancake collapse results in a large pile of debris [10]. When the columns are strong enough not to fracture, the floors can project laterally as they fall forming the *offset* pancake collapse pattern as it is shown in Figure 1-1b. The *mid-story* collapse (see Figure 1-1c) is a sub-category of the pancake collapse as the “pancaking” is restricted to one or more intermediate floors of the building [11]. The pancake collapse patterns decrease the probability of survival due to the limited number of the formed void spaces and the difficulty of the rescue teams to reach the potential survivors [10].

A lean-to collapse (see Figure 1-1d) occurs when the one end of a floor is supported by a fragmented structural member or debris whereas the opposite end stays connected to a column [12]. The angle between the anchored floor and the column is usually between 45 and 55 degrees and the connection is made only via the yielded steel reinforcement [13]. The lean-to collapse pattern is often combined with the pancake collapse [11] and creates voids of triangular shape where potential survivors could be found [14].

Due to a catastrophic earthquake event and regardless the collapse pattern, the structural members of a reinforced concrete building (i.e. beams, columns and slabs) develop individual fractures which lead to the formation of concrete discontinuities along their length. The fragmented parts are connected via the yielded steel reinforcement as it is shown Figure 1-2.

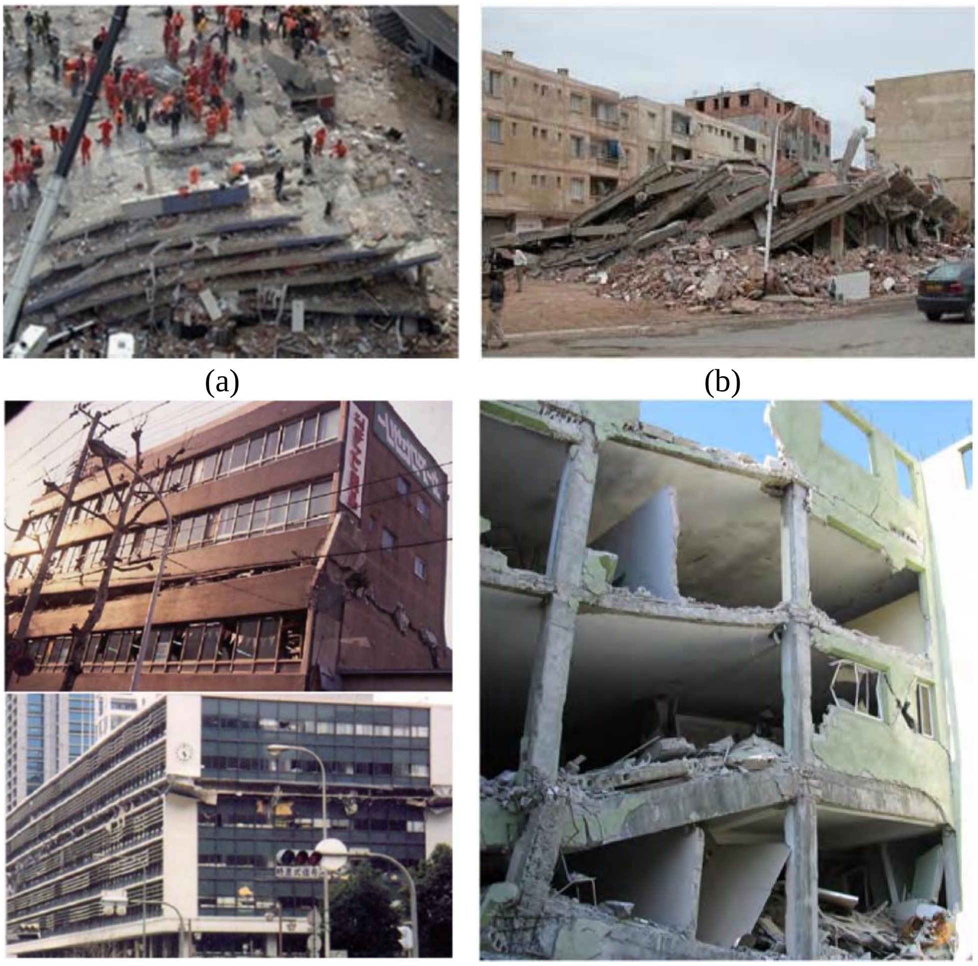

(a) (b)

(c) (d)

Figure 1-1 Collapse patterns in reinforced concrete buildings: (a) complete pancake [15], (b) offset pancake [16], (c) mid-story [17] and (d) lean-to collapse [18].

Figure 1-2 Discontinuities in reinforced concrete structural members [19].

This thesis investigates vibration transmission using FEM and SEA across structural elements that approximate: (a) the pancake collapse pattern and (b) the lean-to collapse pattern with the simplification that only beams and columns are considered, rather than plates representing floors or walls. This facilitates the experimental work as large facilities would be needed for full-scale reinforced concrete slabs. By producing experimentally validated models of reinforced concrete beams it should be feasible to extend the work in the future to plates. In the simplified pancake collapse pattern (see Figure 1-3a), reinforced concrete beams are randomly piled on top of each other without any bonding material whereas in the simplified lean-to collapse pattern (see Figure 1-3b), a reinforced concrete beam is connected to a column only via the yielded steel reinforcement.

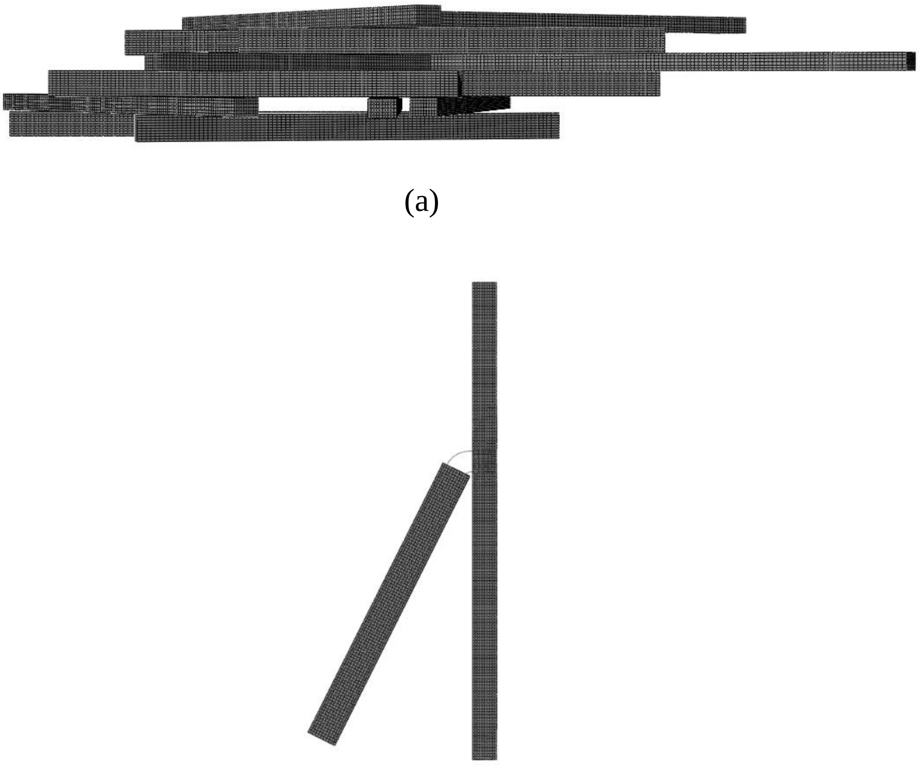

(a)

(b)

Figure 1-3 Simplified collapse patterns using beams and columns: (a) pancake and (b) lean-to collapse.

1.2.2 Finite Element Method

The Finite Element Method is a computational technique used to obtain approximate solutions of boundary value problems in engineering. The method was first applied in the late 1940s for analysis of airframe structures. During the 1960s and 1970s it was extended to applications in plate bending, shell bending, pressure vessels and general three-dimensional problems in elastic structural analysis as well as to fluid flow and heat transfer [20]. More recently the method was extended to cover multiphysics [21].

For heavyweight buildings, the Finite Element Method has mainly been used for modelling the linear and non-linear dynamic behaviour of heavyweight buildings made of masonry (e.g. [22], [23]) and reinforced concrete (e.g. [24], [25]). The main advantage of using FEM is the capability to model complex structures by approximating their geometry and boundary conditions using line (spring/beam) elements, area (shell/plate) elements and volume (solid) elements [26]. The main limitation of FEM is that the accuracy of the method depends on the size and the type of the element used. In structural dynamics, there is strong relationship between the wave frequency and finite element size [27]. In literature, it is suggested that there should be at least six elements per wavelength ([27], [28], [29]). In high frequency problems, typically over 500 Hz [30], this could either significantly increase the computational time or even make the problem impossible to be solved by a desktop computer. However, recent advances in computer hardware allows the solution of detailed finite element models of millions of degrees of freedom [31].

1.2.2.1 Modelling of reinforced concrete beams and columns

Various methods are available in the literature for the FEM modelling of reinforced concrete beams and columns. The most popular procedure is the use of solid elements for the concrete part of the member and the use of truss elements for the reinforcement (e.g. [32], [33], [34]). Truss elements have one degree of freedom per node, can sustain only axial deformation and cannot propagate bending waves [20]. Thus, they are not appropriate for modelling the steel reinforcement in the damaged concrete beams of this thesis. The 3D smeared approach approximates the steel bars using solid elements with equivalent properties calculated as weighted averages of the properties of reinforcement and concrete [34]. However, this method is not applicable to beams with concrete discontinuities. Other researchers used a combination of solid and beam elements [33]. Beam elements can sustain bending wave motion and this approach is adopted for modelling the reinforced concrete members in this thesis.

1.2.2.2 Modelling of piles of beams

For concrete beams it is reasonable to assume that they will remain in contact whilst undergoing vibratory motion. However, there are other engineering applications where vibration is transmitted between lightweight structural elements that are not rigidly bonded together which results in them being in two distinct states, in contact and out-of-contact. For example, Ervin [35] studied impacts between two orthogonal pinned-pinned beams by modelling a point connection between them using an elastic spring. Springs can be used to model complex connections between structural elements (e.g. [36], [37], [38]) and their stiffness can be determined analytically or by model updating [39] against experimental results. Research has been carried out on the investigation of the vibration of coupled beams when aligned parallel to each other when connected with uniformly distributed translational springs (e.g. [40], [41], [42], [43], [44]). However, the literature rarely considers the dynamics of beam systems where the beams are connected along their length rather than at the ends. The exception is Ervin [35] that showed contact stiffness affects the eigenfrequencies and mode shapes of a system of two beams. The Finite Element Method [20] allows study of the dynamic behaviour of unbonded contacts using elastic spring contacts. However, this requires an estimate of the normal contact stiffness which is not commonly available in the literature. Therefore, this thesis investigates the normal contact stiffness between reinforced concrete beams by experimentally validating FEM models.

1.2.3 Statistical Energy Analysis

Statistical Energy Analysis was introduced in 1959 and is a framework analysis for predicting the transmission of sound and vibration in built-up structures by using a statistical approach based on energy flow between weakly coupled parts of the system of interest, called subsystems. SEA calculates the response variables in terms of averages and variances over frequency and space thus it is not possible to obtain the exact response at a precise location and frequency [8]. The main advantage compared to deterministic methods such as FEM is the ability to deal with high frequency problems where the modal density is high without increasing the number of the degrees of freedom in the model ([30], [45]).

1.2.3.1 Subsystem definition

Subsystems are defined by their ability to store modal energy [46]. Craik [47] defines a subsystem as a group of modes with the same properties that will have the same modal energies for all sources of excitation. A beam can support bending waves (in-plane and out-of-plane), longitudinal waves and torsional waves and can be represented in an SEA model by using one subsystem for each wave type. However, there are many situations where only bending waves could be considered and a single subsystem should be sufficient [48].

The piles in this thesis consist of beams which are not rigidly bonded together; hence it is reasonable to assume that each beam represents one subsystem. However, since it is unknown what types of modes will be excited, this thesis investigates whether it is possible to consider one type of wave motion (bending waves) or whether two or more types of wave motion can be considered simultaneously (bending and torsional waves).

Rigid T-junctions in heavyweight buildings are mainly modelled using SEA with three subsystems (e.g. [48], [49]). To the knowledge of the author, limited work has been carried out on damaged T-junctions where the connection between the beam and the column is made only via the yielded steel reinforcement; hence this thesis investigates whether these junctions should be modelled using two or three subsystems and whether it is possible to only consider bending waves or whether two or more types of wave motion could be considered simultaneously (e.g. bending and torsional waves).

1.2.3.2 Coupling between structural subsystems

In SEA, the coupling between two subsystems is defined using the Coupling Loss Factor (CLF) which represents the rate of energy transfer out of a subsystem to another [8].

Point connections between parallel plates (e.g. wall ties, resilient mounts or bridged screeds), between plates and beams (e.g. screws, nails or bolts) and between beams are very common [46]. Simple models to quantify the power flow across a single point connection make use of the driving-point mobility of the plates or beams and the mobility of the point connection ([50], [8]). A resilient point connection could be modelled using a simple linear spring. The analytical model based on a lump spring connector (LSC) is assessed in this thesis for modelling the contact condition between the beams in a pile.

1.2.4 Experimental Statistical Energy Analysis

Experimental Statistical Energy Analysis (ESEA) could be used in complex coupling situations and/or between complex subsystems to determine CLFs when they are not available or difficult to measure [51]. The standard approach of ESEA relies on the power injection method where the coupling loss factors are determined by the inversion of the power balance equations [52]. ESEA and FEM could be combined to determine the CLFs of the entire system by using the FEM calculated energies of each subsystem into the inversed system response matrix for excitation of each subsystem individually [8]. The efficiency of the method decreases for large number of subsystems [8] and to avoid the result of negative CLFs the subsystems must be weakly coupled [46]. ESEA could also work when the subsystems have low modal overlap and low mode counts [49].

In this thesis, FEM ESEA is used to determine the CLFs in beam junctions with surface-to-surface contact conditions and in damaged beam-to-column junctions when either only one type of wave motion is considered or two or more types of wave motion can be considered simultaneously.

1.3 Aims

The main aims of this thesis are:

1. To experimentally validate FEM models of non-bonded concrete beams when in contact with each other and identify a suitable contact stiffness value for surface-to-surface or edge-to-surface contact conditions.
2. To assess the potential to use SEA to model vibration transmission between two reinforced concrete beams when they are stacked on top of each other and investigate are (a) whether it is possible to only consider one type of wave motion (bending waves) or whether two or more types of wave motion can be considered simultaneously (bending and torsional waves) and (b) whether analytical models based on lump spring connectors can be used to model the contact condition.
3. To investigate whether SEA could be used to model vibration transmission in piles of more than two reinforced concrete beams when they are stacked on top of each other.
4. To assess the potential to use SEA to model vibration transmission in damaged beam-to-column junction and investigate (a) whether the number of the subsystems affects the validity and accuracy of FEM ESEA and (b) whether it is possible to only consider one type of wave motion (e.g. bending waves) or whether two or more types of wave motion could be considered simultaneously (e.g. bending and torsional waves).

1.4 Thesis layout

The layout of the chapters in this thesis is as follows.

Chapter 2 describes the experimental work carried out on individual reinforced concrete beams and beam junctions.

Chapter 3 presents the theory and the numerical models used in this thesis.

Chapter 4 investigates the normal contact stiffness between reinforced concrete beams by experimentally validating FEM models of beam junctions where the beams are stacked on top of each other without any bonding material and the interaction between the beams is modelled by using either linear elastic contacts or linear elastic springs.

Chapter 5 assess the potential to use SEA to model vibration transmission between two reinforced concrete beams when they are stacked on top of each other. Numerical experiments with FEM are used to create an ensemble of beam junctions for a Monte Carlo simulation to allow use of FEM SEA to determine CLFs between the beams. These are compared with the CLFs from an analytical model of a lump spring connector.

Chapter 6 applies SEA to two piles of reinforced concrete beams. SEA path analysis is carried out to quantify and assess the strength of the transmission paths between the beams and the general SEA matrix solution is used to estimate the energy ratios between the beams of the piles using: a) FEM ESEA CLFs and b) the CLFs from an analytical model of a lump spring connector. SEA predictions are compared against the results of FEM models.

Chapter 7 assesses the potential to use SEA to model the vibration transmission in seismic damaged reinforced concrete beam-to-column junctions. The FEM model of a rigid T-junction is validated against the wave theory in terms of CLFs that only consider bending wave motion. A concrete discontinuity is then introduced at the connection of the beam with the column and the resulting FEM model is used to carry out numerical experiments with FEM to create an ensemble of damaged beam-to-column junctions for a Monte Carlo simulation. This allows use of ESEA to determine CLFs between the beam and the column.

Chapter 8 summarises the main conclusions and provides suggestions for further work.

2. Experimental work

2.1 Introduction

This chapter describes the experimental work which has been carried out on individual reinforced concrete beams and beam junction used for validating the predictive approaches in chapters 3 – 6.

2.2 Experimental work

2.2.1 Reinforced concrete beams

The experimental samples consist of three reinforced concrete beams with the same dimensions; these were 2.4 m in length with a rectangular cross-section of 200 × 300 mm. A Class 25/30 concrete (C25/30) with a characteristic cylinder crushing strength (f_{ck}) of 25 MPa and cube strength of 30 MPa was selected for casting the beams. C25/30 concrete is commonly used in the construction industry [53]. Grade 500 steel (S500) with a characteristic yield strength (f_{yk}) of 500 MPa was selected for the reinforcement. Grade 500 has replaced Grade 250 and Grade 460 reinforcing steel for construction works [53].

As indicated in Figure 2-1, beam 1 is reinforced with four longitudinal steel bars of 16 mm diameter (4H16) whereas beams 2 and 3 are reinforced with eight longitudinal steel bars of 16 mm diameter (8H16). The transverse reinforcement consists of 8 mm diameter stirrups placed at 200 mm centres (H8/200) along beams 1, 2 and 3. Beam 3 was designed to have a 100 mm wide discontinuity in the centre to simulate an (idealised) fracture that could occur in a collapsed building (see section 1.2.1).

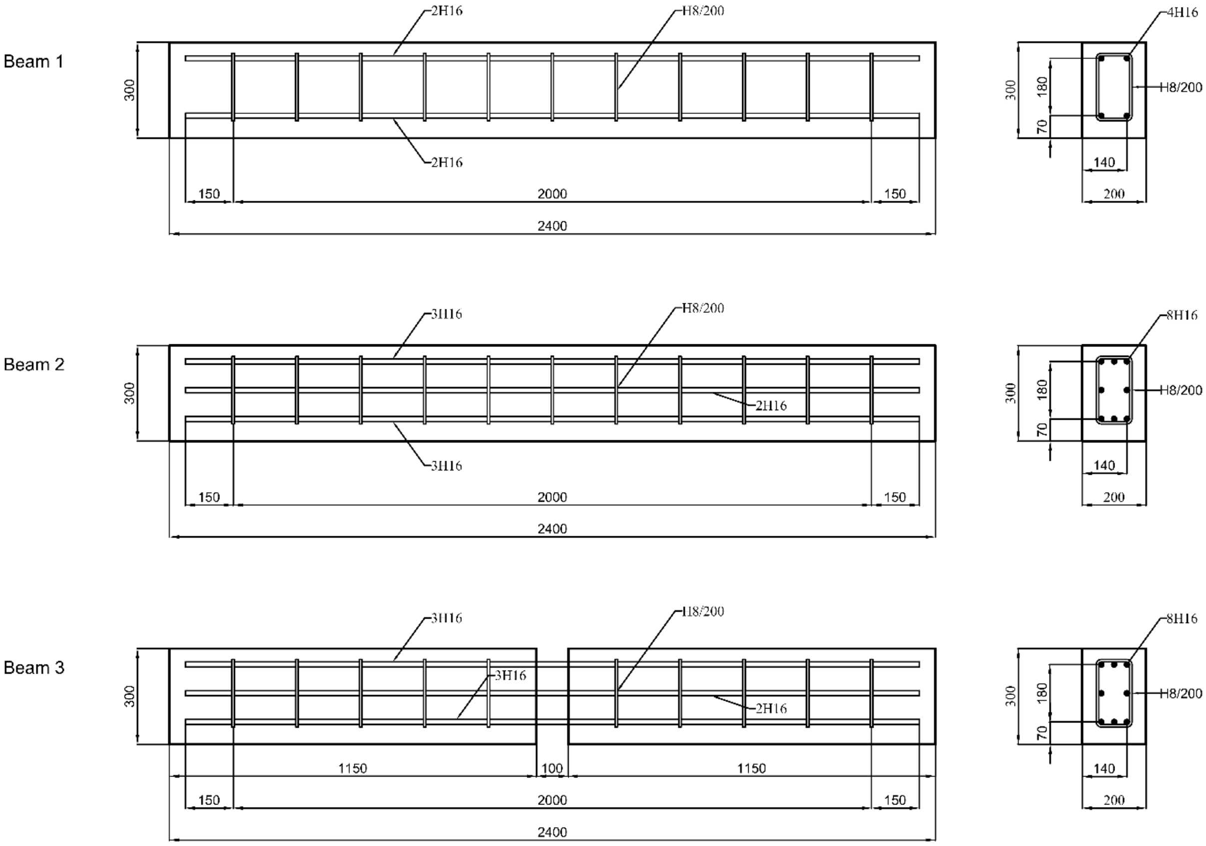

Figure 2-1 Structural details of the experimental samples (units: millimetres).

2.2.2 Test setups

The test setups for the beams were arranged so that they could be tested individually in isolation and when forming a junction with surface-to-surface or edge-to-surface contact conditions. Note that the term edge-to-surface is used because an edge on one beam makes a line connection across the surface area of the other beam.

2.2.2.1 Individual beams

Setups I1, I2 and I3 refer to isolated beams 1, 2 and 3 respectively when suspended from a crane using polyester slings. These beams are assumed to have free support conditions which avoids any additional uncertainty in the model updating process when modelling boundary conditions. The slings were assumed to have negligible effect on the dynamic response. The beams were orientated so that bending wave motion occurred across the longer dimension of the cross-section (i.e. 300 mm thickness).

2.2.2.2 Junctions

For the beam junctions, it was necessary to support the lower beam (beam 1). Hence setup I4 was created with beam 1 orientated such that bending wave motion was across the shorter dimension of the cross-section (i.e. 200 mm thickness) and the lower surface rested upon a square-section solid aluminium bar (25×25 mm) at each end. This aluminium bar rested on two concrete blocks (each 440×215×100 mm) stacked on top of each other; this was necessary to elevate them 200 mm above the ground for the operation of the crane that moved the beams.

Setups J1 - J5 (see Figure 2-2) were selected to investigate the effect of: (a) the contact area, (b) the relative position and the angle between the beams, (c) the contact type (surface-to-surface or edge-to-surface) and (d) the number of the beams on the dynamic behaviour of the junctions.

Setups J1, J2 and J3 were formed after placing beam 2 on top of beam 1 in setup I4 to create a surface-to-surface contact condition. In setups J1 and J2, the angle between the beams is equal to 90° but the beams are in contact at different positions along the length (see Figure 2-2a and b). In Setup J3 the two beams are at an angle of 41°; this angle was determined by the available space in the laboratory (see Figure 2-2c).

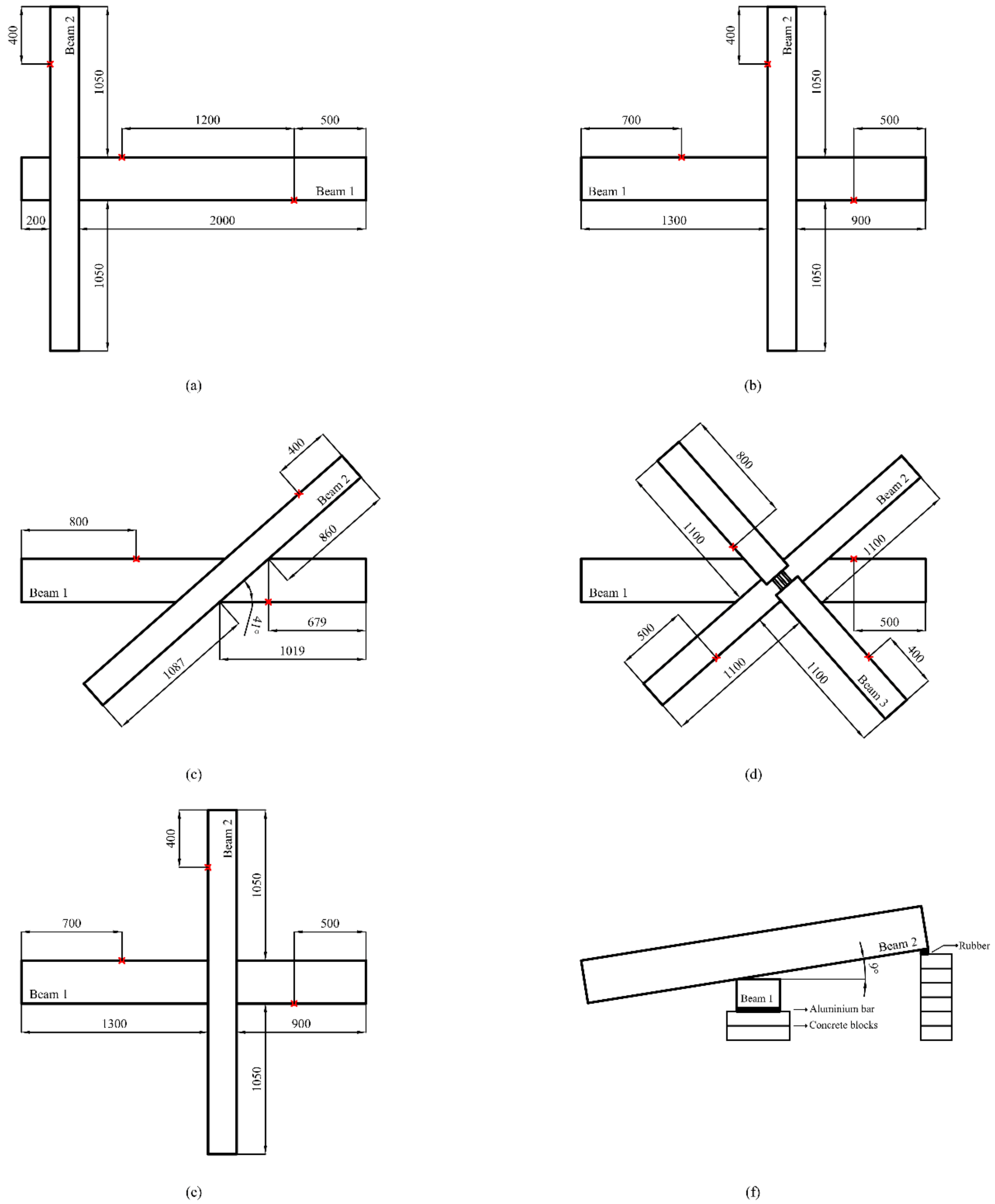

Figure 2-2 Test setups of the beam junctions: (a) Setup J1, (b) Setup J2, (c) Setup J3, (d) Setup J4, (e) Setup J5 – Plan view and (f) Setup J5 – Side view (units: millimetres). The red markers indicate the positions of the accelerometers (see Table 2-1).

In setup J4, beam 3 was placed on top of setup J3 to create a pile of three beams with surface-to-surface contact conditions – see Figure 2-2d. Beams 2 and 3 form a cross for reasons of stability since there are no supports at their ends.

Setup J5 is identical to setup J2 except for the inclination angle of ≈9° between the two beams. To create edge-to-surface contact conditions, one end of beam 2 was elevated by 600 mm using six stacked aggregate concrete blocks with 30 mm thick rubber (60 mm length) to isolate beam B from the concrete blocks (see Figure 2-2e and 2f). The stiffness of the rubber material was measured according to ISO 9052-1 [54] (see section 2.2.4).

2.2.3 Experimental modal analysis

Experimental Modal Analysis (EMA) is used to identify the material properties, damping and the modal characteristics of the individual beams and the beam junctions using FFT analysis with 1 Hz frequency lines. Brüel & Kjær Pulse Reflex software was used for signal processing and EMA. As it is shown in Figure 2-3, the beams were excited using an impact hammer (Brüel & Kjær Type 8200) and the response was measured using accelerometers (Brüel & Kjær Type 4371). The transducers were connected to an FFT analyser (Brüel & Kjær Type 3050-A-060) via a Nexus Conditioning Amplifier (Brüel & Kjær Type 2692).

To avoid altering the natural frequencies of the test setups when removing and remounting the accelerometers at different positions, the roving hammer technique was selected over the roving accelerometers technique for modal testing. The accelerometers remained at fixed positions (see red markers in Figure 2-2) whilst the impact hammer was moved along a mesh of excitation points with spacing between 0.10 and 0.20m.

Table 2-1 shows the number of the accelerometers and the number of the excitation positions for each setup. Only out-of-plane acceleration was measured, except in setups I1, I2 and I3 where the response was measured in all three coordinate directions.

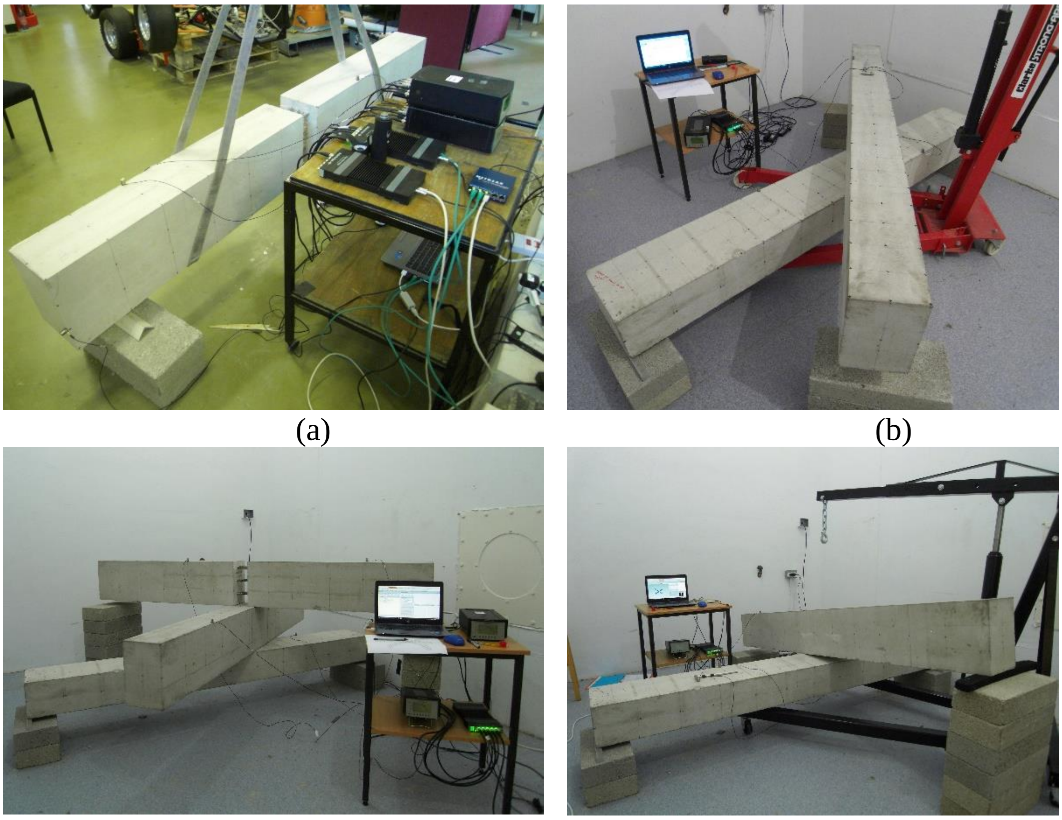
(a) (b)

(c) (d)

Figure 2-3 Test equipment and transducers for test setups: (a) I3, (b) J3, (c) J4 and (d) J5.

Table 2-1 Accelerometers and excitation positions per setup (see Figure 2-2).

Test setup	**Description**	**Accelerometers**		**Hammer positions**	
		In-plane[1]	Out-of-plane[2]	In-plane	Out-of-plane
I1	Beam 1 – sling supports	2	1	128	78
I2	Beam 2 – sling supports	2	1	128	78
I3	Beam 3 – sling supports	4	2	160	84
I4	Beam 1 – aluminium supports	-	3	-	100
J1	Junction of two beams (1&2) (surface-to-surface)	-	3	-	171
J2	Junction of two beams (1&2) (surface-to-surface)	-	3	-	171
J3	Junction of two beams (1&2) (surface-to-surface)	-	3	-	167
J4	Pile of three beams (1,2&3) (surface-to-surface)	-	4	-	242
J5	Junction of two beams (1&2) (edge-to-surface)	-	3	-	171

2.2.4 Dynamic stiffness measurement for the rubber material according to ISO 9052 -1

Figure 2-4 shows the measurement setup for the dynamic stiffness of the rubber material which was used in setup J5 for isolating beam 2 from the concrete blocks (see section 2.2.2.2). This corresponds to a mass – spring system where a sample of rubber material with dimensions 200 x 200 mm is placed on a rigid concrete cube and an 8 kg steel load plate with the same dimensions is installed on the top of the rubber material.

According to ISO 9052 Part 1 [54], between the rubber material and the steel load plate should exist a sheet of a waterproof material and a layer of plaster of Paris to remove any surface irregularities and ensure excitation over the entire surface of the sample.

---

[1] In plane transducer = excites/measure the response in a direction parallel to the ground plane

[2] Out-of-plane transducer = excites/measure the response in a direction normal to the ground plane

However, in this measurement the steel load plate was directly attached to the rubber material.

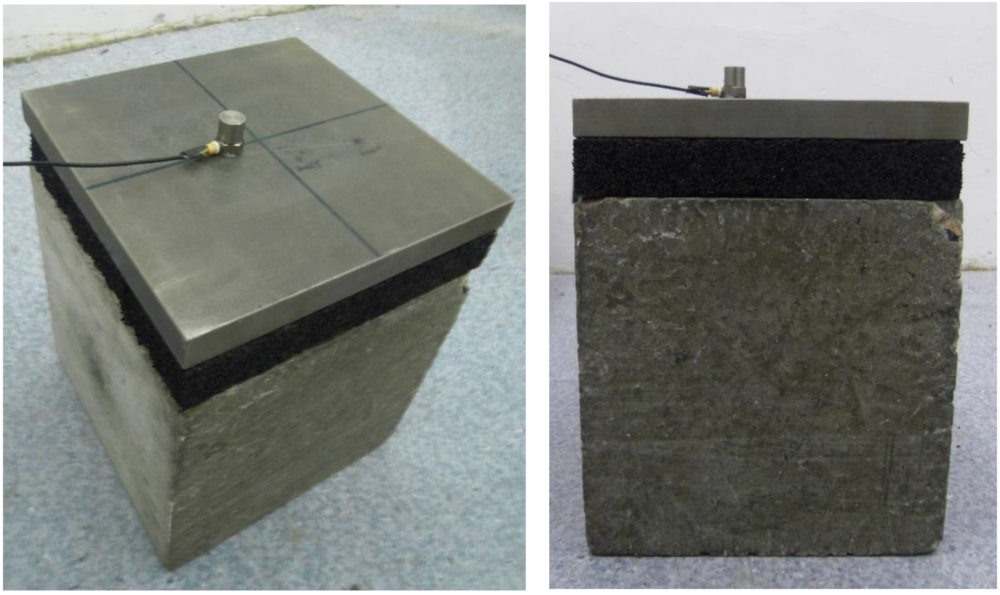

Figure 2-4 Measurement setup for the dynamic stiffness of the rubber material.

An impact hammer (Brüel & Kjær Type 8200) was used to measure the input force and an accelerometer (Brüel & Kjær Type 4371) was positioned slightly off centred to measure the vertical vibration of the load plate. The excitation force was applied to the centre of the load plate so that there is only a vertical component to the vibration. The transducers were connected to an FFT analyser (Brüel & Kjær Type 3050-A-060) via a Nexus Conditioning Amplifier (Brüel & Kjær Type 2692). All the signal processing was carried out using Brüel & Kjær Pulse Reflex using FFT analysis with 0.3125 Hz frequency lines.

The resonant frequency, f_{ms}, of the mass – spring system is given by [46],

$$f_{ms} = \frac{1}{2\pi}\sqrt{\frac{k}{m}} \tag{2.2.1}$$

where k is the stiffness of the rubber sample and m the mass of the steel load plate.

For lightly damped systems the resonant frequency can be determined by the peak in the magnitude of the driving-point mobility, Y_{dp} [46]. Figure 2-5 shows the magnitude of the driving-point mobility in the frequency range from 20 to 500 Hz. The peak occurs at 59.06 Hz. By replacing this value in Eq. (2.2.1), the stiffness k of the rubber material was calculated equal to 27512887.25 N/m^3.

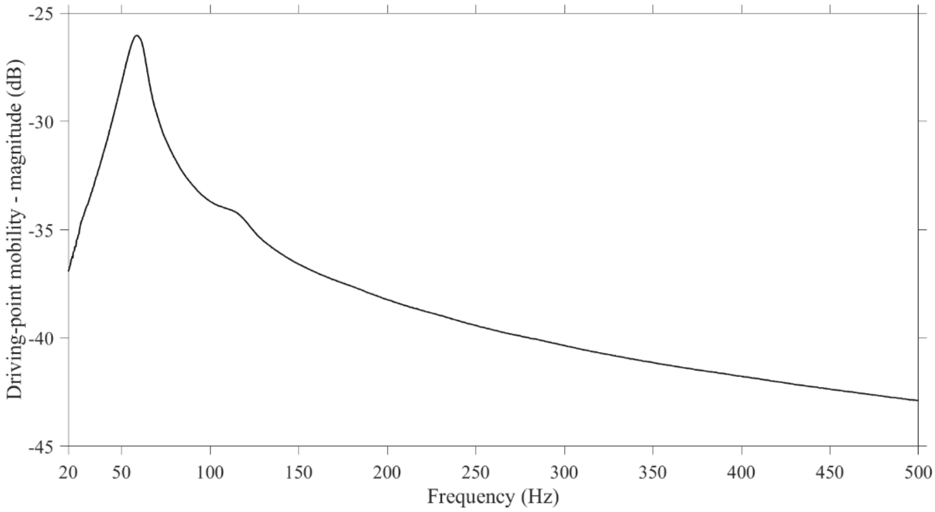

Figure 2-5 Driving-point mobility for the rubber sample.

2.3 Conclusions

Experimental Modal Analysis was carried out using the roving hammer technique to determine the dynamic characteristics of individual reinforced concrete beams and beam junctions with surface-to-surface and edge-to-surface contact conditions. The results of the experimental work will be used for validating the predictive approaches in chapters 3 – 6.

3. Theory and modelling

3.1 Introduction

This chapter describes (a) Finite Element Method and (b) Statistical Energy Analysis as predictive methods used in this thesis.

3.2 Finite Element Method

The fundamental concept of FEM is to divide the domain of interest (e.g. a structure) into a finite number of simple sub-domains (elements) and uses numerical methods (interpolation and integration) to construct an approximation of the solution over the collection of sub-domains [55]. With this approach, problems with complex geometry, complex boundary conditions or other complexities are possible to find an approximate solution whereas this was not possible before using analytical methods.

Today, many commercial finite element analysis software packages are available for use on personal computers to obtain solutions to large problems in static and dynamic analysis, heat transfer, fluid flow, electromagnetics, seismic response and acoustics. For the finite element models of beams in this thesis the finite element software Abaqus was used with the programs Abaqus/Standard and Abaqus/CAE (version 6.14). All FEM models in this thesis used Abaqus software (Version 6.14) [56].

3.2.1 Analysis methods

3.2.1.1 Eigenvalue analysis

Natural frequencies and mode shapes of vibration of a mechanical system were determined using eigenvalue analysis based on the elastic (stiffness, K) and inertia (mass, M) characteristics of the system [20].

The results of the eigenvalue analysis (i.e. eigenfrequencies and mode shapes) are used in this thesis for the validation and updating of the finite element models.

For a multi-degree of freedom system (*N*-DOF), the eigenvalue problem can be written as [57],

$$\left[[K] - \omega_n{}^2[M]\right]\{\Phi_n\} = 0 \tag{3.2.1}$$

where $[K]$ is the stiffness matrix of the system, $[M]$ is the mass matrix of the system, ω_n is the natural angular frequencies of vibration and $\{\Phi_n\}$ is the matrix of the natural modes of vibration.

The natural angular frequencies of an *N*-DOF system can be obtained by solving Eq. 3.2.2 [57]. This equation has N roots and each root corresponds to one independent natural angular frequency, ω_n of the system.

$$det\left[[K] - \omega_n{}^2[M]\right] = 0 \tag{3.2.2}$$

Inserting the N natural angular frequencies, ω_n of the system in Eq. (3.2.1) gives N independent vectors of the natural modes of vibration, $\{\Phi_n\}$. The natural modes, $\{\Phi_n\}$ and $\{\Phi_r\}$ corresponding to different natural angular frequencies, ω_n and ω_r must satisfy the following orthogonality criterion [57],

$$\left\{\Phi_n{}^T\right\}[K]\{\Phi_r\} = 0 \qquad\qquad \left\{\Phi_n{}^T\right\}[M]\{\Phi_r\} = 0 \tag{3.2.3}$$

Orthogonality makes the modal solutions independent and the corresponding mode shapes normal. It also makes the infinite set of modal solutions a complete set, or a basis, so that any arbitrary response can be formed as a linear combination of these normal mode solutions [58].

In Abaqus/Standard the default eigenvalue extraction method is Lanczos. This was used in the frequency range from 1 to 3200 Hz to extract the eigenfrequencies and the mode shapes of: (a) the individual beams and beam junctions in chapters 4 and 5, (b) the pile of beams in chapters 4 and 6 and (c) the beam-to-column junctions in chapter 7. The upper frequency limit of 3200 Hz had to be established since Lanczos solver was resulting to spurious modes for the beam elements of the reinforcement bars above that frequency.

3.2.1.2 Mode-based steady-state dynamic analysis

Steady-state dynamic analysis provides the steady-state amplitude and phase of the response of a system due to harmonic excitation at a given frequency. Usually such analysis is done as a frequency sweep by applying the loading at a series of different frequencies and recording the response [56].

For a multi degree of freedom system that exhibits harmonic excitation, the equation of motion can be written as [59],

$$[M]\{\ddot{u}\} + [C]\{\dot{u}\} + [K]\{u\} = \{f\}\exp(i\omega t) \qquad (3.2.4)$$

where $\{u\}$ is the column matrix of nodal displacements, $[M]$ is the mass matrix, $[C]$ is the damping matrix, $[K]$ is the stiffness matrix, $\{f\}\exp(i\omega t)$ is the column matrix of equivalent harmonic nodal forces and ω is the angular frequency of the harmonic forces.

In this thesis, the mode-based steady-state analysis was chosen over other types of steady-state dynamic analyses which are available in Abaqus/Standard (e.g. direct-solution and subspace) because it is computationally cheaper while the user can select the number and the type of the modes that participate in the analysis. However, when frequency-dependent material damping is involved the mode-based steady-state analysis offers less accurate solutions [56].

In a mode-based steady-state dynamic analysis the response is based on modal superposition techniques where the modes of the system must first be extracted using the eigenfrequency extraction procedure.

The modal mass matrix, $[\bar{M}]$, the modal damping matrix, $[\bar{C}]$ and the modal stiffness matrix, $[\bar{K}]$ of the system are given by [59],

$$\begin{aligned}[\bar{M}] &= [\Phi^T][M][\Phi] \\ [\bar{C}] &= [\Phi^T][C][\Phi] \\ [\bar{K}] &= [\Phi^T][K][\Phi]\end{aligned} \qquad (3.2.5)$$

where $[\Phi]$ is the matrix of the eigenmodes, $[M]$ is the mass matrix, $[C]$ is the damping matrix and $[K]$ is the stiffness matrix of the system.

If Eq. (3.2.3) is satisfied and using the formulas of Eq. (3.2.5) the solution of Eq. (3.2.4) can be expressed in the form [59],

$$\{u\} = [\Phi]\big[[\Lambda] - \omega^2[I] + i\omega[\bar{C}]\big]^{-1}[\Phi]^T\{f\}\exp\,(i\omega t) \qquad (3.2.6)$$

where $\{u\}$ is the column matrix of nodal displacements, $[\Phi]$ is the matrix of the eigenmodes, $[\Lambda]$ is the diagonal matrix of the angular frequencies of the system equal to $[\bar{K}]$, $[I]$ is the unit matrix, $[\bar{C}]$ is the modal damping matrix, ω is the angular frequency of the harmonic forces and $\{f\}\exp\,(i\omega t)$ is the column matrix of equivalent harmonic nodal forces.

For the beam junctions in chapter 4, mode-based steady-state dynamic analysis was used to calculate vibration transmission between the beams in test setups J3, J4 and J5. Only the experimentally validated modes were included into the mode-based analysis.

The nodes of the top surface of the beams were excited sequentially by applying a unit perpendicular force over a 100 mm square grid which approximately corresponds to the hammer positions used in EMA.

In chapter 5, mode-based steady-state dynamic analysis was used to calculate the driving-point mobilities of the individual beams and the dynamic response of the beam junctions up to 3200 Hz considering (a) the out-of-plane bending modes, (b) the torsional modes and (c) the combination of all modes (bending, torsional and others).

In chapter 6, mode-based steady-state dynamic solver to calculate the dynamic response of the piles up to 3200 Hz when considering the combination of all modes.

For the beam-to-column junctions in chapter 7, mode-based steady-state dynamic analysis was used to calculate the dynamic response of the beam-to-column junctions up to 3200 Hz considering (a) out-of-plane bending modes and (b) the combination of all modes.

The direct damping based on the modal damping identified in the experimental work was used for the dynamic analyses of chapter 4. For the numerical experiments, the damping ratio, ζ, was set to be equal to 0.05 except for the steady-state analyses of section 5.4.1 where two values of damping ratios were considered: (a) ζ=0.05 and (b) ζ=0.005. A damping ratio of 5% is commonly recommended for the seismic design of reinforced concrete structures [60] and represents all sources of damping associated with yielding of members including any structural damping due to cracking of concrete members and energy dissipation during pre-yield cycles [17]. A damping ratio of 0.5% approximates internal losses in fully cracked reinforced concrete members without yielded reinforcements [61].

3.2.2 FEM modelling of the experimental setups

3.2.2.1 Beams

The concrete and the steel bars were modelled using solid element C3D20R (20 nodes) and beam element B32 (3 nodes) respectively. Both elements were selected to have interpolation functions of the same order (quadratic) to avoid a reduction in accuracy [20]. In addition, quadratic elements were found to be more accurate than linear elements thus they were preferred in this thesis. The element mesh had dimensions of 25 mm along the length of the beam and 20 mm over the beam cross-section to fulfil the requirement of at least six quadratic elements per bending wavelength up to 3200 Hz [28].

3.2.2.2 Aluminium supports

The linear spring element, SPRING1 was used to approximate the elastic support that the square aluminium bars provide to beam 1 – see Figure 3-1. The stiffness of the springs was estimated to be 4.1E05 N/m after model updating against the experimental results for beam 1 on the aluminium supports (setup I4). Numerical trials with different spring stiffness values were carried out until the lowest eigenfrequency (bending mode) from FEM and measurements were identical to one decimal place (193.8 Hz).

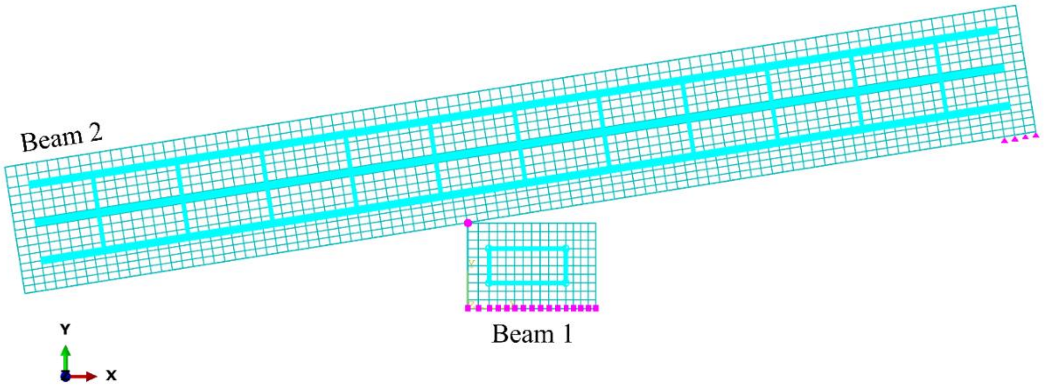

Figure 3-1 FEM model of test setup J5. The purple circles indicate the SPRING2 elements used for modelling the interaction between beams 1 and 2, purple squares indicate the SPRING1 elements that approximate the aluminium support and purple triangles indicate the SPRING1 elements that approximate the rubber support.

3.2.2.3 Rubber support

The linear spring element, SPRING1 (indicated by purple triangular markers in Figure 3-1) was selected from the element library of Abaqus to approximate the elastic support that the rubber material provides to beam 2 in setup J5. The stiffness of each of the springs was estimated to be 3236.8 N/m.

3.2.2.4 Surface-to-surface contact

The unbonded contact between the beams (see Figure 3-2) was modelled using the surface-to-surface contact algorithm of Abaqus/Standard and was defined to have elastic normal behaviour. When a contact is used in a linear perturbation step (such as in the eigenfrequency and steady-state analysis) the contact remains “closed” during the analysis when the starting condition is also closed [56]. Initial checks on the models confirmed that using a surface-to-surface contact with elastic normal behaviour during a linear perturbation step is equivalent to using an array of linear springs between the nodes of the two surfaces of the contact.

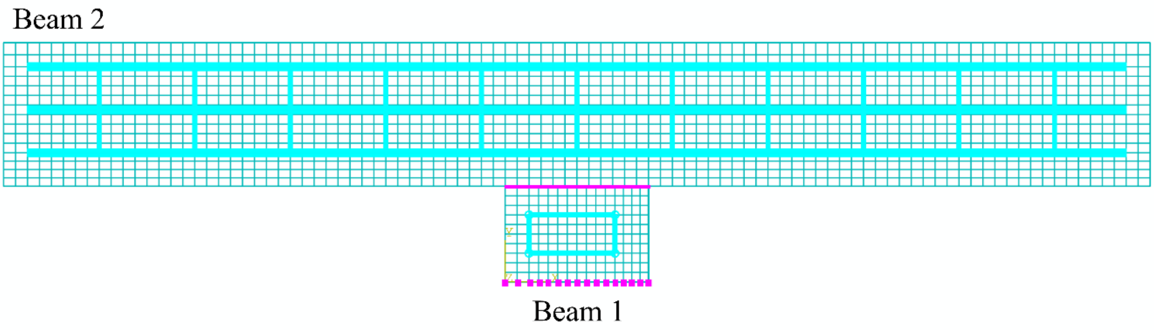

Figure 3-2 FEM model of test setup J2. The purple squares indicate the SPRING1 elements that approximate the aluminium support and the purple line indicates the surface-to-surface contact between beams 1 and 2.

The normal contact stiffness for each mode pair in setups J1, J2 and J3 was determined through model updating to give eigenfrequencies within 2% of the EMA eigenfrequencies.

3.2.2.5 Edge-to-surface contact

The linear spring element, SPRING2, was used to model the interaction between the edge nodes of beam 1 and the nodes along the lower surface of beam 2 in Setup J5 – see Figure 3-1. For every pair of coupled nodes, one horizontal and one vertical spring (acting in the X and Y directions respectively) were used to approximate a spring with a line of action normal to the lower surface plane of beam 2. The mean value of this stiffness was the same as determined from the surface-to-surface contact.

3.2.3 Validation criteria used to assess FEM and EMA

3.2.3.1 Mode shape criteria

The Modal Assurance Criterion (MAC) is used to assess the correlation between mode shapes from FEM and EMA using [62]

$$MAC(A,X) = \frac{|\{\varphi_X\}^{\mathrm{T}}\{\varphi_A\}^*|^2}{(\{\varphi_X\}^{\mathrm{T}}\{\varphi_X\}^*)(\{\varphi_A\}^{\mathrm{T}}\{\varphi_A\}^*)} \tag{3.2.7}$$

where A indicates FEM, X indicates the experiment, $\{\varphi_X\}$ and $\{\varphi_A\}$ are the column vectors of the degrees of freedom for the experimental and FEM mode shapes respectively (superscript T indicates the transpose) and $\{\varphi_X\}^*$ and $\{\varphi_A\}^*$ are the complex conjugate of vectors $\{\varphi_X\}$ and $\{\varphi_A\}$ respectively.

MAC values close to 1 indicate well correlated modes while MAC values close to 0 indicate uncorrelated modes [63]. In the literature (e.g. [64], [65]), MAC values above 0.9 correspond to good correlation whereas MAC<0.7 indicate weak correlation.

An important limitation of MAC is that it is sensitive to large values and insensitive to small values [66]. Therefore, if one subset of the modal vector is significantly larger than the remaining subset of the modal vector, then the MAC value will be mainly determined by the former subset and any lack of correlation related to the latter will not be identified by MAC. In this thesis, a subset is defined as the vector containing the degrees of freedom for each of the beams that form a junction. To overcome this problem, the Partial Modal Assurance Criterion (PMAC) [67] can be used to give insight into individual subsets of the modal vector by applying Eq. (3.2.7) to each subset separately. For two coupled beams it is feasible to consider the degrees-of-freedom on each beam as one subset. However, MAC and PMAC only describe correlation between the mode shapes and do not consider the relative response between different parts of the model. This is essential to assessing the connection between the beams in this thesis because it is necessary to check that the model correctly describes vibration transmission across the springs that are used to model the unbonded contact condition. The proposal in this thesis is to introduce an additional criterion, the Partial Modal Vector Ratio (PMVR) for which the results in chapter 4 will be used to establish PMVR values that indicate close or reasonable agreement between FEM and measurements. The PMVR is defined as the ratio in decibels of the squared modal vectors from EMA relative to FEM. For two subsets of the complete modal vector *i* and *j*, PMVR is given by

$$PMVR(A,X)_{i,j} = \left| 10\log_{10}\left(\left(\frac{\langle|\{\varphi_X\}_i|^2\rangle}{\left\langle\left|\{\varphi_X\}_j\right|^2\right\rangle}\right)\Big/\left(\frac{\langle|\{\varphi_A\}_i|^2\rangle}{\left\langle\left|\{\varphi_A\}_j\right|^2\right\rangle}\right)\right)\right| \qquad (3.2.8)$$

where{ φ_A} and { φ_X} are subsets of the modal vectors for FEM and EMA respectively from beams *i* and *j*.

3.2.3.2 Spatial-average transfer mobility ratio

Using point force excitation, a ratio of spatial-average transfer mobilities can be used to assess vibration transmission between two different beams in a junction. Using data from EMA or FEM, the spatial-average transfer mobility ratio, $YR_{ji,i}$, for two beams *i* and *j*, with force excitation on *i* is given by

$$YR_{ji,i} = 10\log_{10}\left(\frac{\left(\frac{1}{N}\sum_{k=1}^{N}\left|\frac{v_j}{F_i}\right|^2\right)}{\left(\frac{1}{N}\sum_{k=1}^{N}\left|\frac{v_i}{F_i}\right|^2\right)}\right) \qquad (3.2.9)$$

where *v* is the velocity, *F* is the force, *m* is the mass, *N* represents the number of nodes in the FEM model or the number of accelerometer positions used in EMA.

3.2.4 Numerical experiments with FEM

Based on the experimentally validated FEM models, numerical models were created with FEM. This section describes the FEM models used in these numerical experiments.

3.2.4.1 Material properties

Table 3-1 shows the physical and mechanical properties of the materials used in the FEM models of the numerical experiments in chapters 5 – 7. These represent the average of the values determined from the experimentally tested beams given in chapter 4 (see section 4.2.1).

Table 3-1 Material properties.

Material	Density, ρ (kg/m^3)	Young's modulus, E (N/m^2)	Poisson's ratio, ν (-)
Concrete	2287	34.7E09	0.2
Steel	7800	200E09	0.3

3.2.4.2 Junctions of two beams

The junctions of chapter 5 consist of two reinforced concrete beams, SS1 and SS2 (see Figure 3-3). SS1 is the lower beam of the junction with 6.0 m length, 0.3 m width and 0.2 m depth. SS2 is the upper beam of the junction with 5.0 m length, 0.2 m width and 0.3 m depth. Both beams are reinforced with four longitudinal steel bars of 16 mm diameter. The transverse reinforcement of both beams consists of 8 mm diameter stirrups placed at 200 mm centres along the beams.

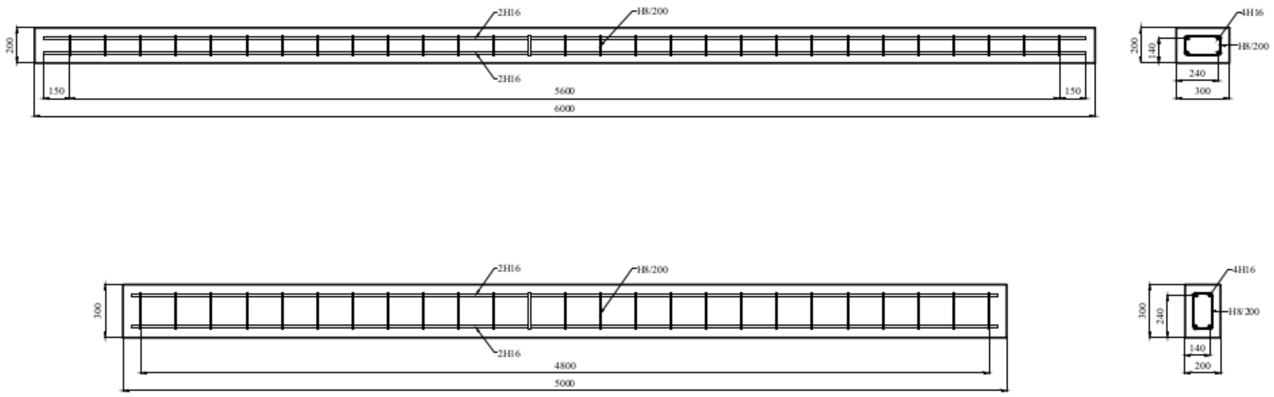

Figure 3-3 Geometry and reinforcement details of beams SS1 (top) and SS2 (bottom).

The solid element C3D20R (20 nodes) and the beam element B32 (3 nodes) were selected from the element library of Abaqus [56] to model the concrete and the steel bars respectively (see Figure 3-4). The mesh density fulfils the requirement for at least six elements per wavelength in structural and vibroacoustic problems [28]. The beams were either simply supported or free at both ends.

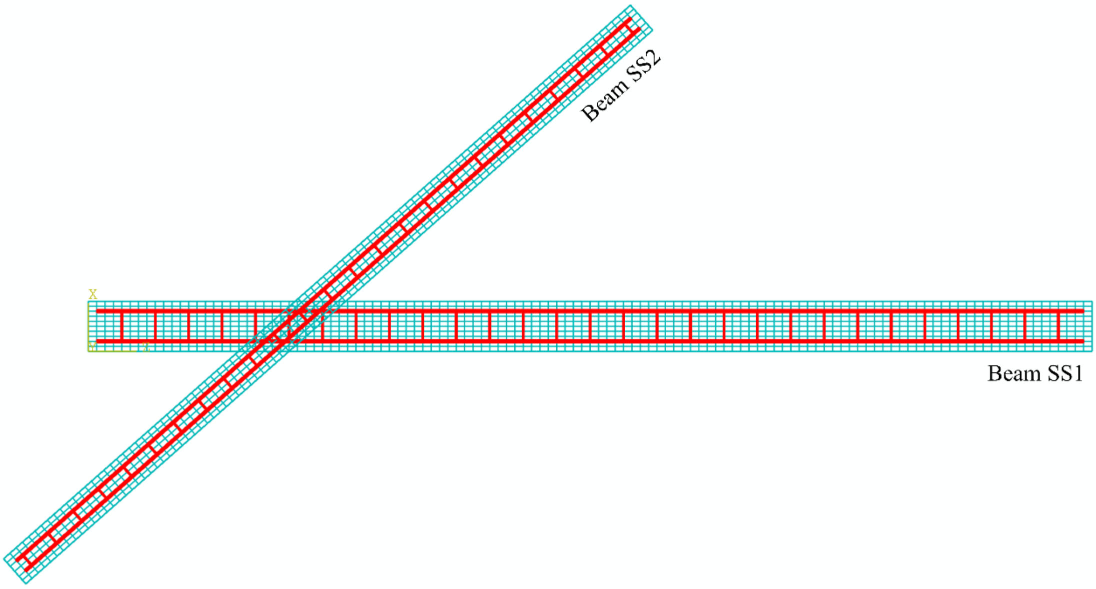

Figure 3-4 Example FEM model showing the surface-to-surface connection between beams SS1 and SS2.

The interaction between the two beams was modelled using an elastic contact in the normal direction as described in detail in section 3.2.2.4. In chapter 4, it will be shown that the contact stiffness follows a log-normal distribution with a mean value equal to 7.038E08 N/m and this value will be used for the elastic contact in the numerical experiments with FEM in chapter 5.

For calculating the driving-point mobilities of the individual beams SS1 and SS2, the upper surface of beam SS1 and the lower surface of beam SS2 were excited using a unit force (perpendicular to the surface) on 124 and 104 nodes respectively, indicated by the red markers in Figure 3-5.

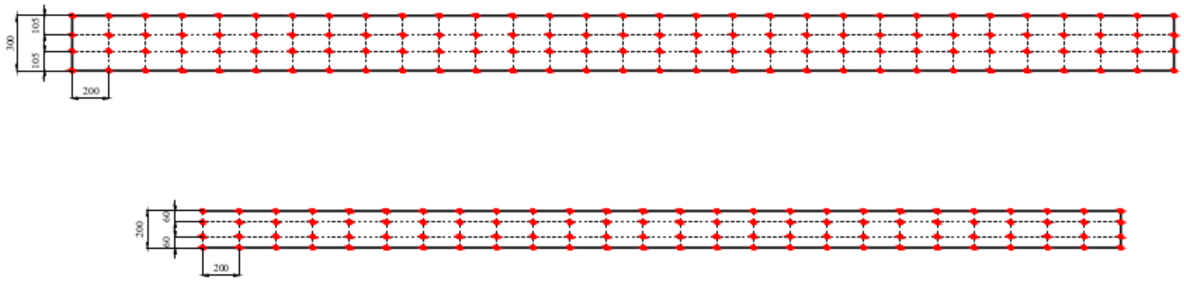

Figure 3-5 Excitation positions for the calculation of the driving-point mobilities of beams SS1 (top) and SS2 (bottom).

3.2.4.3 Piles of beams

Table 3-2 to Table 3-4 give the details of the geometry for piles 1a and 1b. Each colour in Figure 3-6 and Figure 3-7 indicates a different layer of beams. The shaded surfaces show the connection areas (using the colours of the two layers) between the beams of the pile using surface-to-surface contacts. The only difference between piles 1a and 1b is the one additional contact, C10 between beams SS2 and SS5.

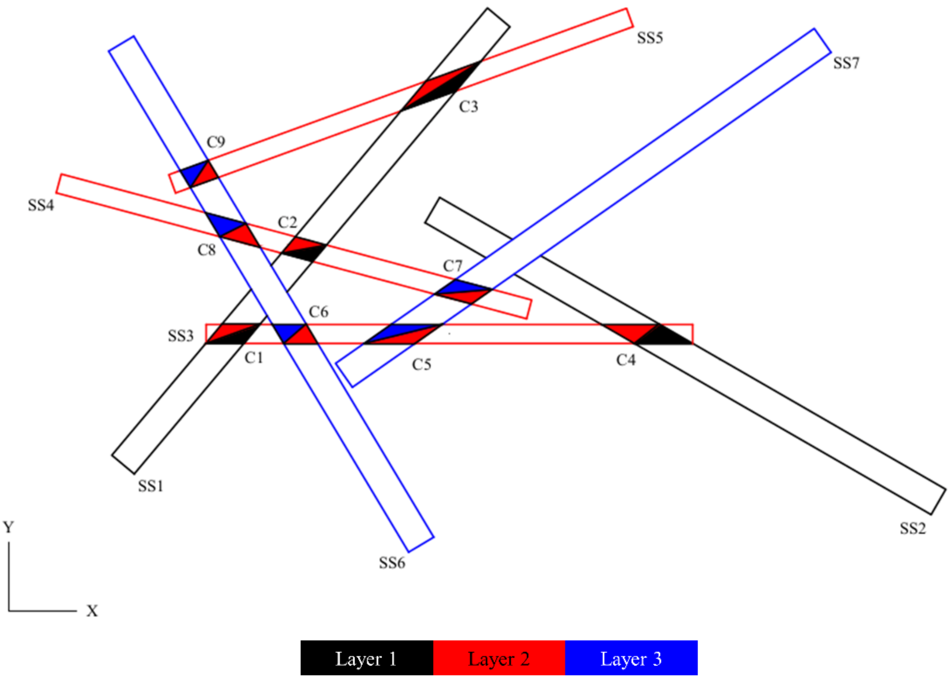

Figure 3-6 Pile 1a consists of seven beams with surface-to-surface contact conditions.

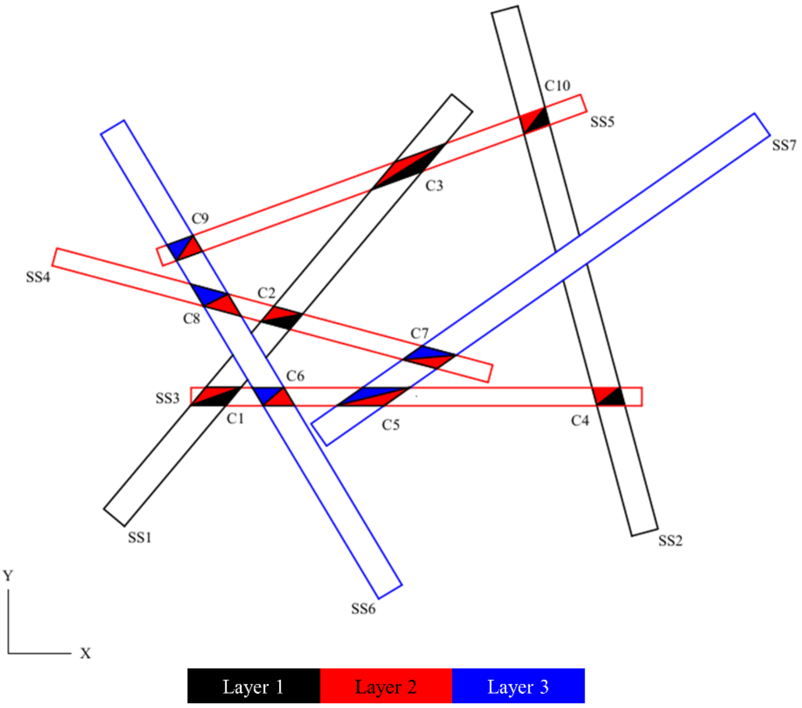

Figure 3-7 Pile 1b consists of seven beams with surface-to-surface contact conditions.

Table 3-2 Geometry of the beams of pile 1 (counter-clockwise angles are positive).

		SS1	**SS2**		**SS3**	**SS4**	**SS5**	**SS6**	**SS7**
			Pile 1a	Pile 1b					
Length (m)		6.0	6.0	6.0	5.0	5.0	5.0	6.0	6.0
Width (m)		0.3	0.3	0.3	0.2	0.2	0.2	0.3	0.3
Depth (m)		0.2	0.2	0.2	0.3	0.3	0.3	0.2	0.2
Centroid	x (m)	-1.4	2.4	1.8	0.0	-1.6	-0.5	-1.8	1.4
	y (m)	0.9	0.2	1.4	0.0	0.9	2.4	0.4	1.3
Angle (degrees)		50	-30	-75	0	-15	20	-59	35

Table 3-3 Contact areas between the beams of pile 1a.

C1 (cm^2)	C2 (cm^2)	C3 (cm^2)	C4 (cm^2)	C5 (cm^2)	C6 (cm^2)	C7 (cm^2)	C8 (cm^2)	C9 (cm^2)
783.2	662.0	1200.0	1200.0	1076.4	699.1	783.2	861.9	611.0

Table 3-4 Contact areas between the beams of pile 1b.

C1 (cm^2)	C2 (cm^2)	C3 (cm^2)	C4 (cm^2)	C5 (cm^2)	C6 (cm^2)	C7 (cm^2)	C8 (cm^2)	C9 (cm^2)	C10 (cm^2)
783.2	662.0	1200.0	621.2	1076.4	699.1	783.2	861.9	611.0	602.3

Table 3-5 and Table 3-6 present the geometry of pile 2. Each colour in Figure 3-8 indicate a different layer of beams, whereas the shaded surfaces show the connection areas between the beams of the pile using surface-to-surface contacts.

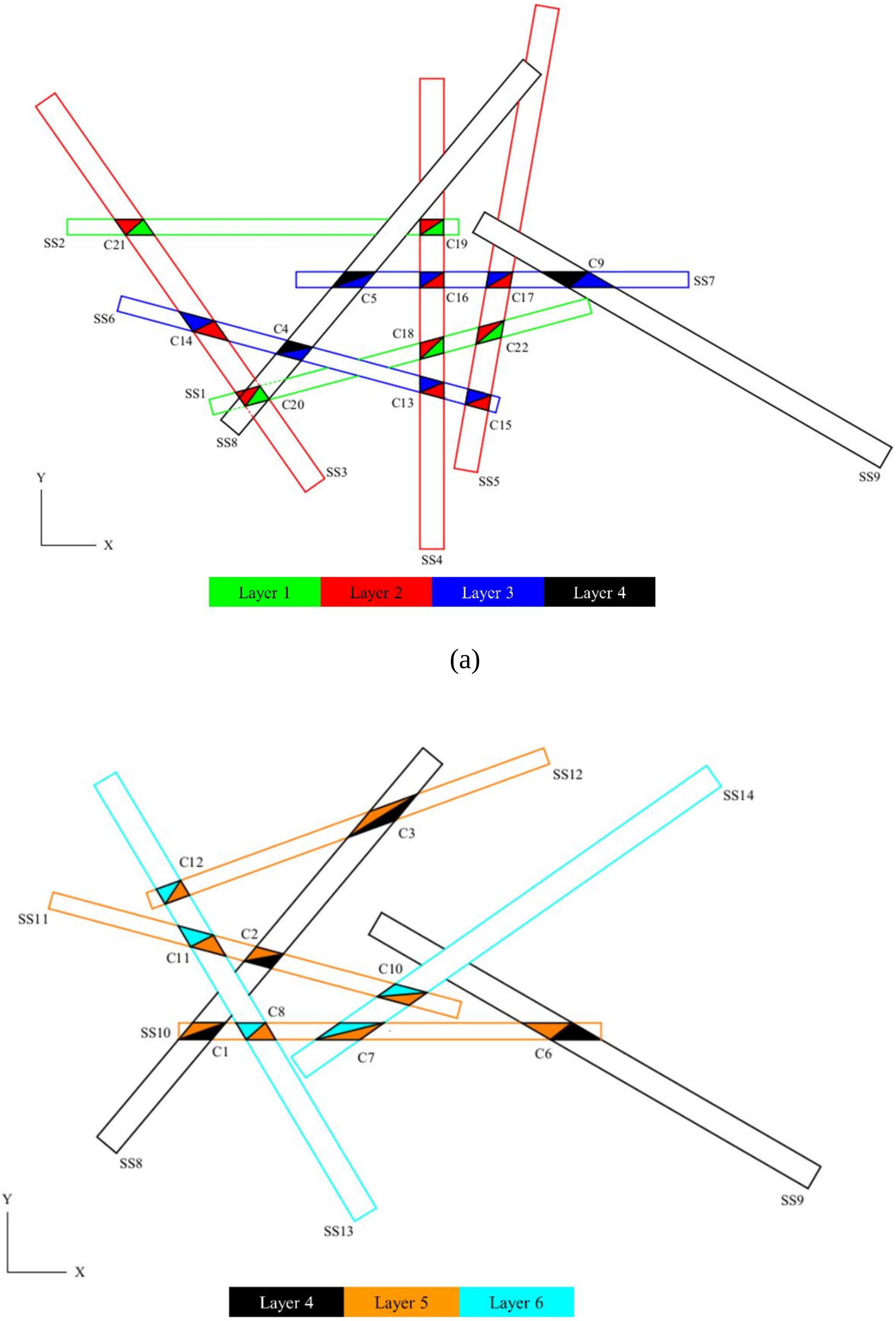

(a)

(b)

Figure 3-8 Pile 2 consists of 14 beams with surface-to-surface contact conditions: (a) layers 1 – 4 and (b) layers 4 – 6.

Table 3-5 Geometry of the beams of pile 2 (counter-clockwise angles are positive).

		SS1	**SS2**	**SS3**	**SS4**	**SS5**	**SS6**	**SS7**
Length (m)		5.0	5.0	6.0	6.0	6.0	5.0	5.0
Width (m)		0.2	0.2	0.3	0.3	0.3	0.2	0.2
Depth (m)		0.3	0.3	0.2	0.2	0.2	0.3	0.3
Centroid	x (m)	-3.6	-5.3	-6.4	-3.2	-2.2	-4.8	-2.4
	y (m)	-0.2	1.4	0.6	0.3	1.3	-0.2	0.8
Angle (degrees)		15	0	-55	90	80	15	0
		SS8	**SS9**	**SS10**	**SS11**	**SS12**	**SS13**	**SS14**
Length (m)		6.0	6.0	5.0	5.0	5.0	6.0	6.0
Width (m)		0.3	0.3	0.2	0.2	0.2	0.3	0.3
Depth (m)		0.2	0.2	0.3	0.3	0.3	0.2	0.2
Centroid	x (m)	-3.8	0.0	-2.4	-4.0	-2.9	-4.2	-1.0
	y (m)	1.2	0.0	0.2	1.1	2.6	0.6	1.5
Angle (degrees)		50	-30	0	-15	20	-59	35

Table 3-6 Contact areas between the beams of pile 2.

C1 (cm^2)	C2 (cm^2)	C3 (cm^2)	C4 (cm^2)	C5 (cm^2)	C6 (cm^2)	C7 (cm^2)	C8 (cm^2)	C9 (cm^2)	C10 (cm^2)	C11 (cm^2)
783.2	662.0	1200.0	662.0	783.2	1200.0	1046.1	699.1	1200.0	783.2	861.9
C12 (cm^2)	C13 (cm^2)	C14 (cm^2)	C15 (cm^2)	C16 (cm^2)	C17 (cm^2)	C18 (cm^2)	C19 (cm^2)	C20 (cm^2)	C21 (cm^2)	C22 (cm^2)
611.0	621.2	933.4	554.2	640.4	609.2	621.2	600.0	638.5	732.5	662.0

The experimentally validated FEM models of the beam junctions with surface-to-surface contact conditions were used as a basis for creating finite element models of three piles with: (a) seven reinforced concrete beams (Pile 1a and 1b) and (b) 14 reinforced concrete beams (Pile 2), arranged in three and six layers respectively (see Figure 3-9 and Figure 3-10). The piles were arranged to give multiple transmission paths between the layers of the beams and trying to avoid the overlapping of connection areas directly above each other. The ends of the beams were assumed to be free or simply supported. More information regarding the FEM modelling and the interaction between the beams of the piles is given in section 3.2.4.1.

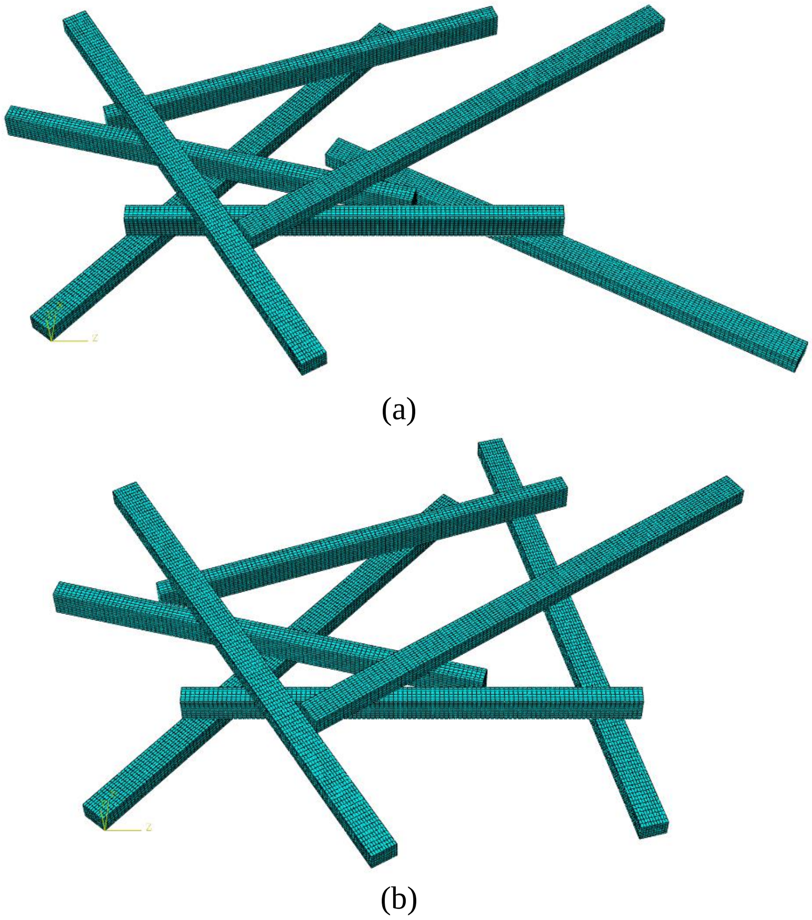

Figure 3-9 FEM models of pile 1a and pile 1b consisted of seven beams arranged in three layers.

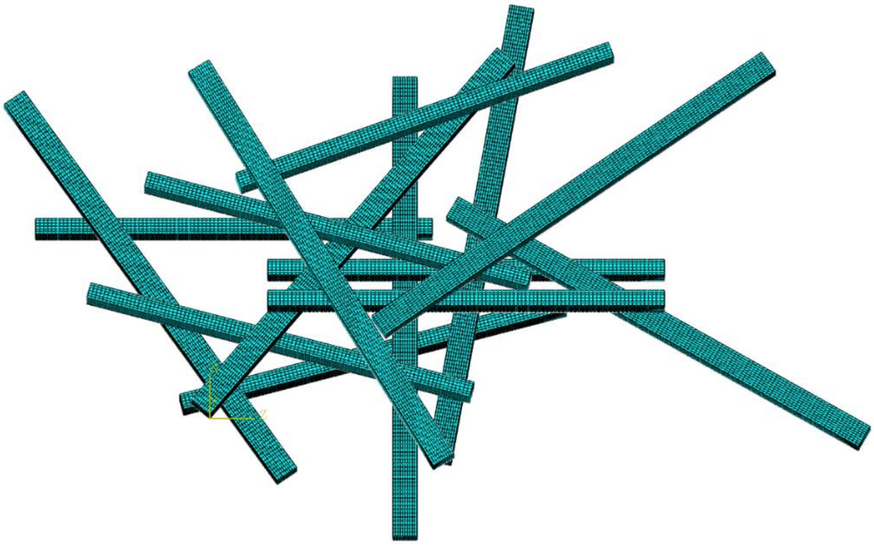

Figure 3-10 FEM model of the pile 2 consisted of 14 beams arranged in six layers.

In piles 1 and 2, all the nodes of the lower surface on beam SS1 were excited using rain-on-the-roof excitation (i.e. forces with unity magnitude and random phase). In both piles the out-of-plane response was extracted on all the nodes of the lower surface of the beams of each pile.

3.2.4.4 Beam-to-column junctions

The junctions consist of a reinforced concrete beam (5.1 m length, 0.3 m width and 0.5 m depth) and a reinforced concrete column (8.0 m length, 0.4 m width and 0.3 m depth) as it is shown in Figure 3-11. The beam and the column are reinforced with six and eight longitudinal steel bars of 16 mm diameter, respectively and the transverse reinforcement consists of 8 mm diameter stirrups placed at 200 mm centres along the beams (see Figure 3-12). Two types of junctions were considered as shown in Figure 3-11: (a) undamaged (rigid T-junction) and (b) damaged with a concrete discontinuity of 50 mm between the beam and the column. In addition, the beam is rotated by the angle, θ and connected to the column via the longitudinal steel reinforcement.

The solid element C3D20R (20 nodes) and the beam element B32 (3 nodes) were selected from the element library of Abaqus [56] to model the concrete and the steel bars respectively (see Figure 3-13 and Figure 3-14). The mesh density fulfils the requirement for at least six elements per wavelength for structural dynamics problems [28]. Tie constraints were used for modelling the rigid connection between the beam and the column in the undamaged junction. Both beam and column were assumed to be simply supported at the ends.

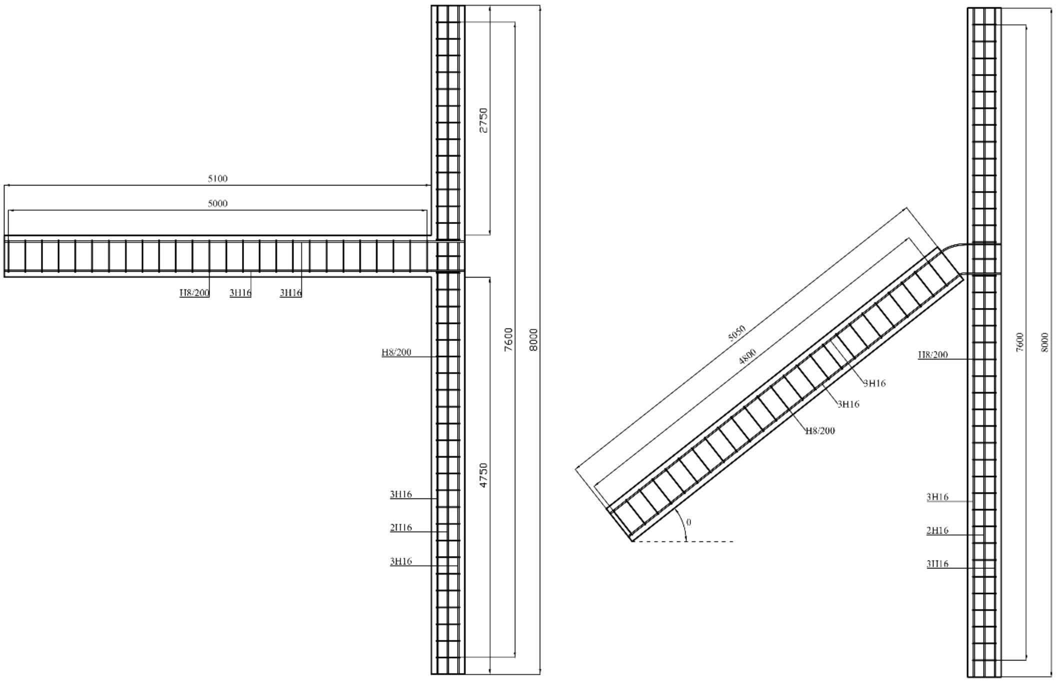

(a) (b)

Figure 3-11 Geometry and reinforcement details of: (a) an undamaged and (b) a damaged beam-to-column junction (units: millimetre).

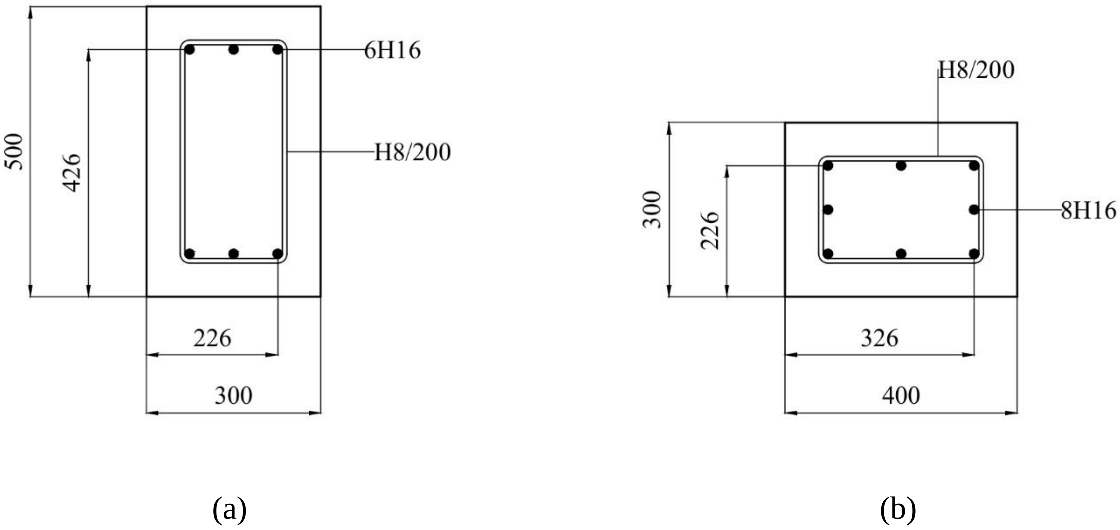

Figure 3-12 Cross-section details of the reinforced concrete members that for the junctions: (a) beam and (b) column (units: millimetre).

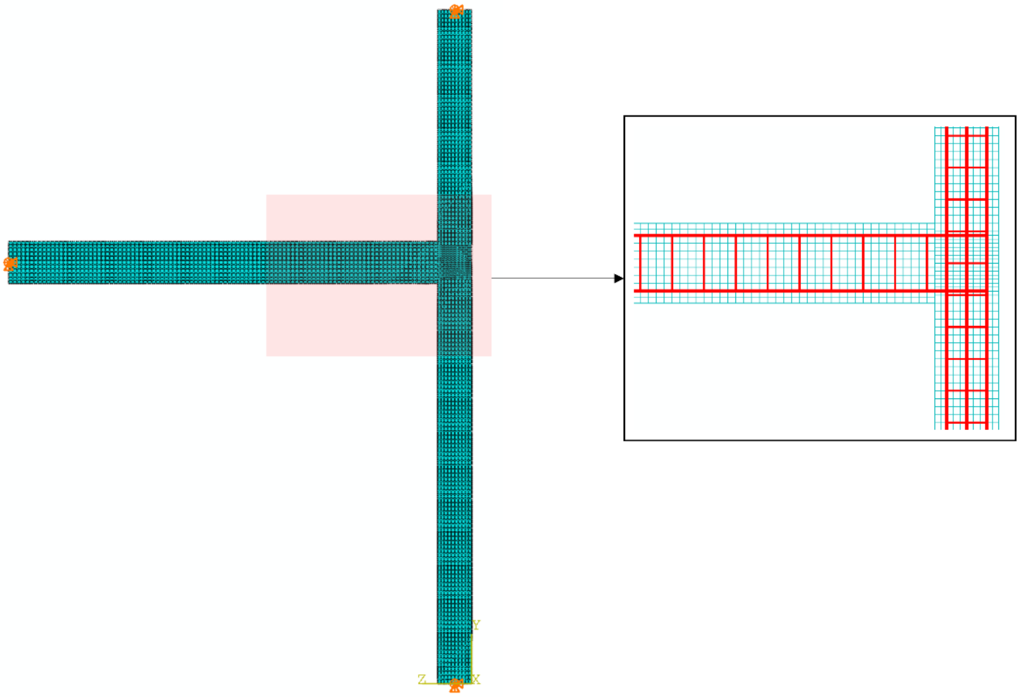

Figure 3-13 FEM model of a rigid beam-to-column T-junction. The orange symbols indicate the positions of the simple supports.

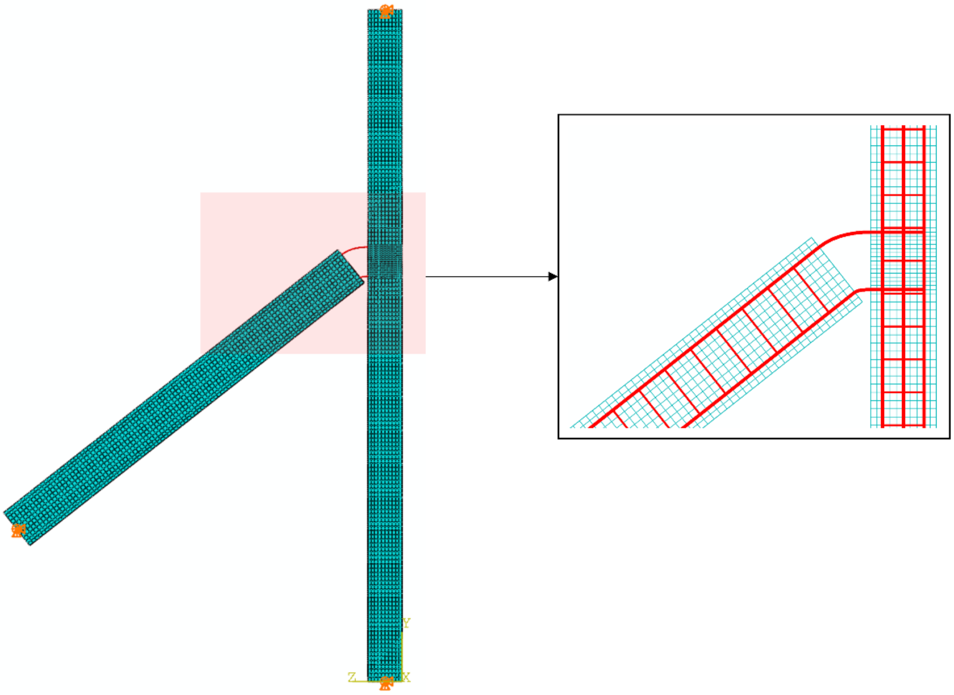

Figure 3-14 FEM model of a damaged beam-to-column T-junction. The orange symbols indicate the positions of the simple supports.

3.3 Statistical Energy Analysis

3.3.1 Classical SEA

SEA considers a structure as a number of coupled structural components (e.g. beams, columns, plates etc) which are called subsystems. Figure 3-15 shows an N-subsystem SEA model with only direct coupling between the subsystems. A power input is applied to subsystem 1 and the transmitted power from subsystem (N-1) to N is denoted by $W_{(N\text{-}1)\mathrm{N}}$. The power dissipated through internal losses and coupling losses to other subsystems is denoted by $W_{\mathrm{d}(N)}$.

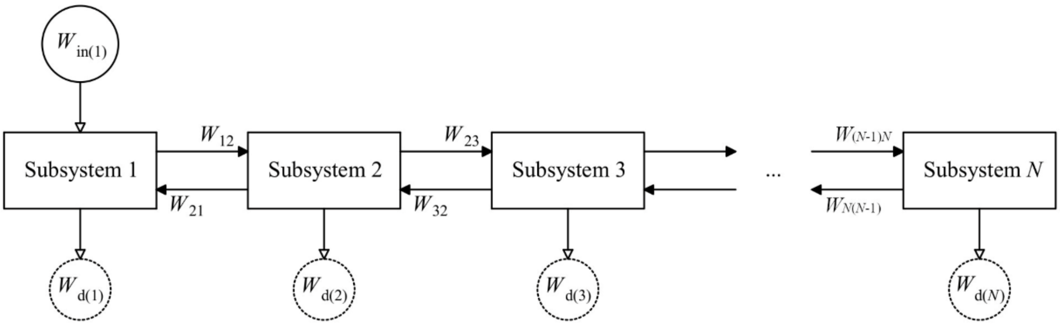

Figure 3-15 Schematic diagram of a N-subsystem SEA model showing only direct coupling.

In a SEA model the losses of a subsystem are described using three loss factors: (a) the internal loss factor (n_{ii}) which accounts for the energy of a subsystem that is mainly converted to heat, (b) the coupling loss factor (n_{ij}) which account for energy transferred to another subsystem and (c) the total loss factor which is the sum of the internal loss factor and all the coupling loss factors from that subsystem [47].

3.3.1.1 General matrix

The general SEA matrix solution for N subsystems is given by [47]

$$\begin{bmatrix} \sum_{n=1}^{N} \eta_{1n} & -\eta_{21} & -\eta_{31} & \cdots & -\eta_{N1} \\ -\eta_{12} & \sum_{n=1}^{N} \eta_{2n} & -\eta_{32} & & \\ -\eta_{13} & -\eta_{23} & \sum_{n=1}^{N} \eta_{3n} & & \\ \vdots & & & \ddots & \\ -\eta_{1N} & & & & \sum_{n=1}^{N} \eta_{Nn} \end{bmatrix} \begin{bmatrix} E_1 \\ E_2 \\ E_3 \\ \vdots \\ E_N \end{bmatrix} = \begin{bmatrix} \frac{W_{\text{in}(1)}}{\omega} \\ \frac{W_{\text{in}(2)}}{\omega} \\ \frac{W_{\text{in}(3)}}{\omega} \\ \vdots \\ \frac{W_{\text{in(N)}}}{\omega} \end{bmatrix} \tag{3.3.1}$$

where η_{ij} is the coupling loss factor from subsystem i to j, η_{ii} is the internal loss factor for subsystem i, E_i is the energy of subsystem i, $W_{\text{in}(i)}$ is the power injected into subsystem i, and ω is the angular frequency.

In chapter 6, each beam in piles 1 and 2 represents one subsystem and SEA has been carried out to calculate the energy, E of each subsystem. The SEA matrix formulations for each pile are given in Appendix B.

3.3.1.2 Path analysis

With SEA it is possible to use path analysis to assess the relative importance of one transmission path compared to another [47].

The energy ratio between subsystem 1 and subsystem N for transmission along the chain of the direct coupled subsystems 1→2→3→⋯→N of Figure 3-15, is given by [47]

$$\frac{E_1}{E_N} = \frac{\eta_2\eta_3 \dots \eta_N}{\eta_{12}\eta_{23} \cdots \eta_{(N-1)N}} \tag{3.3.2}$$

where η_{ij} is the coupling loss factor from subsystem i to j, η_i is the total loss factor for subsystem i and E_i is the energy of subsystem i

Sometimes, it is useful to combine different paths to give E_1/E_N for a specific combination of paths. The energy level differences in decibels (dB) due to transmission between subsystem 1 and subsystem N along P different paths can be calculated from [46]

$$10\lg\left(\frac{E_1}{E_N}\right)_{\substack{\text{Due to}\\ P\text{ paths}}} = -10\lg\left(\sum_{p=1}^{P}\left(\frac{E_1}{E_N}\right)_p^{-1}\right) \tag{3.3.3}$$

Path analysis has been carried out on piles 1 and 2 of chapter 6 to assess the relative importance of one transmission path compared to another. The power was injected into subsystem 1 (see Figure 3-6 - Figure 3-8) and the energy ratio between subsystem 1 and the other subsystems was calculated using Eq. 3.3.2. The path with the lowest energy ratio is the strongest path whereas the path with the highest energy ratio is the weakest path. It is noted that the energy ratio due to a single path (even if dominant) is typically significantly higher than the actual energy ratio between two subsystems. For the path analyses of chapter 6, it was assumed that paths cannot re-enter the subsystems that contain the source and they cannot revisit other subsystems.

3.3.2 Experimental SEA

In collapsed buildings, there are complex coupling situations and/or complex subsystems for which coupling loss factors are either not available or difficult to measure. To overcome this problem, Experimental Statistical Energy Analysis is used to determine CLFs by using FEM to provide ‘experimental’ data.

3.3.2.1 Monte Carlo simulation for ESEA

SEA only predicts the mean response of an ensemble of similar systems; therefore, a Monte Carlo simulation is combined with FEM ESEA in order to provide average responses and consider the inherent uncertainties. The technique is based on random number generation to determine each variable based on a chosen statistical distribution [46].

In chapter 5, the experimentally validated FEM model of the beam junction was used as a basis for creating a sample of 30 beam junctions using a Monte Carlo simulation with FEM. For convenience, the angle between the two beams was fixed at 41° so that the length of the longest side of the surface-to-surface contact area, $L_{C,max}$, was constant. The relative position of the two beams was defined by the coordinates of the centroid of beam SS2, $C_{SS2}(x, y)$. These were sampled from the uniform distributions $C_{SS2}(x) \sim U(-2.68, 2.68)$ and $C_{SS2}(y) \sim U(-1.43, 1.43)$ with the rule that the black shaded area in Figure 3-16 which indicates the surface-to-surface connection area remains constant and equal to 0.091 m^2.

In chapter 7, a sample of 30 damaged beam-to-column junctions was created using a Monte Carlo simulation with FEM. Although the angle θ between the beam and the column in a damaged junction (see Figure 3-11) is often between 45° and 55° [16] in this thesis the angle θ was sampled from a uniform distribution $\theta \sim U(-80, 80)$ to include more extreme angles in the ensemble and assess whether there was a significant variation with angle.

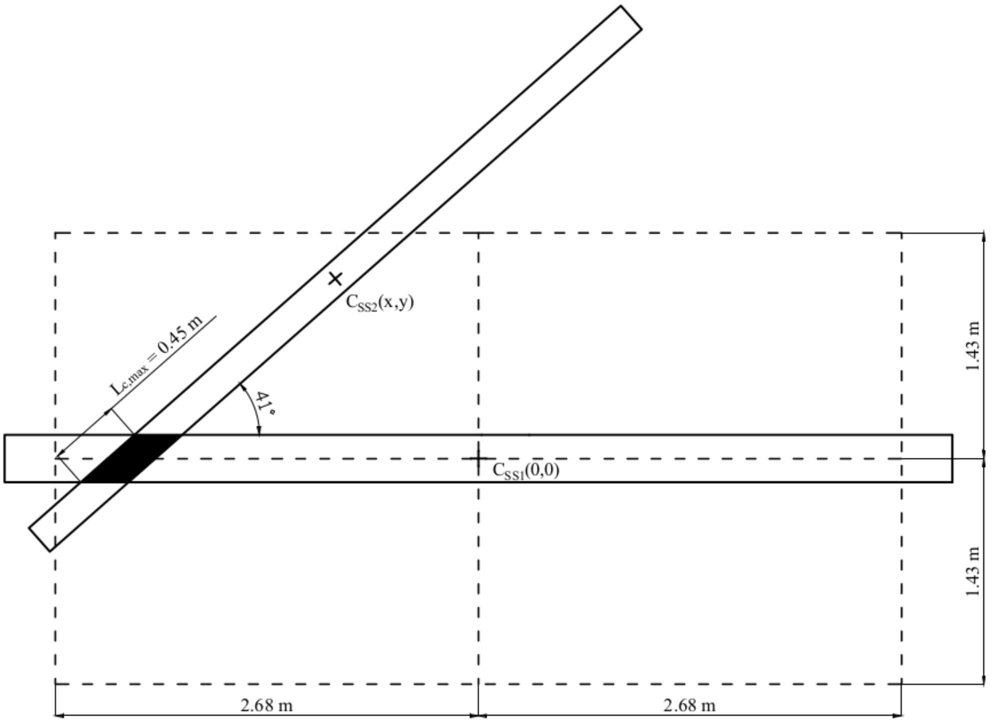

Figure 3-16 Relative beam positions in the ensemble of junctions.

3.3.2.2 General ESEA

The general ESEA can be determined from the general SEA matrix and is given by [48]

$$\begin{bmatrix} \sum_{n=1}^{N} \eta_{1n} & -\eta_{21} & -\eta_{31} & \cdots & -\eta_{N1} \\ -\eta_{12} & \sum_{n=1}^{N} \eta_{2n} & -\eta_{32} & & \\ -\eta_{13} & -\eta_{23} & \sum_{n=1}^{N} \eta_{3n} & & \\ \vdots & & & \ddots & \\ -\eta_{1N} & & & & \sum_{n=1}^{N} \eta_{Nn} \end{bmatrix} \begin{bmatrix} E_{11} & E_{12} & E_{13} & \cdots & E_{1N} \\ E_{21} & E_{22} & E_{23} & & \\ E_{31} & E_{32} & E_{33} & & \\ \vdots & & & \ddots & \\ E_{N1} & & & & E_{NN} \end{bmatrix} \quad (3.3.4)$$

$$= \begin{bmatrix} \frac{W_{\mathrm{in}(1)}}{\omega} & 0 & 0 & \cdots & 0 \\ 0 & \frac{W_{\mathrm{in}(2)}}{\omega} & 0 & & \\ 0 & 0 & \frac{W_{\mathrm{in}(3)}}{\omega} & & \\ \vdots & & & \ddots & \\ 0 & & & & \frac{W_{\mathrm{in(N)}}}{\omega} \end{bmatrix}$$

where E_{ij} is the energy of subsystem i when the power is input into subsystem j

The energy associated with each subsystem is given by

$$E = m\langle v^2 \rangle_{t,s} \quad (3.3.5)$$

where m is the mass of the subsystem and $<v^2>_{t,s}$ is the temporal and spatial average of the mean-square velocity of all the unconstrained nodes of the subsystem.

For rain-on-the-roof excitation (i.e. forces with unity magnitude and random phase) at P nodes, the power input, W_{in} is given by

$$W_{\text{in}} = \frac{\omega}{2}\sum_{p=1}^{P}\left(\text{Im}\{\hat{F}\}Re\{\hat{w}\} - \text{Re}\{\hat{F}\}Im\{\hat{w}\}\right)_p \tag{3.3.6}$$

where F is the force and $\hat{w}$ is the peak out-of-plane displacement associated with each node.

In chapters 5 and 7, numerical experiments with FEM were used as input data for ESEA to calculate CLFs for an SEA model.

In chapter 5, each beam represents one subsystem and the output from the FEM models was used to calculate the subsystem energy and power input that apply to a SEA model of each beam junction. These FEM data were then used in ESEA to determine coupling loss factors. The beams were excited using rain-on-the-roof excitation on all the nodes of the lower surface of beam SS1 and all nodes on the upper surface of beam SS2. These surfaces were selected to avoid applying any forces to the contact nodes. The same node sets were used for extracting the out-of-plane displacements.

In chapter 7, the T-junction formed by two columns and one beam is modelled as either two or three subsystems. When two subsystems are considered, each beam and column of the junction represents one subsystem (see Figure 3-17a). When three subsystems are considered, the beam represents again one subsystem whereas the column is divided in two subsystems as indicated in Figure 3-17b. The output from the FEM models was used to calculate the subsystem energy and power input that apply to a SEA model of each beam-to-column junction. These FEM data were then used in ESEA to determine coupling loss factors. The beam and the column of the junctions were excited using rain-on-the roof excitation at all the nodes of the surfaces which are indicated in Figure 3-17 with red lines.

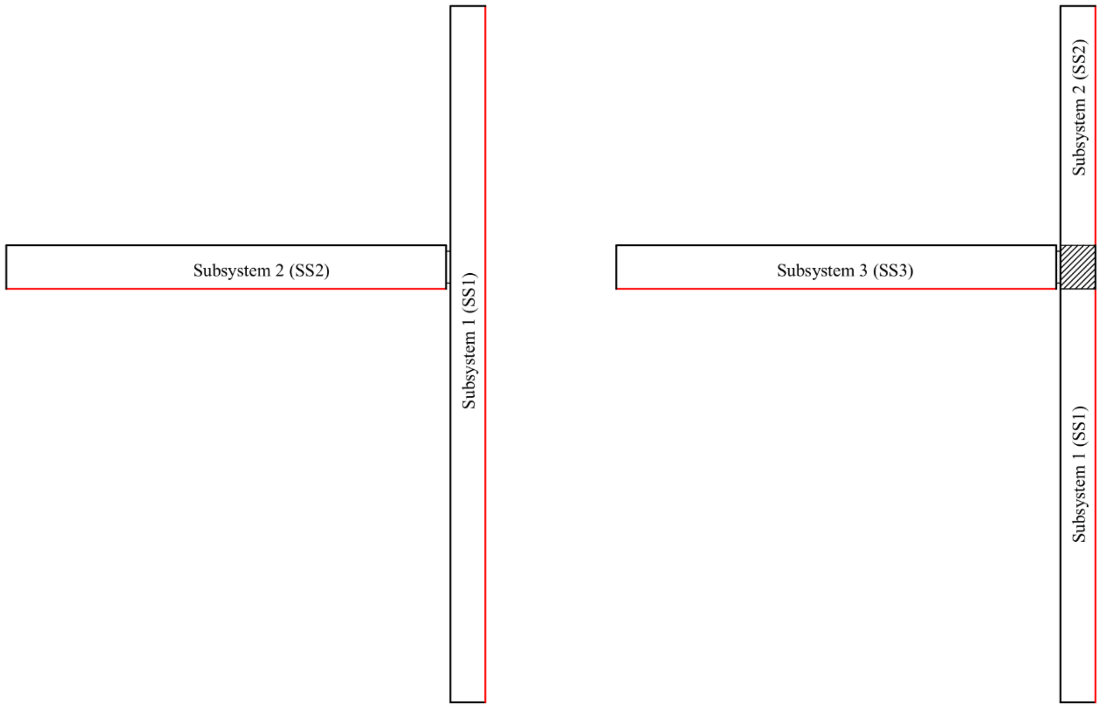

(a) (b)

Figure 3-17 Division of the beam-to-column junctions in: (a) two and (b) three ESEA subsystems. The red lines indicate the surfaces where the rain-on-the-roof excitation is applied and the response is measured.

3.3.3 Theoretical models for Coupling Loss Factors

3.3.3.1 Lump spring connector

An analytical model for the surface-to-surface connection as a lump spring can be used to calculate CLFs for an SEA model. This is expected to be valid when the bending wavelength is much larger than the length of the longest edge of the surface-to-surface connection area.

For *N* identical point connections between two beams, the coupling loss factor from beam *i* to beam *j* can be calculated using (e.g. see [46])

$$\eta_{ij} = \frac{N}{\omega m_i} \frac{Re\{Y_j\}}{\left|Y_i + Y_j + Y_c\right|^2} \tag{3.3.7}$$

where m_i is the mass of beam i, the driving-point mobility of a thin beam of infinite extent (for excitation of bending waves in the central part of the beam) is calculated using [50]

$$Y_{\mathrm{B,Inf}} = \left((1+i)2.67\rho S\sqrt{c_{\mathrm{L,b}} h f}\right)^{-1} \tag{3.3.8}$$

and the mobility of the point spring connection, Y_c, representing the surface-to-surface connection can be calculated using (e.g. see [46])

$$Y_c = \frac{i\omega}{k} \tag{3.3.9}$$

where ρ is the density of the solid beam, S is the cross-sectional area of the beam, f is frequency, h is the depth of the beam, $c_{\mathrm{L,b}}$ is the phase velocity of the beam for quasi-longitudinal waves, k is the dynamic stiffness of the point connection acting as a spring.

3.3.3.2 T-junctions – wave approach: bending waves only

To validate the FEM models of the beam-to-column junctions, the coupling loss factors resulted from the FEM ESEA of the rigid junction with the inclusion of bending modes only are compared with the CLFs calculated using the wave approach.

For a beam that is connected at both ends, the coupling loss factor between two beams i and j is

$$\eta_{ij} = \frac{2c_{\mathrm{B,b},i}\tau_{ij}}{4\pi f L_i} \tag{3.3.10}$$

where $c_{B,b,i}$ is the phase velocity for the propagating bending waves on a solid beam i, τ_{ij} is the transmission coefficient between the beams i and j and L_i is the length of beam i.

In rigid beam-to-column T-junctions (see Figure 3-18) all waves are at normal incidence, so only the normal incidence transmission coefficient is needed.

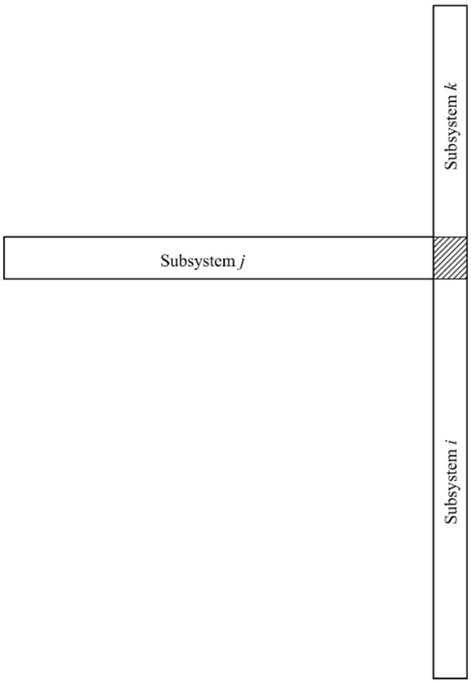

Figure 3-18 Subsystem numbering for the beam-to-column T-junction for the application of the wave approach.

Using the subsystem numbering system in Figure 3-18 with an incident bending wave on subsystem i, the transmission around the corner is given by [47]

$$\tau_{ij} = \frac{0.5 J_i J_j \psi \sqrt{\chi^2}}{\left(J_j \psi\right)^2 + \chi^2 + J_j \psi \left(2\sqrt{\chi^2}\right)} \tag{3.3.11}$$

where J_i=2 and J_j=0.5 when the incident bending wave is on subsystem i and J_i=2 and J_j=2 when the incident bending wave is on subsystem j.

The variables χ and ψ are given by [47]

$$\chi = \sqrt{\frac{h_i c_{Li}}{h_j C_{Lj}}} \tag{3.3.12}$$

$$\psi = \frac{h_j c_{Lj} \rho_{sj}}{h_i c_{Li} \rho_{si}} \tag{3.3.13}$$

where h is the depth, c_L is the quasi-longitudinal phase velocity and ρ_s is the surface density of subsystems i and j.

For an incident bending wave on subsystem i, the transmission across a straight section of a rigid T-junction (Figure 3-18) is given by [47]

$$\tau_{ik} = \frac{0.5\chi^2}{(J_k\psi)^2 + \chi^2 + J_k\psi\left(2\sqrt{\chi^2}\right)} \tag{3.3.14}$$

where J_k=0.5 for T-junctions.

The variables χ and ψ are given by [47]

$$\chi = \sqrt{\frac{h_i c_{Li}}{h_k c_{Lk}}} \tag{3.3.15}$$

$$\psi = \frac{h_k C_{Lk} \rho_{sk}}{h_i C_{Li} \rho_{si}} \tag{3.3.16}$$

3.4 Conclusions

This chapter described in detail the FEM models of the experimental setups and the numerical experiments, as long as the correlation criteria used for the validation of FEM models against EMA results. Furthermore, prediction models based on Statistical Energy Analysis were developed for modelling the vibration transmission in beam junctions, piles of beams and beam-to-column junctions. Finally, theoretical models for the determination of the coupling loss factors in beam junctions and beam-to-column T-junctions were presented in this chapter.

4. Experimental validation of finite element models representing stacked concrete beams with unbonded surface contacts

4.1 Introduction

This chapter investigates the normal contact stiffness between reinforced concrete beams by experimentally validating FEM models in the frequency range up to 3200 Hz. In each junction, the beams are stacked on top of each other without any bonding material and the interaction between the beams is modelled by using either linear elastic contacts (e.g. surface-to-surface junctions) or linear elastic springs (e.g. edge-to-surface junctions). The contact stiffness is determined after model updating against the experimental eigenfrequencies. The main aims of this investigation are to experimentally validate FEM models of non-bonded concrete beams when in contact with each other and identify a suitable contact stiffness value for surface-to-surface or edge-to-surface contact conditions.

4.2 Individual beams

4.2.1 Material properties

Table 4-1 shows the material properties for the beams. The density of the concrete for each beam was calculated by dividing the measured weight of the beams by the volume of concrete after extracting the weight of the steel reinforcement. The Young's modulus of the concrete was estimated after model updating for beams 1 and 2 against the experimental results for the individual beams. Numerical trials were carried out until the lowest eigenfrequency from FEM and measurements were identical to one decimal place (138.2 and 131.1 Hz for beams 1 and 2 respectively). The estimated value of the Young's modulus for beam 1 is relatively higher than beam 2 but it is within the range proposed in the literature for C25/30 concrete [68]. A possible reason for this discrepancy is that beam 1 was cast on a different day to beams 2 and 3. The material properties for the steel and Poisson's ratio for the concrete were taken from the literature ([68], [53]). The average damping ratios for Setups J3, J4 and J5 determined from EMA were 0.53, 0.49 and 0.49% respectively.

Table 4-1 Material properties of beams 1, 2 and 3.

Material	**Density, ρ (kg/m^3)**		**Young's modulus, E (N/m^2)**	**Poisson's ratio, ν (-)**
Concrete	Beam 1	2329	36875E6	0.2
	Beam 2	2245	32475E6	
	Beam 3	2235	32475E6	
Steel	7800		200E9	0.3

4.2.2 Frequencies

Figure 4-1 compares FEM and experimental eigenfrequencies for setups I1, I2 and I3. Close agreement was achieved with differences less than 5% for the majority of the mode pairs in the frequency range up to 3200 Hz.

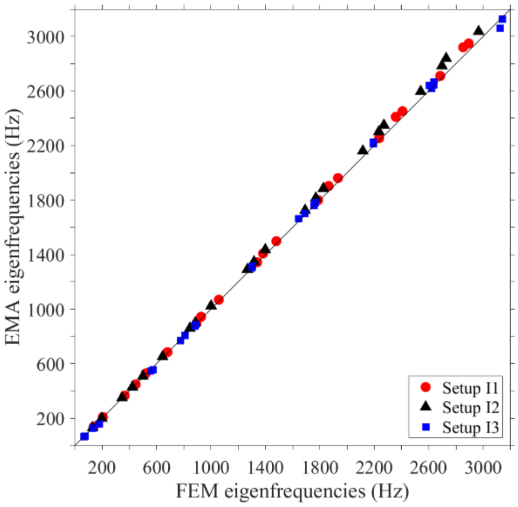

Figure 4-1 Comparison of FEM against experimental eigenfrequencies for Setups I1, I2 and I3.

4.2.3 Mode shapes

Figure 4-2 to Figure 4-4 compare EMA and FEM results for setups I1, I2 and I3 in terms of MAC. For setups I1 and I2, close agreement was achieved for bending and torsional modes (MAC > 0.95) for all the modes up to 3200 Hz (see Figure 4-2 and Figure 4-3).

For setup I3 (see Figure 4-4), whilst there is close agreement for the majority of the bending modes (*MAC* > 0.8 for 11 out of 18 bending modes) there was weaker agreement for the torsional modes (MAC > 0.8 for two out of seven torsional modes). This indicates that the discontinuity mainly affects the accuracy of the torsional modes and therefore it could be that the torsional stiffness of the reinforcement bars needs to be modelled differently.

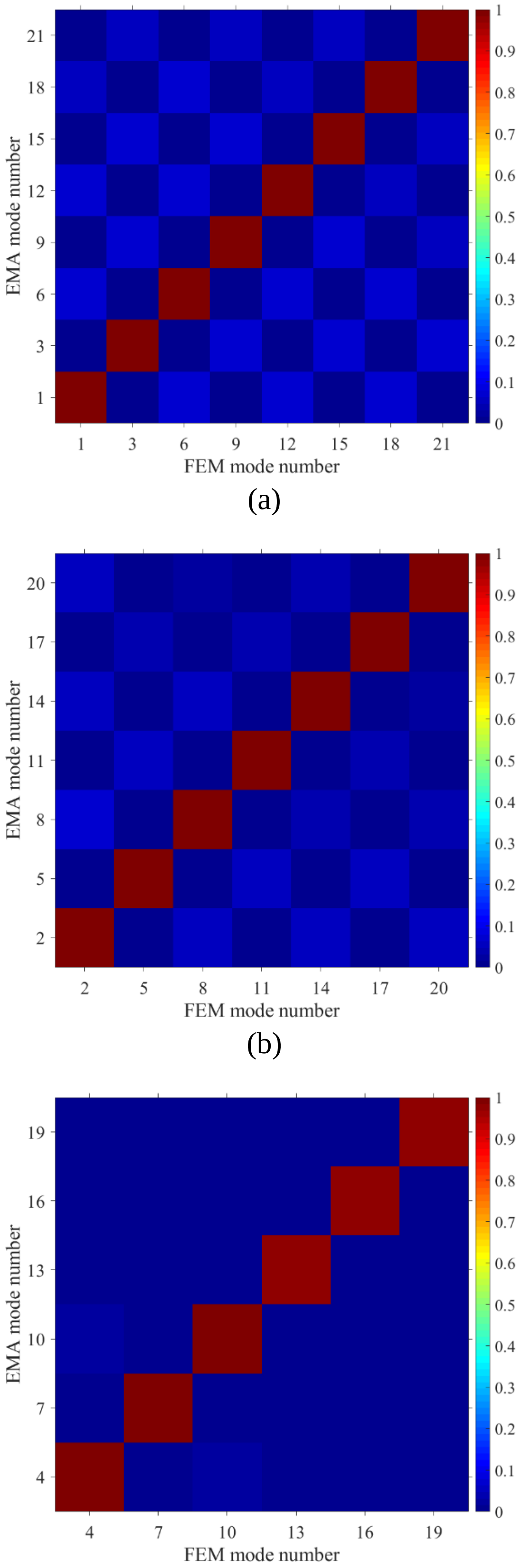

(a)

(b)

(c)

Figure 4-2 MAC values for FEM model of Setup I1: (a) in-plane bending modes, (b) out-of-plane bending modes and (c) torsional modes.

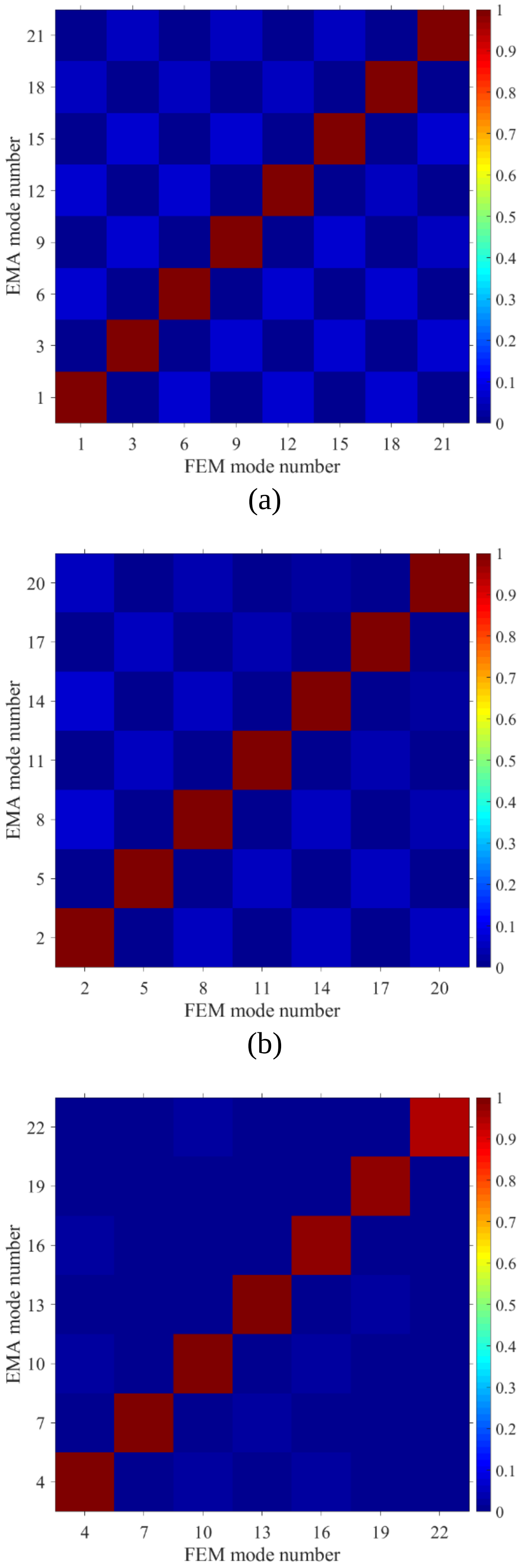

(a)

(b)

(c)

Figure 4-3 MAC values for FEM model of Setup I2: (a) in-plane bending modes, (b) out-of-plane bending modes and (c) torsional modes.

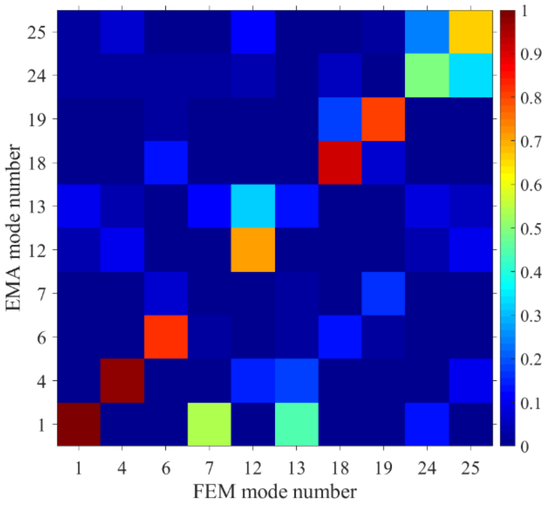

(a)

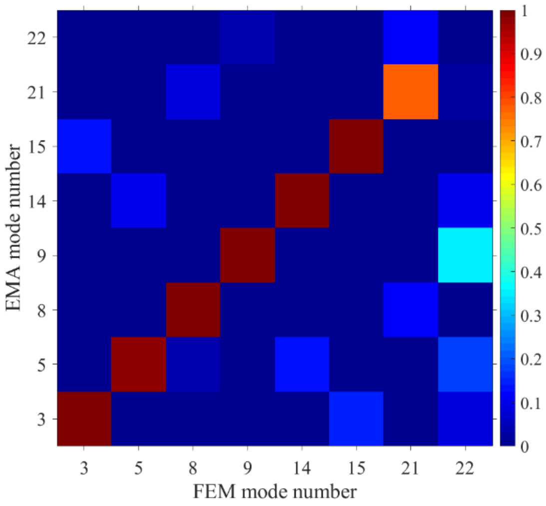

(b)

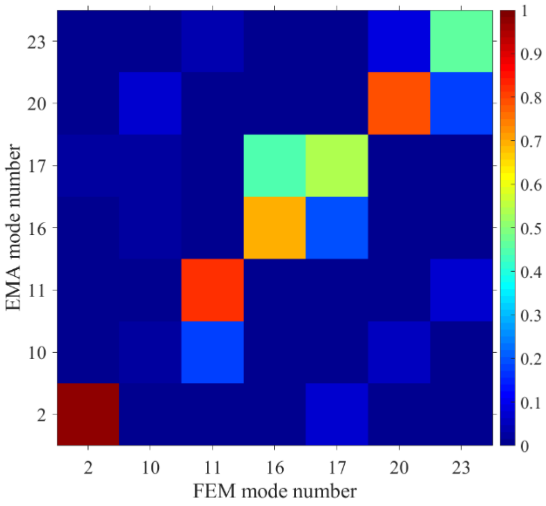

(c)

Figure 4-4 MAC values for FEM model of Setup I3: (a) in-plane bending modes, (b) out-of-plane bending modes and (c) torsional modes.

4.3 Junctions of two beams (surface-to-surface contact)

4.3.1 Normal contact stiffness

Normal contact stiffness values were determined from model updating of the FEM model against EMA for the first 24 modes in each of the setups J1, J2 and J3. These are shown in Table 4-2 in terms of the mean, minimum and maximum values. During the model updating, the eigenfrequencies of some modes were mainly dependent on the eigenfrequencies of the individual beams rather than the value of the contact stiffness. This resulted to a relatively wide range of values for the modes and along with the significantly different mean values for setup J2, the validity of the FEM models was assessed using the mean stiffnesses for each individual setup (J1, J2 and J3) in the following sections.

Table 4-2 Normal contact stiffness values determined from model updating for the surface-to-surface contacts in setups J1, J2 and J3.

Test setup	**Number of modes**	**Contact area (m^2)**	**Normal contact stiffness (N/m)**		
			Mean	**Minimum**	**Maximum**
J1	22	0.06	7.6E8	5.1E5	3.9E9
J2	22	0.06	4.5E8	1.5E6	2.2E9
J3	23	0.09	7.5E8	5.0E5	4.3E9

4.3.2 Eigenfrequencies

Figure 4-5 compares FEM and experimental eigenfrequencies for setups J1, J2 and J3. Close agreement was achieved with differences less than 5% for the majority of the mode pairs in the frequency range from 700 to 3200 Hz. The three setups have similar eigenfrequencies because the global modes of the three setups are partly determined by the eigenfrequencies of the individual isolated beams, and these beams are the same in each of these setups.

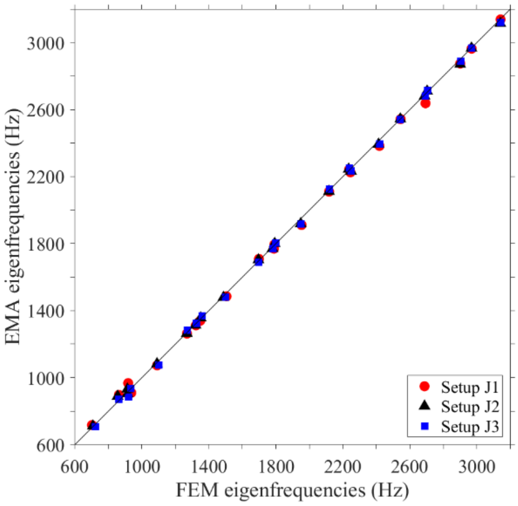

Figure 4-5 Comparison of FEM against experimental eigenfrequencies for Setups J1, J2 and J3.

4.3.3 Mode shapes

In this section, setup J3 is chosen to assess the FEM model in terms of MAC, PMAC and PMVR because the other two setups give similar findings.

Correlation between EMA and FEM is shown using the MAC in Figure 4-6. Note that only bending and torsional modes were included in the validation procedure of the FEM models. Whilst there is close agreement for the first two modes (*MAC* > 0.8) there was poor agreement for modes three, four and five. Close agreement was achieved above the first five global modes (i.e. between 1000 and 3200 Hz) with *MAC* > 0.8 for 17 of the mode pairs (only mode pair 17 had MAC<0.8).

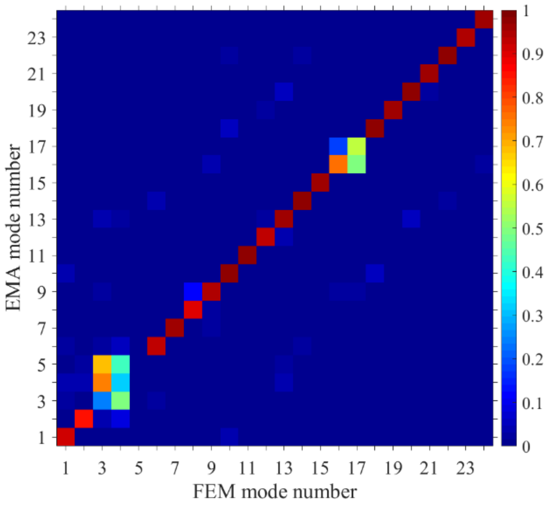

Figure 4-6 MAC values for FEM model of Setup J3.

For setup J3 that comprises two beams, Figure 4-7 shows the PMAC for beams 1 and 2 for comparison with the MAC. Note that there is no data for the fifth mode pair as this pair was not identifiable. It is seen that for each mode pair there is often a PMAC value for one beam that is higher or similar to the MAC, and one PMAC value for the other beam that is lower than the MAC. The reason for this is the sensitivity of MAC to large values in the modal vector. Note that only seven of the 24 mode pairs had $PMAC > 0.8$ for both beams. The global modes of the coupled beams are related to the local modes of each isolated beam where one or both beams have an identifiable modal response that is similar to the local mode shape. Hence there are some global modes where only one beam has a clear modal response and the other has a low response; in this situation, the modal vectors of the former beam primarily determine the MAC and the influence of the other beam will be negligible. For example, in Figure 4-8a the modal vectors of beam 2 determine the MAC value of mode pair 12, whereas in Figure 4-8b the MAC value of mode pair 18 is determined by the modal vectors of beam 1 (see Figure 4-7).

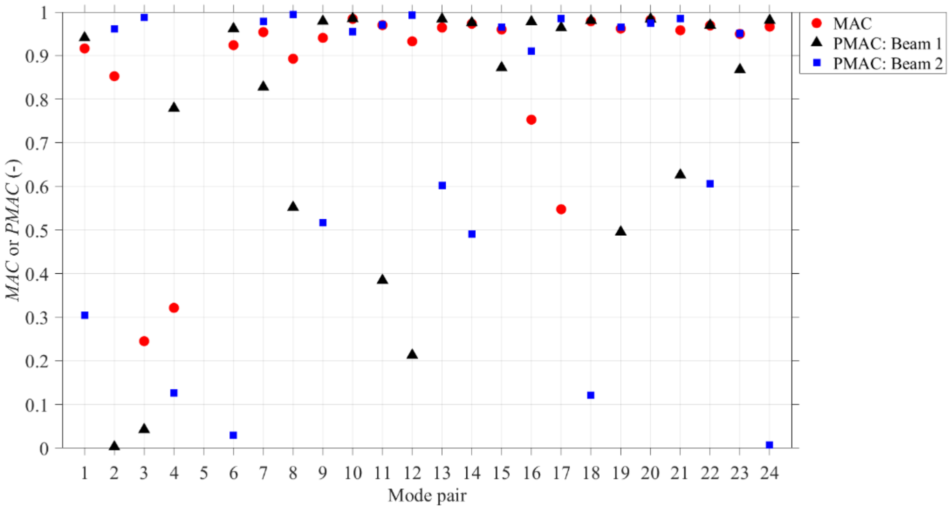

Figure 4-7 PMAC values for FEM model of Setup J3.

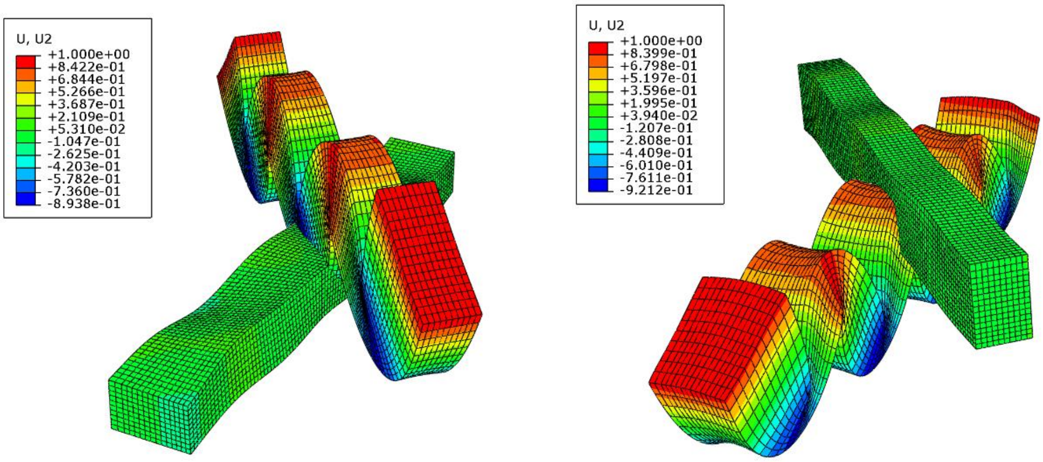

(a) (b)

Figure 4-8 FEM mode shapes of Setup J3: (a) Mode 12 at 1782.3 Hz and (b) Mode 18 at 2418.8 Hz. The legends show the normalized out-of-plane modal displacements.

Figure 4-9 compares FEM and experimental results for setup J3 using PMVR. When introducing this new descriptor in section 3.2.3.1 it was noted that a criterion could not be assigned *a priori*. A value of 0 dB would indicate complete correlation between EMA and FEM. However, as the contact condition is modelled using a single contact stiffness value it is expected that low values, such as between 0 and 2 dB, might only occur for a few mode pairs. In this thesis the application considers the response in frequency bands; hence the velocity level difference between two beams when one is excited a point force will be determined by more than one mode pair. For this reason, two criteria are proposed based on the results from all beam junctions, close agreement being $PMVR \leq 5$ dB (33% of mode pairs) and reasonable agreement being 5 dB < $PMVR \leq 10$ dB (25% of mode pairs). Only 38% of mode pairs had $PMVR > 10$ dB. These results indicate that the model for the interaction between the two beams with FEM is appropriate.

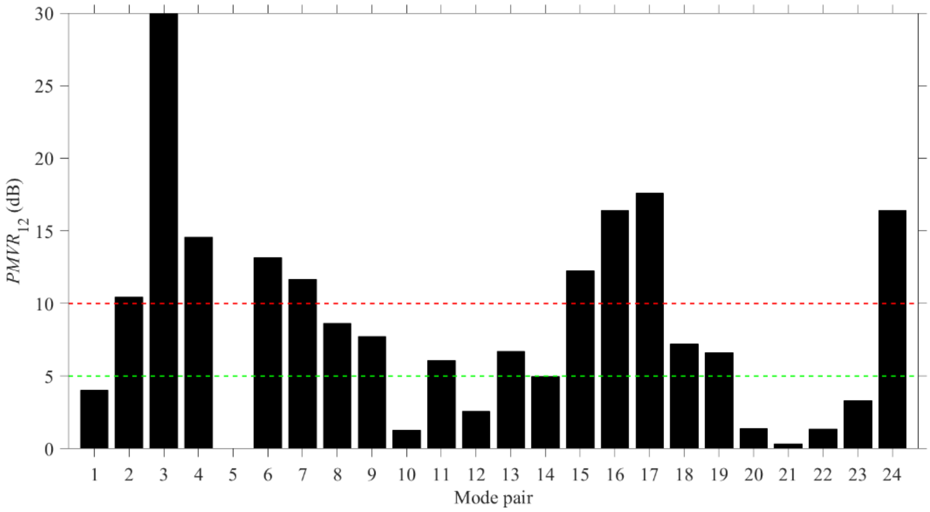

Figure 4-9 PMVR values for FEM model of Setup J3. The green and red straight lines indicate difference levels of 5 and 10 dB respectively while the empty column indicates an unidentified mode pair.

4.3.4 Spatial-average transfer mobility ratio

As in the previous section, setup J3 is used to illustrate features of the spatial-average transfer mobility ratio. Figure 4-10a and b allow comparison of these ratios from FEM and measurements when a point force is applied to beams 1 and 2 respectively. Below 650 Hz there are only rigid body modes; hence results are shown above 650 Hz using 17 frequency bands with a 150 Hz bandwidth to simplify the comparison.

The results for FEM and measurements have similar curves, except in the lowest and highest frequency bands, with the average difference being 2.4 dB. This indicates that the FEM model is able to provide reasonable estimates of vibration transmission between coupled beams by using a single value for the contact stiffness. The next section will consider a three beam junction (setup J4) and combine the stiffness values determined from J1, J2 and J3 by treating them as a sample of the population in order to identify a single contact stiffness that could be used in FEM models of larger combinations of coupled beams.

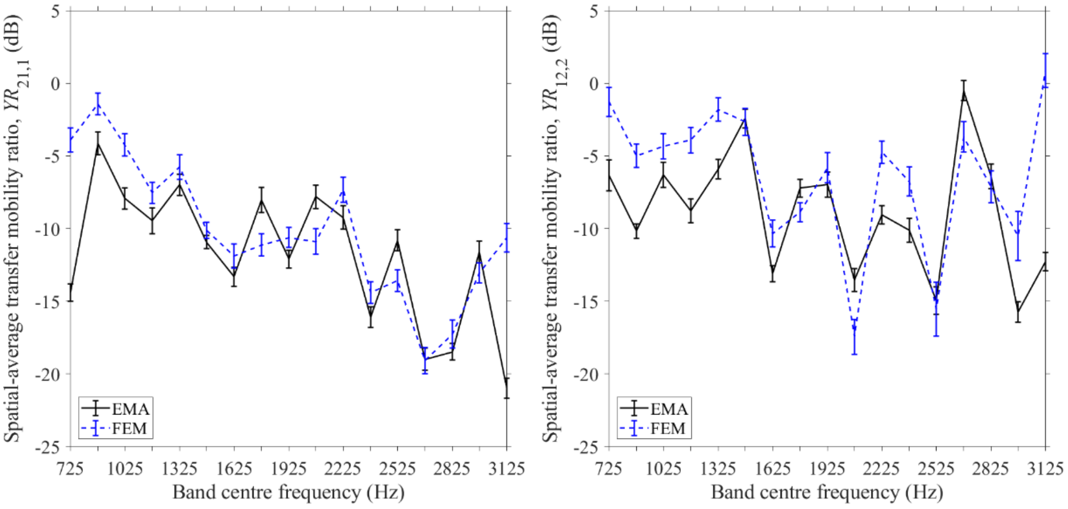

(a) (b)

Figure 4-10 Spatial-average transfer mobility ratio between the beams of setup J3: (a) $YR_{21,1}$ and (b) $YR_{12,2}$.

4.4 Junction of three beams (surface-to-surface contact)

This section aims to identify and assess the use of a single, representative value for the contact stiffness that could be used to model collapsed buildings where there is a high level of uncertainty in the modal properties of the fragmented structure as well as the position of the contact and its surface area.

4.4.1 Normal contact stiffness derived from model updating

In Section 4.3, model updating with setups J1, J2 and J3 resulted in 67 individual values for the normal contact stiffness. It is now assumed that these values represent a sample from a population from which a representative average value could be identified that has general application to two coupled beams. The contact stiffness values for each mode were divided into classes and a probability distribution was fitted to the data using the MATLAB distribution fitter toolbox [69]. The stiffness values are sub-divided into nine bins with a width of 4.78E08 N/m for which the fitted probability distribution is a lognormal distribution as shown in Figure 4-11 with a mean value of 7.038E08 N/m. As the first bin contains 66% of the values it is also feasible to consider the mean of the values in this bin which was 8.77E07 N/m. Previous work [48] has also identified that lognormal distributions describe structural coupling parameters between stiff, heavy structures (i.e. concrete) where there are relatively few modes; this applies to the situation assessed in this thesis with the concrete beams.

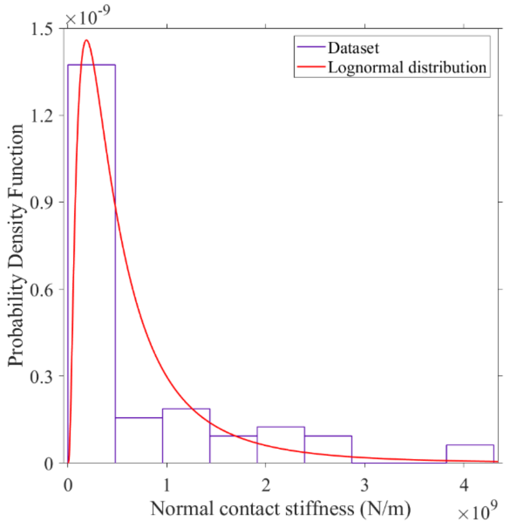

Figure 4-11 Lognormal probability distribution fitted to the dataset of the normal contact stiffness.

4.4.2 Eigenfrequencies

An assessment of the FEM model is now made through comparison with EMA when the normal contact stiffness is (a) the mean value of the first bin, i.e. 8.77E07 N/m which is referred to as FEM model No.1 and (b) the mean value of the lognormal distribution, i.e. 7.038E08 N/m which is referred to as FEM model No.2.

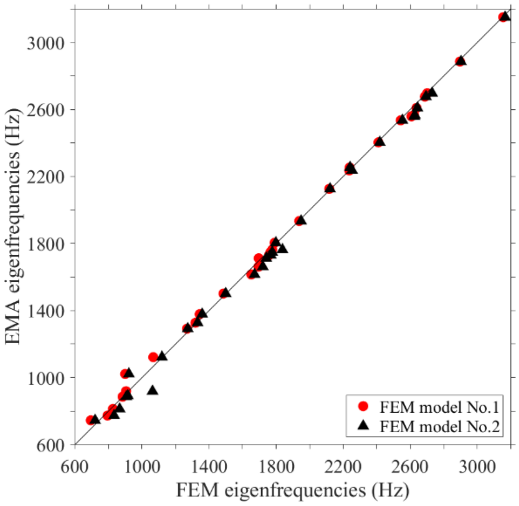

Figure 4-12 Comparison of FEM model No.1 and 2 against experimental eigenfrequencies for Setup J4.

Figure 4-12 allows comparison of FEM models No.1 and 2 against EMA for setup J4. Both FEM models show close agreement with differences less than 5% for the majority of mode pairs. Considering only the first eight mode pairs the average difference (3.7%) is lower for FEM model No.1 than No.2 (6.0%). Whilst the value chosen for the normal contact stiffness affects the global eigenfrequencies below 1200 Hz, both FEM models have similar eigenfrequencies above 1200 Hz (average differences equal to 0.98 and 1.3% for FEM models No.1 and 2 respectively). This indicates that the global eigenfrequencies of the junction are mainly determined by the eigenfrequencies of the individual beams rather than their interaction.

4.4.3 Mode shapes

MAC results for Setup J4 are shown in Figure 4-13a and Figure 4-13b. For the first eight correlated mode pairs (i.e. below 1200 Hz), $MAC>0.8$ for seven mode pairs with FEM model No.1 but only three mode pairs with No.2. Above the eighth mode (i.e. between 1200 and 3200 Hz), both FEM models showed equally close agreement with $MAC > 0.8$ for 17 of the 32 mode pairs.

In terms of PMAC, neither of the FEM models had $PMAC > 0.8$ for all three beams – see Figure 4-14a and b. This issue with one or two of the individual beams was not detected with MAC because (as discussed in section 4.3.3) the MAC value is primarily determined by the modal vectors of one beam.

In terms of PMVR, close agreement (≤ 5 dB) was achieved for 16% and 29% of the mode pairs from FEM models No.1 and 2 respectively. It is seen that for FEM model No.1, many PMVR values are >10 dB (see Figure 4-15a, b and c). Hence, whilst FEM model No.1 had higher MAC values than No.2, PMVR indicates that FEM model No.2 gives an improved representation of the interaction between the coupled beams.

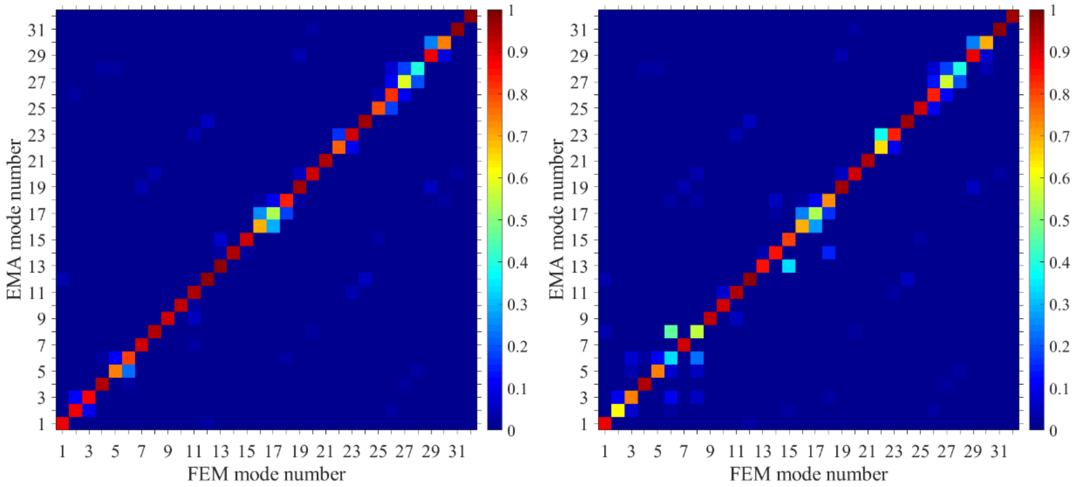

(a) (b)

Figure 4-13 MAC values for Setup J4: (a) FEM model No.1 and (b) FEM model No.2.

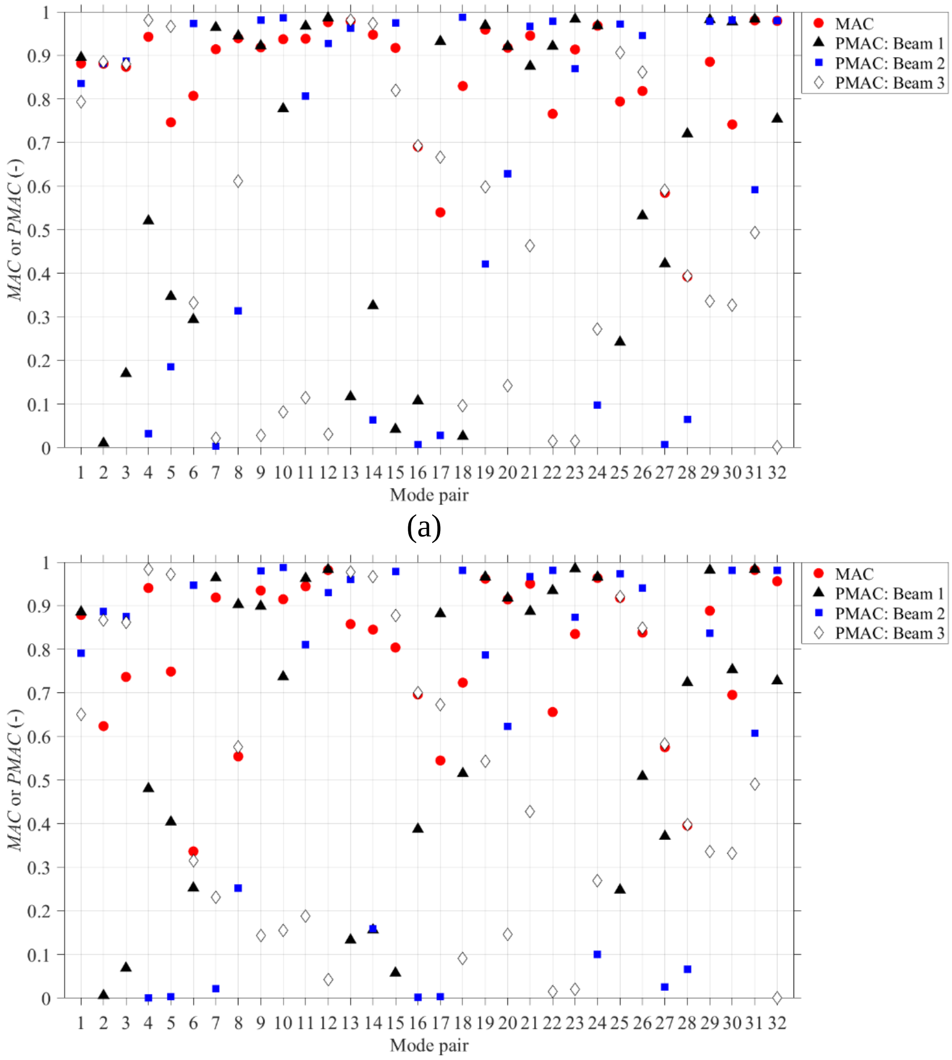

(a)

(b)

Figure 4-14 PMAC values for Setup J4: (a) FEM model No.1 and (b) FEM model No.2.

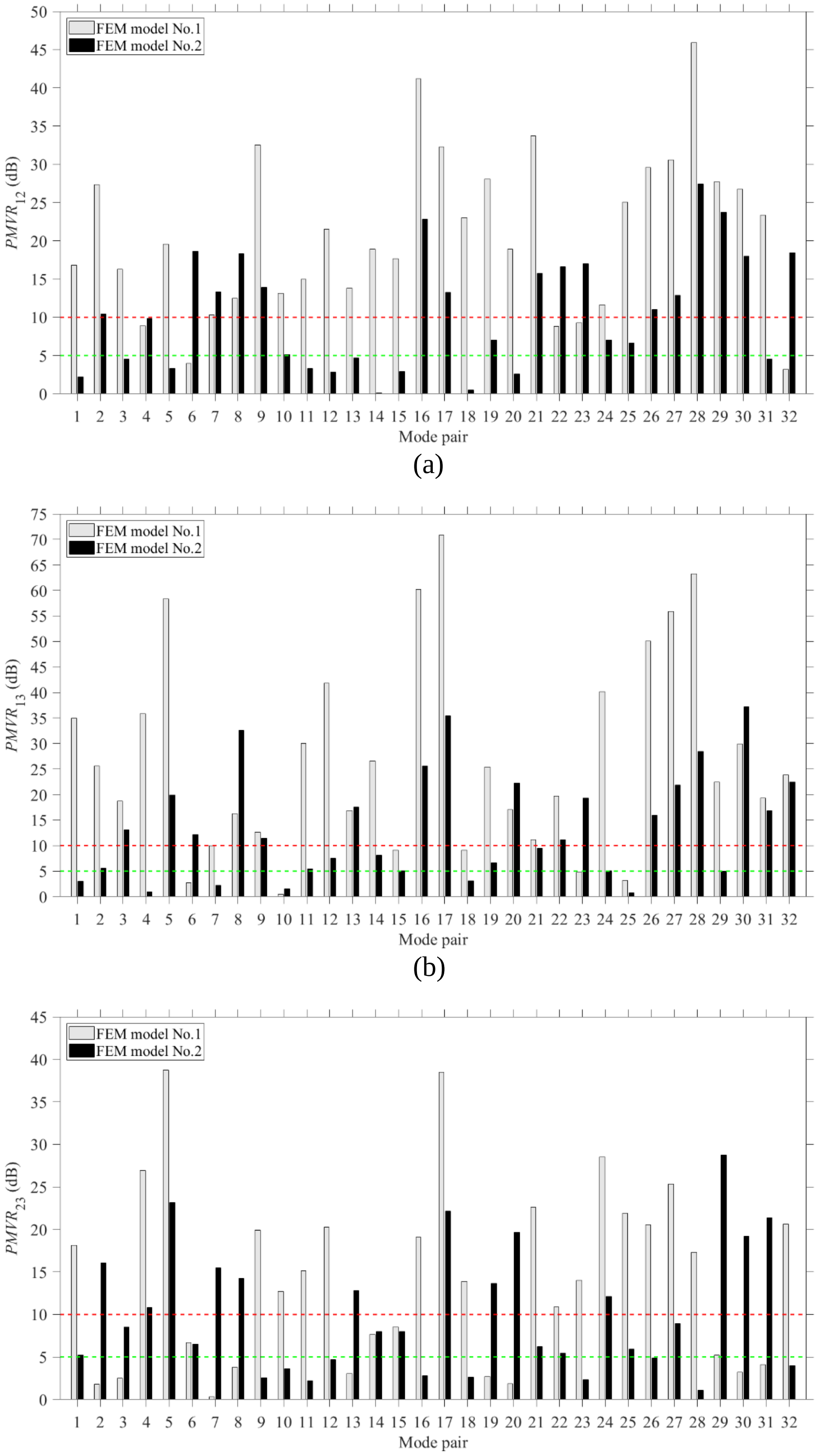

(a)

(b)

(c)

Figure 4-15 PMVR for FEM models No.1 and 2 with Setup J4: (a) $PMVR_{12}$, (b) $PMVR_{13}$ and (c) $PMVR_{23}$.

4.4.4 Spatial-average transfer mobility ratio

Figure 4-16 allows comparison of FEM models No.1 and No.2 with EMA for the beams in setup J4. When the force is applied to beam 1 (Figure 4-16a and b), FEM model No.2 shows closest agreement with EMA (differences less than 4 dB) whereas FEM model No.1 was offset with differences up to 12 dB on average.

When the force is applied to beam 2 (Figure 4-16c) or beam 3 (Figure 4-16e), FEM model No.2 also shows significantly closer agreement with EMA than No.1. However, both FEM models Nos. 1 and 2 show reasonable agreement when the force is applied to beam 2 (Figure 4-16d) or beam 3 (Figure 4-16f) and the velocity response is measured on beams 2 and 3. This indicates that the choice of normal contact stiffness might be less critical where the size of the area connection is reduced, in this case the area is reduced due to the discontinuity in beam 3.

In general, the results show that FEM model No.2 is significantly better than No.1 for modelling vibration transmission between the beams in setup J4. Therefore, the mean value of the lognormal distribution provides the better approximation of the normal contact stiffness to model the dynamic behaviour of beam junctions where the beams are connected with surface-to-surface contact conditions. The next section assesses the potential of using this normal contact stiffness value in beam junctions with edge-to-surface contact conditions.

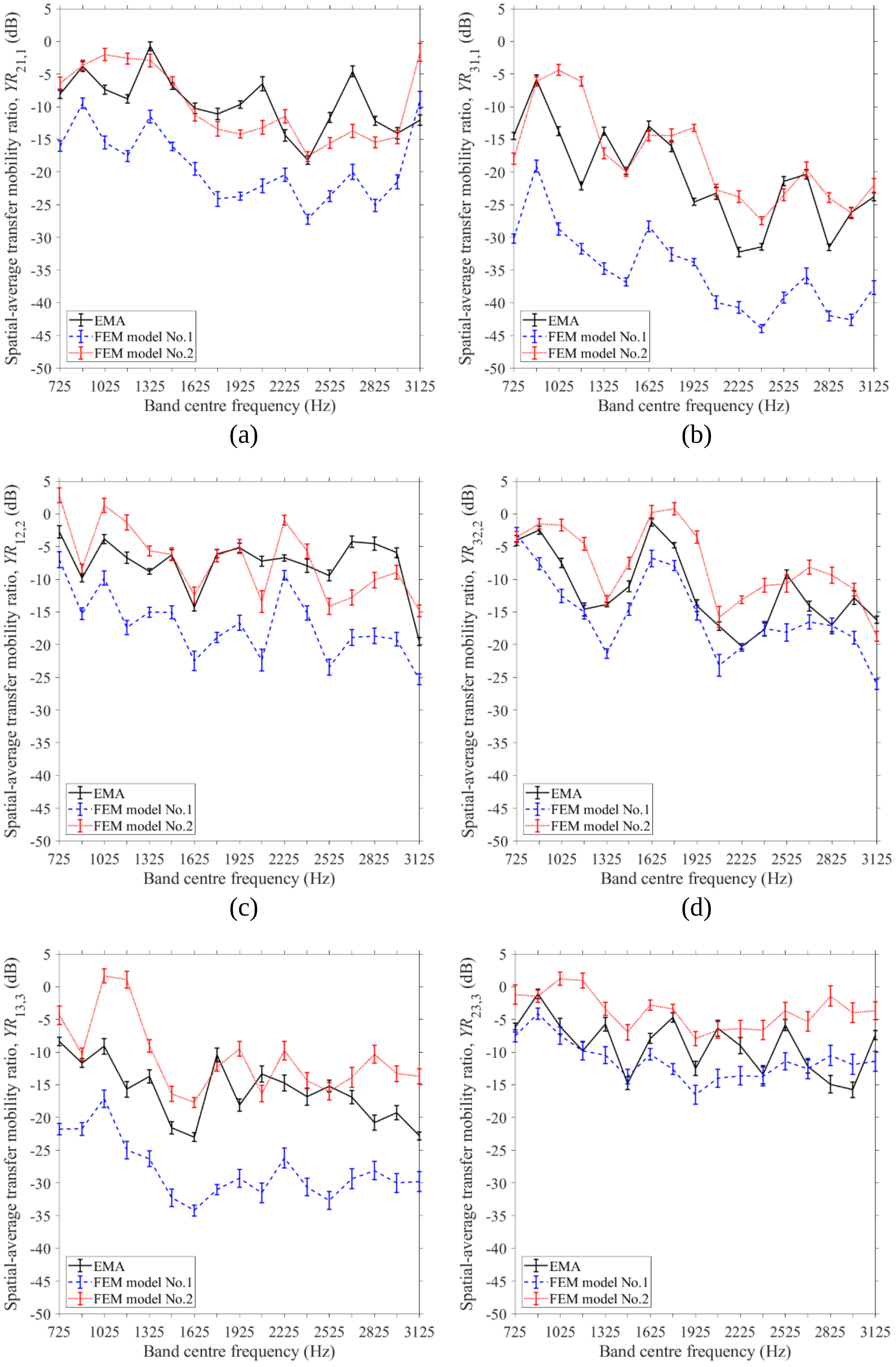

(a) (b)

(c) (d)

(e) (f)

Figure 4-16 Spatial-average transfer mobility ratio for the beams in setup J4: (a) $YR_{21,1}$, (b) $YR_{31,1}$, (c) $YR_{12,2}$, (d) $YR_{32,2}$, (e) $YR_{13,3}$ and (f) $YR_{23,3}$.

The FEM model that best represented the physical situation was identified by PMVR but not by MAC which led to a misleading validation by indicating that FEM model No.1 was more accurate than No.2. MAC is very sensitive to large values, so any correlation problem caused by the interaction between the beams is not reflected in its value. For this reason, it is proposed here that PMVR is a computationally efficient supplement to MAC when validating FEM models where structural components are coupled by elastic connections of unknown stiffness.

4.5 Junction of two beams (edge-to-surface contact)

Following the findings in the previous section, only one FEM model is used in this section which uses the mean value of the lognormal distribution for the normal contact stiffness.

4.5.1 Eigenfrequencies

Figure 4-17 compares FEM and experimental eigenfrequencies for setup J5. Close agreement was achieved with differences less than 3% for mode pairs in the frequency range from 700 to 3200 Hz.

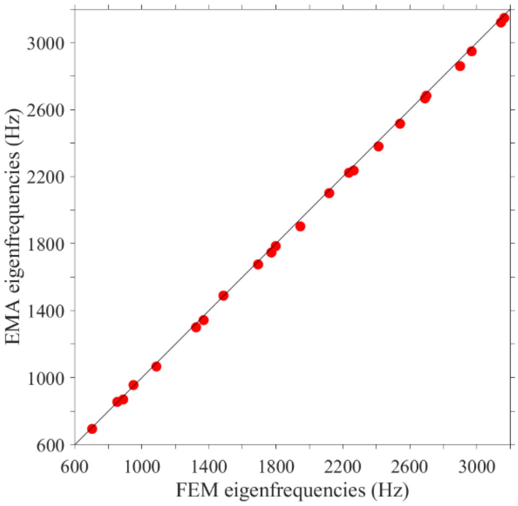

Figure 4-17 Comparison of FEM against experimental eigenfrequencies for Setup J5.

4.5.2 Mode shapes

In terms of MAC, close agreement was achieved for 21 out of 23 mode pairs with $MAC > 0.8$ and reasonable agreement was achieved for mode pairs 8 and 23 with $MAC > 0.7$ – see Figure 4-18. In terms of PMAC, beams 1 and 2 have $PMAC > 0.8$ for 15 out of the 23 mode pairs – see Figure 4-19. These PMAC results are higher than occurred with the surface-to-surface contact conditions which indicates that the reduced contact area which occurs with an edge-to-surface contact introduces lower errors when modelling the coupling using springs.

In terms of PMVR, close agreement ($PMVR \leq 5$ dB) was achieved for 22% of the mode pairs with reasonable agreement for 52% of the mode pairs (5 dB < $PMVR \leq 10$ dB) and only 26% of mode pairs had $PMVR > 10$ dB – see Figure 4-20.

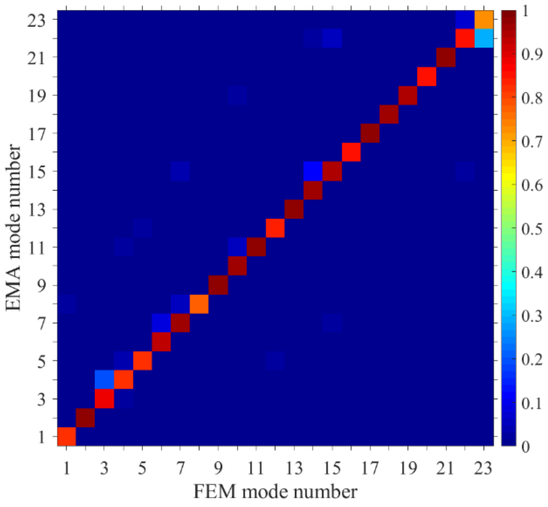

Figure 4-18 MAC values for FEM model of Setup J5.

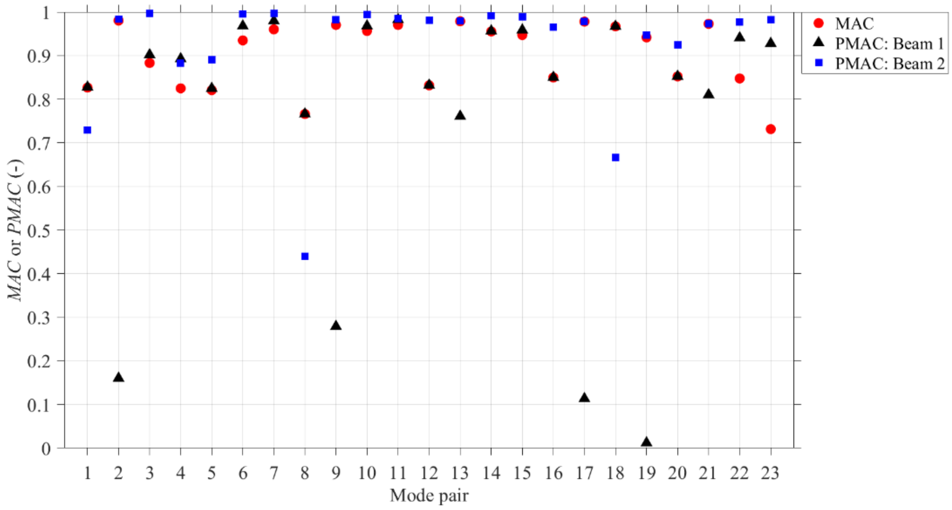

Figure 4-19 PMAC values for FEM model of Setup J5.

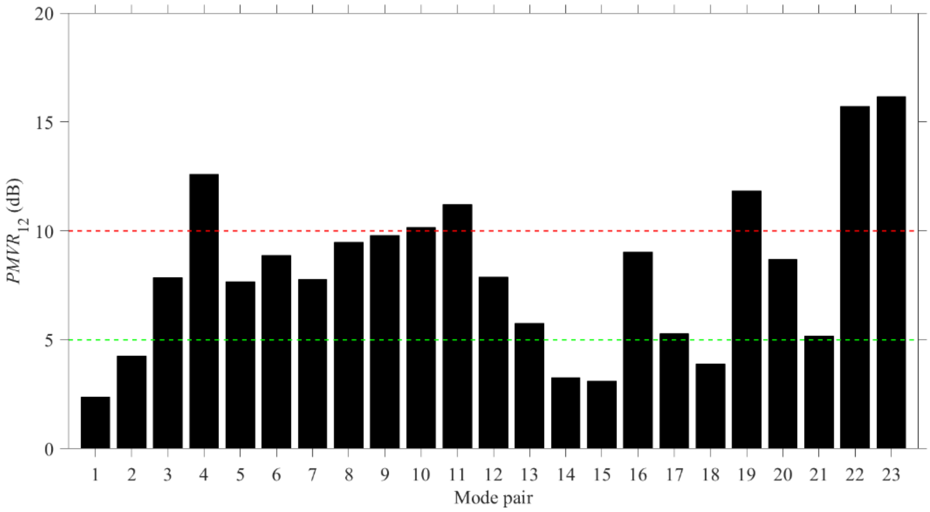

Figure 4-20 PMVR values for FEM model with Setup J5.

4.5.3 Spatial-average transfer mobility ratio

Figure 4-21a and b allow comparison of FEM and EMA in terms of the spatial-average transfer mobility ratio for setup J5. For a point force applied to beam 1 (Figure 4-21a) and beam 2 (see Figure 4-21b), FEM and EMA show close agreement within 4 dB on average. This confirms that the mean value of the lognormal distribution can be used for the contact stiffness in FEM models where the beams are connected with edge-to-surface contact conditions.

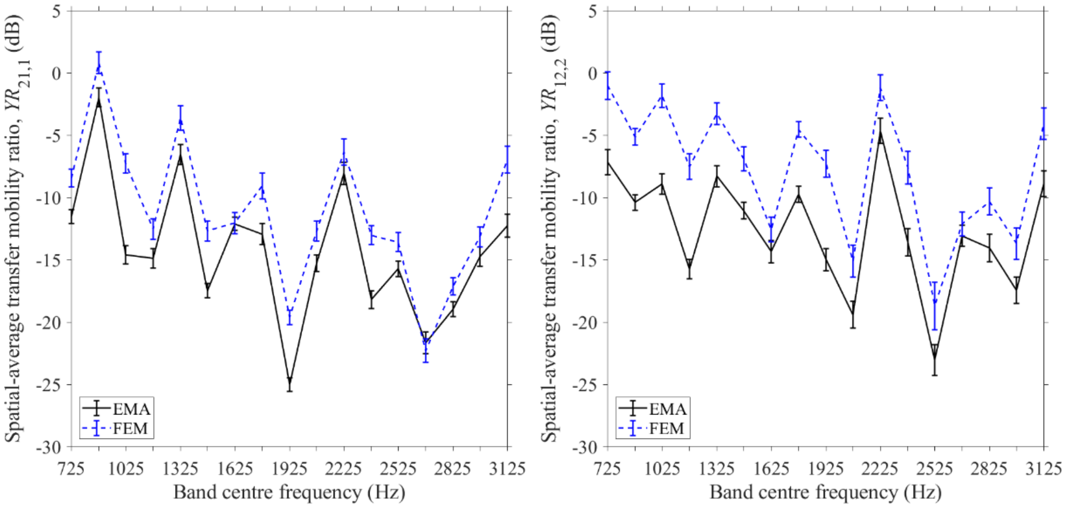

Figure 4-21 Spatial-average transfer mobility ratio for the beams in setup J5: (a) $YR_{21,1}$, (b) $YR_{12,2}$.

4.6 Conclusions

FEM models have been developed and validated with experimental modal analysis for beams connected with surface-to-surface and edge-to-surface contact conditions. These models were validated in terms of eigenfrequencies, mode shapes and spatial-average response. It was shown that the interaction between the beams could be approximated using a normal contact stiffness. This stiffness showed some dependence on the modal response with values forming a lognormal distribution. It was shown that the mean value of this lognormal distribution could be used to approximate the contact stiffness in FEM models of beams junctions with surface-to-surface or edge-to-surface contact conditions. This approximation was more effective in junctions with two than three beams and especially with edge-to-surface contact conditions.

For concrete beams that are stacked on top of each other without any rigid bonding material it was shown that MAC is not able to assess the validity of the FEM model and led to misleading results. Using PMAC for these beams, it was shown that MAC was mainly determined by the modal vectors of one beam whereas the contribution of the other beam(s) to the MAC value was negligible. To overcome the shortcomings of MAC when validating FEM models of structural coupling between elastic systems using spring connectors to model the unbonded contact condition, an additional criterion, the Partial Modal Vector Ratio was introduced in this thesis. This criterion allowed identification of the FEM model that gave the most appropriate representation of the interaction between the coupled beams.

Compared to running FEM models with applied loads to assess vibration transmission between the coupled beams, PMVR is a time efficient approach and can be used as a supplementary criterion to MAC to identify potential correlation problems caused by the interaction of the beams.

5. Vibration transmission between reinforced concrete beams with surface-to-surface contact conditions

5.1 Introduction

The aim of this chapter is to assess the potential to use SEA to model vibration transmission between two reinforced concrete beams when they are stacked on top of each other (i.e. without any bond connecting the two beams) to make a surface-to-surface connection. This is carried out using numerical experiments with FEM to create an ensemble of beam junctions for a Monte Carlo simulation which will allow use of ESEA to determine Coupling Loss Factors between the beams.

The two main aspects to investigate are (a) whether it is possible to only consider one type of wave motion (bending waves) or whether two or more types of wave motion can be considered simultaneously (bending and torsional waves) and (b) whether analytical models based on lump spring connectors can be used to model the contact condition. The first aspect concerning the use of ESEA with multiple wave types is necessary because in a collapsed structure it is not known whether one or more wave type will be excited at the surface-to-surface connection. For coupled plates with wave conversion at the junction, Hopkins [48] previously showed that with ESEA it was not always possible to identify the existence of multiple wave types when only bending waves are excited on one plate. In chapter 4, it was shown that the contact conditions between reinforced concrete beams with a dry unbonded contact could be modelled by using an array of springs. This provides the impetus to assess analytical models based on lump spring connectors to calculate CLFs for SEA models.

5.2 Mode types

The global modes identified by the eigenfrequency analysis of the beam junctions were grouped into three categories according to the deformed shape of each of the beams that form the junctions as: (a) bending modes, (b) torsional modes and (c) combination of bending and torsional modes (see Figure 5-1). Even though in-plane bending and longitudinal modes were identified by Lanczos eigen solver, these are not relevant to this study since they are not excited by the rain-on-the-roof force and they do not significantly affect the out-of-plane response of the beam junctions.

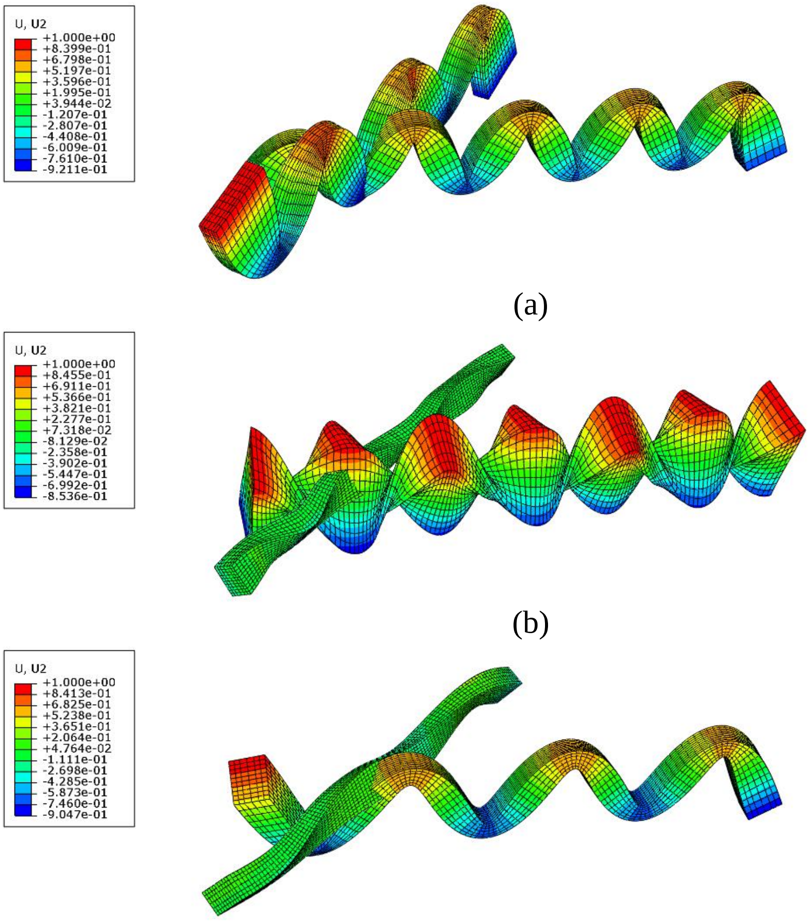

(a)

(b)

(c)

Figure 5-1 Types of global modes: (a) bending modes, (b) torsional modes and (c) combination of bending and torsional modes. The legends show the normalized out-of-plane modal displacements.

5.3 Mode count

Figure 5-2 and Figure 5-3 show the average mode count for out-of-plane bending, torsional and combinations of all the modes for beam junctions with simply supported and free support conditions respectively. Results are shown for 16 frequency bands of 200 Hz bandwidth. These were preferred than one-third octave bands so there is at least one mode in each frequency band. The later has been shown to improve the efficiency of SEA [46].

For the simply supported junctions, there is at least one bending mode in 13 out of the 16 frequency bands whereas there is less than one torsional mode in 10 out of the 16 frequency bands. When all the modes are combined, all the frequency bands have at least seven modes.

For free support conditions, all the frequency bands have at least one bending mode except for the 2900 Hz band. In addition, there is less than one torsional mode in 10 out of the 16 frequency bands. When all the modes are combined, all the frequency bands have at least six modes.

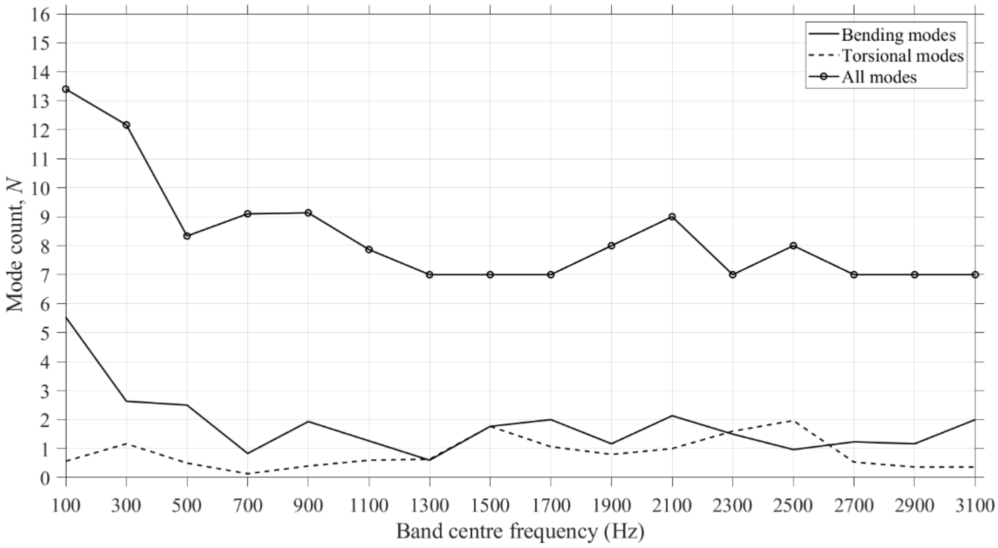

Figure 5-2 Average mode count for bending, torsional and combination of all modes of the 30 beam junctions when simply supported.

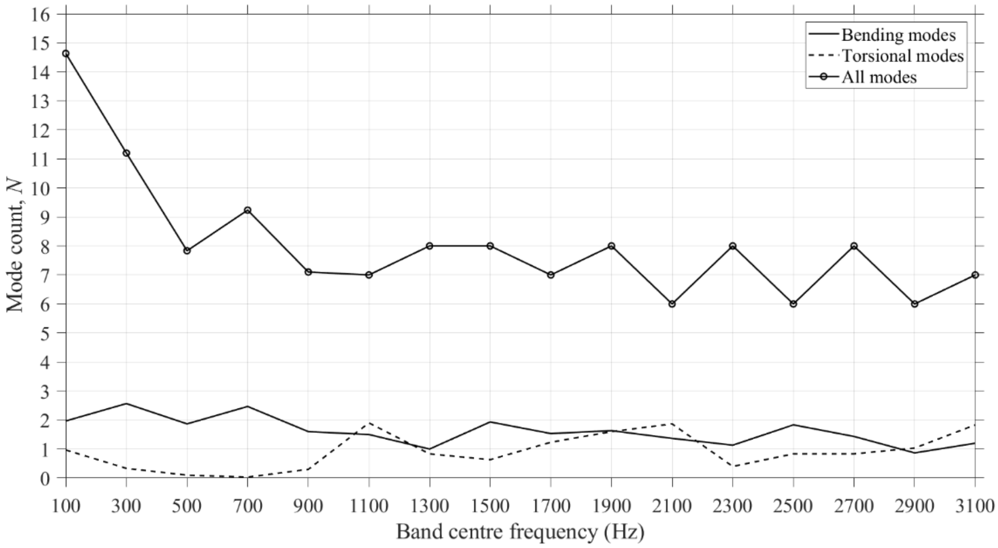

Figure 5-3 Average mode count for bending, torsional and combination of all modes of the 30 beam junctions with free support conditions.

5.4 Assessment of the FEM driving-point mobilities

5.4.1 Assessment of damping

This section compares the ratio of the spatial average driving-point mobilities from FEM (with only bending modes) to infinite beam theory for beam SS1 with simple supports at both ends. Two values of internal loss factors were considered: (a) η=0.1 and (b) η=0.01. In the absence of measured damping data from collapsed buildings, these values were selected as the two extremes damping conditions that are likely to occur in practice (see section 3.2.1.2 considering that $\eta=2\zeta$ [46]); η=0.1 is assumed to represent the situation where a beam is connected to many concrete beams/plates and η=0.01 represents a situation where there is only one connection to a concrete beam/plate. Results are shown for both the real part (Figure 5-4) and the magnitude (Figure 5-5) of the driving-point mobility as this is required for the lump spring connector model (see Eq. 3.3.7). As expected, the lower damping leads to more peaks and troughs than the higher damping where the latter is a much smoother curve.

The difference of the ratio $10\lg(<Y_{\mathrm{B,FEM}}>_{\mathrm{s}}/Y_{\mathrm{B,Inf}})$ for the two values of damping is within 1.5 dB for the real part and up to 3 dB for the magnitude between the 100 and 3100 Hz frequency bands. This indicates that the driving-point mobility of an infinite beam is a good estimate for the driving-point mobility of a reinforced concrete beam regardless the value of the internal loss factor. In a collapsed building, it is more likely to have multiple connections between the fragmented structural members than only one, thus the internal loss factor η=0.1 is adopted for the next sections of this thesis.

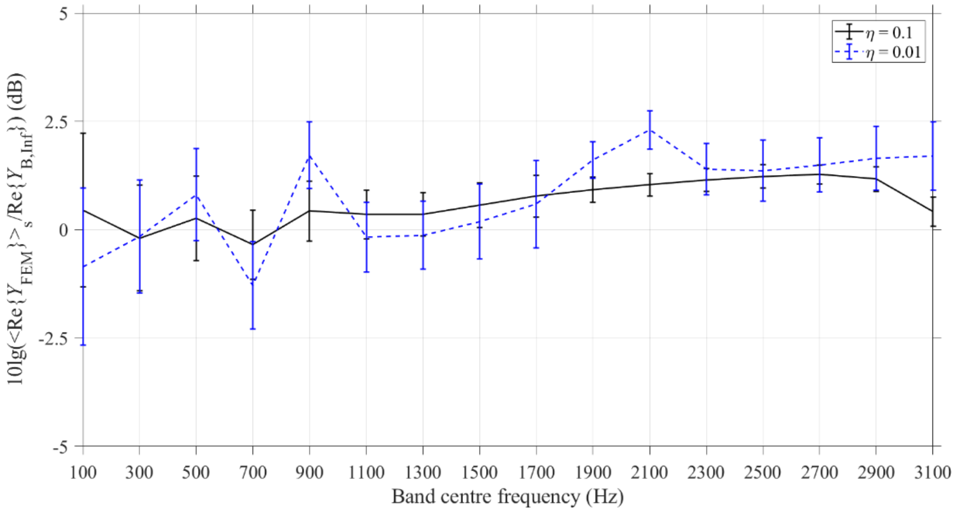

Figure 5-4 Beam SS1 (simply supported) – Ratio of the real part of the driving-point mobilities (FEM using bending modes only to infinite beam theory) along with the 95% confidence intervals for two different internal loss factors.

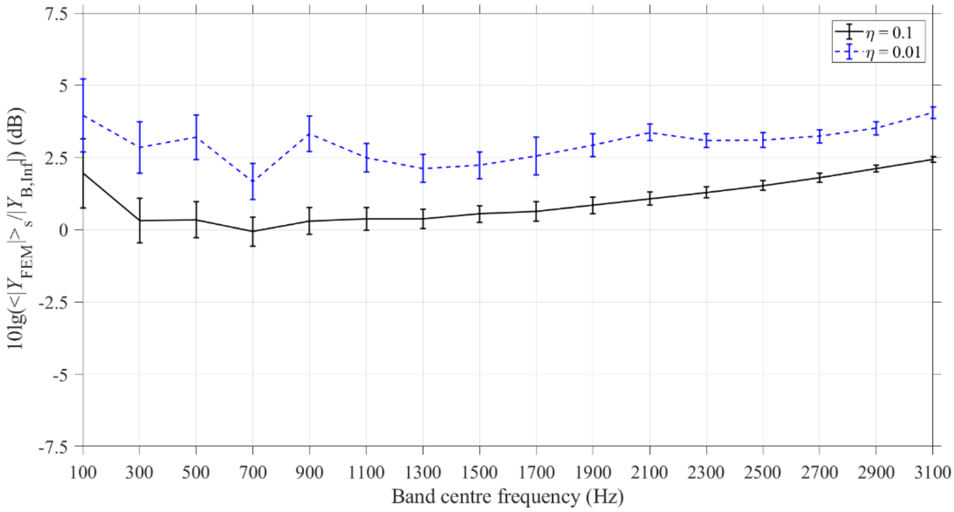

Figure 5-5 Beam SS1 (simply supported) – Ratio of the magnitude of the driving-point mobilities (FEM using bending modes only to infinite beam theory) along with the 95% confidence intervals for two different internal loss factors.

5.4.2 Simply supported condition

Figure 5-6 to Figure 5-11 show the ratio of the real part of the driving-point mobilities from FEM relative to infinite beam theory over the surface of beams SS1 and SS2 using one contour plot for each frequency band. Figure 5-12 and Figure 5-13 compare the spatial average of the driving-point mobilities of the simply supported beams SS1 and SS2 from FEM using either bending or torsional or all modes against the driving-point mobilities of a thin beam of infinite extent for bending wave excitation (Eq. 3.3.8). Results are shown for 16 frequency bands of 200 Hz bandwidth, in terms of a mean value with 95% confidence intervals for both the real part and the magnitude of the mobilities that are used in Eq. (3.3.7) to calculate the CLF.

The lowest frequency bending modes for the isolated simply supported beams SS1 and SS2 occur at 9.7 and 21.4 Hz respectively. For excitation of only bending waves on beams SS1 and SS2, the ratio of the real part of the driving point mobilities, $10\lg(Y_{\mathrm{B,FEM}}/Y_{\mathrm{B,Inf}})$ is less than 5 dB for 94% and 76% of the excitation positions on beams SS1 and SS2 respectively (see Figure 5-6 and Figure 5-7). Higher differences were observed at positions close to the ends of the beams. In terms of the spatial average, the ratio $10\lg(\langle Y_{\mathrm{B,FEM}}\rangle_{\mathrm{s}}/Y_{\mathrm{B,Inf}})$ is between -1 and 3.8 dB between the 100 and 3100 Hz frequency bands, for both the real part and the magnitude of the driving point mobilities.

The lowest frequency torsional modes for the isolated simply supported beams SS1 and SS2 occur at 164.4 and 172.8 Hz respectively. For excitation of only torsional waves, the ratio of the real part of the driving point mobilities, $10\lg(Y_{\mathrm{T,FEM}}/Y_{\mathrm{B,Inf}})$ is less than 5 dB for 46% and 44% of the excitation positions on beams SS1 and SS2 respectively (see Figure 5-8 and Figure 5-9). This is partially expected since the driving point mobility of a beam of infinite extent is valid only for bending wave excitation. However, in terms of the spatial average the ratio $10\lg(<Y_{\mathrm{T,FEM}}>_{\mathrm{s}} / Y_{\mathrm{B,Inf}})$ is between -4 and 3 dB between the 300 and 3100 Hz bands. At 100 Hz the differences are up to -7 and -5.6 dB for the real part and magnitude respectively.

For all modes (i.e. the combination of bending, torsional and longitudinal modes) of beams SS1 and SS2, the ratio of the real part of the driving point mobilities, $10\lg(Y_{\mathrm{A,FEM}} / Y_{\mathrm{B,Inf}})$ is less than 5 dB for 66% and 67% of the excitation positions of beam SS1 and SS2 respectively (see Figure 5-10 and Figure 5-11). In terms of the spatial average, the ratio $10\lg(<Y_{\mathrm{A,FEM}}>_{\mathrm{s}} / Y_{\mathrm{B,Inf}})$ is positive and up to 5.7 dB between the 100 and 3100 Hz frequency bands, both for the real part and the magnitude of the driving point mobilities.

The main finding is that the infinite beam equation gives close estimates for bending modes for which it is derived but can still give reasonable estimates for torsional modes and for the combination of all modes.

5.4.3 Free support condition

Figure 5-14 to Figure 5-19 show the ratio of the real part of the driving-point mobilities from FEM relative to infinite beam theory across the excitation positions of beams SS1 and SS2 using one contour plot for each frequency band. Figure 5-20 and Figure 5-21 compare the spatial average of the driving-point mobilities of the free-free supported beams SS1 and SS2 from FEM using either bending or torsional or all modes against the driving-point mobilities of a thin beam of infinite extent for bending wave excitation (Eq. 3.3.8). Results are shown for 16 frequency bands of 200 Hz bandwidth, in terms of a mean value with 95% confidence intervals for both the real part and the magnitude of the mobilities that are used in Eq. (3.3.7) to calculate the CLF.

The lowest frequency bending modes for the isolated free beams SS1 and SS2 occurs at 22.0 and 48.2 Hz respectively. For bending wave excitation of beams SS1 and SS2, the ratio of the real part of the driving point mobilities, $10\lg(Y_{B,FEM}/Y_{B,Inf})$ is less than 5 dB for 88% and 72% of the excitation positions of beam SS1 and SS2 respectively (see Figure 5-14 and Figure 5-15). As it was observed with the simple supports, the differences were higher at positions close to the ends of the beams. In terms of the spatial average, the ratio $10\lg(<Y_{B,FEM}>_s/Y_{B,Inf})$ is between -0.4 and 2 dB between the 100 and 3100 Hz frequency bands, for both the real part and the magnitude of the driving point mobilities. Compared to the simply supported beams, slightly better agreement is achieved when the beams are free at both ends.

The lowest frequency torsional modes for the isolated free beams SS1 and SS2 occurs at 174.4 and 209.3 Hz respectively. For torsional wave excitation, the ratio of the real part of the driving point mobilities, $10\lg(Y_{T,FEM}/Y_{B,Inf})$ is less than 5 dB for the 45% and 43% of the excitation positions of beam SS1 and SS2 respectively (see Figure 5-16 and Figure 5-17). As before, this difference is reasonable since the driving point mobility of a beam of infinite extent is valid only for bending wave excitation. However, in terms of the spatial average the ratio $10\lg(<Y_{T,FEM}>_s/Y_{B,Inf})$ is between -3.2 and 3.3 dB between the 300 and 3100 Hz bands for both the real part and the magnitude of the driving point mobilities. At 100 Hz the differences are up to -5 and -12.3 dB for beams SS1 and SS2 respectively.

For the combination of bending, torsional and longitudinal modes of beams SS1 and SS2, the ratio of the real part of the driving point mobilities, $10\lg(Y_{A,FEM}/Y_{B,Inf})$ is less than 5 dB for the 65% and 67% of the excitation positions of beam SS1 and SS2 respectively (see Figure 5-18 and Figure 5-19). In terms of the spatial average, the ratio $10\lg(<Y_{A,FEM}>_s/Y_{B,Inf})$ is positive and up to 6 dB between the 100 and 3100 Hz frequency bands, both for the real part and the magnitude of the driving point mobilities.

As for the simply supported beams, the infinite beam equation gives close estimates for bending wave only modes and reasonable estimates for torsional modes only and with all modes.

5.4.4 Discussion

For beam SS1 (which is thinner in the direction of bending wave motion) the infinite beam mobility is a reasonable estimate for both bending and torsional modes and whilst it is also reasonable for bending waves on SS2, it is less reasonable for torsional modes. For both beams the infinite beam theory gives the least reasonable estimate for the combination of all modes. However, in the absence of any alternative equation, both will be used to calculate the CLF in section 5.6.

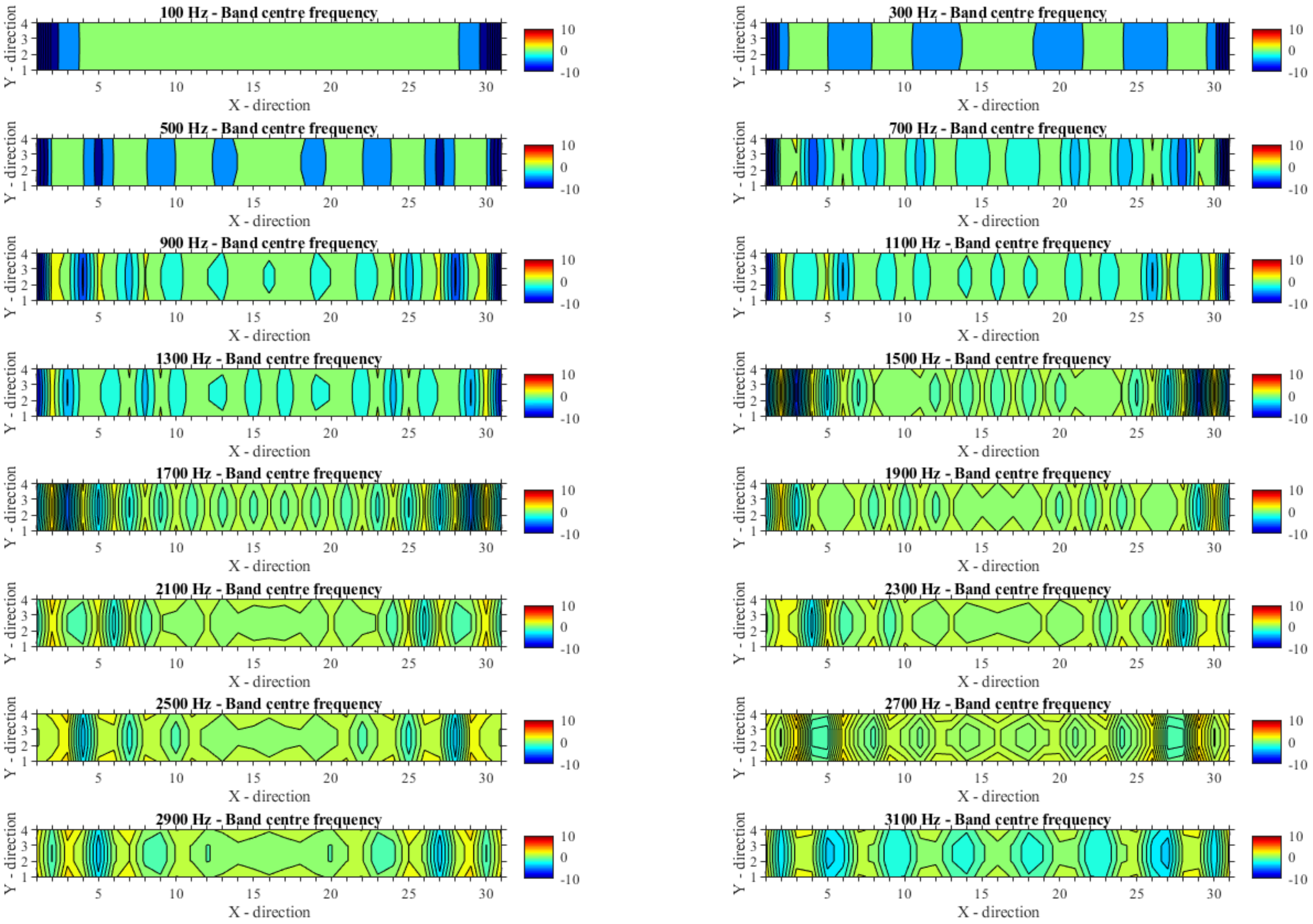

Figure 5-6 Contour plots of the ratio of the real part of the driving-point mobilities (FEM to infinite beam theory in decibels) for simply supported beam SS1 for excitation of bending waves only. X and Y axis indicate the grid of the measuring positions of $Y_{\mathrm{B,FEM}}$.

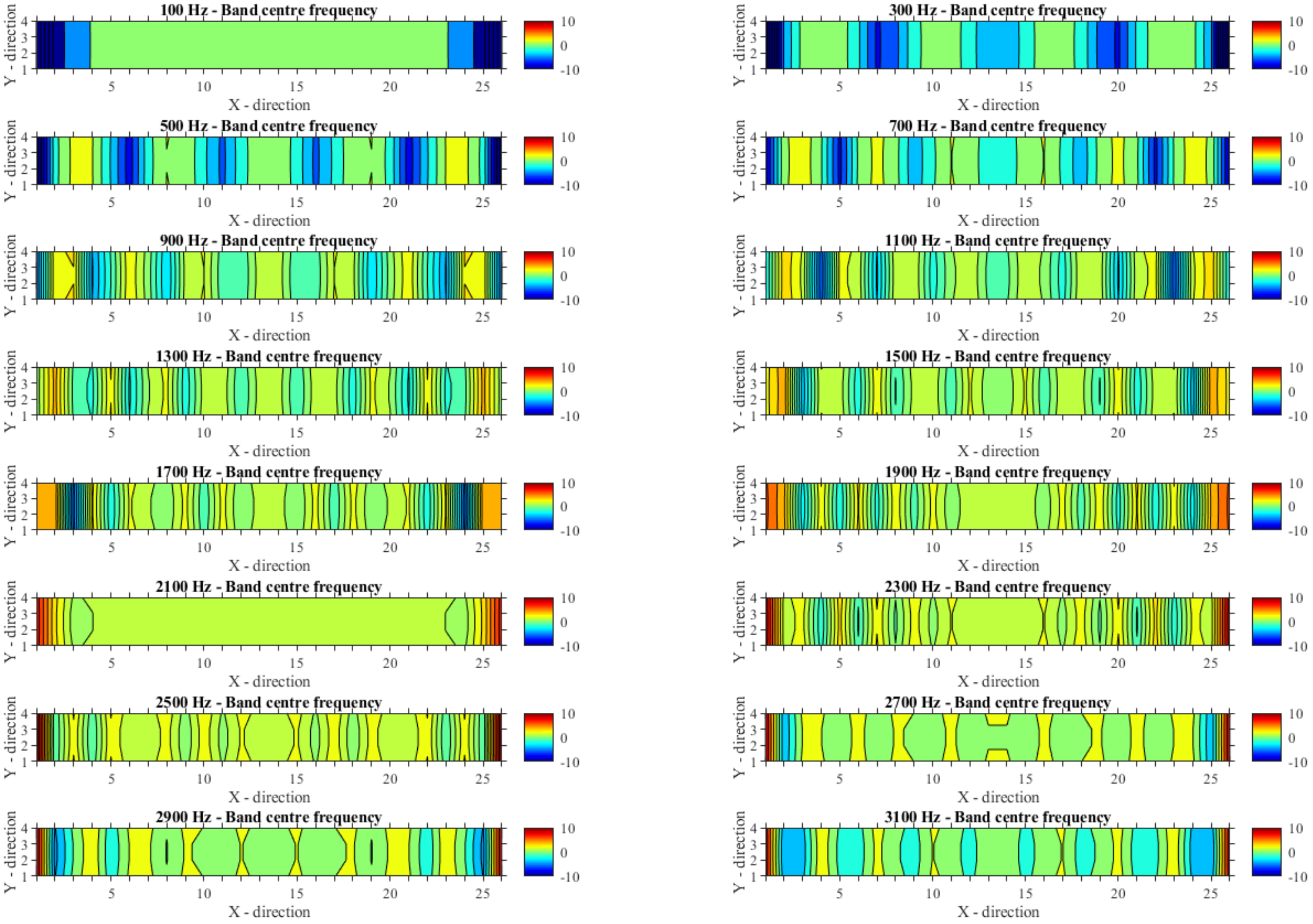

Figure 5-7 Contour plots of the ratio of the real part of the driving-point mobilities (FEM to infinite beam theory in decibels) for simply supported beam SS2 for excitation of bending waves only. X and Y axis indicate the grid of the measuring positions of $Y_{\mathrm{B,FEM}}$.

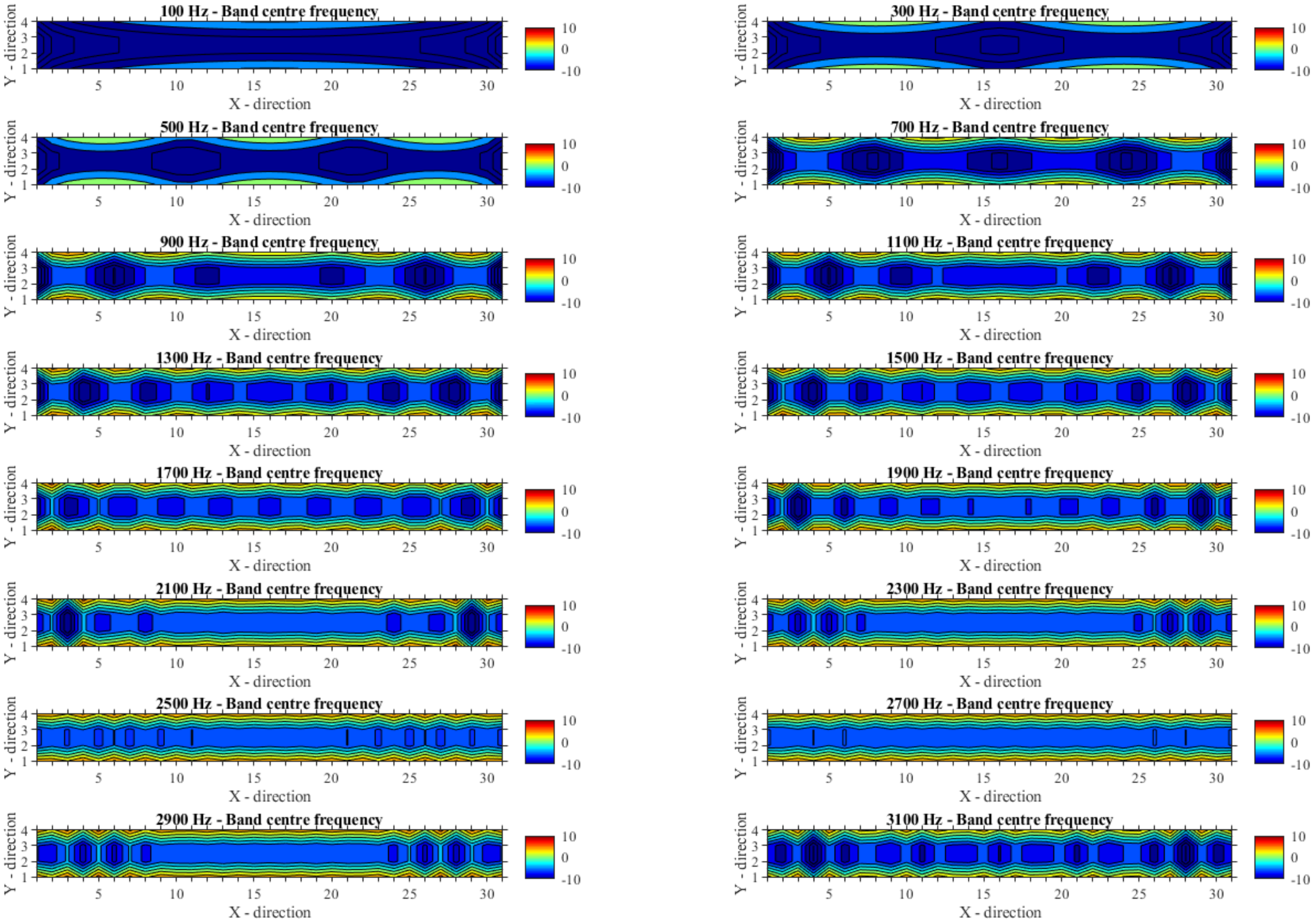

Figure 5-8 Contour plots of the ratio of the real part of the driving-point mobilities (FEM to infinite beam theory in decibels) for simply supported beam SS1 for excitation of torsional waves only. X and Y axis indicate the grid of the measuring positions of $Y_{\mathrm{T,FEM}}$.

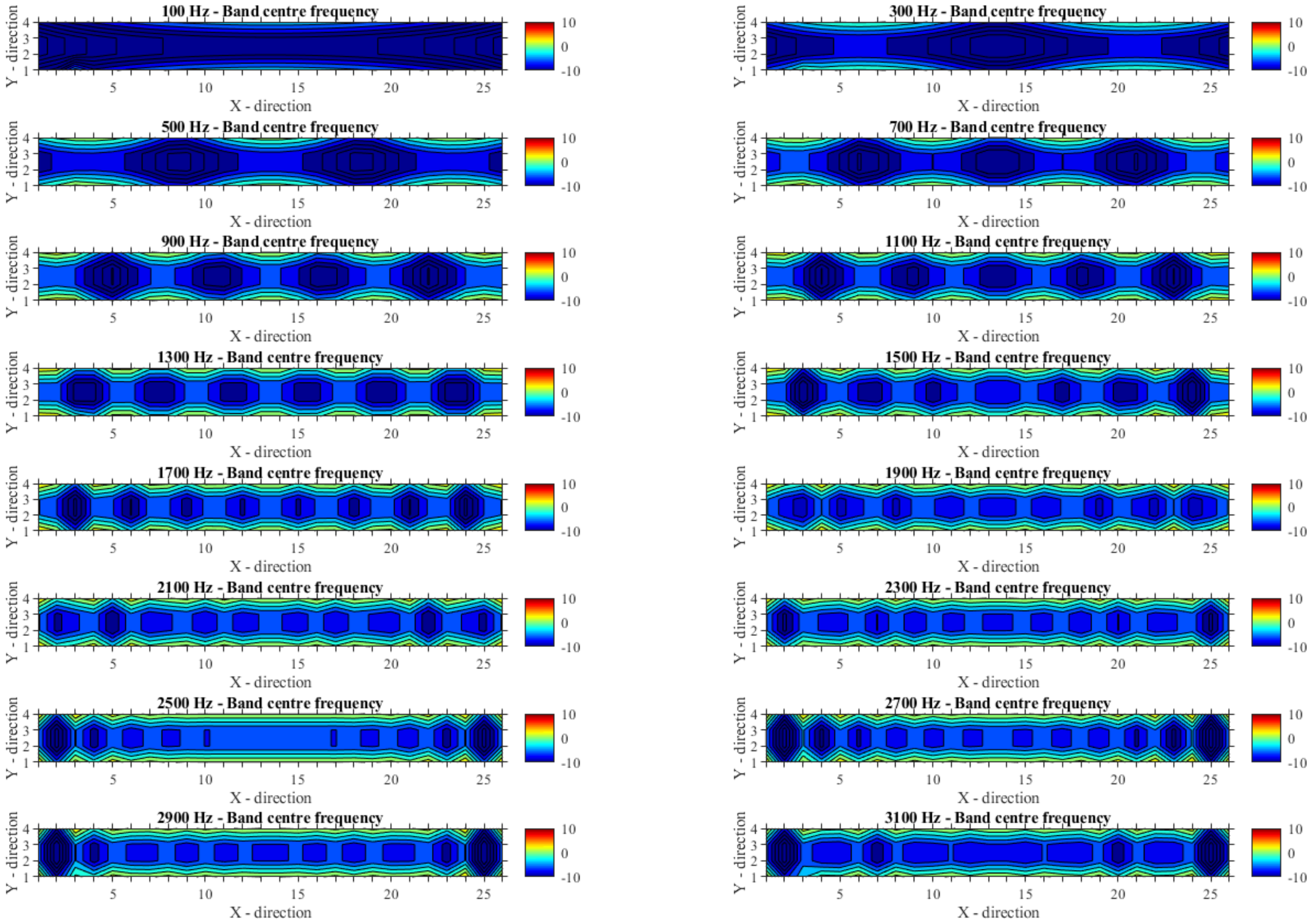

Figure 5-9 Contour plots of the ratio of the real part of the driving-point mobilities (FEM to infinite beam theory in decibels) for simply supported beam SS2 for excitation of torsional waves only. X and Y axis indicate the grid of the measuring positions of $Y_{\mathrm{T,FEM}}$.

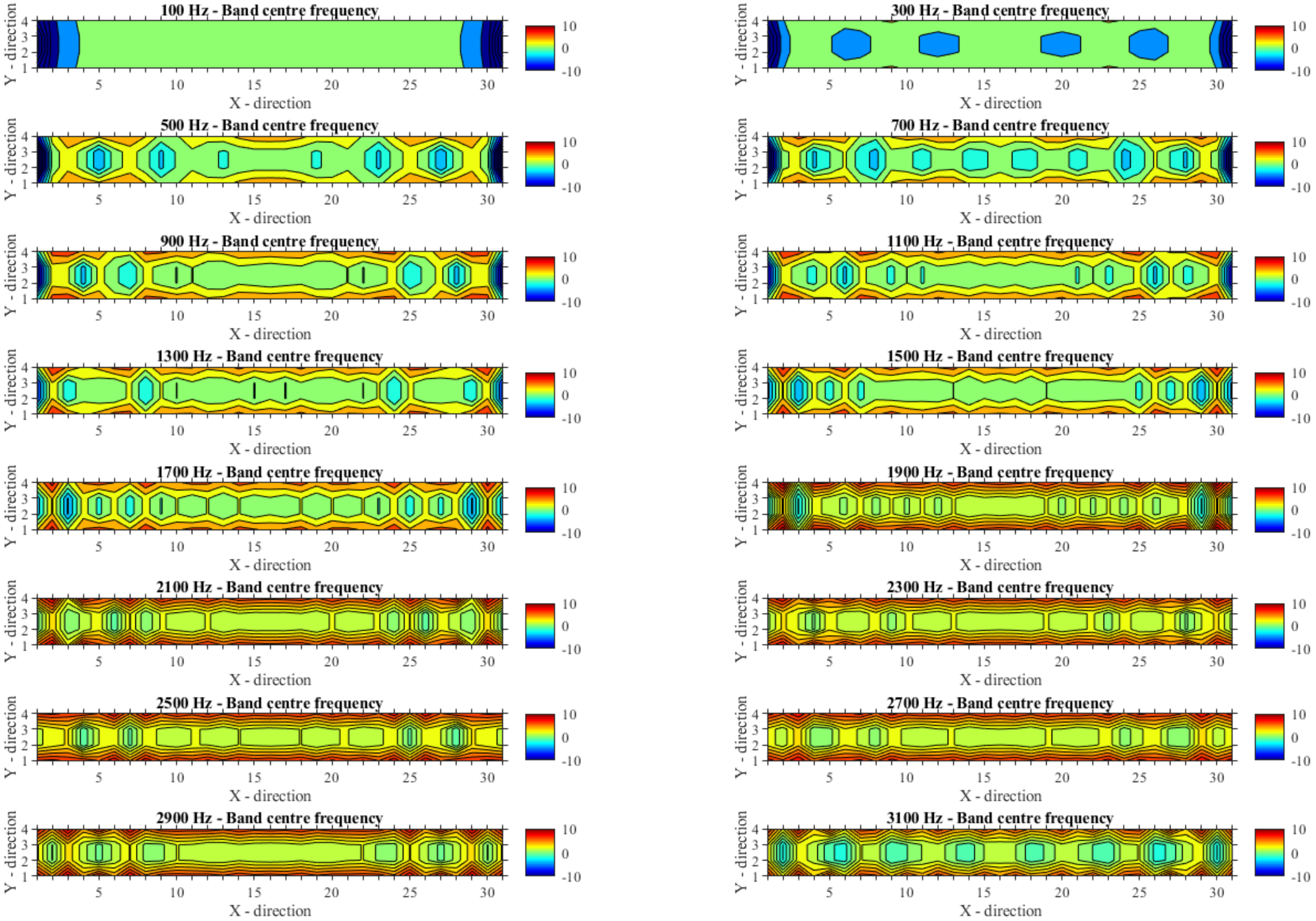

Figure 5-10 Contour plots of the ratio of the real part of the driving-point mobilities (FEM to infinite beam theory in decibels) for simply supported beam SS1 for combination of all types of waves. X and Y axis indicate the grid of the measuring positions of $Y_{\mathrm{A,FEM}}$.

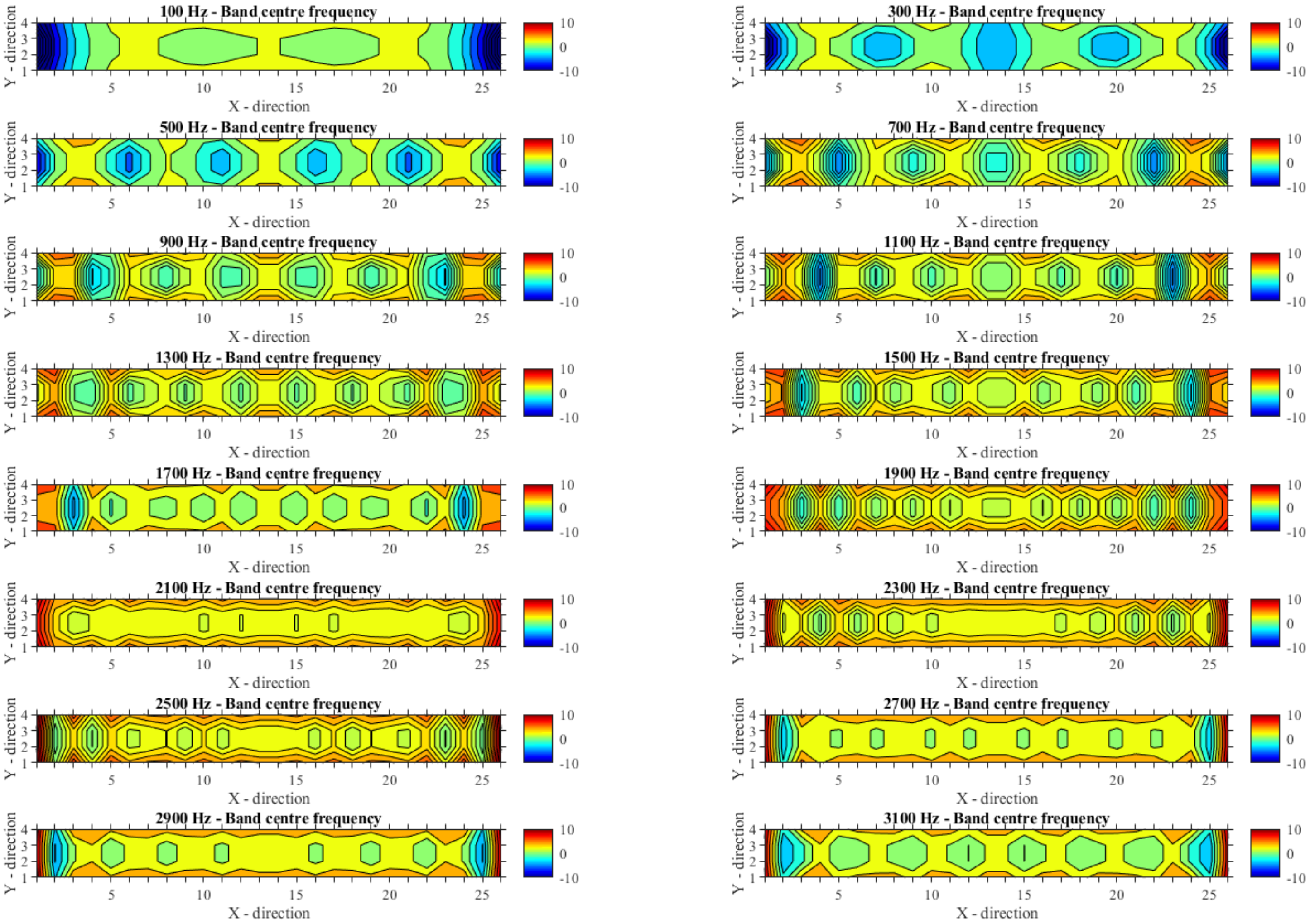

Figure 5-11 Contour plots of the ratio of the real part of the driving-point mobilities (FEM to infinite beam theory in decibels) for simply supported beam SS2 for combination of all types of waves. X and Y axis indicate the grid of the measuring positions of $Y_{A,FEM}$.

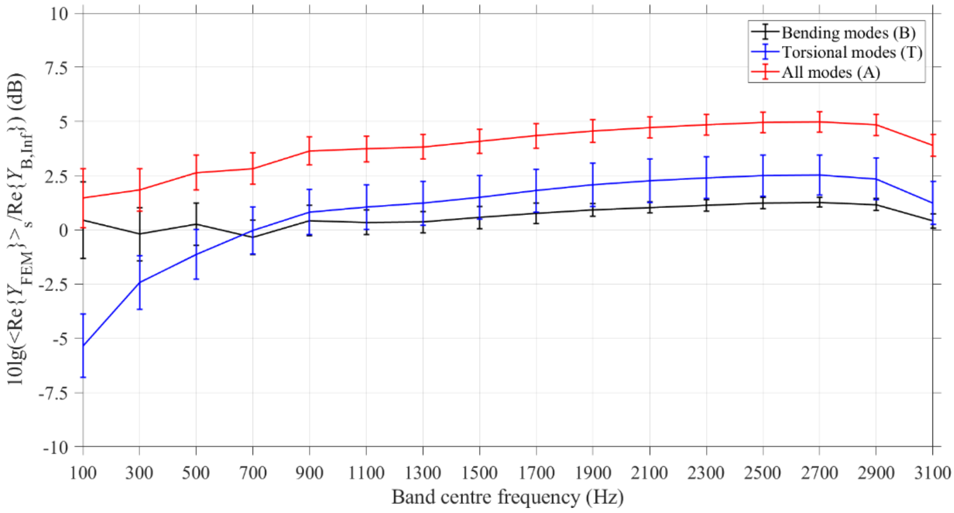

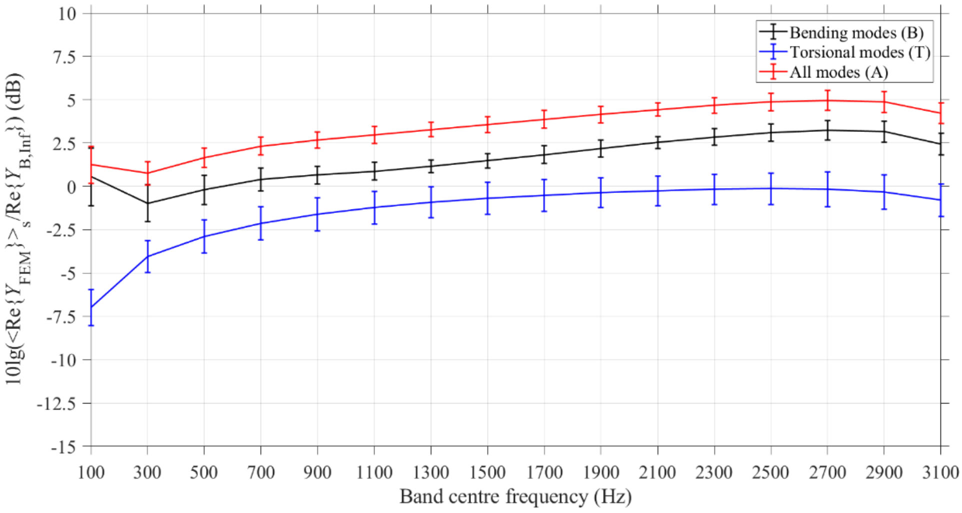

Figure 5-12 Ratio of the real part of the driving-point mobilities (FEM to infinite beam theory) along with the 95% confidence intervals for beam SS1 (top) and beam SS2 (bottom) when they are simply supported.

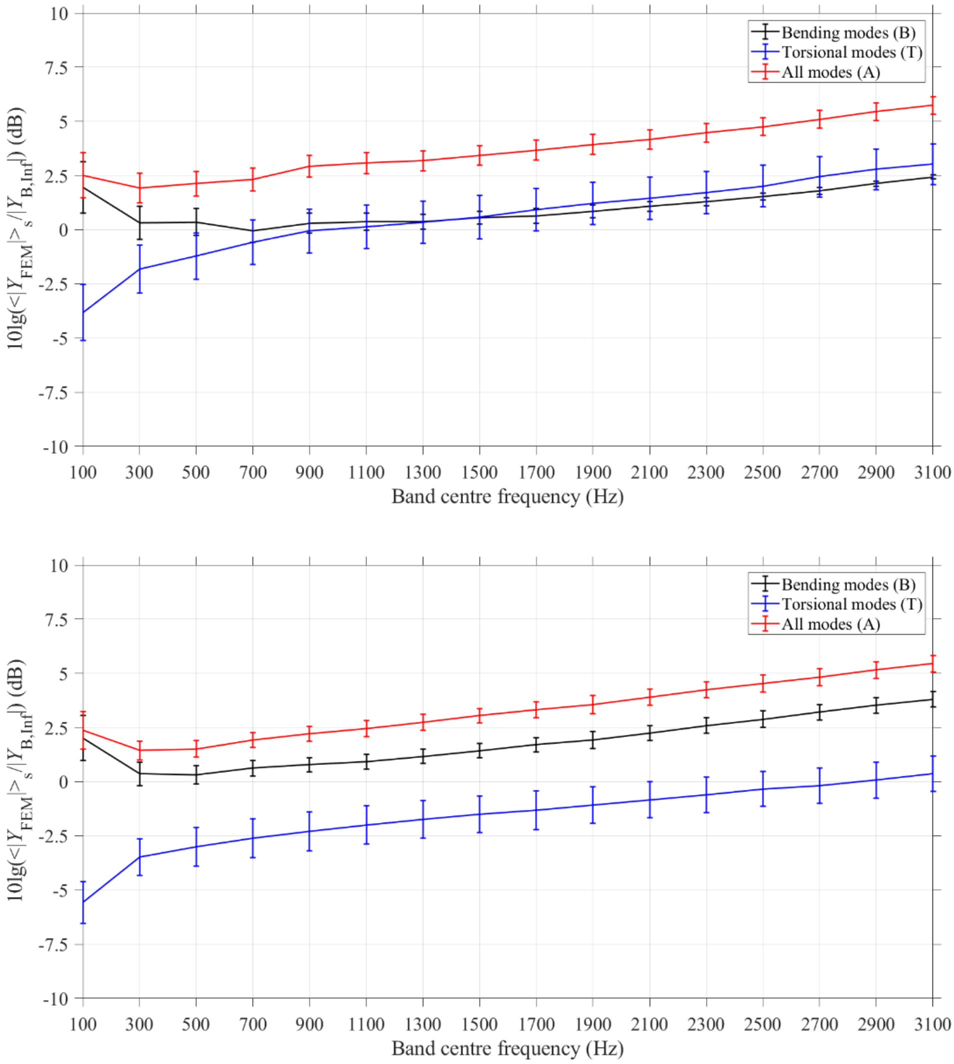

Figure 5-13 Ratio of the magnitude of the driving-point mobilities (FEM to infinite beam theory) along with the 95% confidence intervals for beam SS1 (top) and beam SS2 (bottom) when they are simply supported.

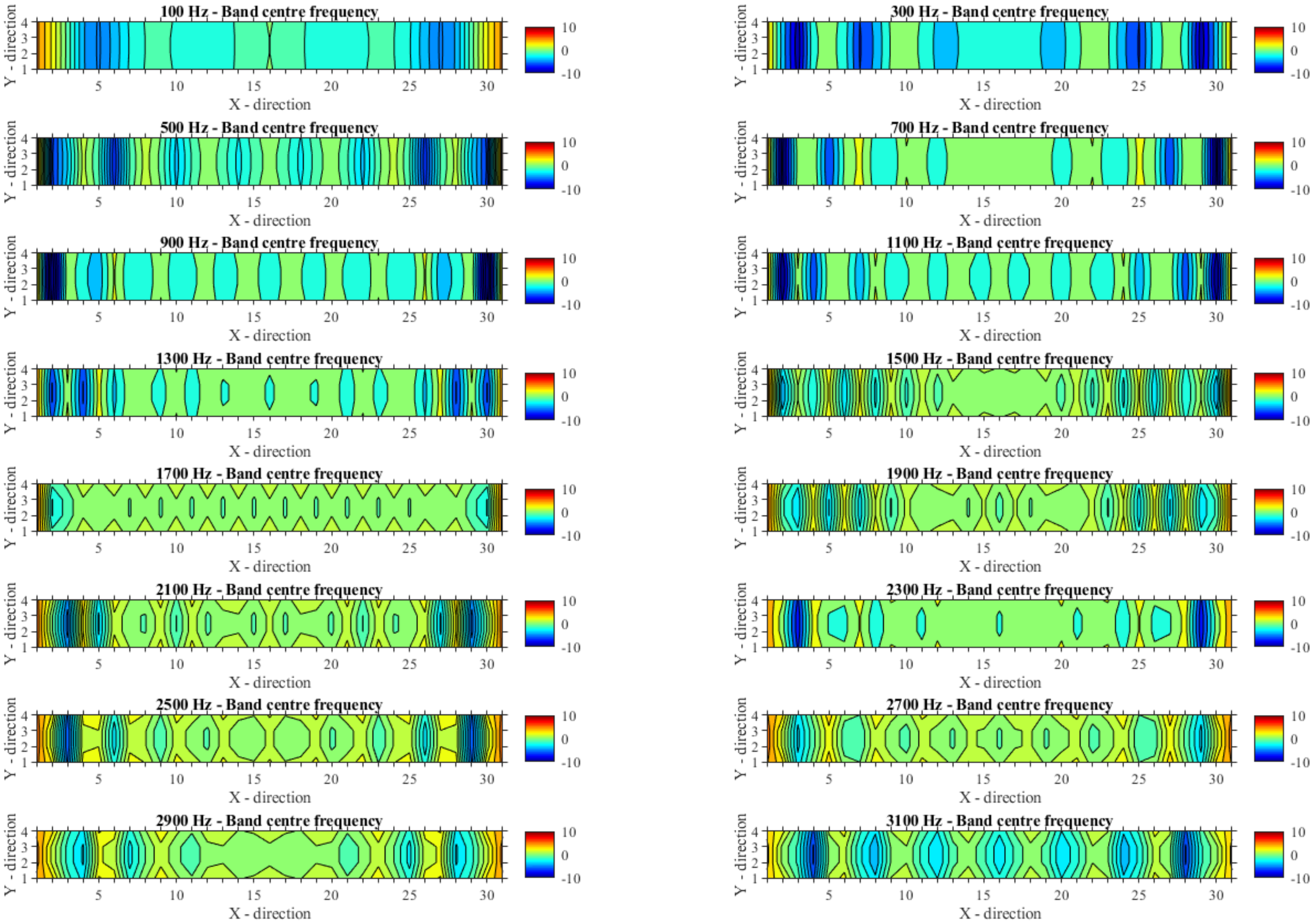

Figure 5-14 Contour plots of the ratio of the real part of the driving-point mobilities (FEM to infinite beam theory in decibels) for the free supported beam SS1 for excitation of bending waves only. X and Y axis indicate the grid of the measuring positions of $Y_{\mathrm{B,FEM}}$.

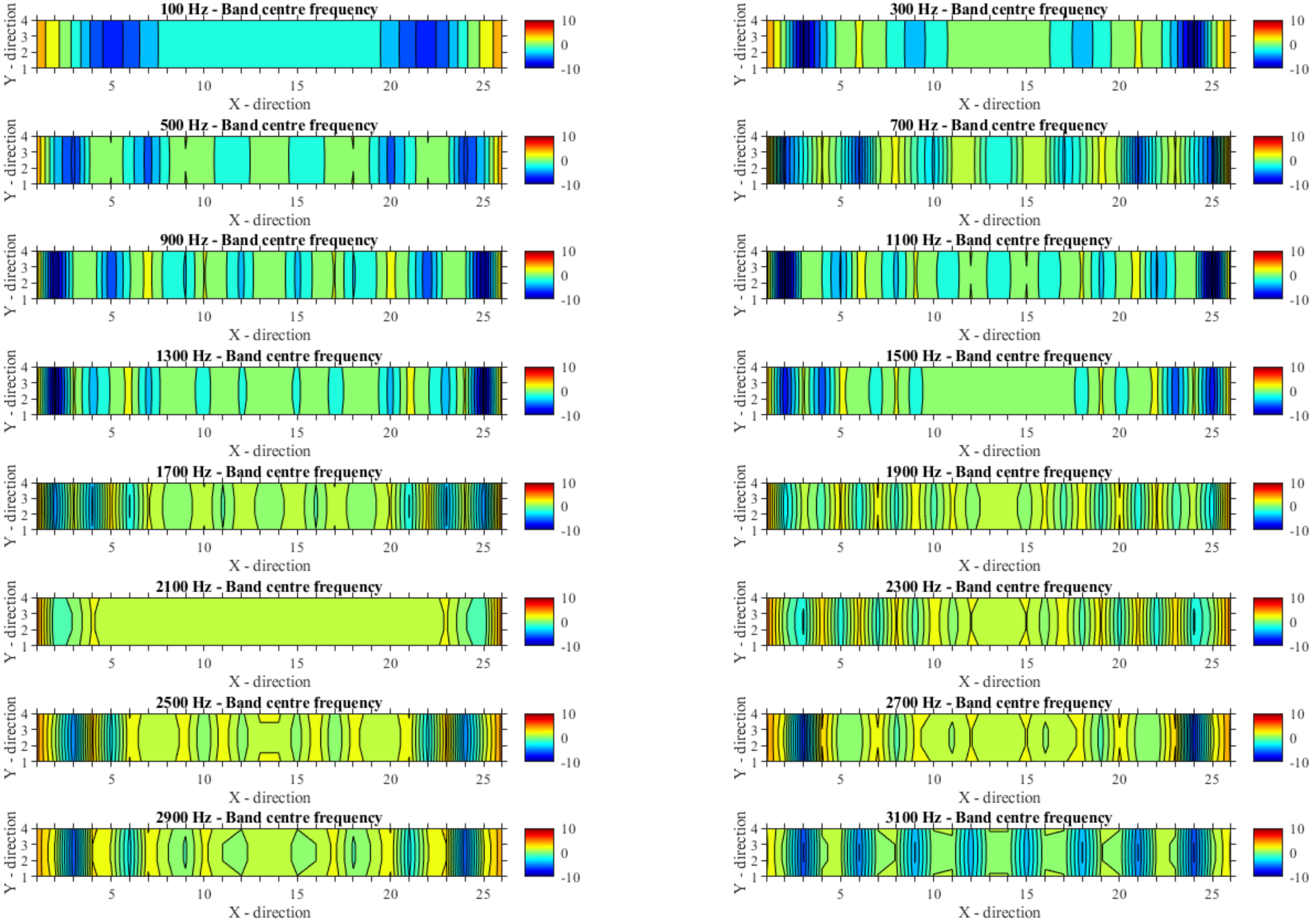
100 Hz - Band centre frequency
300 Hz - Band centre frequency
500 Hz - Band centre frequency
700 Hz - Band centre frequency
900 Hz - Band centre frequency
1100 Hz - Band centre frequency
1300 Hz - Band centre frequency
1500 Hz - Band centre frequency
1700 Hz - Band centre frequency
1900 Hz - Band centre frequency
2100 Hz - Band centre frequency
2300 Hz - Band centre frequency
2500 Hz - Band centre frequency
2700 Hz - Band centre frequency
2900 Hz - Band centre frequency
3100 Hz - Band centre frequency

Figure 5-15 Contour plots of the ratio of the real part of the driving-point mobilities (FEM to infinite beam theory in decibels) for the free supported beam SS2 for excitation of bending waves only. X and Y axis indicate the grid of the measuring positions of $Y_{B,FEM}$.

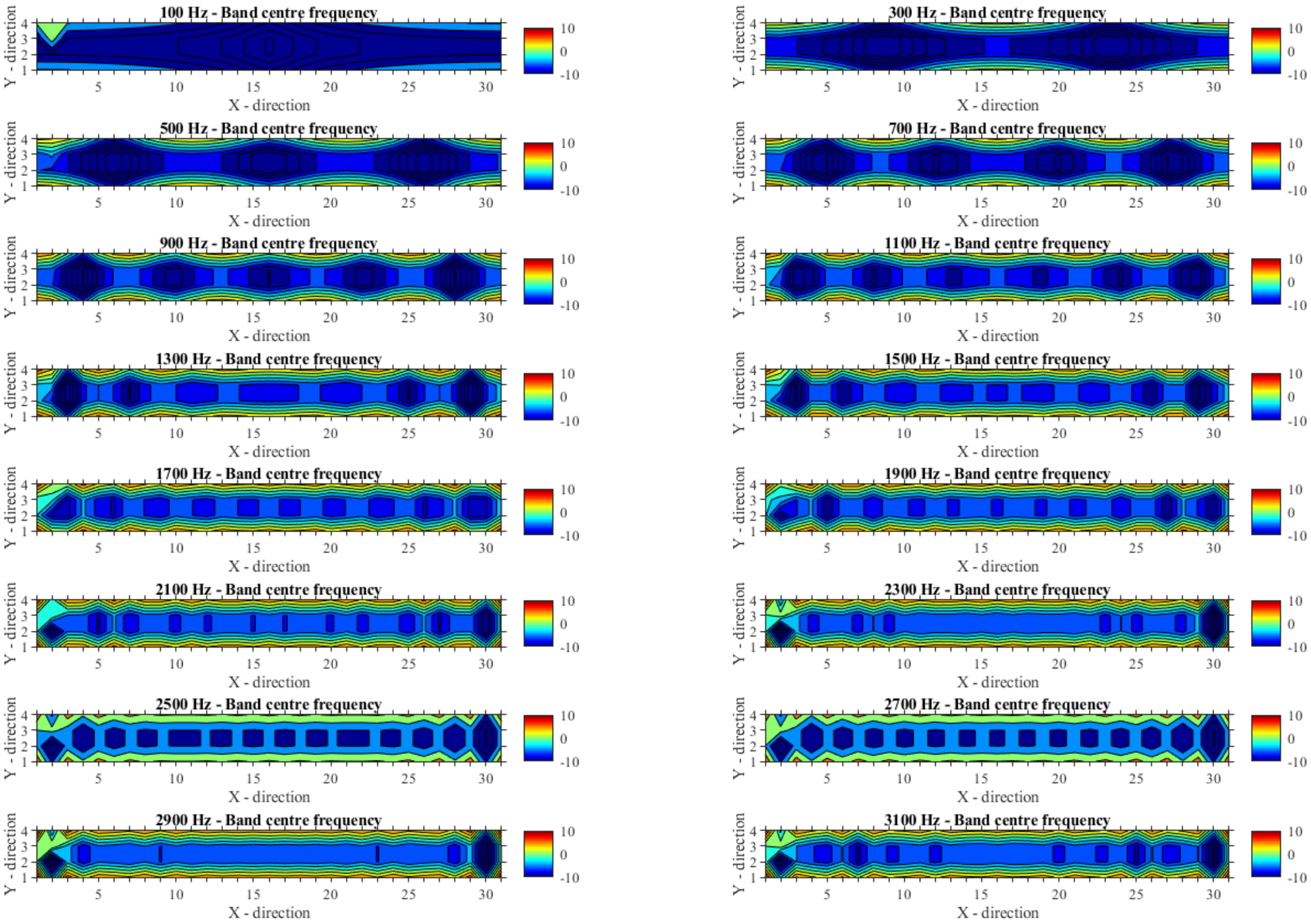

Figure 5-16 Contour plots of the ratio of the real part of the driving-point mobilities (FEM to infinite beam theory in decibels) for the free supported beam SS1 for excitation of torsional waves only. X and Y axis indicate the grid of the measuring positions of $Y_{T,FEM}$.

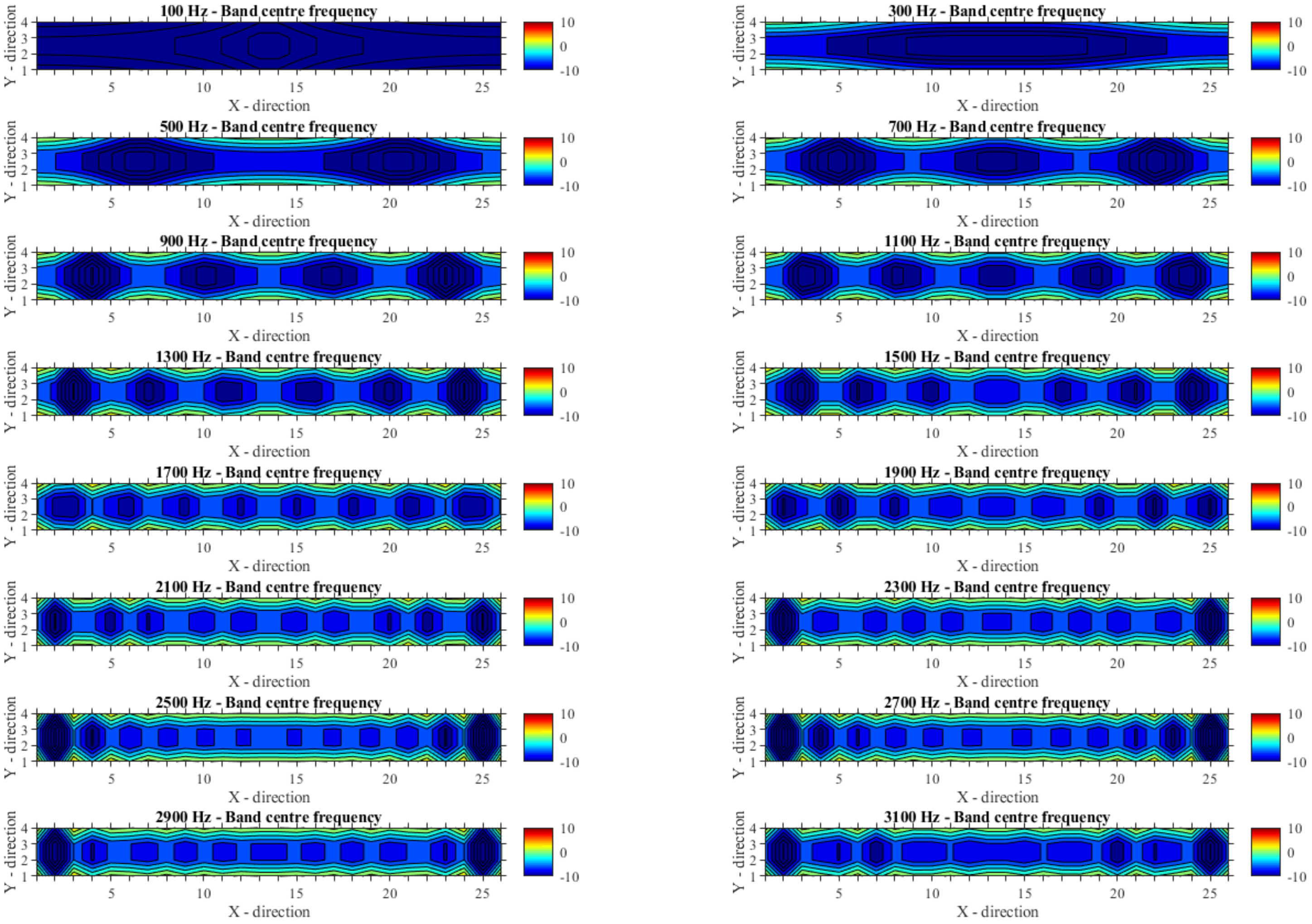

Figure 5-17 Contour plots of the ratio of the real part of the driving-point mobilities (FEM to infinite beam theory in decibels) for the free supported beam SS2 for excitation of torsional waves only. X and Y axis indicate the grid of the measuring positions of $Y_{\mathrm{T,FEM}}$.

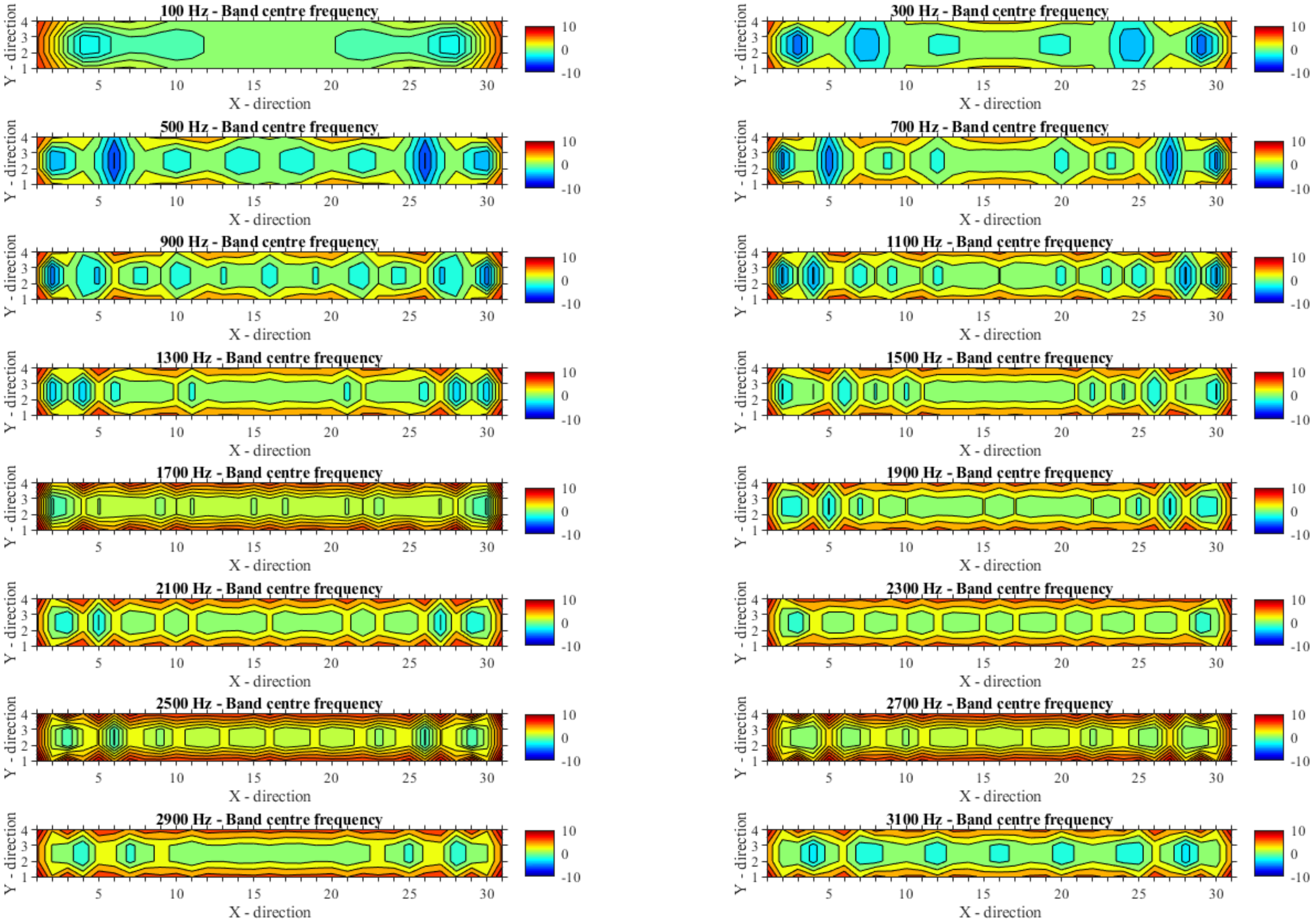

Figure 5-18 Contour plots of the ratio of the real part of the driving-point mobilities (FEM to infinite beam theory in decibels) for the free supported beam SS1 for combination of all types of waves. X and Y axis indicate the grid of the measuring positions of $Y_{\mathrm{A,FEM}}$.

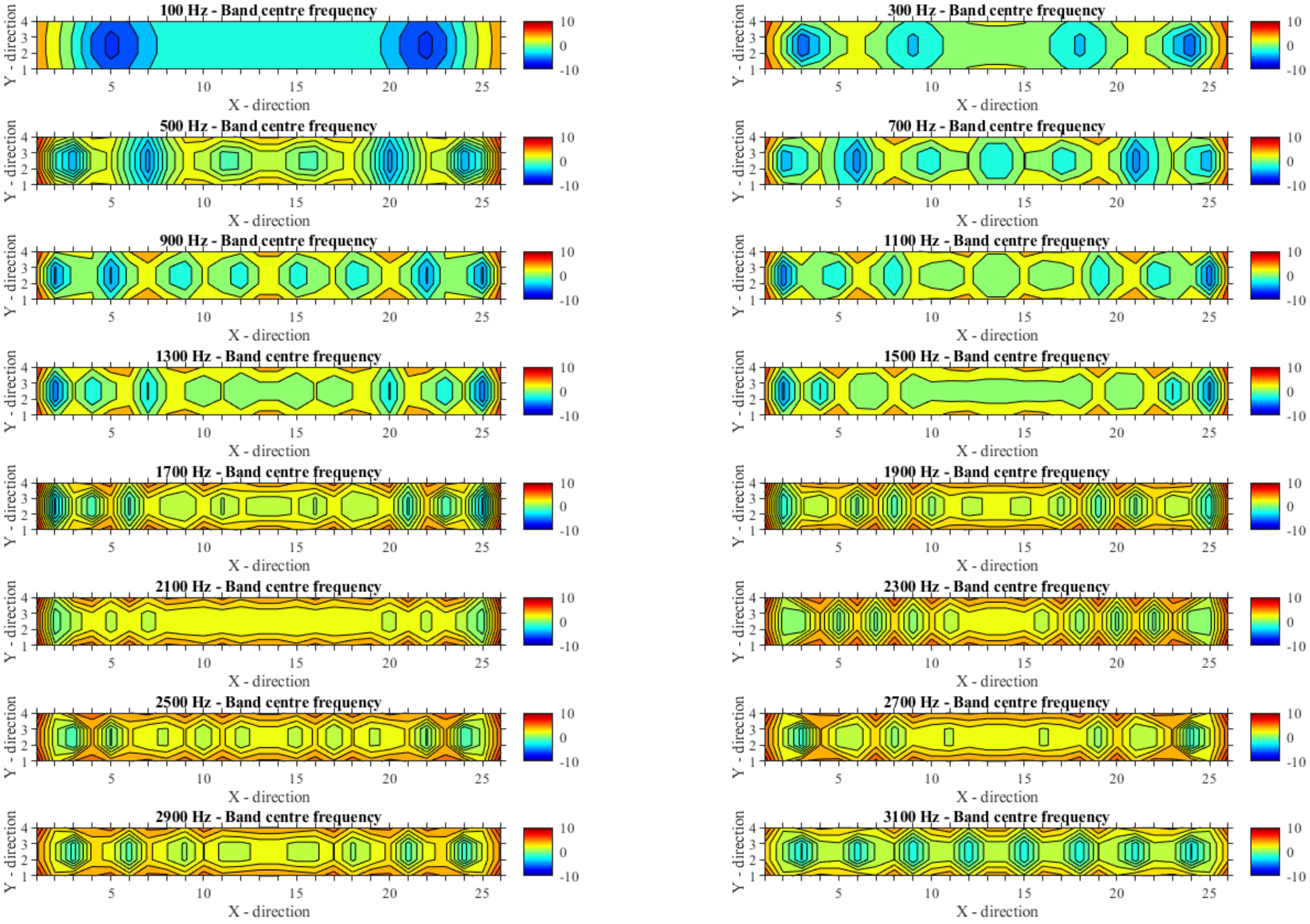
100 Hz - Band centre frequency

300 Hz - Band centre frequency

500 Hz - Band centre frequency

700 Hz - Band centre frequency

900 Hz - Band centre frequency

1100 Hz - Band centre frequency

1300 Hz - Band centre frequency

1500 Hz - Band centre frequency

1700 Hz - Band centre frequency

1900 Hz - Band centre frequency

2100 Hz - Band centre frequency

2300 Hz - Band centre frequency

2500 Hz - Band centre frequency

2700 Hz - Band centre frequency

2900 Hz - Band centre frequency

3100 Hz - Band centre frequency

Figure 5-19 Contour plots of the ratio of the real part of the driving-point mobilities (FEM to infinite beam theory in decibels) for the free supported beam SS2 for combination of all types of waves. X and Y axis indicate the grid of the measuring positions of $Y_{\mathrm{A,FEM}}$.

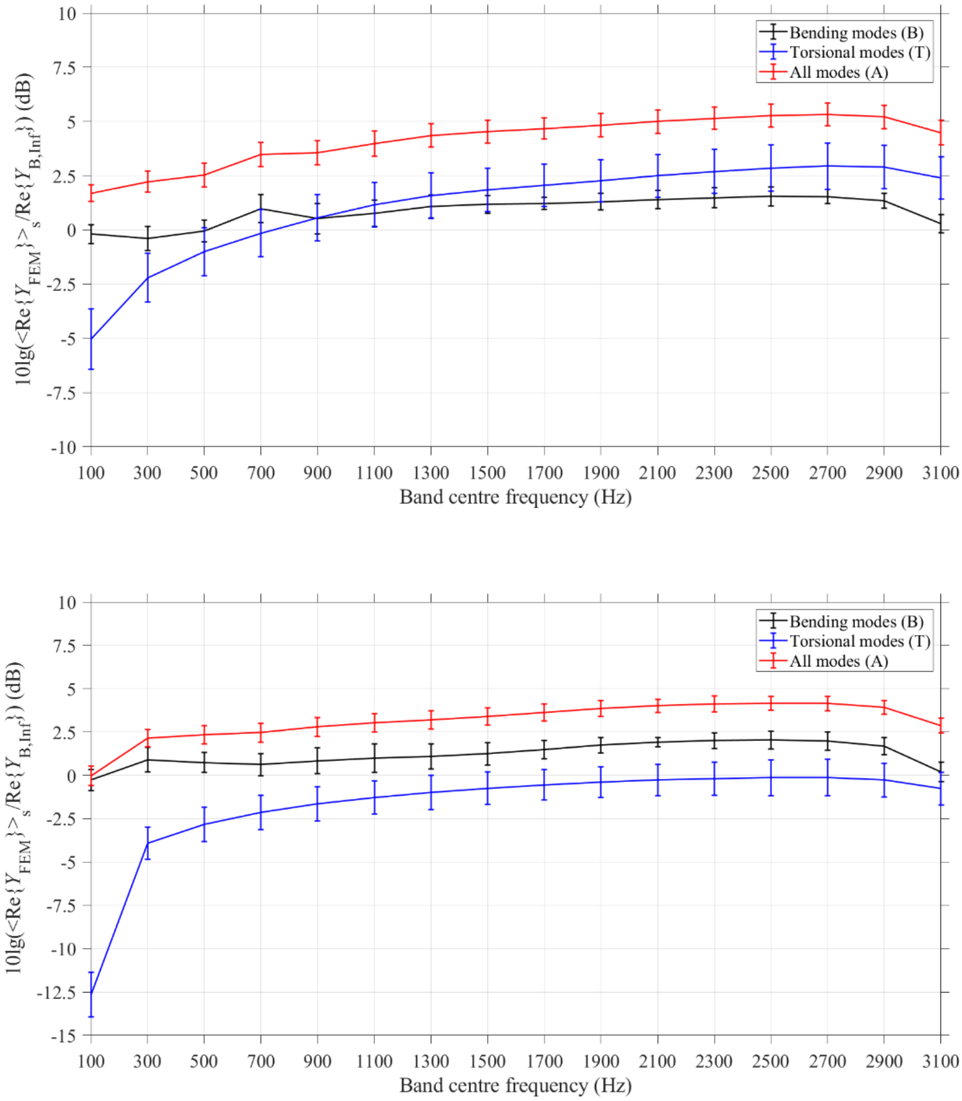

Figure 5-20 Ratio of the real part of the driving-point mobilities (FEM to infinite beam theory) along with the 95% confidence intervals for beam SS1 (top) and beam SS2 (bottom) with free-free support conditions.

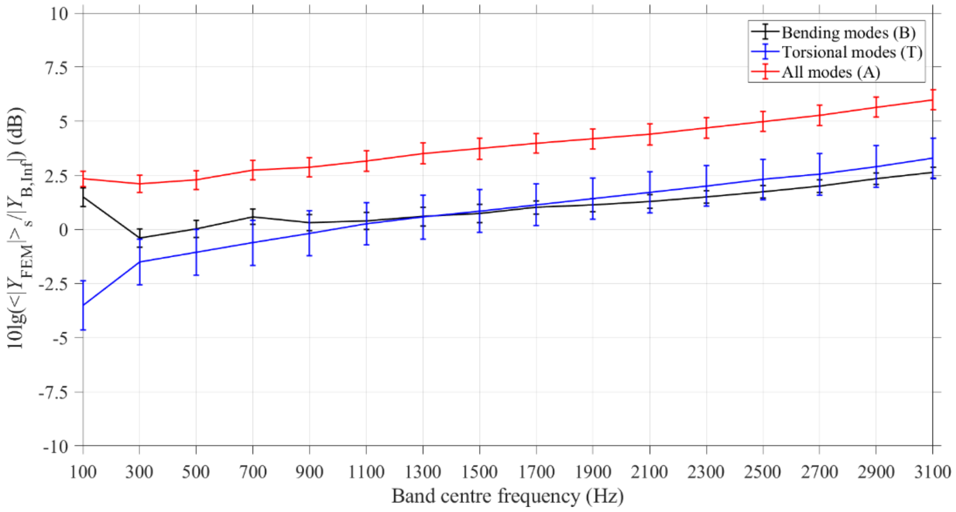

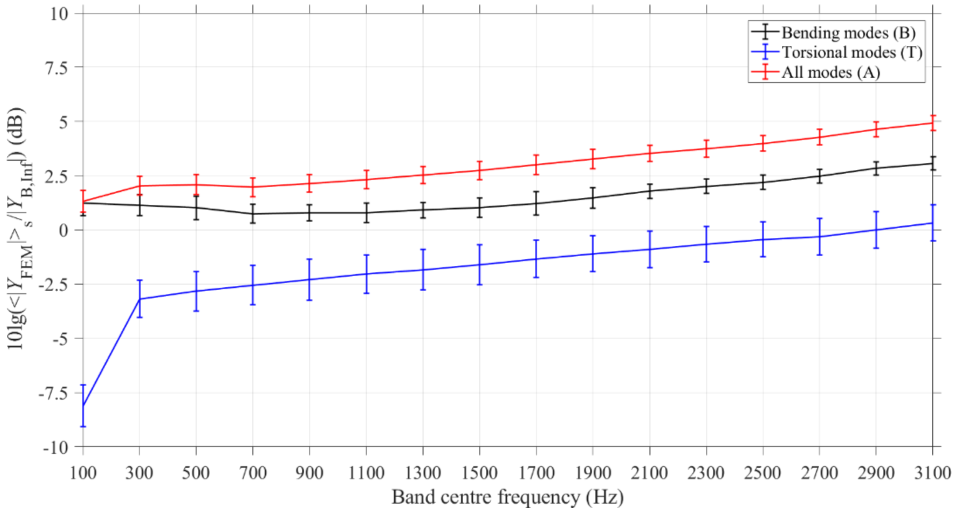

Figure 5-21 Ratio of the magnitude of the driving-point mobilities (FEM to infinite beam theory) along with the 95% confidence intervals for beam SS1 (top) and beam SS2 (bottom) with free-free support conditions.

5.5 Bending and torsional wavelength

To assess the potential frequency range of application for the lump spring model, the length of the longest side of the surface-to-surface contact area, $L_{C,max}$, is compared with the bending and torsional wavelength. It is assumed that the lump spring model will be valid at frequencies where $\lambda_B/2 > L_{C,max}$ for bending motion and $\lambda_T/2 > L_{C,max}$ for torsional motion [70].

Figure 5-22 shows the bending wavelength, λ_B and the half-wavelength, $\lambda_B/2$ for beam SS1 and SS2. $L_{C,max}$ is equal to $\lambda_B/2$ for beams SS1 and SS2 at 1720 Hz and 2580 Hz respectively. For torsional waves, $L_{C,max}$ is equal to $\lambda_T/2$ for beams SS1 and SS2 at 2360 Hz (see Figure 5-23). This information will be used in assessing the validity of the lump spring model in section 5.6.

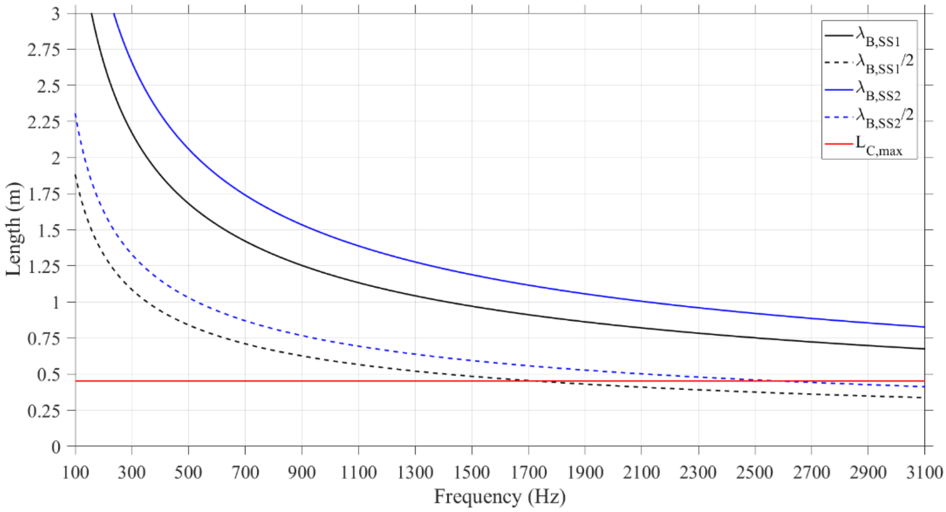

Figure 5-22 Bending wavelength of beams SS1 and SS2. The red line indicates the length of the longest side, $L_{C,max}$=0.45 m of the contact area.

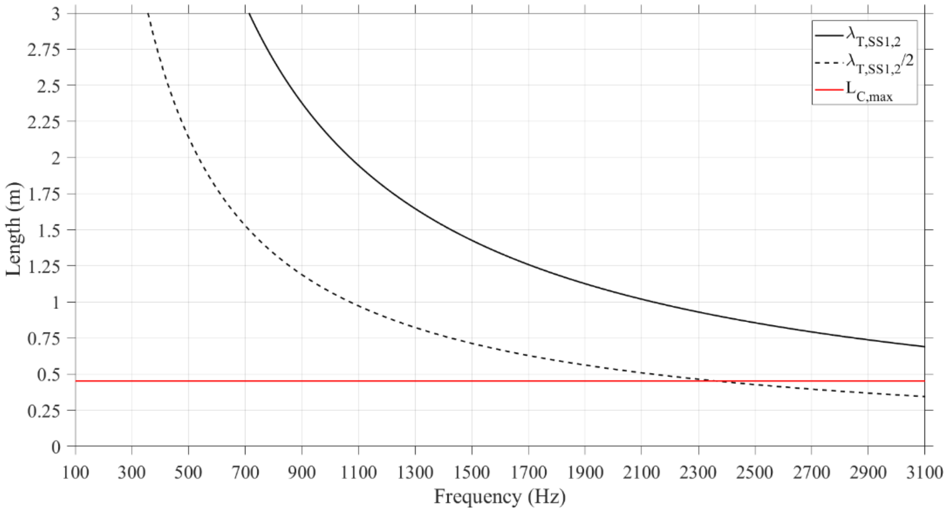

Figure 5-23 Torsional wavelength of beams SS1 and SS2. The red line indicates the length of the longest side, $L_{C,max}$=0.45 m of the contact area.

5.6 Comparison of coupling loss factors from lump spring theory and FEM ESEA

Figure 5-24 to Figure 5-29 show the coupling loss factors, η_{12} and η_{21} from FEM ESEA for the 30 beam junctions along with two prediction models based on the lump spring connector model (see section 3.3.3.1). The analytical lump spring model is calculated using (a) the driving point mobilities, $Y_{B,Inf}$, of thin beams of infinite extent for excitation of bending waves in the central part of the beams and (b) the spatial average of the FEM driving point mobilities, Y_{FEM}, over the surface of beams SS1 and SS2 with simply supported and free support conditions (see section 5.4). The FEM ESEA results for simply supported and free supported beams are shown in terms of a mean value with 95% confidence intervals.

5.6.1 Simply supported condition

For bending waves only in the FEM model (Figure 5-24), there is close agreement between the coupling loss factors from FEM ESEA and the analytical model up to the 1700 Hz frequency band (where $\lambda_B/2 > L_{C,max}$), with differences up to 5 dB. Above 1700 Hz, the differences increased up to 12 dB where the contact area between SS1 and SS2 can no longer be considered as a point connection. Using FEM mobilities instead of the infinite beam mobilities for bending wave motion does not significantly improve the agreement. This is expected because the real part and the magnitude are between -1 and 3.8 dB of $Y_{B,inf}$ in this frequency range.

For torsional waves only in the FEM model (Figure 5-25), there is close agreement between FEM ESEA and the analytical model up to the 2300 Hz frequency band (where $\lambda_T/2 > L_{C,max}$), with differences up to 5 dB. Note that in two low frequency bands (100 Hz and 300 Hz) the spread of the FEM ESEA coupling loss factors was ± 5 dB. Above 2300 Hz, the differences were between 5 and 12 dB where the contact area between SS1 and SS2 can no longer be considered as a point connection. The infinite beam mobilities are intended for bending rather than torsional motion but are shown for reference. However, using FEM mobilities instead of the infinite beam mobilities for torsional motion did not significantly improve the agreement.

For the combination of all modes (Figure 5-26), close agreement was achieved between the FEM ESEA and the analytical model between 100 and 900 Hz, with differences up to 5 dB. Considering only bending modes, the analytical model is not expected to be valid above 1700 Hz (where $\lambda_B/2 > L_{C,max}$). However, the combination of all modes seems to reduce the frequency where close agreement is obtained from 1700 to 900 Hz. The infinite beam mobilities are an approximation as they intended for bending rather than all types of wave motion; hence it is a coincidence that the infinite beam mobilities show better agreement than the FEM calculated mobilities with the analytical model above 1100 Hz.

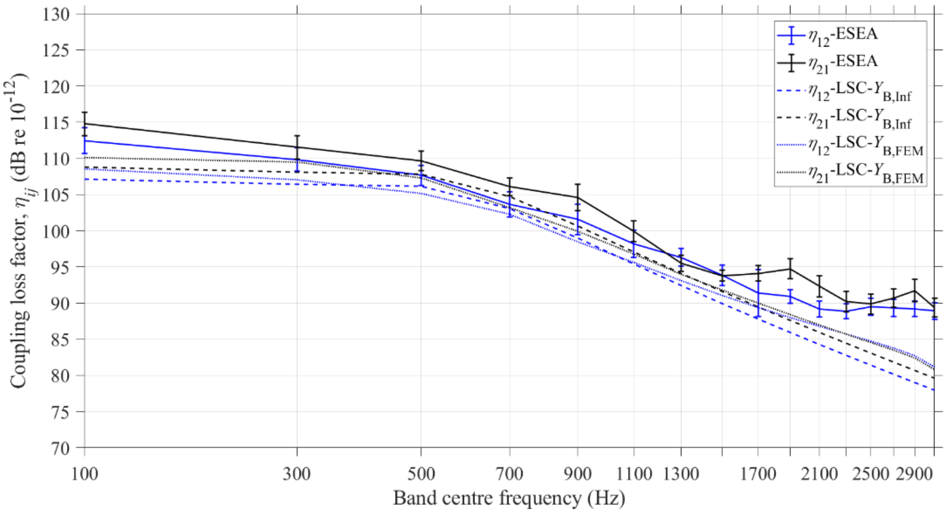

Figure 5-24 Comparison of FEM ESEA (bending modes) and the analytical model (LSC) coupling loss factors η_{12} and η_{21}. The error bars denote the 95% confidence intervals.

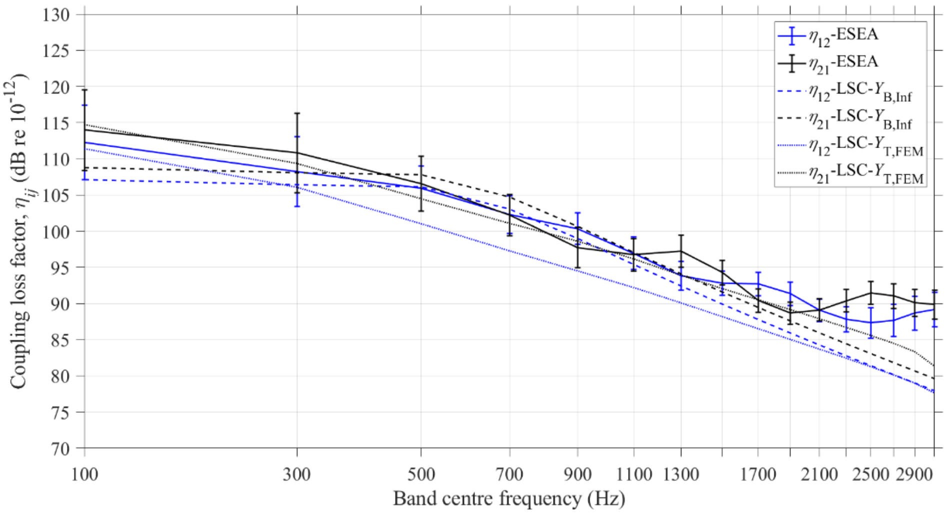

Figure 5-25 Comparison of FEM ESEA (torsional modes) and the analytical model (LSC) coupling loss factors η_{12} and η_{21}. The error bars denote the 95% confidence intervals.

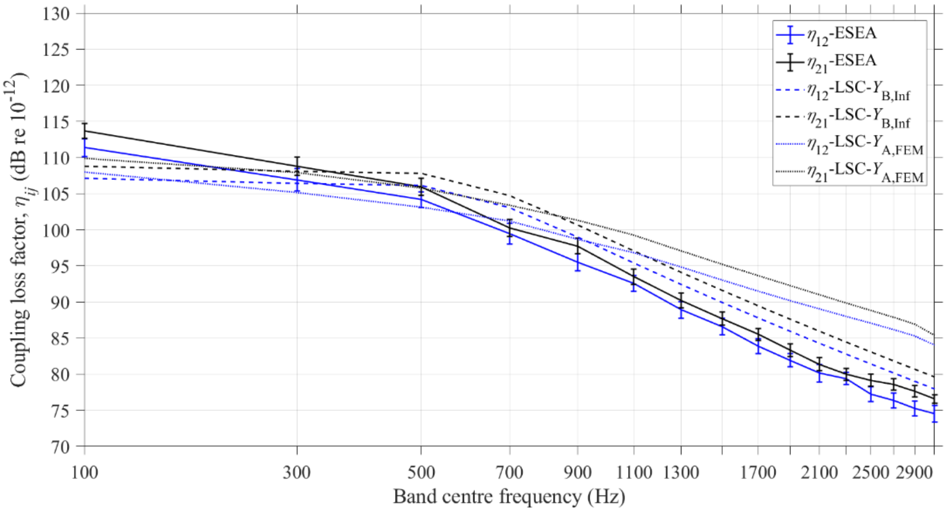

Figure 5-26 Comparison of FEM ESEA (combination of all modes) and the analytical model (LSC) coupling loss factors η_{12} and η_{21}. The error bars denote the 95% confidence intervals.

5.6.2 Free supported condition

For bending waves only in the FEM model (Figure 5-27), there is reasonable agreement between the coupling loss factors from FEM ESEA and the analytical model between 500 and 1900 Hz, with differences up to 6 dB. Below 500 Hz, the curves of the FEM ESEA and theoretical coupling loss factors follow the same trend although the differences are up to 9.8 dB. Above 1900 Hz, the differences increased up to 10.7 dB where the contact area between SS1 and SS2 can no longer be considered as a point connection. Using FEM mobilities instead of the infinite beam mobilities for bending wave motion did not significantly improve the agreement. This is expected because the real part and the magnitude are within 3 dB of $Y_{\mathrm{B,inf}}$ in this frequency range

For torsional waves only in the FEM model (Figure 5-28), there is reasonable agreement between FEM ESEA and the analytical model between 500 and 2300 Hz (where $\lambda_{\mathrm{T}}/2 > L_{\mathrm{C,max}}$), with differences up to 6 dB. In the 300 Hz band the differences are up to 7 dB, but the agreement can be considered reasonable since the spread of the FEM ESEA coupling loss factors was ± 4 dB. At 100 Hz, the differences are up to 18 dB and the spread of the FEM ESEA coupling loss factors was ± 8 dB. Above 2300 Hz, the differences were between 5 and 10 dB where the contact area between SS1 and SS2 cannot be considered as a point connection. The infinite beam mobilities are intended for bending rather than torsional motion but are shown for reference. However, as with the simply supported beams, using FEM mobilities instead of the infinite beam mobilities for torsional motion did not significantly improve the agreement except in the 100 Hz frequency band. This is expected because the real part and the magnitude are between -1 and 3.1 dB of $Y_{B,\mathrm{inf}}$ in this frequency range.

For the combination of bending, torsional and longitudinal modes (Figure 5-29), close agreement was achieved between the FEM ESEA and the analytical model between 100 and 900 Hz, with differences up to 5 dB. Above 900 Hz, the curves of the FEM ESEA and theoretical coupling loss factors do not follow the same trend even though the differences are up to 7 dB. The analytical model is not expected to be valid above 1700 Hz (where $\lambda_B/2 > L_{C,\mathrm{max}}$) but the combination of all modes seems to reduce the frequency where reasonable agreement is obtained from 1700 to 900 Hz. The infinite beam mobilities are an approximation as they intended for bending rather than all wave motion; hence it is a coincidence that the infinite beam mobilities show better agreement than the FEM calculated mobilities with the analytical model above 1100 Hz.

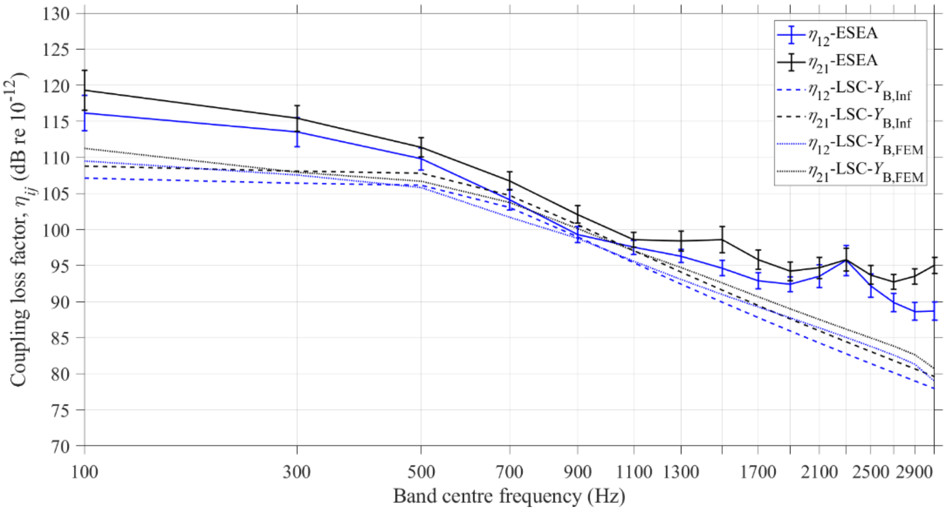

Figure 5-27 Comparison of FEM ESEA (bending modes) and the analytical model (LSC) coupling loss factors η_{12} and η_{21}. The error bars denote the 95% confidence intervals.

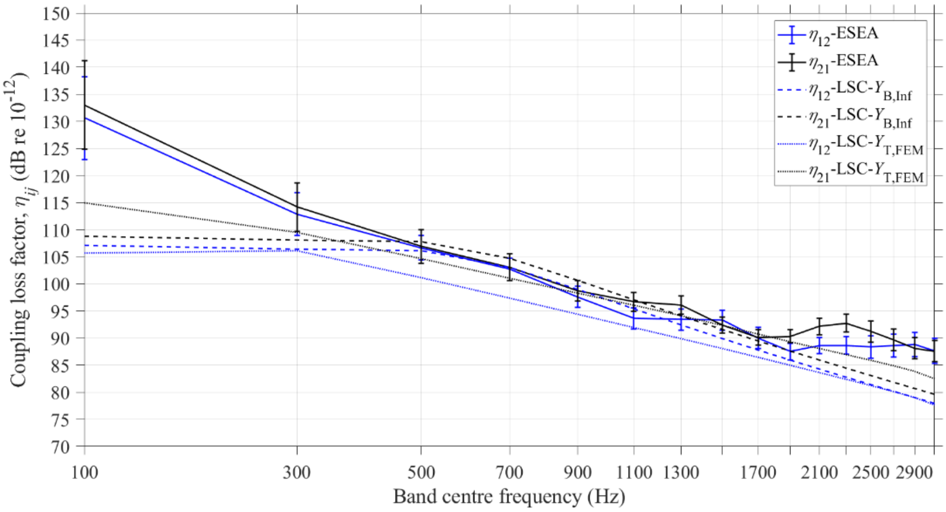

Figure 5-28 Comparison of FEM ESEA (torsional modes) and the analytical model (LSC) coupling loss factors η_{12} and η_{21}. The error bars denote the 95% confidence intervals.

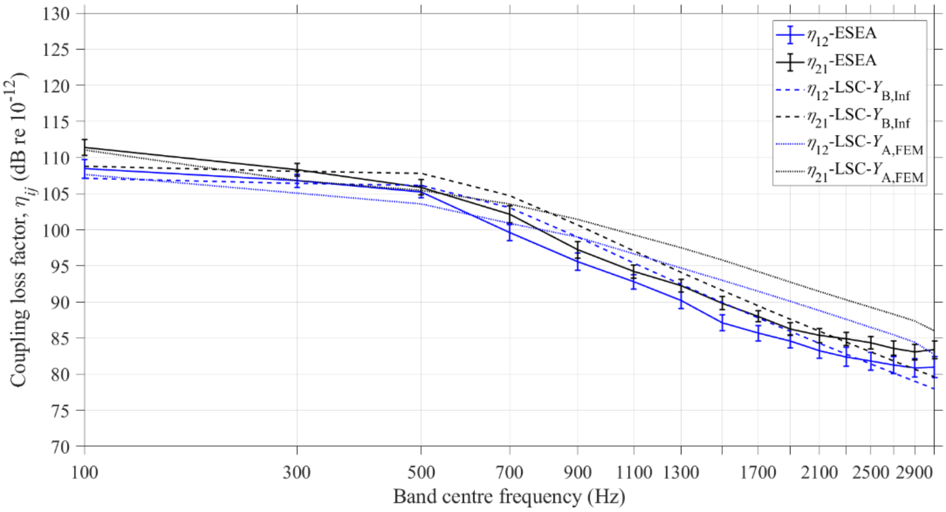

Figure 5-29 Comparison of FEM ESEA (combination of all modes) and the analytical model (LSC) coupling loss factors η_{12} and η_{21}. The error bars denote the 95% confidence intervals.

5.7 Conclusions

Finite element models were used to calculate the driving-point mobilities of reinforced concrete beams for bending modes only, torsional modes only and the combination of all modes in the frequency range up to 3200 Hz with free and simply supported conditions. These mobilities were in close agreement (differences within 5 dB) with the theoretical driving-point mobilities of a thin beam of infinite extent for bending wave excitation but not for the combination of all modes.

An ensemble of 30 random beam junctions with free and simply supported conditions was generated for Monte Carlo simulations with FEM that allowed ESEA to be used to determine coupling loss factors between the two beams. These were compared with coupling loss factors calculated using an analytical model based on a lump spring connector. For only bending waves or torsional waves, close agreement was achieved between FEM ESEA and the analytical model up to the frequency where half the bending or torsional wavelength equalled the longest side of the contact area. Above this frequency the interaction between the two beams cannot be considered as a point connection. The inclusion of the FEM driving-point mobilities in the prediction model (instead of the infinite beam model) did not significantly `improve the agreement. When all wave types are combined, close agreement can still be achieved at frequencies below 900 Hz.

6. Vibration transmission in piles of reinforced concrete beams with surface-to-surface contact conditions

6.1 Introduction

The aim of this chapter is to assess the potential to use Statistical Energy Analysis to model the vibration transmission in two piles of seven and one pile of fourteen reinforced concrete beams when they are stacked on top of each other (i.e. without any bond connecting the beams) to make a surface-to-surface connection. SEA path analysis is carried out to quantify and assess the strength of the transmission paths between the beams. Next, the general SEA matrix solution is used to estimate the energy ratios between the beams of the piles using: a) FEM ESEA CLFs and b) the CLFs from an analytical model of a lump spring connector. SEA predictions are compared against the results of FEM models.

Average coupling loss factors are determined from ESEA for the 30 beam junctions (for combination of all wave types) and the theoretical coupling loss factors based on an analytical model of a lump spring connector (see sections 5.6.1 and 5.6.2). The analytical lump spring model is calculated using (a) the driving-point mobilities of thin beams of infinite extent for excitation of bending waves in the central part of the beams, $Y_{\mathrm{B,Inf}}$ and (b) the spatial average of the FEM driving-point mobilities (for combination of all wave types) over the surface of beams, $Y_{\mathrm{A,FEM}}$. Figure 6-1 and Figure 6-2 shows the CLFs which are used throughout the SEA analysis in this chapter.

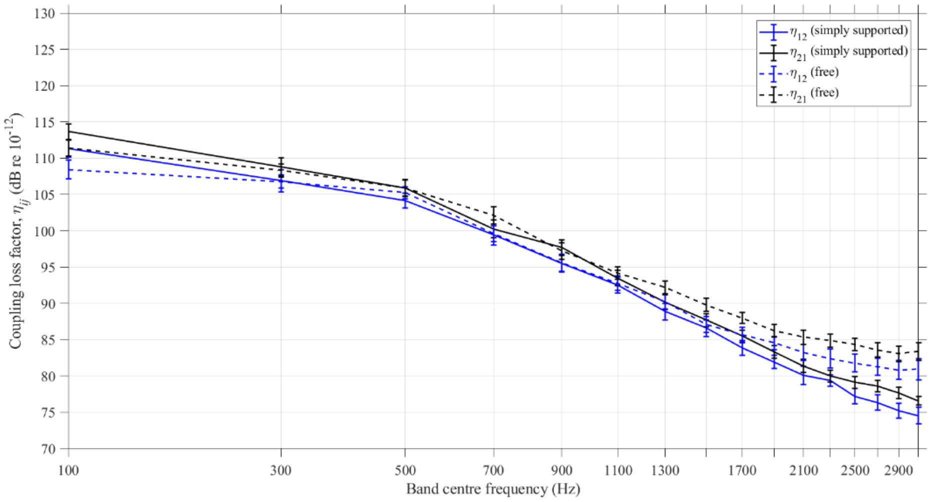

Figure 6-1 Coupling loss factors η_{12} and η_{21} with 95% confidence intervals from FEM ESEA for beams with simply supported and free support conditions at the end of each beam.

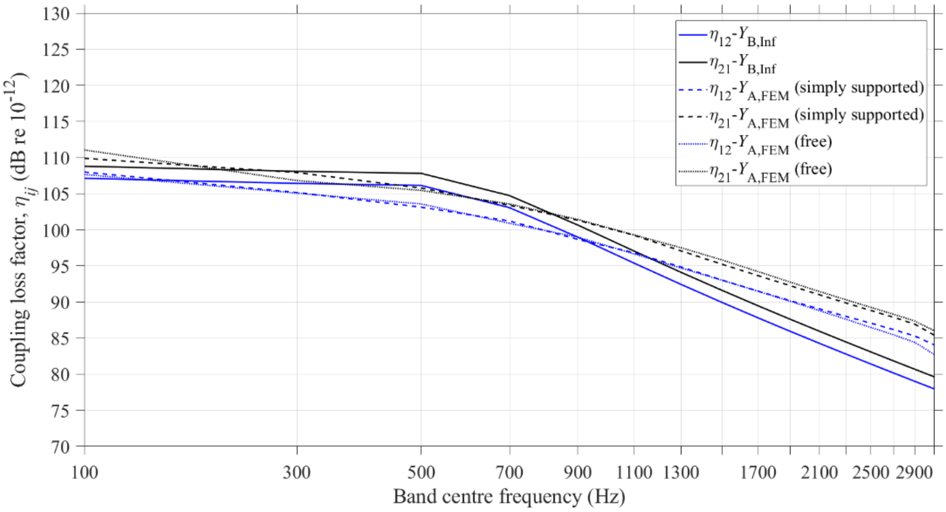

Figure 6-2 Coupling loss factors η_{12} and η_{21} resulted from an analytical model based on a lump spring connector using driving-point mobilities of an infinite beam and FEM.

6.2 Path analysis

This section presents the results of SEA path analysis carried out to quantify and assess the strength of the transmission paths between the seven beams of piles 1a and 1b (see Figure 3-6 and Figure 3-7). The path analysis results of pile 2 (see Figure 3-8) lead to similar findings and are therefore given in Appendix C.

6.2.1 Pile 1a

For power input to source beam SS1, Table 6-1 shows the transmission paths from source beam SS1 to receiving beams SS2 up to SS7. For each energy ratio, the paths are grouped according to the number of the intermediate subsystems.

Figure 6-3 to Figure 6-8 show the differences between the energy level differences resulting from the SEA matrix solution and path analysis. The curves are coloured according to the number of intermediate subsystems in each transmission path. The path that gives the lowest energy ratio difference is the strongest path (shaded grey in Table 6-1).

Between beams SS1 and SS2 there is no direct connection and path No.1 (1→3→2) is the strongest path with beam SS3 being the only intermediate subsystem. For this path, there was close agreement between the SEA matrix solution and the path analysis with differences between -1.5 and 0 dB in the frequency range up to 3100 Hz (see Figure 6-3). Paths with three and five intermediate subsystems were at least 10 dB higher than the matrix solution. Note that all the transmission paths between beams SS1 and SS2 pass through subsystem 3 (beam SS3).

Beam SS1 is directly connected to beams SS3, SS4 and SS5 hence the direct transmission paths 1→3, 1→4 and 1→5 are the strongest paths with differences between -1.5 and 0 dB between the SEA matrix solution and path analysis (see Figure

6-4 - Figure 6-6). Energy level differences from paths with two and four intermediate subsystems were at least 10 dB higher than the matrix solution. This indicates that longer paths were less important than the direct paths.

Table 6-1 Transmission paths to beams SS2 to SS7 through the pile 1a shown in Figure 3-6 for power input to beam SS1 (grey shading indicates the strongest path).

Energy ratio	**Number of intermediate subsystems**					
	0	1	2	3	4	5
E_1/E_2	-	1→3→2	-	1→4→6→3→2 1→4→7→3→2 1→5→6→3→2	-	1→5→6→4→7→3→2
E_1/E_3	1→3	-	1→4→6→3 1→4→7→3 1→5→6→3	-	1→5→6→4→7→3	-
E_1/E_4	1→4	-	1→5→6→4 1→3→6→4 1→3→7→4	-	1→5→6→3→7→4	-
E_1/E_5	1→5	-	1→4→6→5 1→3→6→5	-	1→3→7→4→6→5 1→4→7→3→6→5	-
E_1/E_6	-	1→3→6 1→4→6 1→5→6	-	1→3→7→4→6 1→4→7→3→6	-	-
E_1/E_7	-	1→3→7 1→4→7	-	1→3→6→4→7 1→5→6→3→7 1→5→6→4→7 1→4→6→3→7	-	-

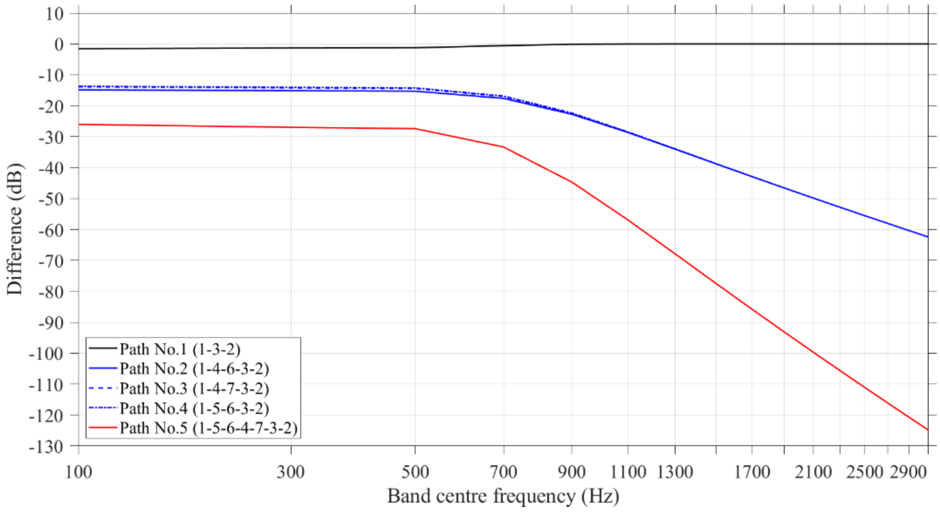

Figure 6-3 Difference between the energy ratio, E_1/E_2, from the SEA matrix solution and path analysis (pile 1a).

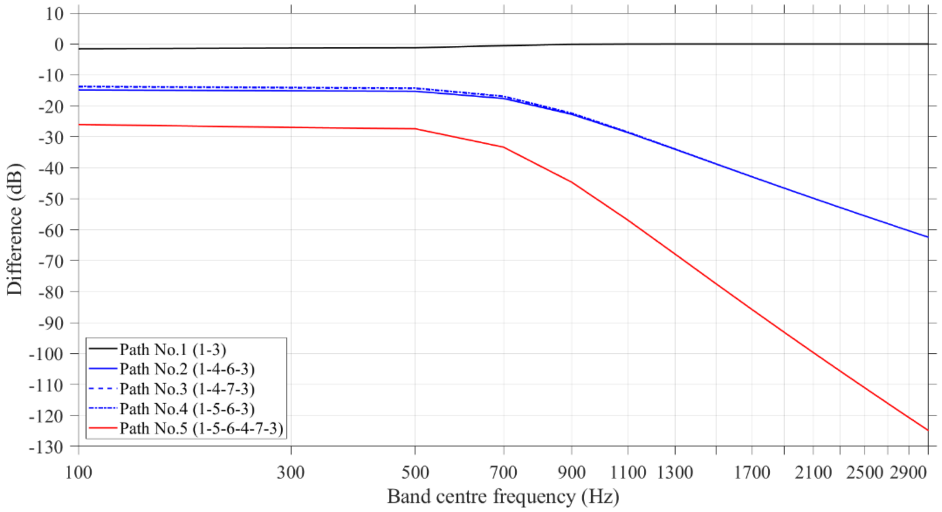

Figure 6-4 Difference between the energy ratio, E_1/E_3, from the SEA matrix solution and path analysis (pile 1a).

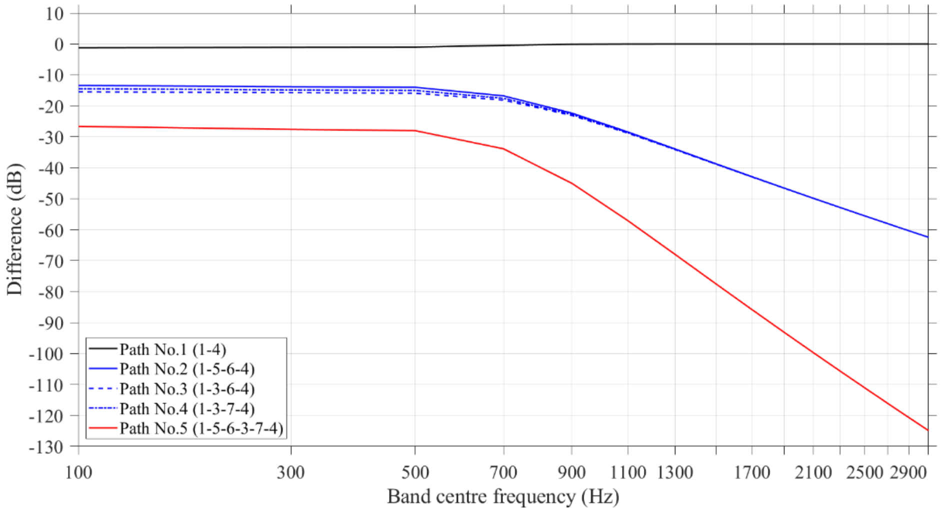

Figure 6-5 Difference between the energy ratio, E_1/E_4, from the SEA matrix solution and path analysis (pile 1a).

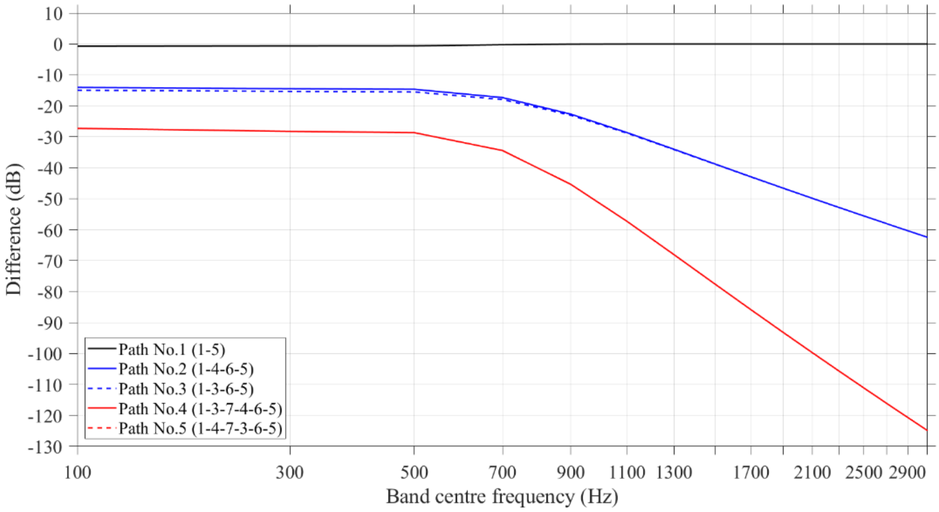

Figure 6-6 Difference between the energy ratio, E_1/E_5, from the SEA matrix solution and path analysis (pile 1a).

Between beams SS1 and SS6 there is no direct connection and although path No.3 (1→5→6) is the strongest path, the difference between the SEA matrix solution and the path analysis is up to 5 dB. Similar results occur for the other two paths with one intermediate subsystem, path No.1 (1→3→6) and path No.2 (1→4→6) with differences up to 6 and 7 dB respectively. When paths No.1-3 are combined, close agreement is achieved between the SEA matrix solution and the path analysis with differences between -1.2 and 0 dB in the frequency range up to 3100 Hz (see Figure 6-7). This indicates that these are the dominant three paths.

The energy ratios E_1/E_7 from the SEA matrix solution and path analysis between beams SS1 and SS7 differ up to 4 dB for path No.2 (1→4→7) and up to 4.8 dB for path No.1 (1→3→7). When path No.2 is combined with path No.1, there is close agreement between the SEA matrix solution and the path analysis with differences between -1.4 and 0 dB in the frequency range up to 3100 Hz (see Figure 6-8). Hence these two paths can be considered to be the dominant paths.

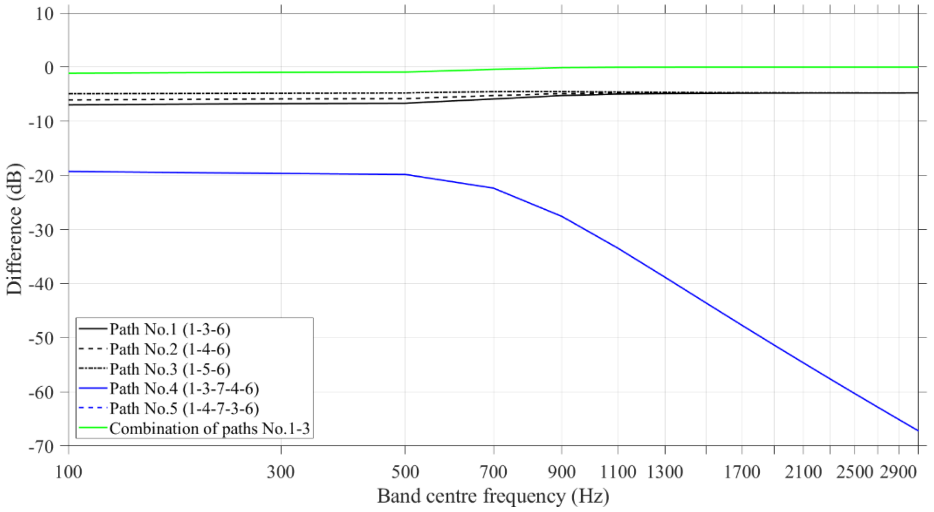

Figure 6-7 Difference between the energy ratio, E_1/E_6, from the SEA matrix solution and path analysis (pile 1a).

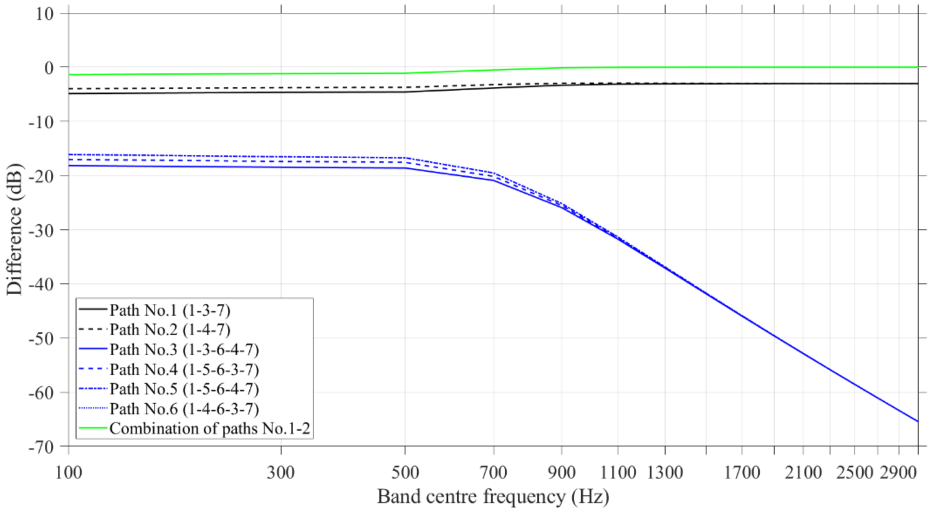

Figure 6-8 Difference between the energy ratio, E_1/E_7, from the SEA matrix solution and path analysis (pile 1a).

6.2.2 Pile 1b

The only difference between piles 1a and 1b is one additional contact between beams SS2 and SS5. For power input to source beam SS1, Table 6-2 shows the transmission paths from source beam SS1 to receiving beams SS2 up to SS7. For each energy ratio, the paths are grouped according to the number of the intermediate subsystems.

Figure 6-9 to Figure 6-14 present the differences between the energy ratios from the SEA matrix solution and path analysis.

Table 6-2 Transmission paths to beams SS2 to SS7 through pile 1b shown in Figure 3-7 for power input to beam SS1 (grey shading indicates the strongest path).

Energy ratio	**Number of intermediate subsystems**					
	0	1	2	3	4	5
E_1/E_2	-	1→3→2 1→5→2	-	1→3→6→5→2 1→4→6→3→2 1→4→6→5→2 1→4→7→3→2 1→5→6→3→2	-	1→3→7→4→6→5→2 1→4→7→3→6→5→2 1→5→6→4→7→3→2
E_1/E_3	1→3	-	1→4→6→3 1→4→7→3 1→5→2→3 1→5→6→3	-	1→4→6→5→2→3 1→5→6→4→7→3	-
E_1/E_4	1→4	-	1→5→6→4 1→3→6→4 1→3→7→4	-	1→3→2→5→6→4 1→5→2→3→6→4 1→5→2→3→7→4 1→5→6→3→7→4	-
E_1/E_5	1→5	-	1→3→2→5 1→3→6→5 1→4→6→5	-	1→3→7→4→6→5 1→4→6→3→2→5 1→4→7→3→2→5 1→4→7→3→6→5	-
E_1/E_6	-	1→3→6 1→4→6 1→5→6	-	1→3→2→5→6 1→3→7→4→6 1→4→7→3→6 1→5→2→3→6	-	1→4→7→3→2→5→6 1→5→2→3→7→4→6
E_1/E_7	-	1→3→7 1→4→7	-	1→3→6→4→7 1→5→6→3→7 1→5→6→4→7 1→4→6→3→7 1→5→2→3→7	-	1→3→2→5→6→4→7 1→4→6→5→2→3→7 1→5→2→3→6→4→7

Between beams SS1 and SS2 there is no direct connection and path No.2 (1→5→2) is the strongest path. As shown in Figure 6-9, close agreement was achieved between the SEA matrix solution and the path analysis for path No.2 with differences up to 4 dB in the frequency range up to 3100 Hz. Differences up to 5 dB occurred for path No.1 (1→3→2). When paths No.1 and 2 are combined, close agreement is achieved between the SEA matrix solution and the path analysis with differences up to 2.0 dB. This indicates the importance of these two short paths.

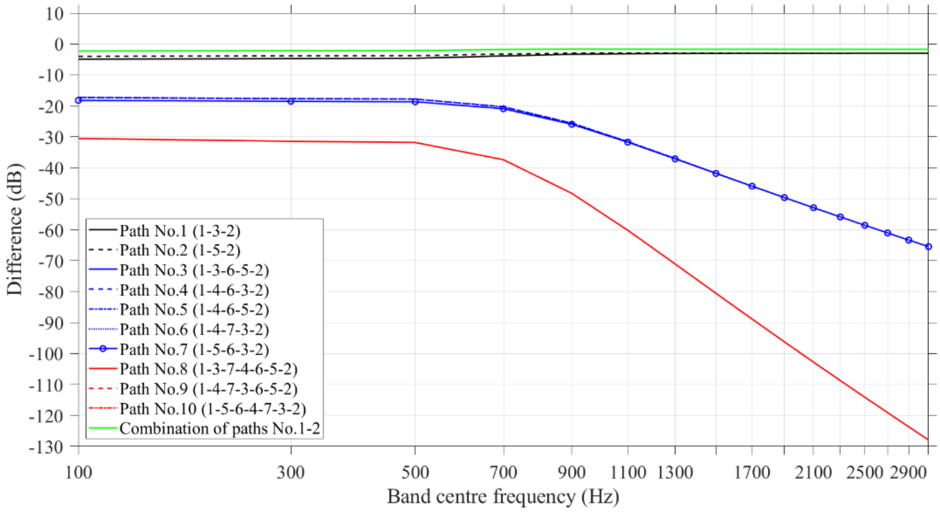

Figure 6-9 Difference between the energy ratio, E_1/E_2, from the SEA matrix solution and path analysis (pile 1b).

Beam SS1 is directly connected with beams SS3, SS4 and SS5 hence the transmission paths 1→3, 1→4 and 1→5 are the strongest paths with differences up to 2 dB between the SEA matrix solution and the path analysis (see Figure 6-10 - Figure 6-12).

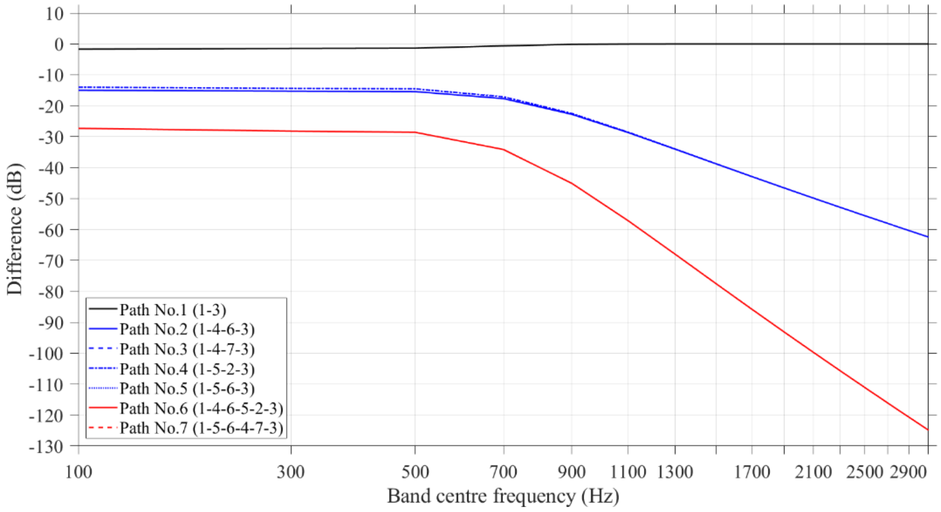

Figure 6-10 Difference between the energy ratio, E_1/E_3, from the SEA matrix solution and path analysis (pile 1b).

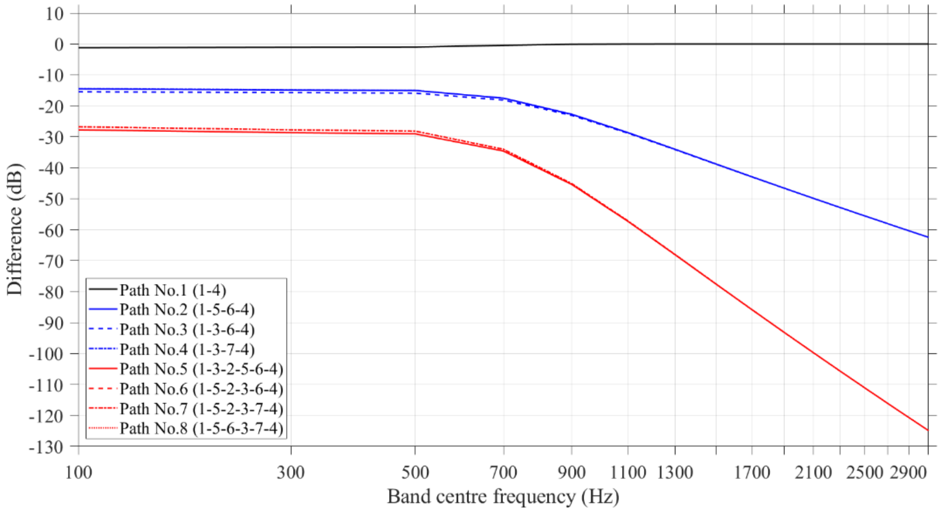

Figure 6-11 Difference between the energy ratio, E_1/E_4, from the SEA matrix solution and path analysis (pile 1b).

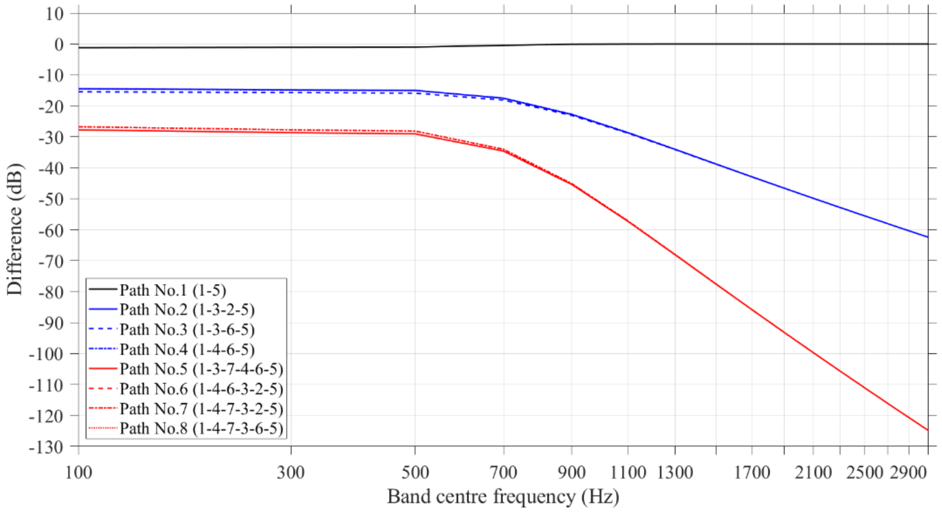

Figure 6-12 Difference between the energy ratio, E_1/E_5, from the SEA matrix solution and path analysis (pile 1b).

Between beams SS1 and SS6 there is no direct connection and paths No. 2 (1→4→6) and 3 (1→5→6) are equally strong paths with differences between the SEA matrix solution and the path analysis up to 5.9 dB. Similar results are obtained for the other path with one intermediate subsystem, path No.1 (1→3→6) with differences up to 6.8 dB. When paths No.1-3 are combined, close agreement is achieved between the SEA matrix solution and the path analysis with differences up to 1.4 dB in the frequency range up to 3100 Hz (see Figure 6-13).

The energy ratios E_1/E_7 resulted from the SEA matrix solution and the path analysis between beams SS1 and SS7 differ by 4 dB for path No.2 (1→4→7) and by 4.9 dB for path No.1 (1→3→7). Thus, path No.2 is the strongest path and when it is combined with path No.1, close agreement is achieved between the SEA matrix solution and the path analysis with differences up to 1.5 dB in the frequency range up to 3100 Hz (see Figure 6-14).

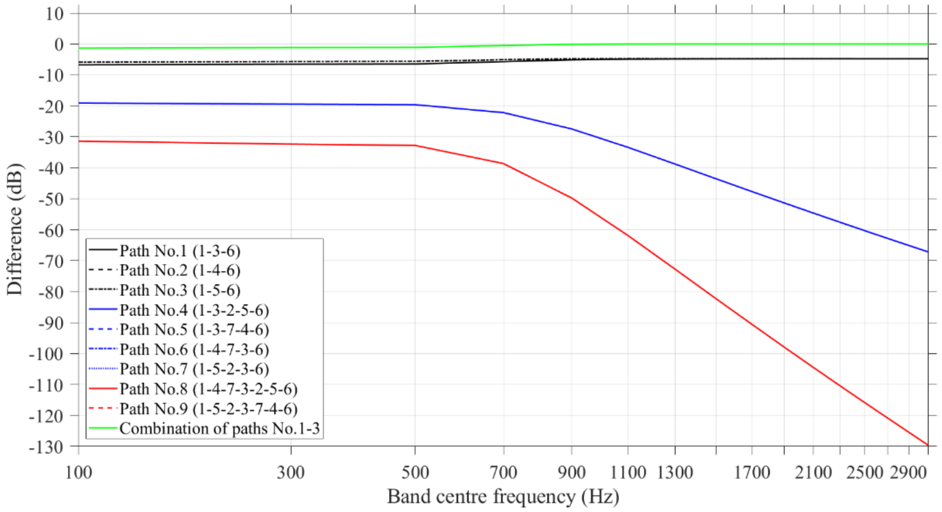

Figure 6-13 Difference between the energy ratio, E_1/E_6, from the SEA matrix solution and path analysis (pile 1b).

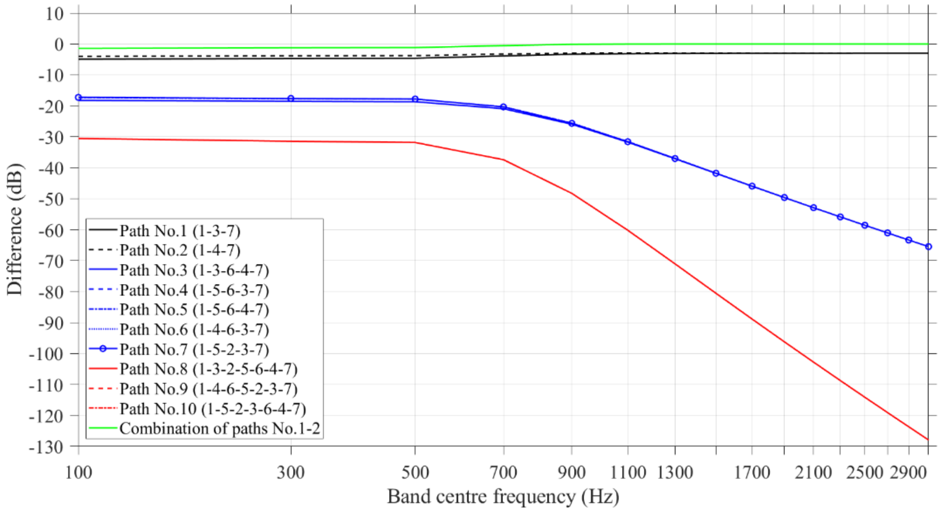

Figure 6-14 Difference between the energy ratio, E_1/E_7, from the SEA matrix solution and path analysis (pile 1b).

6.2.3 Discussion

From path analysis of piles 1a and 1b it was found that when direct paths (i.e. a transmissions paths with no intermediate subsystems between the first and the last subsystem) were present, these were always the strongest and the transmitted energy was in close agreement with the energy determined by the SEA matrix formulation. In absence of a direct path between two subsystems, the transmission paths with the smaller number of intermediate subsystems were the strongest and a few paths could often be combined to give a result within 2 dB of the matrix solution.

6.3 Pile 1a - Comparison between SEA and FEM

Figure 6-15 to Figure 6-20 show the difference between the energy ratios from FEM and SEA for the seven beams (simply supported or free) of pile 1a when the power is injected on beam SS1. The colour of each curve is analogous to the colour index of Figure 3-6 and indicates the layer of the pile where the energy is transmitted. Positive differences indicate that SEA overestimates the energy ratios whereas negative differences indicate that SEA underestimates the energy ratios compared with FEM.

6.3.1 Simply supported beams

When the FEM ESEA coupling loss factors are used in the SEA model (Figure 6-15), reasonable agreement was achieved between SEA and FEM for beams SS3 to SS7 with differences between -7.6 and 7 dB, in the frequency range from 100 to 3100 Hz. The difference of the energy ratios for beam SS2 (E_1/E_2) is in general between -6.6 and 1.5 dB (except for the frequency bands of 2300 and 2900 Hz where the differences are -10.5 and -11.6 dB). This agreement is reasonable considering the CLFs estimates are derived from FEM.

When the SEA model uses the coupling loss factors from an analytical model based on a lump spring connector with the infinite beam mobilities (see Figure 6-16), reasonable agreement was achieved between SEA and FEM for all the beams of the pile up to the frequency band of 1100 Hz, with differences between -9.3 and 5.3 dB. Above 1100 Hz, the difference of the energy ratios for beam SS2 (E_1/E_2) is up to -18.4 dB. Between 1100 and 1700 Hz, the difference of the energy ratios for beams SS3 to SS7 is negative and up to -7.6 dB whereas above 1700 Hz the differences are up to -12.4 dB.

When the SEA model uses the coupling loss factors from the analytical model with the inclusion of the FEM mobilities (see Figure 6-17), reasonable agreement was achieved between SEA and FEM for all the beams of the pile up to the frequency band of 900 Hz, with differences between -8.5 and 4.5 dB. This is reasonable since 900 Hz is the estimated upper frequency for the theoretical model of the lump spring connector to be valid (see Figure 5-26 in section 5.6.1). Above 900 Hz, SEA underestimates the energy ratio for beam SS2 (E_1/E_2) with differences up to -30.84 dB. Between 900 and1500 Hz, the differences were up to -8.8 and -14.8 dB for the beams of the second (SS3-5) and third (SS6-7) layer of the pile respectively. Above 1500 Hz, the energy ratios for beams SS3 to SS7 had negative differences over 10 dB.

To conclude, the lowest differences between FEM and SEA were achieved when the FEM ESEA coupling loss factors were used in the SEA model.

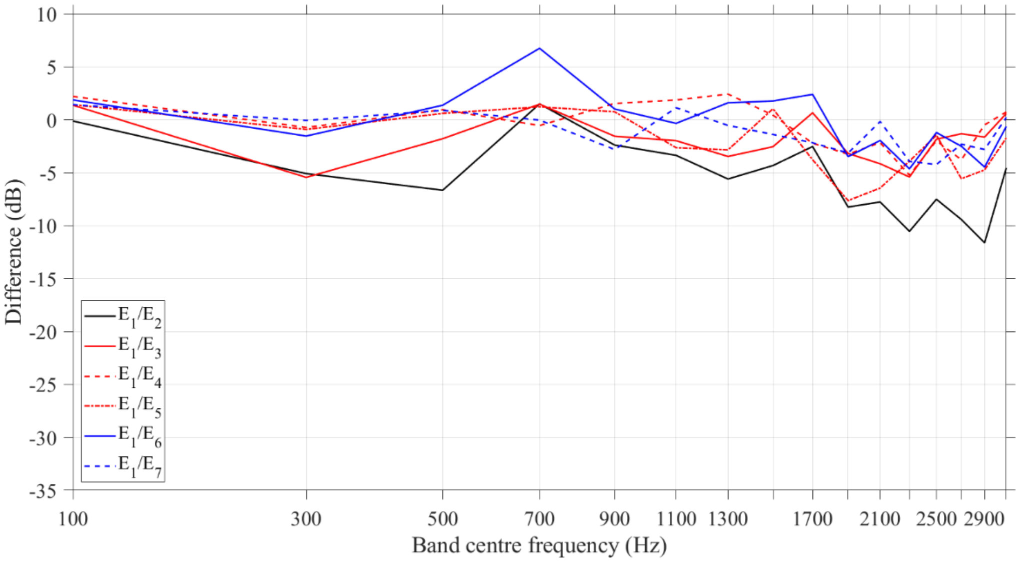

Figure 6-15 Difference between the energy ratios from FEM and SEA with CLFs from FEM ESEA (combination of bending, torsional and longitudinal modes).

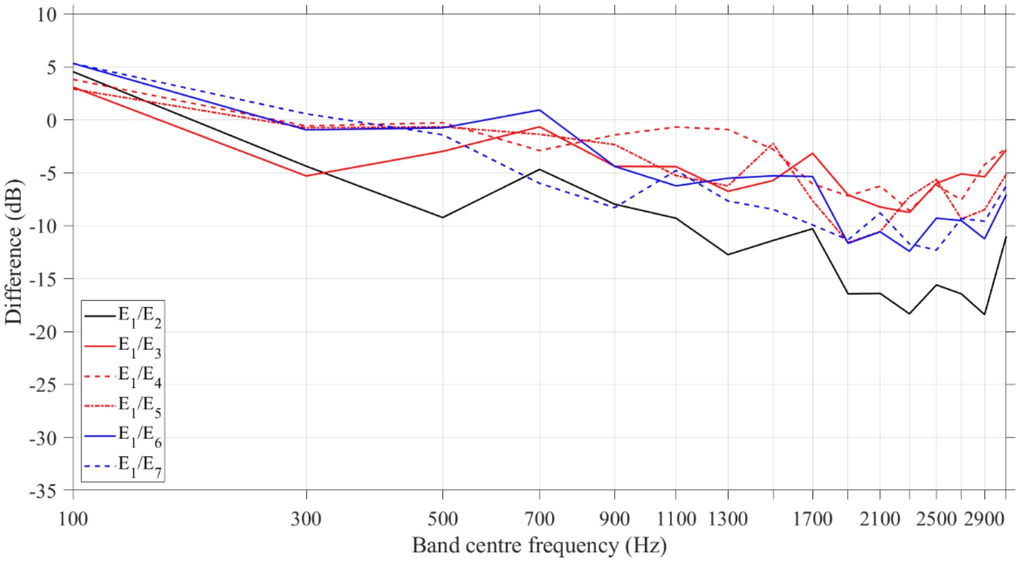

Figure 6-16 Difference between the energy ratios from FEM and SEA with CLFs from an analytical model (LSC with infinite beam mobilities).

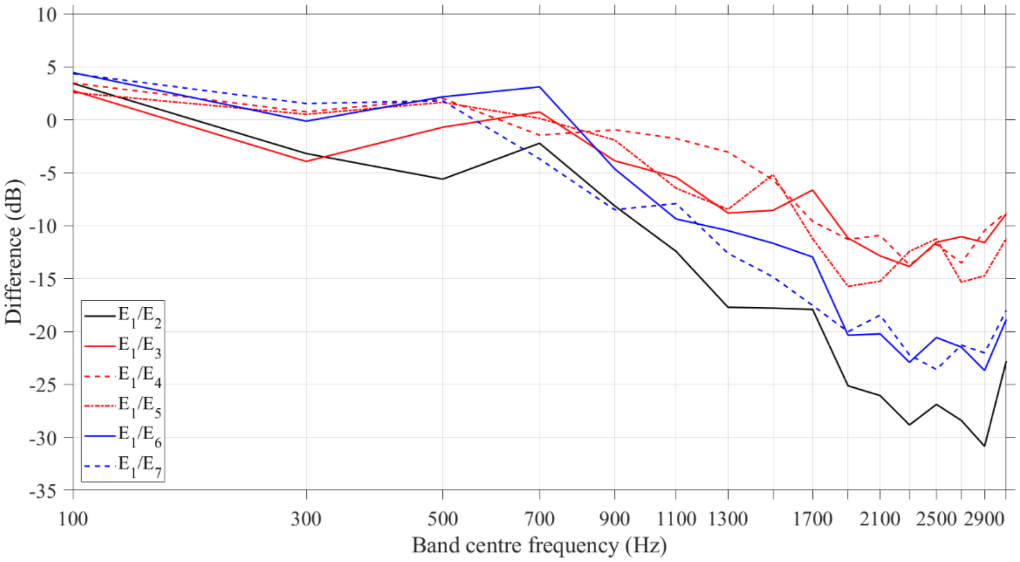

Figure 6-17 Difference between the energy ratios from FEM and SEA with CLFs from an analytical model (LSC with FEM mobilities).

6.3.2 Free supports

When the FEM ESEA coupling loss factors are used in the SEA model (Figure 6-18), reasonable agreement is achieved between SEA and FEM for beams SS3 to SS7 with differences between -8.7 and 6.6 dB in the frequency range from 100 to 1700 Hz. Above 1700 Hz, the differences of the energy ratios were between -9.1 and 0.5 dB for the beams of the first (SS2) and second (SS3-5) layer of the pile whereas differences up to 15.6 dB were occurred for the beams in the third layer of the pile.

When the SEA model uses the coupling loss factors from an analytical model based on a lump spring connector with infinite beam mobilities (see Figure 6-19), reasonable agreement was achieved between SEA and FEM for beams SS3 to SS7 with differences within -10 and 8 dB between 100 and 1900 Hz. Above 1900 Hz, the differences were up to -10.1 dB and 22.3 dB for the beams of the second (SS3-SS5) and third (SS6-SS7) layer of the pile respectively. For beam SS2, the difference was within ±10 dB except for the frequency bands of 700, 900 and 1500 Hz with differences up to -14.6 dB.

When the SEA model uses the coupling loss factors from the analytical model with the inclusion of the FEM mobilities (see Figure 6-20), reasonable agreement was achieved between SEA and FEM for beams SS3 to SS7 with differences between -4.1 and 7.3 dB up to the frequency band of 700 Hz. Above 700 Hz, the differences were up to -14.5 dB and 11.2 dB for the beams of the second (SS3-SS5) and third (SS6-SS7) layer of the pile respectively. SEA underestimates the energy ratio for beam SS2, with differences up to -18.7 dB between 700 and 2300 Hz. Outside this frequency range the difference was within ±10 dB.

As with the simply supported beams, the lowest differences between FEM and SEA were achieved when the FEM ESEA coupling loss factors were used in the SEA model. Note that closer agreement both in terms of level differences and frequency range was achieved for the pile with the simple supports.

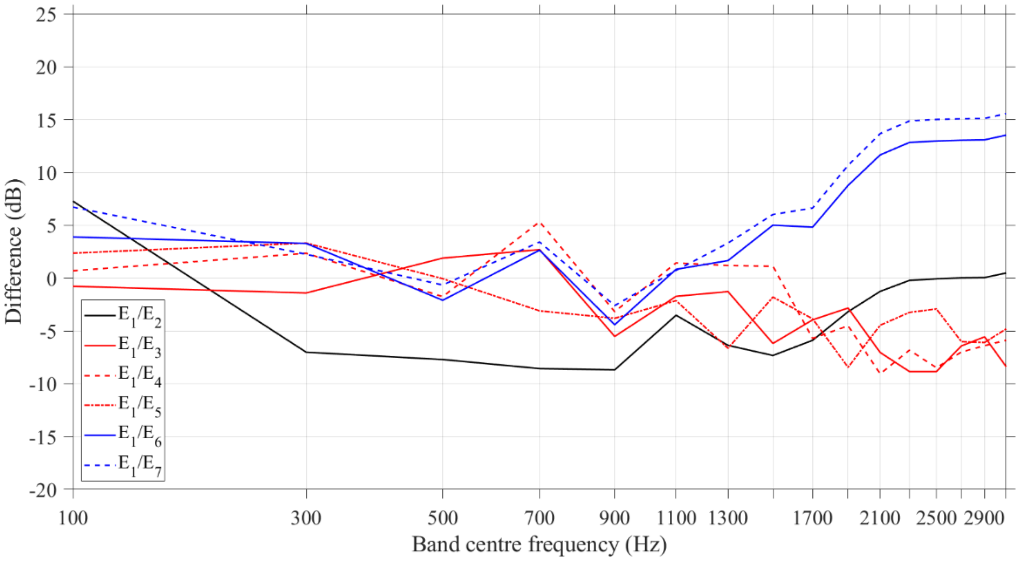

Figure 6-18 Difference between the energy ratios from FEM and SEA with CLFs from FEM ESEA (combination of bending, torsional and longitudinal modes).

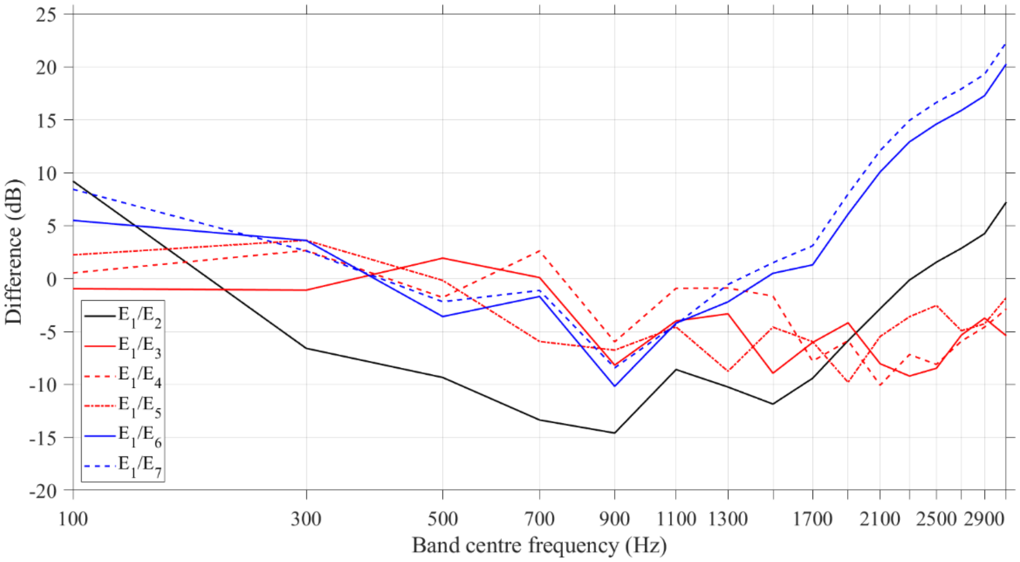

Figure 6-19 Difference between the energy ratios from FEM and SEA with CLFs from an analytical model (LSC with infinite beam mobilities).

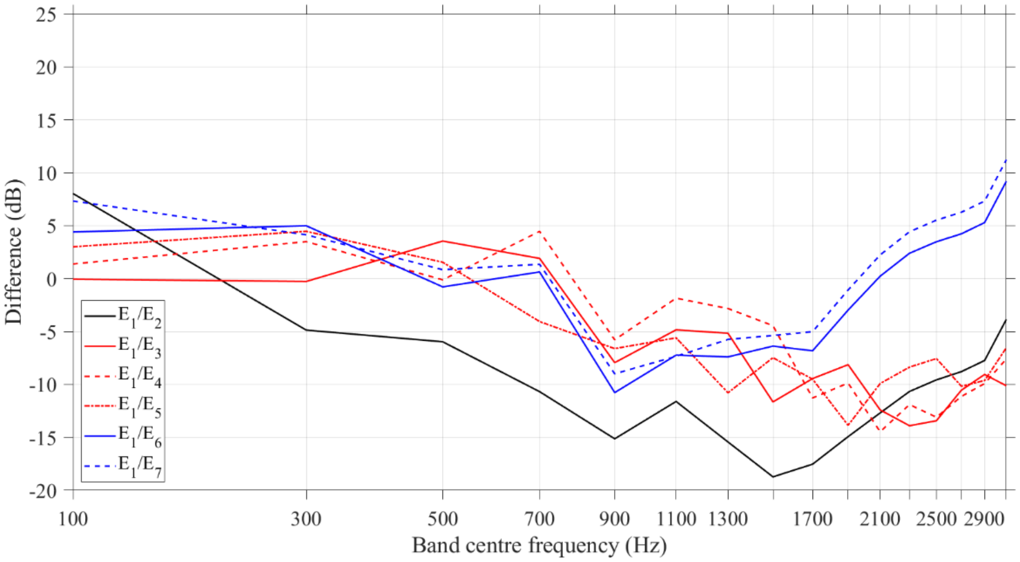

Figure 6-20 Difference between the energy ratios from FEM and SEA with CLFs from an analytical model (LSC with FEM mobilities).

6.4 Pile 1b – Comparison between SEA and FEM

Figure 6-21 to Figure 6-26 show the difference between the energy ratios from FEM and SEA for the seven either simply supported or free-free beams of pile 1b when the power is injected on beam SS1. The colour of each curve is analogous to the colour index of Figure 3-7 and indicates the layer of the pile where the energy is transmitted. As in the previous section, positive differences indicate that SEA overestimates the energy ratios whereas negative differences indicate that SEA underestimates the energy ratios compared with FEM.

6.4.1 Simply supported beams

When using FEM ESEA coupling loss factors in the SEA model (Figure 6-21), reasonable agreement was achieved between SEA and FEM for all the beams of the pile with differences between -7.7 and 7 dB, between 100 and 3100 Hz.

When the SEA model uses the coupling loss factors from an analytical model based on a lump spring connector with the infinite beam mobilities (see Figure 6-22), reasonable agreement was achieved between SEA and FEM for all the beams of the pile up to the frequency band of 1100 Hz, with differences between -7.5 and 6.3 dB. Above 1100 Hz, the difference of the energy ratios for beam SS2 (E_1/E_2) is up to -13.4 dB. Between 1100 and 1700 Hz, the difference of the energy ratios for beams SS3 to SS7 is up to -10 dB whereas above 1700 Hz the differences are up to -12.4 dB.

When the SEA model uses the coupling loss factors from the analytical model with the inclusion of the FEM mobilities (see Figure 6-23), reasonable agreement was achieved between SEA and FEM for all the beams up to the frequency band of 900 Hz, with differences between -8.7 and 5.5 dB. This is reasonable since 900 Hz is the estimated upper frequency for the theoretical model of the lump spring connector to be valid (see Figure 5-26 in section 5.6.1). Between 900 and1500 Hz, the differences were up to -8.8 dB for the beams of the second layer of the pile (SS3-5) whereas for SS2 and SS6-7 the differences were and up to -16.4 dB. Above 1500 Hz, SEA underestimates the energy ratios for all the beams with differences up to -23.9 dB.

As with pile 1a, the lowest differences between FEM and SEA were achieved when the FEM ESEA coupling loss factors were used in the SEA model.

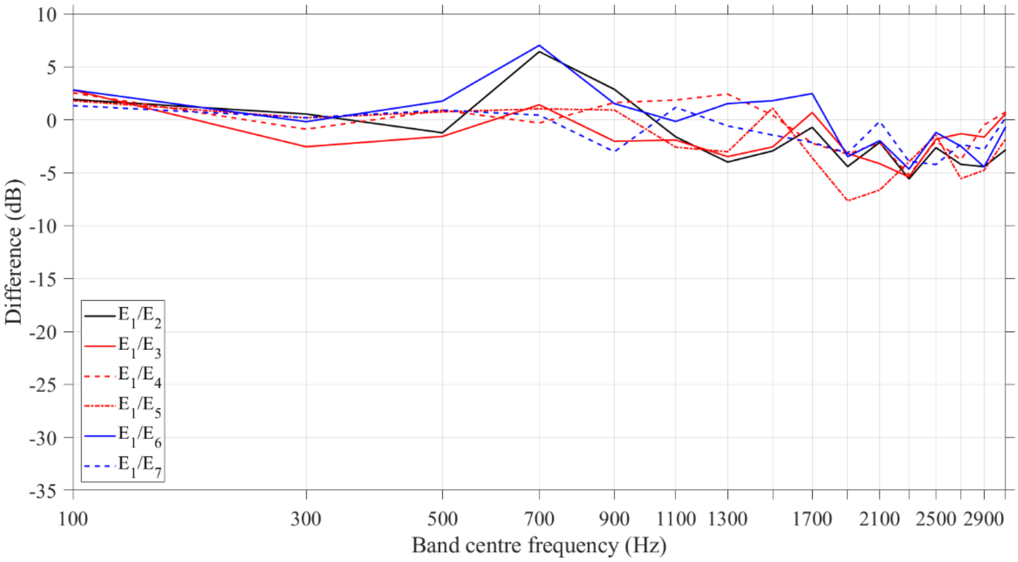

Figure 6-21 Difference between the energy ratios from FEM and SEA with CLFs from FEM ESEA (combination of bending, torsional and longitudinal modes).

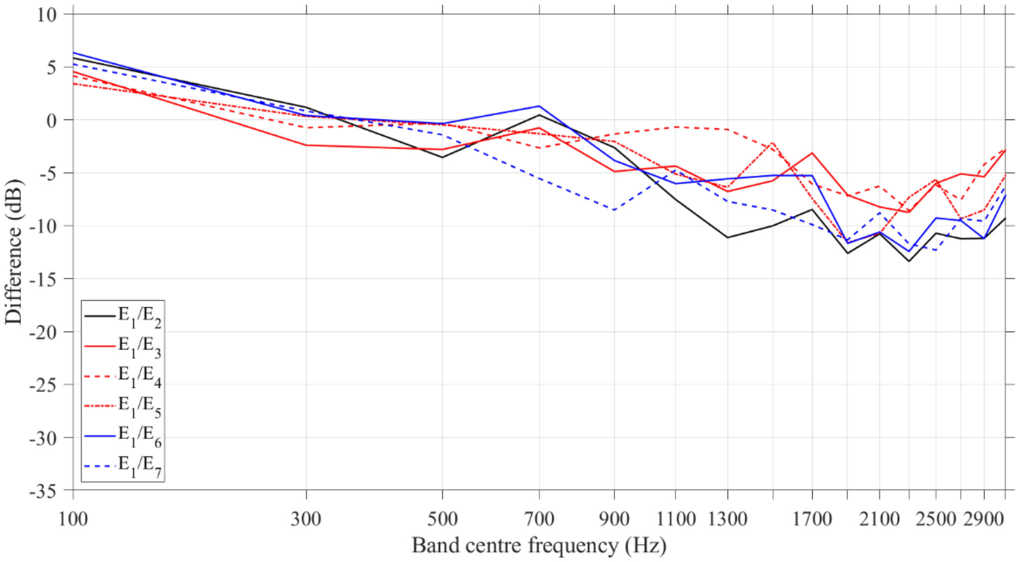

Figure 6-22 Difference between the energy ratios from FEM and SEA with CLFs from an analytical model (LSC with infinite beam mobilities).

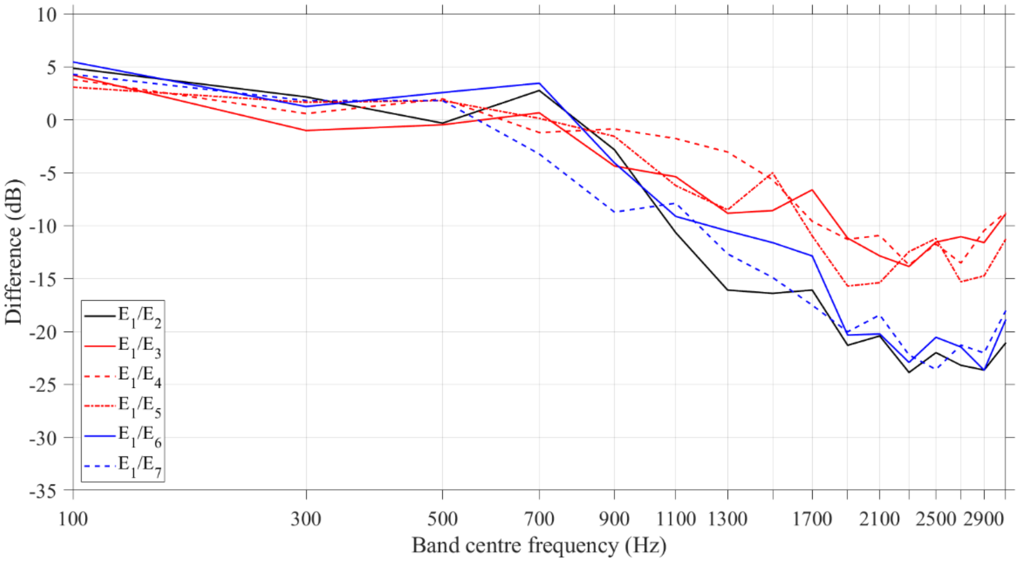

Figure 6-23 Difference between the energy ratios from FEM and SEA with CLFs from an analytical model (LSC with FEM mobilities).

6.4.2 Free support

When the FEM ESEA coupling loss factors are used in the SEA model (Figure 6-24), reasonable agreement was achieved between SEA and FEM for beams SS2 to SS7 with differences within -9.3 and 8.4 dB, between 100 and 1900 Hz. Above 1900 Hz, the differences of the energy ratios were up to -9 dB for the beams of the second layer of the pile (SS3-SS5) which are connected directly with beam SS1. For the remaining beams of the pile which are not directly connected with beam SS1, the difference curves had a similar shape with differences up to 13.2 dB.

When the SEA model uses the coupling loss factors from an analytical model based on a lump spring connector with infinite beam mobilities (see Figure 6-25), reasonable agreement was achieved between SEA and FEM for beams SS2 to SS7 with differences within -9.8 and 5.4 dB, between 100 and 1700 Hz. Above 1700 Hz, the differences were up to -10.7 dB for the beams of the second layer of the pile (SS3-SS5). For the beams of the first and third layer of the pile (SS2, SS6 and SS7) where there is no direct connection with the source beam SS1, the differences were below 10 dB between 1700 and 2100 Hz. Above this frequency the differences were up to 20 dB. Note that above 900 Hz the difference curves for beams SS2, SS6 and SS7 follow the same trend.

When the SEA model uses the coupling loss factors from the analytical model with the inclusion of the FEM mobilities (see Figure 6-26), reasonable agreement was achieved between SEA and FEM for beams SS2 to SS7 with differences between -10.3 and 4.3 dB up to the frequency band of 1100 Hz. Above 1100 Hz, the differences were up to -14.7 dB for the beams of the second layer of the pile (SS3-SS5) whereas reasonable agreement with differences between -8.6 and 8.9 dB was achieved for the beams of the first and third layer (SS2, SS6 and SS7) of the pile.

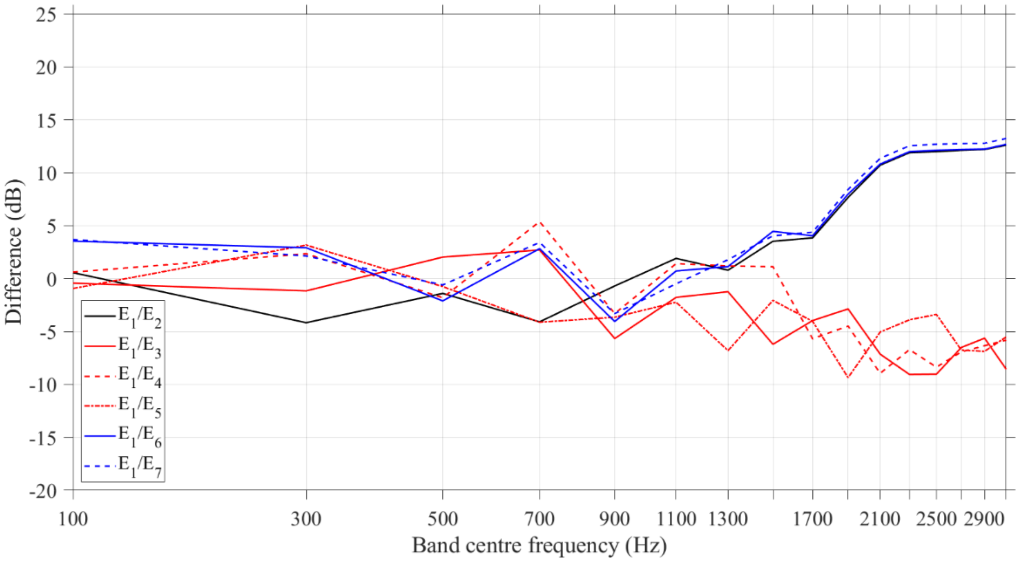

Figure 6-24 Difference between the energy ratios, E_1/E_i from FEM and SEA with CLFs from FEM ESEA (combination of bending, torsional and longitudinal modes).

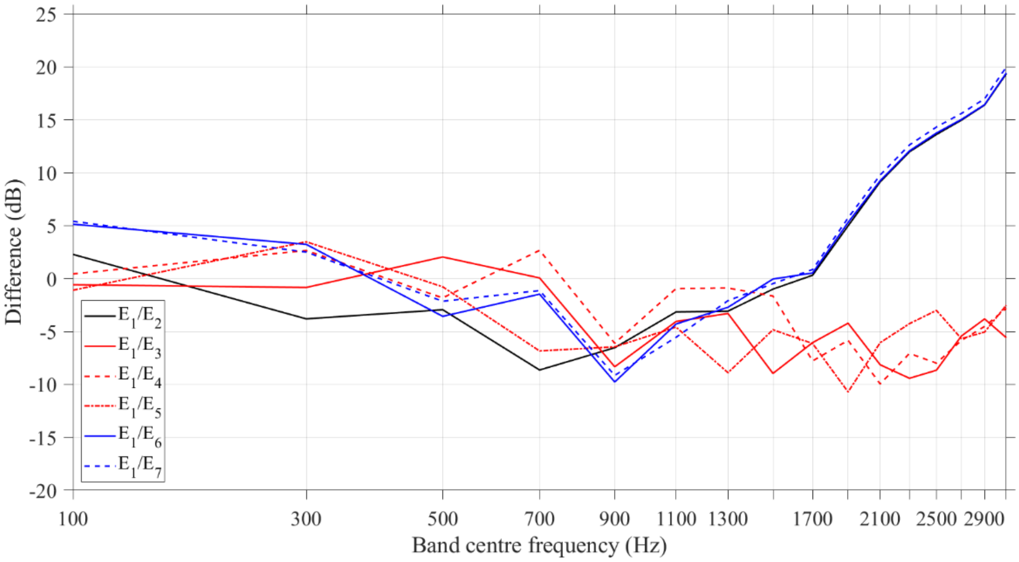

Figure 6-25 Difference between the energy ratios, E_1/E_i from FEM and SEA with CLFs from an analytical model (LSC with infinite beam mobilities).

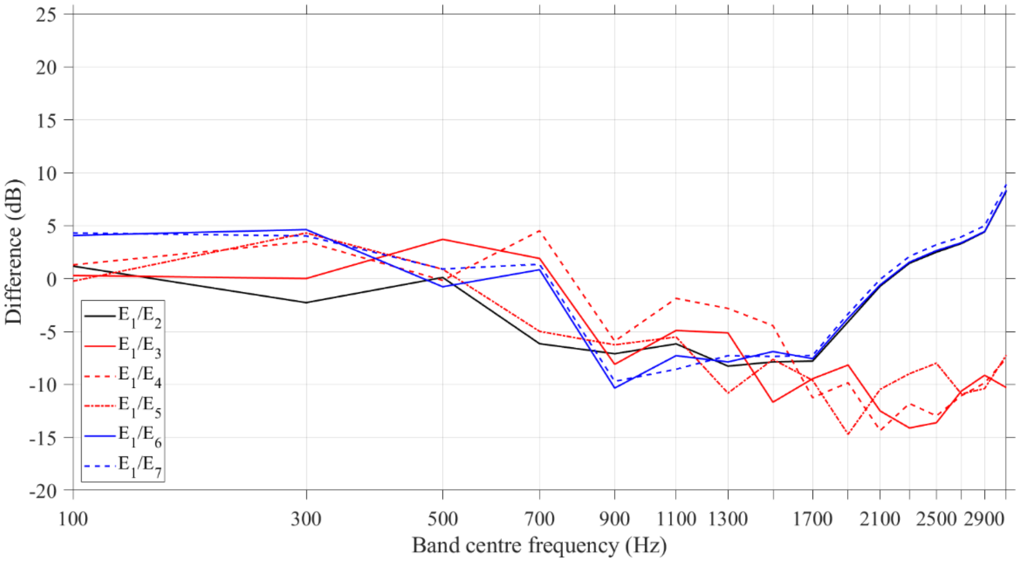

Figure 6-26 Difference between the energy ratios, E_1/E_i from FEM and SEA with CLFs from an analytical model (LSC with FEM mobilities).

6.5 Piles 1a and 1b – Discussion

In piles 1a and 1b with either simply or free-free support conditions, the beams of the second layer (SS3-SS5) which were directly connected with beam SS1 achieved the closest agreement between SEA and FEM in terms of energy ratio difference, regardless of the coupling loss factors used in the SEA matrix calculation.

In pile 1a it was observed that among the beams with no direct connection with the beam where the power is injected (SS1), the largest differences between SEA and FEM occurred for beam SS2. In addition, the E_1/E_2 difference curve had a different shape than the rest of the E_1/E_i curves. This problem did not occur in pile 1b where the difference curves of beams SS2, SS6 and SS7 had similar values and followed the same trend.

The main reason for this improvement was that in pile 1b the number of transmission paths between subsystems 1 and 2 was doubled after connecting beam SS2 with beam

SS5 (see Table 6-1 and Table 6-2) leading to SEA to work more efficiently. This was partially expected considering that a SEA model with many short paths is less affected by errors than a model that consists of a few long paths [71]. This indicates the potential for SEA to predict the energy transmission between the beams in a pile as the number of the interconnected members and consequently the complexity of the pile increases.

6.6 Pile 2 – Comparison between SEA and FEM

Figure 6-27 to Figure 6-32 present the difference between the energy ratios, E_1/E_i from FEM and SEA for the 14 beams of pile 2 when the power is injected on beam SS1. Results are shown for simply supported and free-free beams. The colour of each curve is analogous to the colour indexes of Figure 3-8 and indicates the layer of the pile where the energy is transmitted. Positive differences indicate that SEA overestimates the energy ratios whereas negative differences indicate that SEA underestimates the energy ratios compared with FEM.

6.6.1 Simply supported beams

When the FEM ESEA coupling loss factors are used in the SEA model (Figure 6-27), reasonable agreement was achieved between SEA and FEM for beams SS2 to SS14 (except for beam SS9) with differences within ±10 dB, for the majority of the frequency bands between 100 and 1500 Hz. Above 1500 Hz, reasonable agreement was still achieved for the beams of the first five layers of the pile, although for beam SS12 the differences were up to -15.1 dB at 1700 Hz. For beams SS13 and SS14 the differences between SEA and FEM were up to 39 dB. The difference of the energy ratios for beam SS9 was negative and over 10 dB for most of the frequency bands above 100 Hz. Above 700 Hz, the shape of the difference curve is also different than the other curves of Figure 6-27.

When the SEA model uses the coupling loss factors from an analytical model based on a lump spring connector with the infinite beam mobilities (see Figure 6-28), reasonable agreement was achieved between SEA and FEM for all the beams of the pile up to the frequency band of 300 Hz, with differences within ±10 dB. Above 300 Hz and up to the frequency band of 1300 Hz, reasonable agreement was achieved for the beams of layers 1-4 of the pile (except for the beam SS9) with differences between -8 and 1.6 dB. Above 1300 Hz the differences were up to -13.6 dB. For beams SS9 to SS14 differences over ±10 dB was received for the majority of the frequency bands above 300 Hz. Note that above 900 Hz the difference curve of beam SS9 had different trend than the other curves of Figure 6-28.

When the SEA model uses the coupling loss factors from the analytical model with the inclusion of the FEM mobilities (see Figure 6-29), reasonable agreement was achieved between SEA and FEM for all the beams of the pile up to the frequency band of 300 Hz, with differences within ±10 dB. Above 300 Hz and up to the frequency band of 700 Hz, reasonable agreement with differences between -7.6 and 4 dB was achieved for the all the beams of the pile except for beam SS9. Above 700 Hz the differences were over -10 dB for most of the beams of the pile. Note that the difference of the energy ratios for beam SS9 was greater than 10 dB in all the frequency bands above 300 Hz.

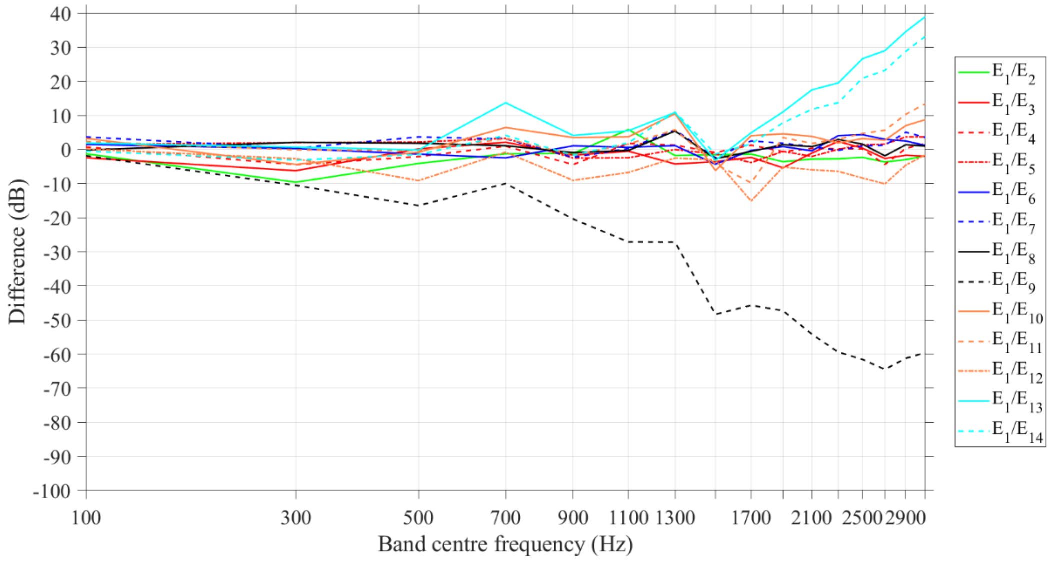

Figure 6-27 Difference between the energy ratios, E_1/E_i from FEM and SEA with CLFs from FEM ESEA (combination of bending, torsional and longitudinal modes) – Excitation on subsystem SS1.

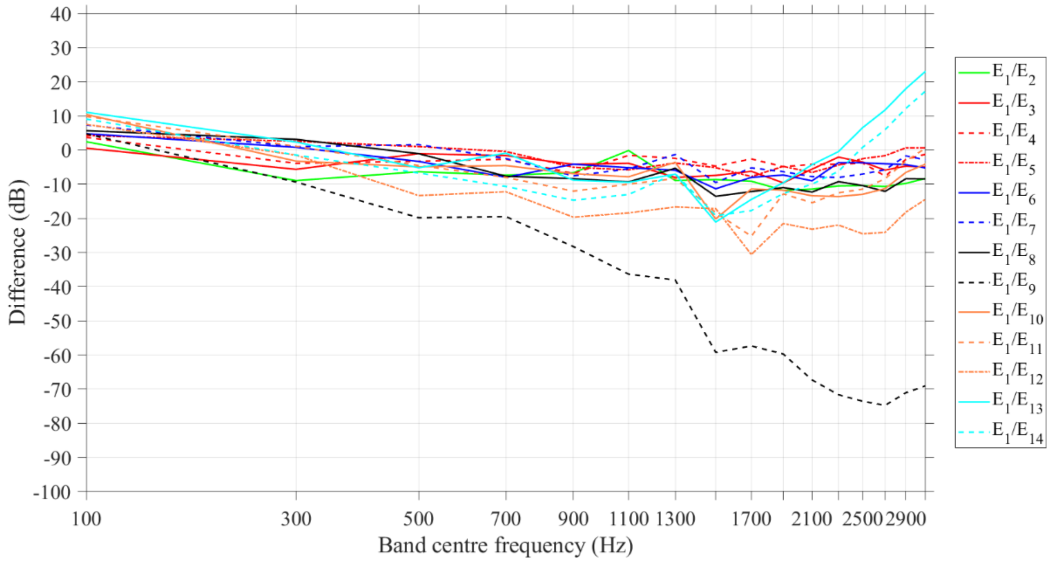

Figure 6-28 Difference between the energy ratios, E_1/E_i from FEM and SEA with CLFs from an analytical model (LSC with infinite beam mobilities) – Excitation on subsystem SS1.

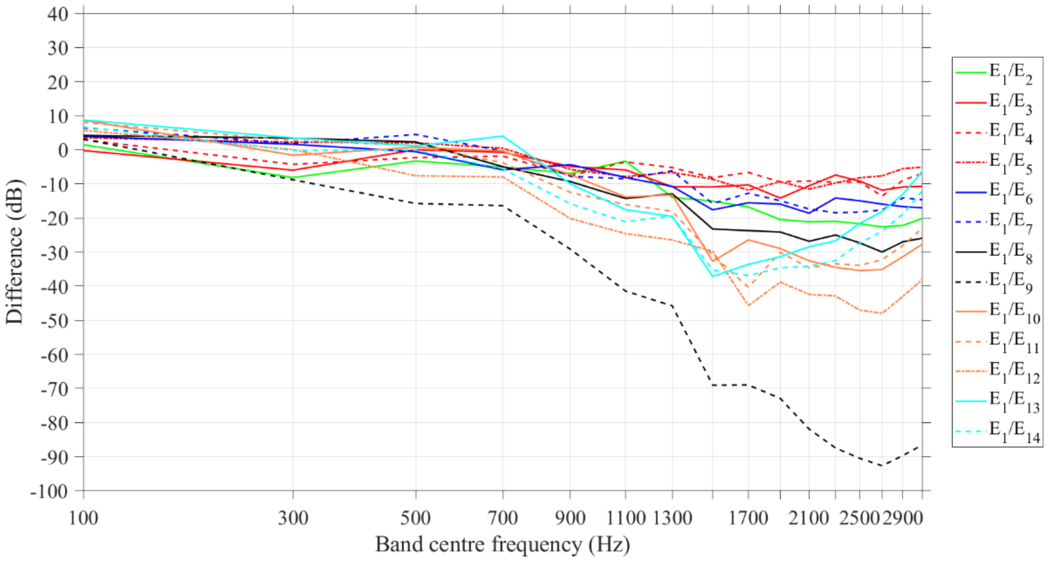

Figure 6-29 Difference between the energy ratios, E_1/E_i from FEM and SEA with CLFs from an analytical model (LSC with FEM mobilities) – Excitation on subsystem SS1.

6.6.2 Free supports

When the FEM ESEA coupling loss factors are used in the SEA model (Figure 6-30), reasonable agreement was achieved between SEA and FEM for beams SS2 to SS14 with differences within ±10 dB, for the vast majority of the frequency bands between 100 and 700 Hz. Above 700 Hz, reasonable agreement was achieved mainly for the beams of the first three layers of the pile (SS2 – SS7). For beams SS8 to SS14 the difference between SEA and FEM was greater than 10 dB for the majority of the frequency bands above 700 Hz.

When the SEA model uses the coupling loss factors from an analytical model based on a lump spring connector with the infinite beam mobilities (see Figure 6-31), reasonable agreement was achieved between SEA and FEM for the most beams of the pile up to the frequency band of 300 Hz, with differences within ±10 dB. Between 300 and 900 Hz, the difference curves of the 14 beams follow the same trend but reasonable agreement was achieved mainly for beams SS2-SS8. Above 900 Hz, differences within ±10 dB were achieved for the majority of the frequency bands of beams SS2 – SS7 whereas for beams SS9 to SS14 the differences were in general over ±10 dB.

When the SEA model uses the coupling loss factors from the analytical model with the inclusion of the FEM mobilities (see Figure 6-32), reasonable agreement was achieved between SEA and FEM for all the beams of the pile up to the frequency band of 300 Hz, with differences between -8 and 8.8 dB. Above 300 Hz and up to the frequency band of 900 Hz, reasonable agreement with differences within ±10 dB was achieved for the most beams of the pile. However, above 900 Hz the majority of the beams had differences over ±10 dB.

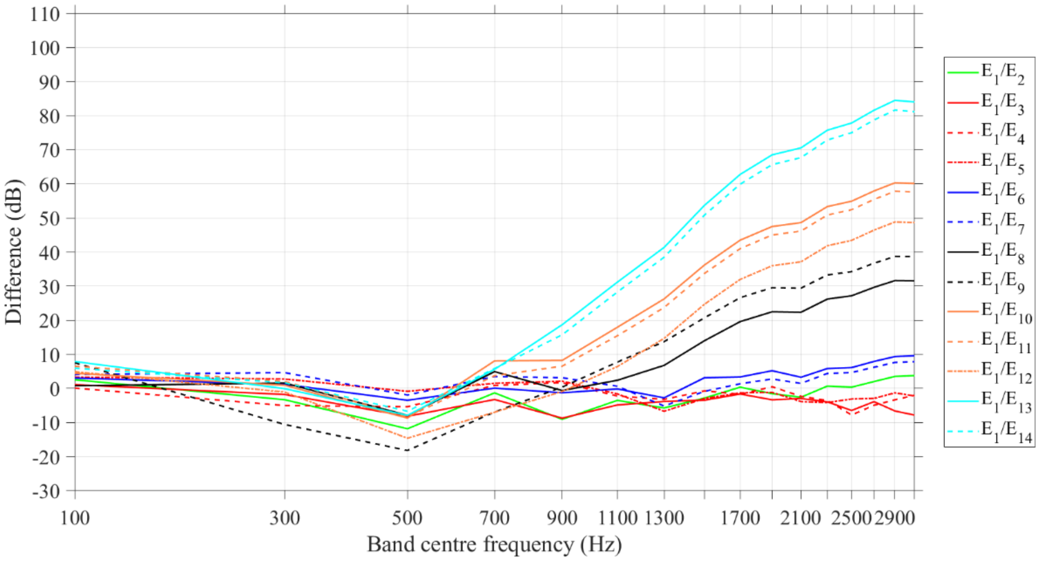

Figure 6-30 Difference between the energy ratios, E_1/E_i from FEM and SEA with CLFs from FEM ESEA (combination of bending, torsional and longitudinal modes) – Excitation on subsystem SS1.

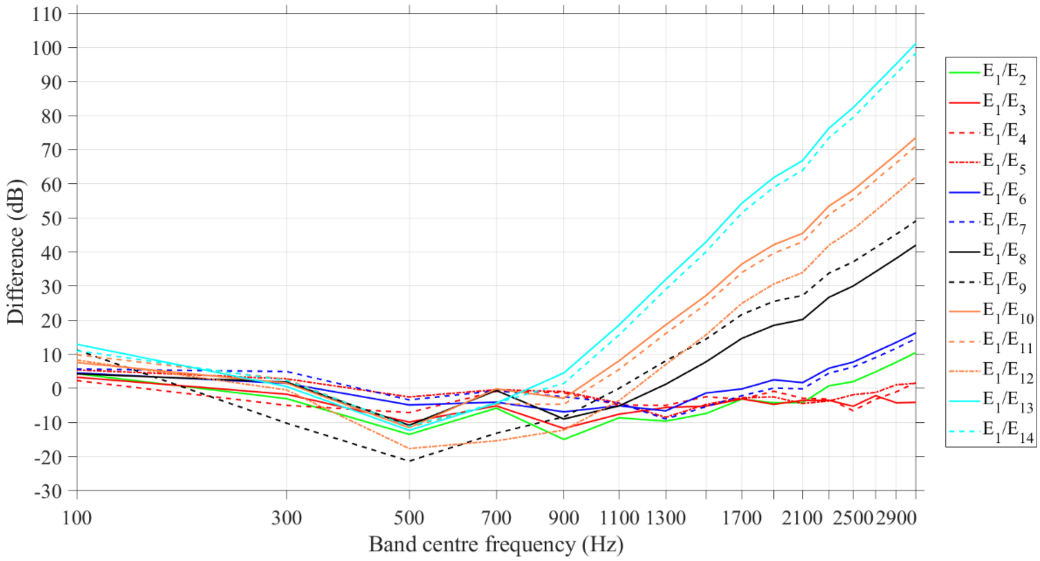

Figure 6-31 Difference between the energy ratios, E_1/E_i from FEM and SEA with CLFs from an analytical model (LSC with infinite beam mobilities) – Excitation on subsystem SS1.

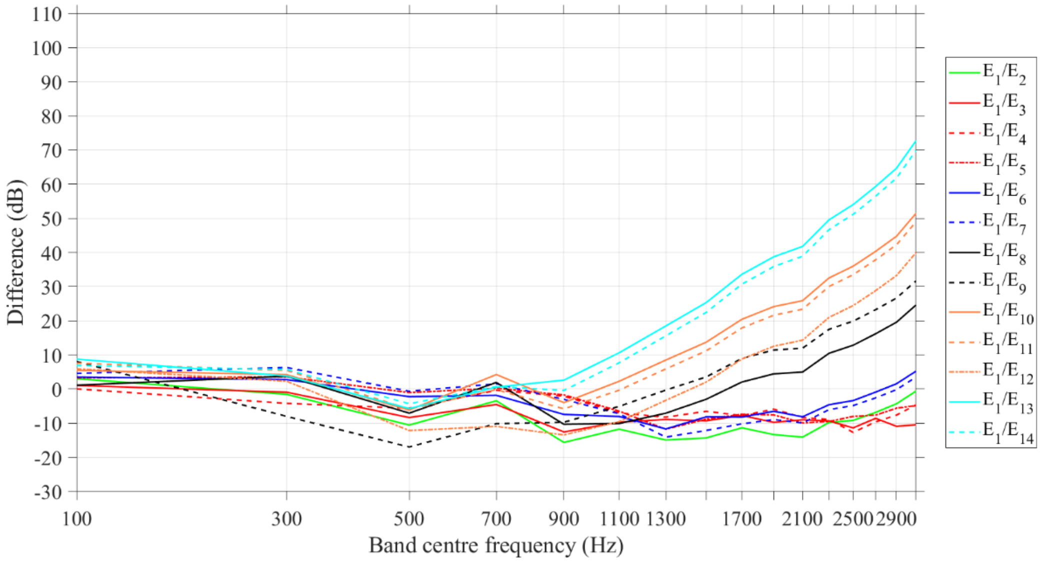

Figure 6-32 Difference between the energy ratios, E_1/E_i from FEM and SEA with CLFs from an analytical model (LSC with FEM mobilities) – Excitation on subsystem SS1.

6.7 Pile 2 – Discussion

For pile 2 it was observed that the largest differences between SEA and FEM occurred for beam SS9. Specifically, for simply supported conditions the E_1/E_9 difference curve was different than the rest of the E_1/E_i curves both in terms of shape and value, regardless of the CLFs used in the SEA matrix calculation. This is explained considering that between beams SS1 and SS9 there are only two transmission paths that approximate the SEA matrix solution when they are combined (Table C-8 and Figure C-8) and SEA is less prone to error when multiple transmission paths exist between the source and receiver subsystems.

From the study of the pile 2 with either simply supported or free support conditions it is seen that when the coupling loss factors from an analytical model of a lump spring connector are used in the SEA matrix, the energy ratios between the subsystems of the pile are predicted with reasonable accuracy in the frequency range from 100 to 700 Hz. Reasonable accuracy does not occur at higher frequencies.

6.8 Conclusions

SEA path analysis has been carried out in two piles with seven and one pile with 14 beams to assess the strength of the various transmission paths. The comparison of the energy ratios with the results of the SEA matrix solution shows that a direct path between two subsystems transfers more energy than the other paths. If a direct path does not exist, the transmission paths with the smaller number of intermediate subsystems will be the strongest and tends to approximate the SEA matrix solution.

FEM models of the piles with simply supported and free support conditions were used to calculate the energy ratios between the beams of the piles. These were compared with the energy ratios calculated from a SEA model which used a) FEM ESEA coupling loss factors and b) CLFs resulted from an analytical model of a lump spring connector. For piles 1a and 1b reasonable agreement (differences within 10 dB) was achieved between SEA and FEM up to 900 Hz and 1100 Hz for simply supported and free supports respectively regardless the CLFs used in the SEA matrix. It was also shown that the SEA works more efficiently as the number of transmission paths between the subsystems increases. For pile 2 with either simply supported or free support conditions, reasonable agreement was achieved between SEA (for any CLFs) and FEM for the majority of the beams with differences up to 10 dB in the frequency range from 100 to 700 Hz.

7. Vibration transmission in damaged reinforced concrete beam-to-column junctions

7.1 Introduction

The aim of this chapter is to assess the potential to use SEA to model the vibration transmission in seismic damaged reinforced concrete beam-to-column junctions where the connection between the beam and the column is made only via the steel reinforcement according to the lean-to collapse pattern which was introduced in Figure 1-3b. A FEM model of a rigid T-junction defined in section 3.3.3.2 is validated against the wave theory in terms of CLFs that only consider bending wave motion. A concrete discontinuity is then introduced at the connection of the beam with the column and the resulting FEM model is used to carry out numerical experiments with FEM to create an ensemble of damaged beam-to-column junctions for a Monte Carlo simulation. This allows use of ESEA to determine CLFs between the beam and the column.

The two main aspects to be investigated are (a) whether two or three subsystems should be used for FEM ESEA (refer back to Figure 3-17) and (b) whether it is possible to only consider one type of wave motion (e.g. bending waves) or whether two or more types of wave motion could be considered simultaneously (e.g. bending and torsional waves). The second aspect concerning the use of ESEA with multiple wave types is necessary because in a collapsed structure it is not known whether one or more wave type will be excited at the damaged beam-to-column connections.

7.2 Mode count

Figure 7-1 shows the mode count from FEM for out-of-plane bending (rotation about X-axis – see Figure 3-14) and combinations of all modes for damaged and rigid beam-to-column junctions. On average, there are at least two bending modes in all the frequency bands for the damaged junctions. The rigid T-junctions have at least one bending mode in all the frequency bands. When all the modes are combined, all the frequency bands have at least eight and seven modes for the damaged and rigid T-junctions respectively.

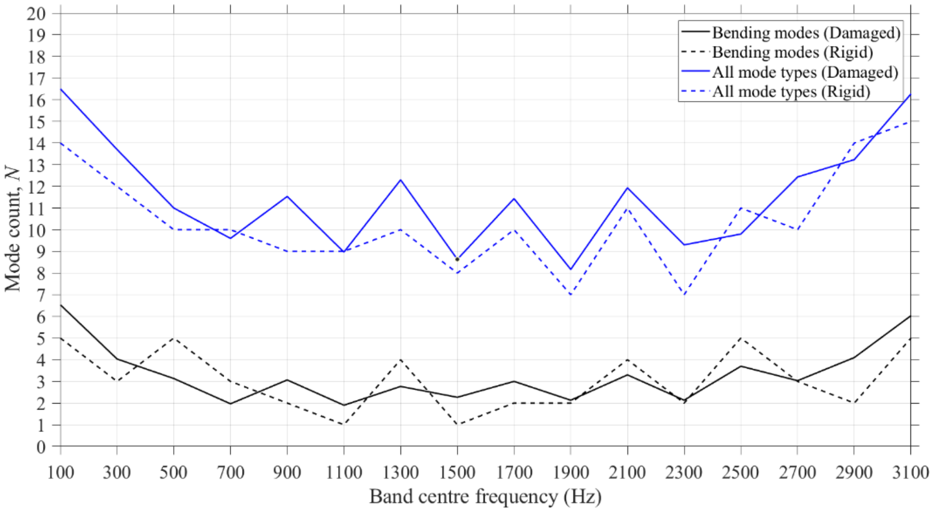

Figure 7-1 Comparison of the average mode count of the 30 damaged junctions with the mode count of the rigid T-junction for out-of-plane bending modes and combination of all mode types.

7.3 Comparison of coupling loss factors from FEM ESEA and wave approach (bending waves only) for the rigid T-junction

In this section, the FEM model of the rigid T-junction is validated against the wave theory in terms of CLFs, considering only bending wave motion. Figure 7-2 - Figure 7-4 compare the coupling loss factors resulted from FEM ESEA and the wave approach (bending waves only) for the rigid T-junction. As shown in Figure 7-2, the CLFs, η_{12} and η_{21}, from FEM ESEA are negative below 500 and 300 Hz respectively. However, reasonable agreement was achieved for η_{12} and η_{21} from 300 to 1700 Hz (differences $\leq$ 4 dB) and from 1700 to 2500 Hz (differences $\leq$ 10 dB). Above 2500 Hz the differences were up to 15 dB.

The CLFs η_{13} and η_{31} resulted from FEM ESEA are negative above 2700 and 2900 Hz respectively (see Figure 7-3). Close agreement was achieved for η_{13} and η_{31} between 500 and 1500 Hz with differences within 5 dB. In the higher frequency bands the differences were within 10 dB except for the frequency band of 2300 Hz where the difference for η_{13} were up to 21 dB.

As Figure 7-4 shows, nine out of 16 frequency bands between 100 and 3100 Hz achieved close agreement for η_{23} and η_{32} with differences within 5 dB. Reasonable agreement was achieved for the remaining seven frequency bands with differences within 10 dB except for the frequency band of 3100 Hz where the difference for η_{23} were up to 11 dB.

To conclude, differences up to ±10 dB and negative CLFs were noticed at low frequencies whereas the agreement was in between ±5 dB from 500 to 1700 Hz. At higher frequencies, errors larger than ±10 dB were noticed for most of the frequency bands.

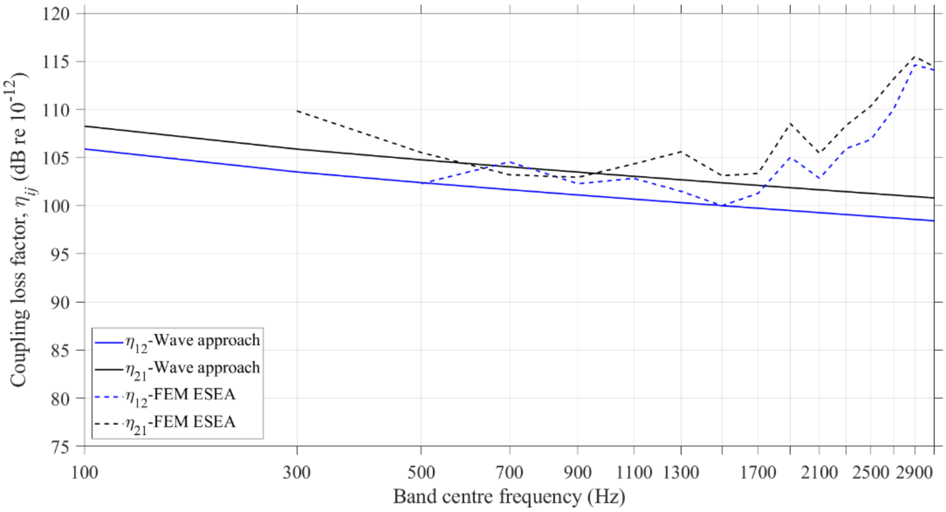

Figure 7-2 Comparison of FEM and the analytical (wave approach) coupling loss factors η_{12} and η_{21}.

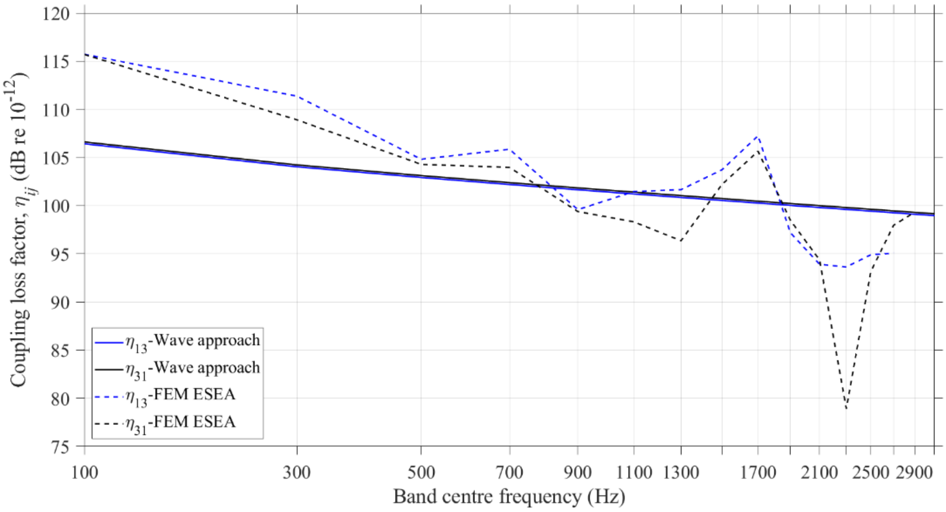

Figure 7-3 Comparison of FEM and the analytical (wave approach) coupling loss factors η_{13} and η_{31}.

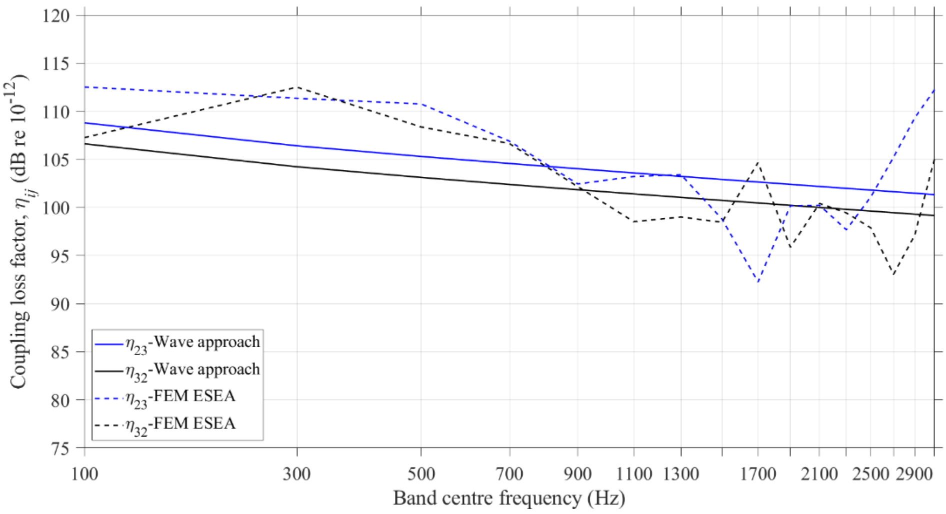

Figure 7-4 Comparison of FEM and the analytical (wave approach) coupling loss factors η_{23} and η_{32}.

7.4 Coupling loss factors from FEM ESEA for damaged and rigid T-junctions

This section compares the CLFs from FEM ESEA for damaged and rigid beam-to-column junctions to investigate whether the number of the subsystems affects the efficiency of FEM ESEA and whether it is possible to only consider one type of wave motion (e.g. bending waves) or whether two or more types of wave motion could be considered simultaneously (e.g. bending and torsional waves).

7.4.1 Two subsystems

Figure 7-5 compares the coupling loss factors η_{12} and η_{21} from FEM ESEA with two subsystems, considering either only bending modes or the combination of all modes in the frequency range from 1 to 3200 Hz. Results are shown for rigid and damaged junctions. The FEM ESEA results for the 30 damaged beam-to-column junctions are shown in terms of a mean value with 95% confidence intervals.

In the damaged junctions, the coupling is weaker than the rigid junction because subsystems 1 and 2 are connected only via the steel reinforcement.

For the damaged junctions, the comparison of the CLFs from FEM ESEA with bending modes and the combination of all modes showed close agreement (differences within 5 dB) from 100 to 2500 Hz. Above 2500 Hz, the differences were up to 10 dB. The 95% confidence intervals for the damaged junctions show that the uncertainty is sufficiently low that it should be feasible to estimate the coupling even when the exact angle between the beam and the column is unknown in the damaged junctions of a real collapsed building.

For the rigid junction, there were differences up to 5 dB between the CLFs from FEM ESEA with bending modes and the combination of all modes up to 3200 Hz. The higher CLFs with bending modes indicate that the bending modes are dominating over the combination of all the modes for the dynamic response of a beam-to-column junction either if the beam is connected to the column rigidly or only via the steel reinforcement.

For consideration of either only bending modes or the combination of all modes, FEM ESEA resulted in positive CLFs for each of the 30 damaged junctions except for one junction in the frequency band of 100 Hz as Figure 7-6 indicates.

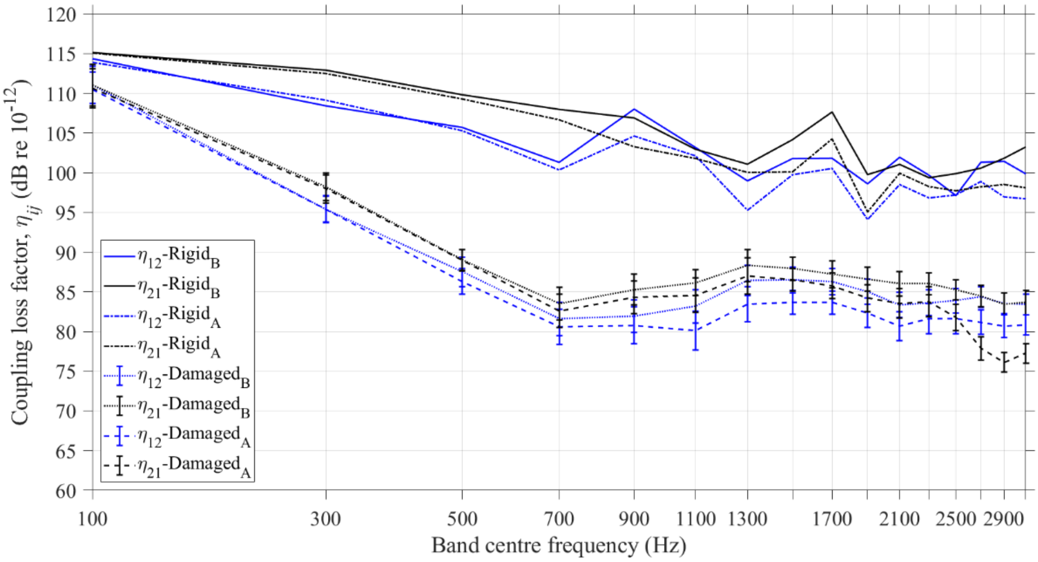

Figure 7-5 Coupling loss factors η_{12} and η_{21} resulted from FEM ESEA with two subsystems with bending only (B) and the combination of all modes (A). The error bars denote the 95% confidence intervals.

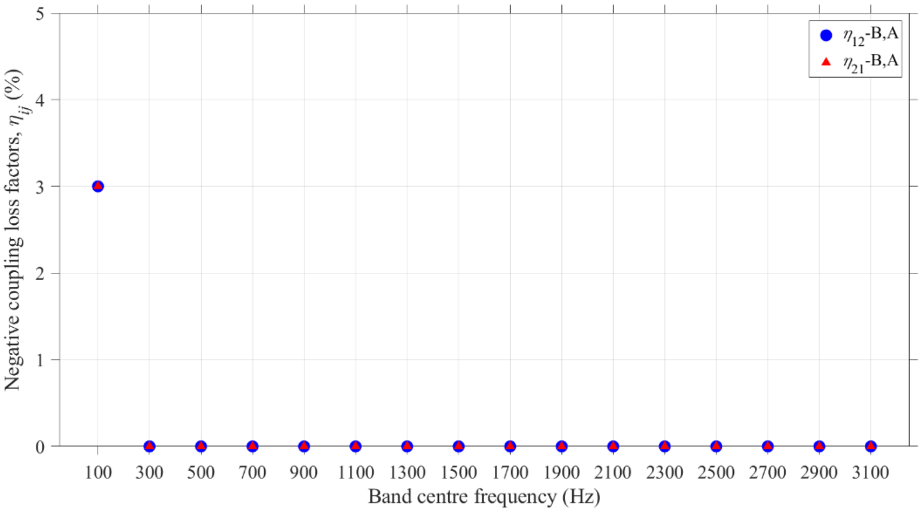

Figure 7-6 Damaged junctions – Percentage of negative CLFs η_{12} and η_{21} resulted from FEM ESEA with two subsystems with bending only (B) and the combination of all modes (A).

7.4.2 Three subsystems

Figure 7-7 to Figure 7-9 allow comparison of the coupling loss factors from FEM ESEA with three subsystems, considering either bending or combination of all modes in the frequency range from 1 to 3200 Hz. Results are shown for rigid and damaged junctions. The FEM ESEA results for the 30 damaged beam-to-column junctions are shown in terms of a mean value with 95% confidence intervals.

The CLFs η_{12} and η_{21} from FEM ESEA with damaged junctions are comparable to the CLFS of the rigid one (see Figure 7-7). This was partially expected since subsystems 1 and 2 are located in the column of the junction where there is no damage. The remaining CLFs (η_{13}, η_{31}, η_{23}, and η_{32}) are smaller in the damaged than in the rigid T-junction. This is expected because in the damaged junctions, subsystem 3 is connected to subsystems 1 and 2 only via the steel reinforcement and weaker coupling is expected (see Figure 7-8 and Figure 7-9).

For the rigid T-junction, the differences of the CLFs η_{12}, η_{13} and η_{31} from FEM ESEA by using bending and combination of all modes were up to 5 dB between 100 and 900 Hz. Above 900 Hz, the differences were between 5 and 10 dB for the vast majority of the frequency bands. For $\eta_{21,}$ η_{23} and η_{32} the differences were typically up to 5 dB over the complete frequency range. FEM ESEA resulted in negative CLFs below 500 Hz and over 2700 Hz as it is shown in Figure 7-7.

For the damaged junctions, the differences between the CLFs from the FEM ESEA for bending only and the combination of all modes were up to 5 dB between 100 and 2500 Hz. Above 2500 Hz, the differences were between 5 and 10 dB. The 95% confidence intervals show that the uncertainty is sufficiently low that it should be feasible to estimate the coupling even when the exact angle between the beam and the column is unknown in the damaged junctions of a real collapsed building.

Regardless of the type of modes (bending or combination of all modes), the consideration of three subsystems for the FEM ESEA of the 30 damaged beam-to-column junctions resulted in a significant number of negative coupling loss factors (see Figure 7-10 and Figure 7-11). Specifically, below 1500 Hz the percentage of the junctions with negative loss factors was between 17 and 54%. These mainly occurred with the CLFs from the column (SS1 and SS2) to the beam (SS3) and vice versa. Above 1500 Hz, the percentage of the junctions with negative loss factors was between 3 and 10%.

Comparing the above percentages with the 3% of negative CLFs of Figure 7-6 (FEM ESEA with two subsystems), it is seen that in damaged junctions the use of two instead of three subsystems in FEM ESEA significantly decrease the number of negative coupling loss factors.

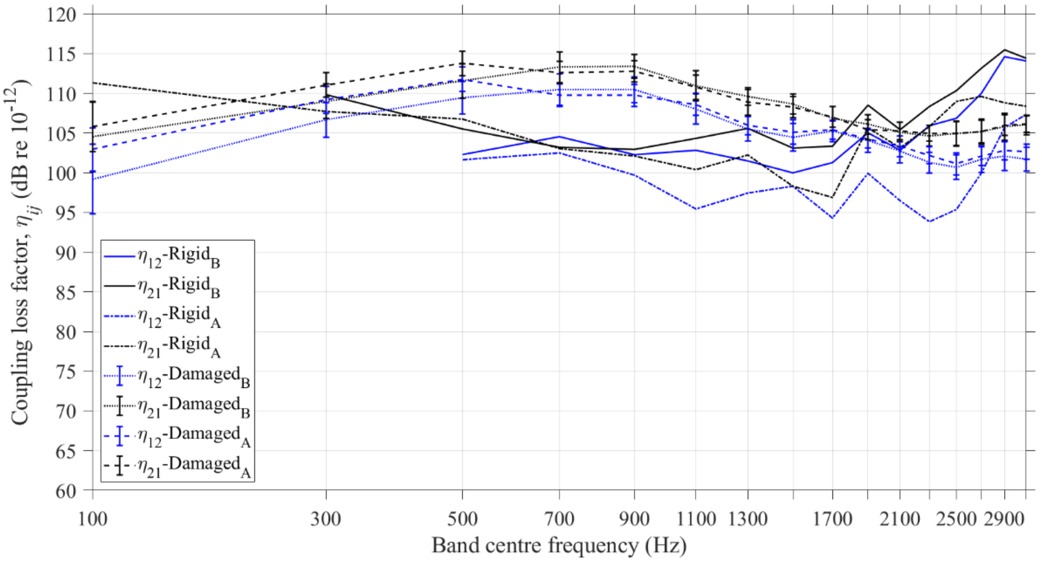

Figure 7-7 Coupling loss factors η_{12} and η_{21} resulted from FEM ESEA with three subsystems with bending only (B) and the combination of all modes (A). The error bars denote the 95% confidence intervals.

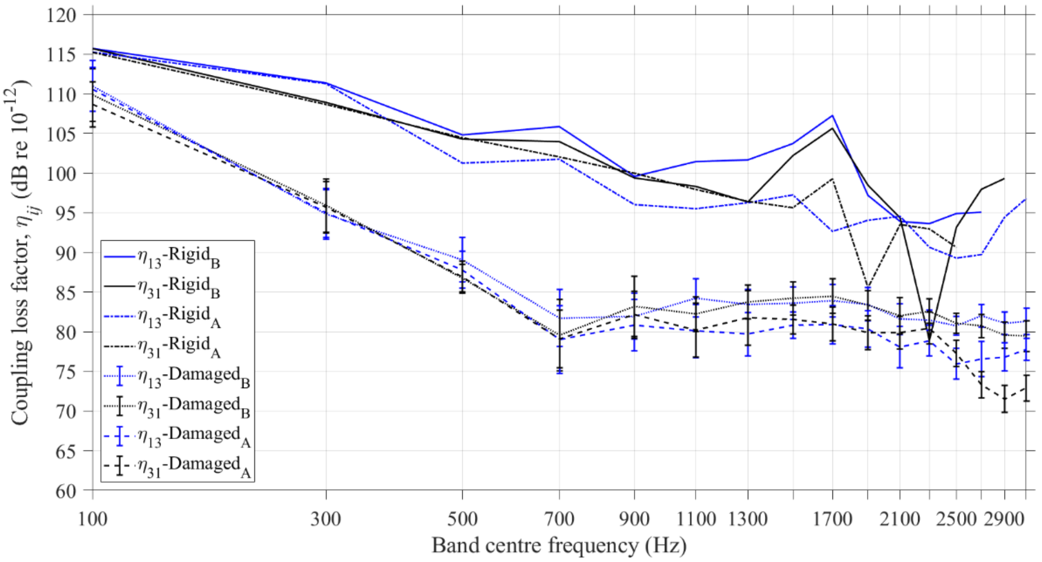

Figure 7-8 Coupling loss factors η_{13} and η_{31} resulted from FEM ESEA with three subsystems with bending only (B) and the combination of all modes (A). The error bars denote the 95% confidence intervals.

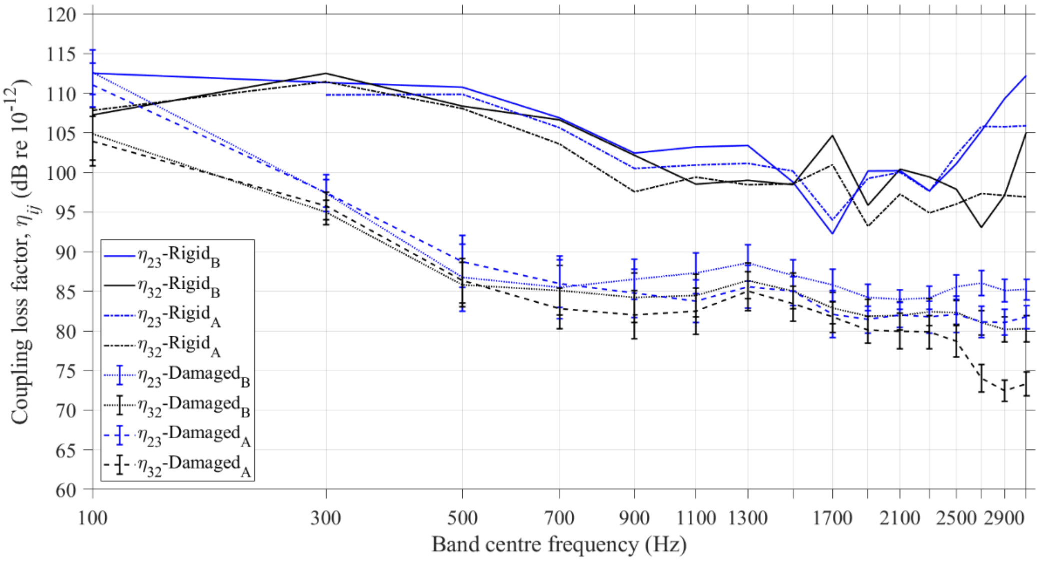

Figure 7-9 Coupling loss factors η_{23} and η_{32} resulted from FEM ESEA with three subsystems with bending only (B) and the combination of all modes (A). The error bars denote the 95% confidence intervals.

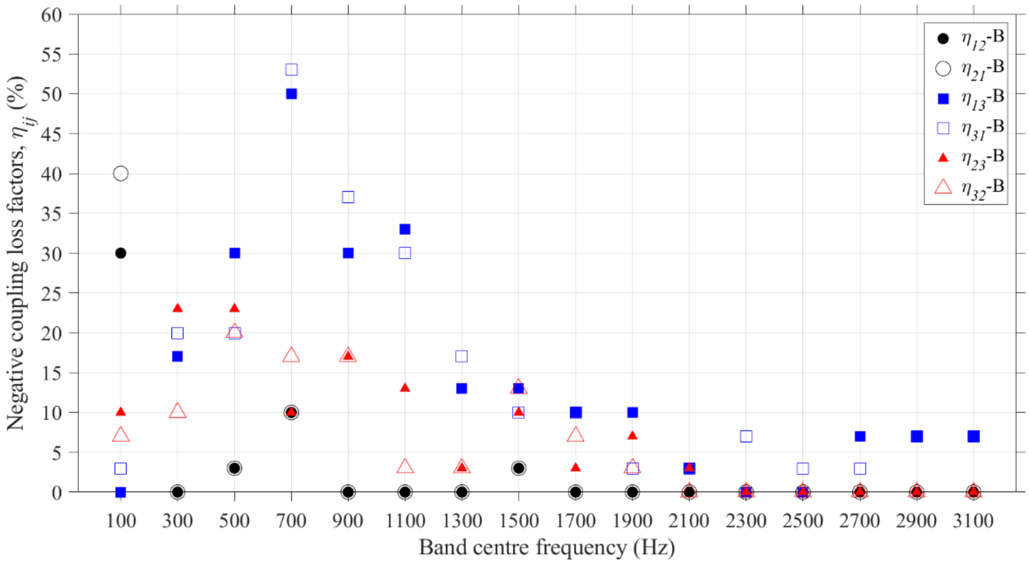

Figure 7-10 Damaged junctions – Percentage of negative CLFs resulted from FEM ESEA with three subsystems with bending modes only (B).

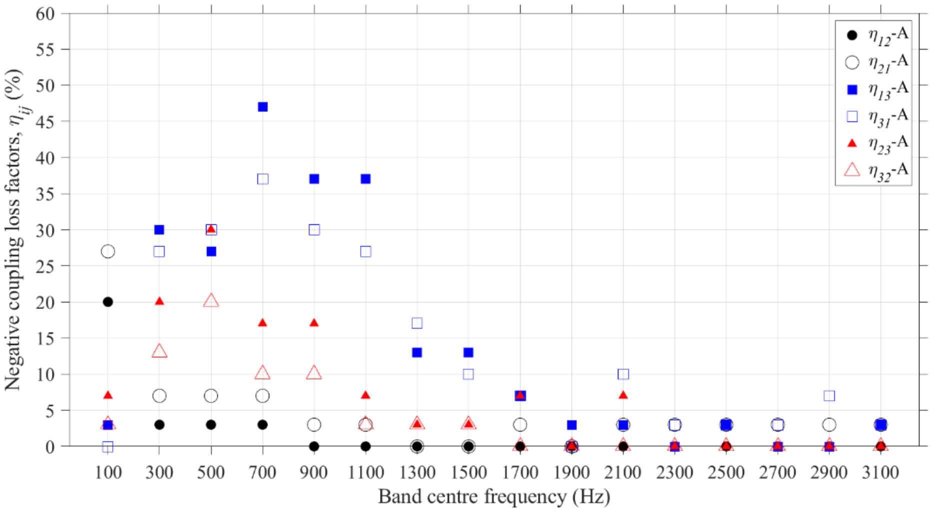

Figure 7-11 Damaged junctions – Percentage of negative CLFs resulted from FEM ESEA with three subsystems with the combination of all modes (A).

7.5 Conclusions

The FEM model of a rigid reinforced concrete T-junction was validated by comparing the FEM ESEA coupling loss factors against the theoretical CLFs which were calculated using the wave approach for only bending modes. An ensemble of 30 randomly damaged beam-to-column junctions was generated using Monte Carlo simulation with FEM that allowed ESEA with two or three subsystems to be used to determine the CLFs between the beam and the column considering either only bending or the combination of all modes.

Regardless of the number of the subsystems and the wave types in FEM ESEA, the coupling between the beam and the column was weaker in the damaged than in the rigid junction. In both rigid and damaged junctions, the CLFs from FEM ESEA were similar with only bending and the combination of all modes, regardless of the number of the subsystems. This indicated that the bending modes are dominating the dynamic response of a beam-to-column junction over the combination of all the modes, either if the beam is connected to the column rigidly or only via the steel reinforcement.

In damaged junctions, it was shown that the uncertainty of predicting the CLFs using FEM ESEA is sufficiently low that it should be feasible to estimate the coupling even when the exact angle between the beam and the column is unknown. In addition, the use of two instead of three subsystems should be preferred in FEM ESEA since it significantly decreases the number of negative coupling loss factors.

8. Conclusions

8.1 Introduction

This thesis has investigated the vibration transmission between reinforced concrete beams in situations that represent fragmented concrete buildings after an earthquake using Experimental Modal Analysis (EMA), Finite Element Methods (FEM) and Statistical Energy Analysis (SEA).

8.2 Main findings

The research in this thesis provides evidence of the potential to use SEA to predict vibration transmission in fragmented concrete buildings after an earthquake. The main extensions to SEA modelling were for concrete elements that are in contact with each other and to beam-column junctions where the rigid connection has broken leaving only the reinforcement. Whilst the findings apply to reinforced concrete beams, the experimentally validated FEM models provide a basis on which to model reinforced concrete walls and floors.

FEM models were developed and validated with experimental modal analysis for beams connected with surface-to-surface and edge-to-surface contact conditions. These models were validated in terms of eigenfrequencies, mode shapes and spatial-average response. It was shown that the interaction between the beams could be approximated using a normal contact stiffness. This stiffness showed some dependence on the modal response with values forming a lognormal distribution. It was shown that the mean value of this lognormal distribution could be used to approximate the contact stiffness in FEM models of beams junctions with surface-to-surface or edge-to-surface contact conditions.

For concrete beams that are stacked on top of each other without any rigid bonding material it was shown that MAC is inadequate to assess the validity of the FEM model as this led to misleading results. Whilst shortcomings of MAC have been identified in other work [66], this problem may have gone unnoticed because most connections tend to be rigid rather than spring-coupled. Using PMAC for these beams, it was shown that MAC was mainly determined by the modal vectors of one beam whereas the contribution of the other beam(s) to the MAC value was negligible. To overcome the shortcomings of MAC when validating FEM models of structural coupling between elastic systems using spring connectors to model the unbonded contact condition, an additional criterion, the Partial Modal Vector Ratio was introduced in this thesis. This criterion allowed identification of the FEM model that gave the most appropriate representation of the interaction between the coupled beams.

Compared to running FEM models with applied loads to assess vibration transmission between the coupled beams, PMVR is a time-efficient approach that can be used as a supplementary criterion to MAC to identify potential correlation problems caused by the interaction of structural elements.

Finite element models were used to calculate the driving-point mobilities of reinforced concrete beams for bending modes only, torsional modes only and the combination of all modes in the frequency range up to 3200 Hz with free and simply supported conditions. These mobilities were in close agreement (difference within 5 dB) with the theoretical driving-point mobilities of a thin beam of infinite extent for bending wave excitation but not for the combination of all modes.

Coupling loss factors between two beams were determined using an ensemble of 30 random beam junctions (free and simply supported boundary conditions) for Monte Carlo simulations with FEM and ESEA. These were compared with CLFs calculated using an analytical model based on a lump spring connector. For only bending waves or torsional waves, close agreement (difference within 5 dB) was achieved between FEM ESEA and the analytical model up to the frequency where half the bending or torsional wavelength equalled the longest side of the contact area. Above this frequency the interaction between the two beams cannot be considered as a lump spring connection. The inclusion of the FEM driving-point mobilities in the analytical model (instead of the infinite beam equation for the driving-point mobility) did not significantly improve the agreement. When all wave types are combined, close agreement can still be achieved at frequencies below 900 Hz.

To extend the validation of vibration transmission between two beams, SEA path analysis was carried out on two piles with seven beams and one pile with 14 beams to assess the strength of the various transmission paths. The comparison of the energy ratios with the results of the SEA matrix solution showed that a direct path between two subsystems will transfer more energy than the other paths. If a direct path does not exist, the transmission paths with the smaller number of intermediate subsystems will be the strongest and will approximate better the SEA matrix solution.

FEM models of these piles were used to calculate the energy ratios between the beams of the piles. These were compared with the energy ratios calculated from an SEA model which used a) FEM ESEA coupling loss factors and b) CLFs resulted from an analytical model of a lump spring connector. For the piles of seven beams, reasonable agreement (difference within 10 dB) was achieved between SEA and FEM up to at least 900 Hz and it was shown that SEA can become more accurate when the number of transmission paths increases. For the pile of 14 beams, reasonable agreement was achieved between SEA and FEM for the majority of the beams in the frequency range up to 700 Hz.

The next step was to broaden the approach using FEM and SEA to other types of damaged beam or column elements found in a building after an earthquake. Initially, FEM models of a rigid reinforced concrete T-junction were validated by comparing FEM ESEA coupling loss factors against theoretical CLFs calculated using the wave approach for only bending modes. In this situation it was apparent that the T-junction needed to be modelled as three subsystems. However, for the damaged T-junction, an ensemble of 30 randomly damaged beam-to-column junctions was generated using a Monte Carlo simulation with FEM. This allowed an assessment of ESEA with two or three subsystems to be used to determine the CLFs between the beam and the column considering either only bending modes or the combination of all modes. Regardless of the number of the subsystems and the wave types in FEM ESEA, the coupling between the beam and the column was weaker in the damaged than in the rigid junction. In both rigid and damaged junctions, the CLFs from FEM ESEA were similar with only bending and the combination of all modes, regardless of the number of the subsystems. This indicated that the bending modes are dominating the dynamic response of a beam-to-column junction over the combination of all the modes, either if the beam is connected to the column rigidly or only via the steel reinforcement. In damaged junctions, it was shown that the uncertainty of predicting the CLFs using FEM ESEA is sufficiently low that it should be feasible to estimate the coupling even when the exact angle between the beam and the column is unknown. The use of two instead of three subsystems for the junction significantly decreases the number of negative coupling loss factors in FEM ESEA. This indicates that the two-subsystem model provides a reasonable basis on which to build an SEA model.

8.3 Future work

Future work could assess the structure borne power input from a person banging on concrete with their hand or a piece of rubble. This will identify the relevant frequency range that needs to be considered.

Results in chapter 4 indicate that the mean value of the lognormal distribution could be used to approximate the contact stiffness in FEM models of beams junctions with edge-to-surface contact conditions. To extend the validity of this approach it would be useful: (a) to assess the potential to use SEA to model the vibration transmission in these junctions and (b) investigate whether an analytical model based on a lump spring connector is valid.

Results in chapters 6 and 7 shown that SEA could be used to model the vibration transmission in piles of reinforced concrete beams and in damaged beam-to-column junctions separately. Next stage of the work would be to combine these collapse patterns and assess the potential to use SEA to model the vibration transmission.

A. MAC values for experimental setups J1 and J2

Figure A-1 and Figure A-2 compare FEM and EMA results for setups J1 and J2 in terms of mode shapes. Close agreement was achieved for the vast majority of the mode pairs with MAC > 0.8.

- **Setup J1**

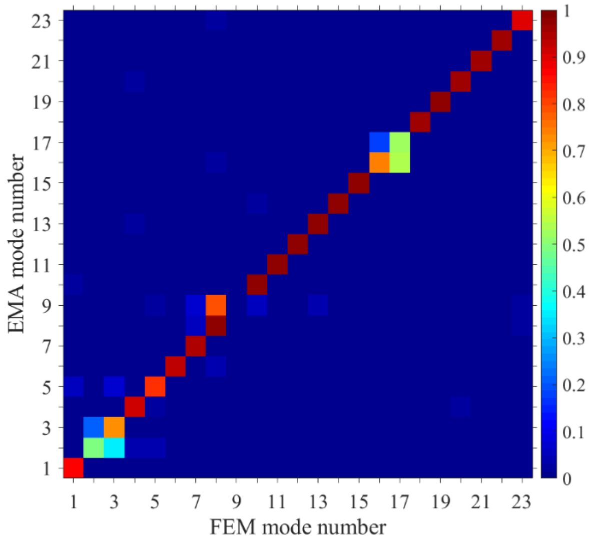

Figure A-1 MAC values for FEM model of Setup J1.

- **Setup J2**

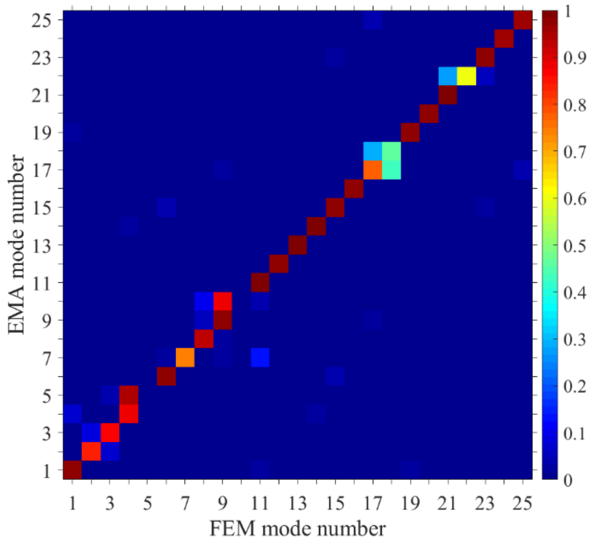

Figure A-2 MAC values for FEM model of Setup J2.

B. SEA matrix solution for piles 1a, 1b and 2

The general SEA matrix solution for the seven subsystems of pile 1a and 1b and for the 14 subsystems of pile 2 for excitation on subsystem 1 is given by Eq. B.1, B.2 and B.3. For subsystems that are not directly connected, the coupling loss factor was set equal to zero.

- **Pile 1a**

$$\begin{bmatrix} \sum_{n=1}^{N}\eta_{1n} & 0 & -\eta_{31} & -\eta_{41} & -\eta_{51} & 0 & 0 \\ 0 & \sum_{n=1}^{N}\eta_{2n} & -\eta_{32} & 0 & 0 & 0 & 0 \\ -\eta_{13} & -\eta_{23} & \sum_{n=1}^{N}\eta_{3n} & 0 & 0 & -\eta_{63} & -\eta_{73} \\ -\eta_{14} & 0 & 0 & \sum_{n=1}^{N}\eta_{4n} & 0 & -\eta_{64} & -\eta_{74} \\ -\eta_{15} & 0 & 0 & 0 & \sum_{n=1}^{N}\eta_{5n} & -\eta_{65} & 0 \\ 0 & 0 & -\eta_{36} & -\eta_{46} & -\eta_{56} & \sum_{n=1}^{N}\eta_{6n} & 0 \\ 0 & 0 & -\eta_{37} & -\eta_{47} & 0 & 0 & \sum_{n=1}^{N}\eta_{7n} \end{bmatrix} \begin{bmatrix} E_1 \\ E_2 \\ E_3 \\ E_4 \\ E_5 \\ E_6 \\ E_7 \end{bmatrix} = \begin{bmatrix} \frac{W_{\mathrm{in}(1)}}{\omega} \\ 0 \\ 0 \\ 0 \\ 0 \\ 0 \\ 0 \end{bmatrix} \qquad \text{(B.1)}$$

- **Pile 1b**

$$\begin{bmatrix} \sum_{n=1}^{N} \eta_{1n} & 0 & -\eta_{31} & -\eta_{41} & -\eta_{51} & 0 & 0 \\ 0 & \sum_{n=1}^{N} \eta_{2n} & -\eta_{32} & 0 & -\eta_{52} & 0 & 0 \\ -\eta_{13} & -\eta_{23} & \sum_{n=1}^{N} \eta_{3n} & 0 & 0 & -\eta_{63} & -\eta_{73} \\ -\eta_{14} & 0 & 0 & \sum_{n=1}^{N} \eta_{4n} & 0 & -\eta_{64} & -\eta_{74} \\ -\eta_{15} & -\eta_{25} & 0 & 0 & \sum_{n=1}^{N} \eta_{5n} & -\eta_{65} & 0 \\ 0 & 0 & -\eta_{36} & -\eta_{46} & -\eta_{56} & \sum_{n=1}^{N} \eta_{6n} & 0 \\ 0 & 0 & -\eta_{37} & -\eta_{47} & 0 & 0 & \sum_{n=1}^{N} \eta_{7n} \end{bmatrix} \begin{bmatrix} E_1 \\ E_2 \\ E_3 \\ E_4 \\ E_5 \\ E_6 \\ E_7 \end{bmatrix} = \begin{bmatrix} \frac{W_{\mathrm{in}(1)}}{\omega} \\ 0 \\ 0 \\ 0 \\ 0 \\ 0 \\ 0 \end{bmatrix} \qquad \text{(B.2)}$$

- **Pile 2**

$$\begin{bmatrix}
\sum_{n=1}^{N}\eta_{1n} & 0 & -\eta_{31} & -\eta_{41} & -\eta_{51} & 0 & 0 & 0 & 0 & 0 & 0 & 0 & 0 & 0 \\
0 & \sum_{n=1}^{N}\eta_{2n} & -\eta_{32} & -\eta_{42} & 0 & 0 & 0 & 0 & 0 & 0 & 0 & 0 & 0 & 0 \\
-\eta_{13} & -\eta_{23} & \sum_{n=1}^{N}\eta_{3n} & 0 & 0 & -\eta_{63} & 0 & 0 & 0 & 0 & 0 & 0 & 0 & 0 \\
-\eta_{14} & -\eta_{24} & 0 & \sum_{n=1}^{N}\eta_{4n} & 0 & -\eta_{64} & -\eta_{74} & 0 & 0 & 0 & 0 & 0 & 0 & 0 \\
-\eta_{15} & 0 & 0 & 0 & \sum_{n=1}^{N}\eta_{5n} & -\eta_{65} & -\eta_{75} & 0 & 0 & 0 & 0 & 0 & 0 & 0 \\
0 & 0 & -\eta_{36} & -\eta_{46} & -\eta_{56} & \sum_{n=1}^{N}\eta_{6n} & 0 & -\eta_{86} & 0 & 0 & 0 & 0 & 0 & 0 \\
0 & 0 & 0 & -\eta_{47} & -\eta_{57} & 0 & \sum_{n=1}^{N}\eta_{7n} & -\eta_{87} & -\eta_{97} & 0 & 0 & 0 & 0 & 0 \\
0 & 0 & 0 & 0 & 0 & -\eta_{68} & -\eta_{78} & \sum_{n=1}^{N}\eta_{8n} & 0 & -\eta_{108} & -\eta_{118} & -\eta_{128} & 0 & 0 \\
0 & 0 & 0 & 0 & 0 & 0 & -\eta_{79} & 0 & \sum_{n=1}^{N}\eta_{9n} & -\eta_{109} & 0 & 0 & 0 & 0 \\
0 & 0 & 0 & 0 & 0 & 0 & 0 & -\eta_{810} & -\eta_{910} & \sum_{n=1}^{N}\eta_{10n} & 0 & 0 & -\eta_{1310} & -\eta_{1410} \\
0 & 0 & 0 & 0 & 0 & 0 & 0 & -\eta_{811} & 0 & 0 & \sum_{n=1}^{N}\eta_{11n} & 0 & -\eta_{1311} & -\eta_{1411} \\
0 & 0 & 0 & 0 & 0 & 0 & 0 & -\eta_{812} & 0 & 0 & 0 & \sum_{n=1}^{N}\eta_{12n} & -\eta_{1312} & 0 \\
0 & 0 & 0 & 0 & 0 & 0 & 0 & 0 & 0 & -\eta_{1013} & -\eta_{1113} & -\eta_{1213} & \sum_{n=1}^{N}\eta_{13n} & 0 \\
0 & 0 & 0 & 0 & 0 & 0 & 0 & 0 & 0 & -\eta_{1014} & -\eta_{1114} & 0 & 0 & \sum_{n=1}^{N}\eta_{14n}
\end{bmatrix}
\begin{bmatrix} E_1 \\ E_2 \\ E_3 \\ E_4 \\ E_5 \\ E_6 \\ E_7 \\ E_8 \\ E_9 \\ E_{10} \\ E_{11} \\ E_{12} \\ E_{13} \\ E_{14} \end{bmatrix}
=
\begin{bmatrix} \frac{W_{\mathrm{in}(1)}}{\omega} \\ 0 \\ 0 \\ 0 \\ 0 \\ 0 \\ 0 \\ 0 \\ 0 \\ 0 \\ 0 \\ 0 \\ 0 \\ 0 \end{bmatrix} \qquad (B.3)$$

C. Path analysis of pile 2

For power input to source beam SS1, Table C-1 to Table C-13 show the transmission paths to receiving beams SS2 to SS14. For each energy ratio, the paths are grouped according to the number of the intermediate subsystems.

Figure C-1 to Figure C-13 present the differences between the energy ratios from the SEA matrix solution and path analysis. Results are shown for 16 frequency bands of 200 Hz bandwidth. The difference curves are coloured according to the number of the intermediate subsystems of each transmission path and the path that gives the lowest energy ratio difference is considered as the strongest path.

Table C-1 Transmission paths to beam SS2 through pile 2 shown in Figure 3-8 for power input to beam SS1 (grey shading indicates the strongest path).

Number of intermediate subsystems	**Number of paths**	**Paths**	
0	-	-	
1	2	No.1 (1→3→2)	
		No.2 (1→4→2)	
2	-	-	
3	5	No.3 (1→3→6→4→2)	
		No.4 (1→4→6→3→2)	
		No.5 (1→5→6→3→2)	
		No.6 (1→5→6→4→2)	
		No.7 (1→5→7→4→2)	
4	-	-	
5	8	No.8 (1→3→6→5→7→4→2)	No.12 (1→5→6→8→7→4→2)
		No.9 (1→3→6→8→7→4→2)	No.13 (1→5→7→4→6→3→2)
		No.10 (1→4→7→5→6→3→2)	No.14 (1→5→7→8→6→3→2)
		No.11 (1→4→7→8→6→3→2)	No.15 (1→5→7→8→6→4→2)

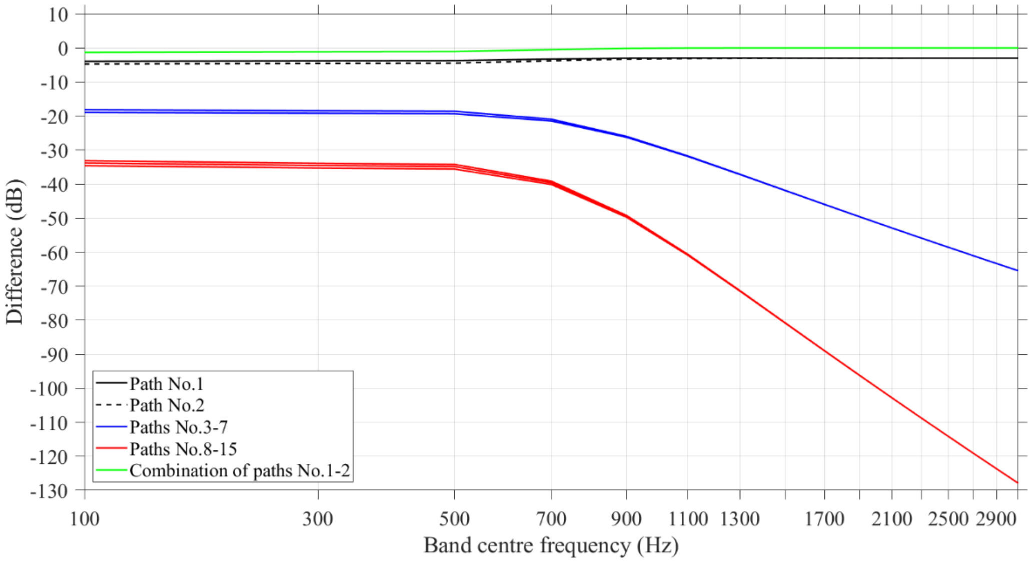

Figure C-1 Difference between the energy ratio, E_1/E_2, from the SEA matrix solution and path analysis.

Table C-2 Transmission paths to beam SS3 through pile 2 shown in Figure 3-8 for power input to beam SS1 (grey shading indicates the strongest path).

Number of intermediate subsystems	**Number of paths**	**Paths**	
0	1	No.1 (1→3)	
1	-	-	
2	3	No.2 (1→4→2→3)	
		No.3 (1→4→6→3)	
		No.4 (1→5→6→3)	
3	-	-	
4	6	No.5 (1→4→7→5→6→3)	No.8 (1→5→7→4→2→3)
		No.6 (1→4→7→8→6→3)	No.9 (1→5→7→4→6→3)
		No.7 (1→5→6→4→2→3)	No.10 (1→5→7→8→6→3)
5	-	-	

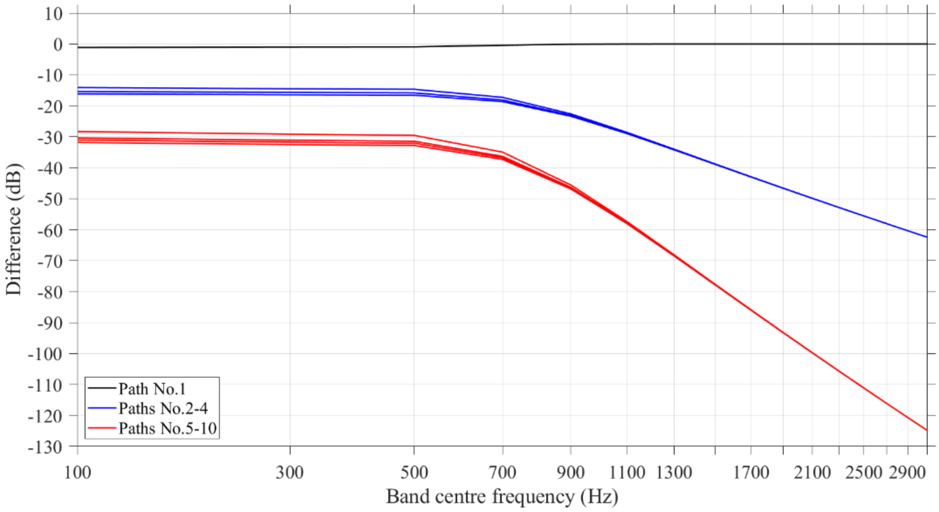

Figure C-2 Difference between the energy ratio, E_1/E_3, from the SEA matrix solution and path analysis.

Table C-3 Transmission paths to beam SS4 through pile 2 shown in Figure 3-8 for power input to beam SS1 (grey shading indicates the strongest path).

Number of intermediate subsystems	**Number of paths**	**Paths**
0	1	No.1 (1→4)
1	-	-
2	4	No.2 (1→3→2→4) No.3 (1→3→6→4) No.4 (1→5→6→4) No.5 (1→5→7→4)
3	-	-
4	5	No.6 (1→3→6→5→7→4) No.7 (1→3→6→8→7→4) No.8 (1→5→6→3→2→4) No.9 (1→5→6→8→7→4) No.10 (1→5→7→8→6→4)
5	-	-

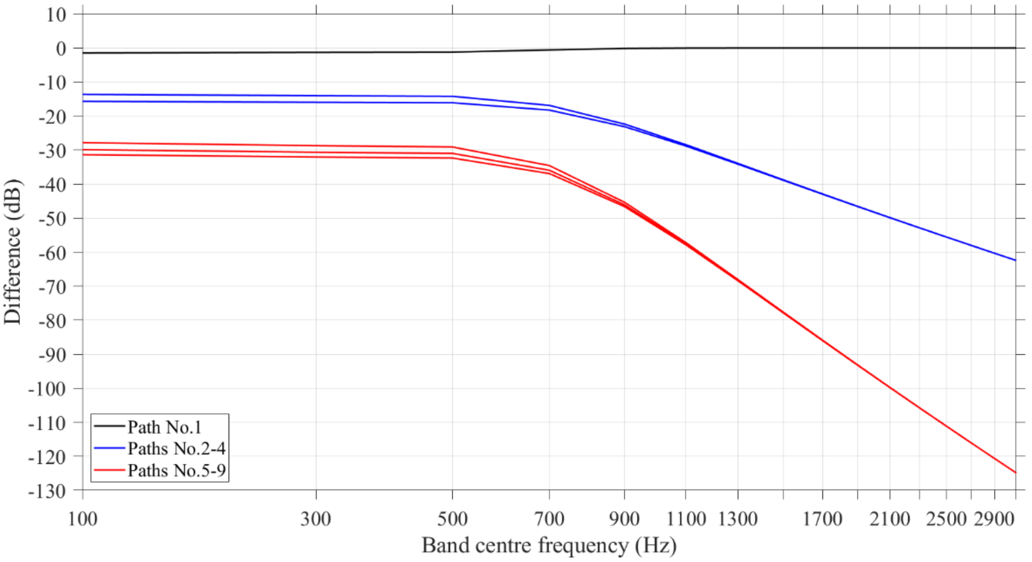

Figure C-3 Difference between the energy ratio, E_1/E_4, from the SEA matrix solution and path analysis.

Table C-4 Transmission paths to beam SS5 through pile 2 shown in Figure 3-8 for power input to beam SS1 (grey shading indicates the strongest path).

Number of intermediate subsystems	**Number of paths**	**Paths**	
0	1	No.1 (1→5)	
1	-	-	
2	3	No.2 (1→3→6→5)	
		No.3 (1→4→6→5)	
		No.4 (1→4→7→5)	
3	-	-	
4	6	No.5 (1→3→2→4→6→5)	No.8 (1→4→2→3→6→5)
		No.6 (1→3→2→4→7→5)	No.9 (1→4→6→8→7→5)
		No.7 (1→3→6→8→7→5)	No.10 (1→4→7→8→6→5)
5	-	-	

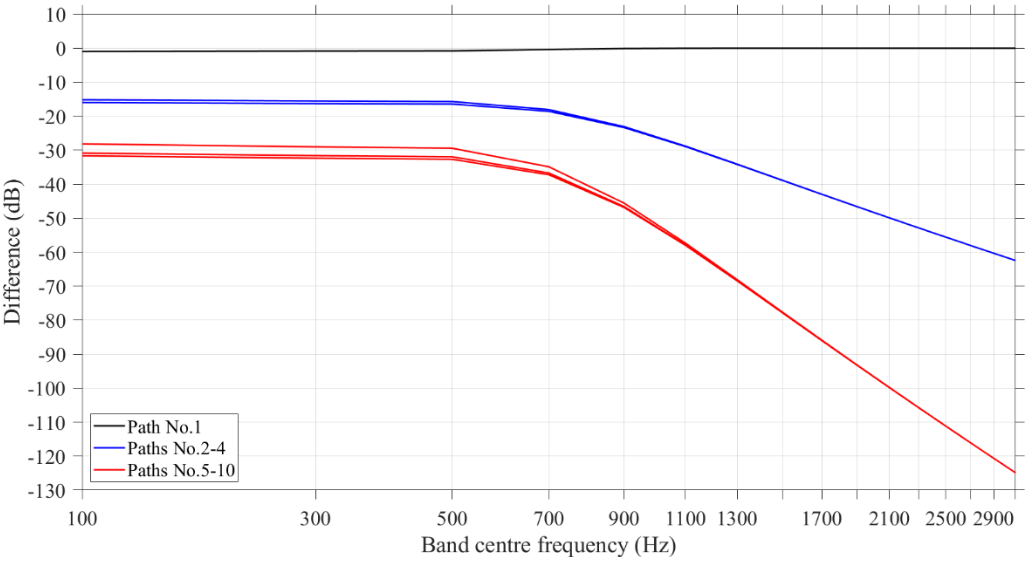

Figure C-4 Difference between the energy ratio, E_1/E_5, from the SEA matrix solution and path analysis.

Table C-5 Transmission paths to beam SS6 through pile 2 shown in Figure 3-8 for power input to beam SS1 (grey shading indicates the strongest path).

Number of intermediate subsystems	**Number of paths**	**Paths**	
0	-	-	
1	3	No.1 (1→3→6)	
		No.2 (1→4→6)	
		No.3 (1→5→6)	
2	-	-	
3	6	No.4 (1→3→2→4→6)	No.7 (1→4→7→8→6)
		No.5 (1→4→2→3→6)	No.8 (1→5→7→4→6)
		No.6 (1→4→7→5→6)	No.9 (1→5→7→8→6)
4	-	-	
5	5	No.10 (1→3→2→4→7→5→6)	
		No.11 (1→3→2→4→7→8→6)	
		No.12 (1→4→7→9→10→8→6)	
		No.13 (1→5→7→4→2→3→6)	
		No.14 (1→5→7→9→10→8→6)	

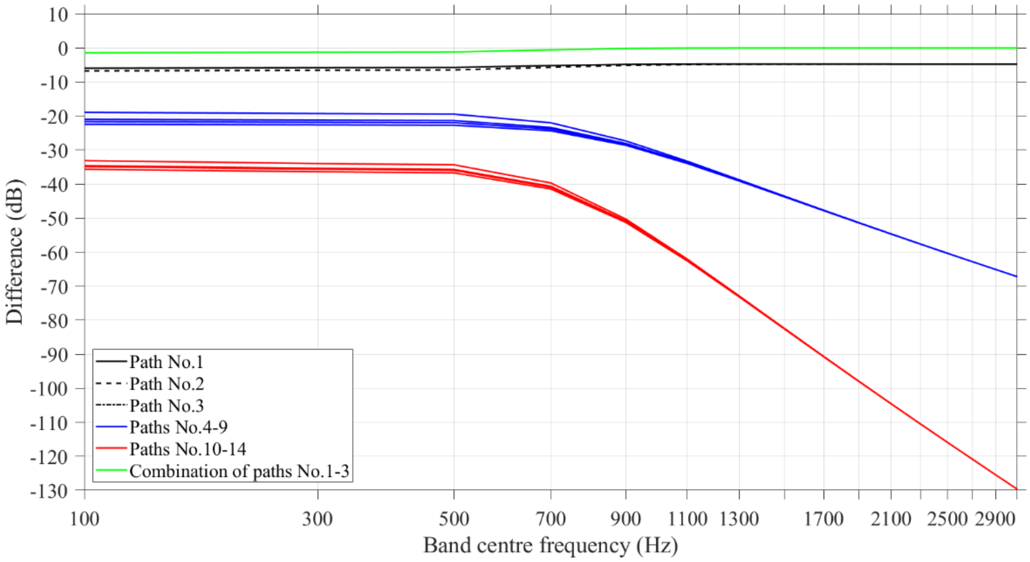

Figure C-5 Difference between the energy ratio, E_1/E_6, from the SEA matrix solution and path analysis.

Table C-6 Transmission paths to beam SS7 through pile 2 shown in Figure 3-8 for power input to beam SS1 (grey shading indicates the strongest path).

Number of intermediate subsystems	**Number of paths**	**Paths**	
0	-	-	
1	2	No.1 (1→4→7)	
		No.2 (1→5→7)	
2	-	-	
3	8	No.3 (1→3→2→4→7)	No.7 (1→4→6→5→7)
		No.4 (1→3→6→4→7)	No.8 (1→4→6→8→7)
		No.5 (1→3→6→5→7)	No.9 (1→5→6→4→7)
		No.6 (1→3→6→8→7)	No.10 (1→5→6→8→7)
4	-	-	
5	8	No.11 (1→3→2→4→6→5→7)	No.15 (1→4→2→3→6→8→7)
		No.12 (1→3→2→4→6→8→7)	No.16 (1→4→6→8→10→9→7)
		No.13 (1→3→6→8→10→9→7)	No.17 (1→5→6→3→2→4→7)
		No.14 (1→4→2→3→6→5→7)	No.18 (1→5→6→8→10→9→7)

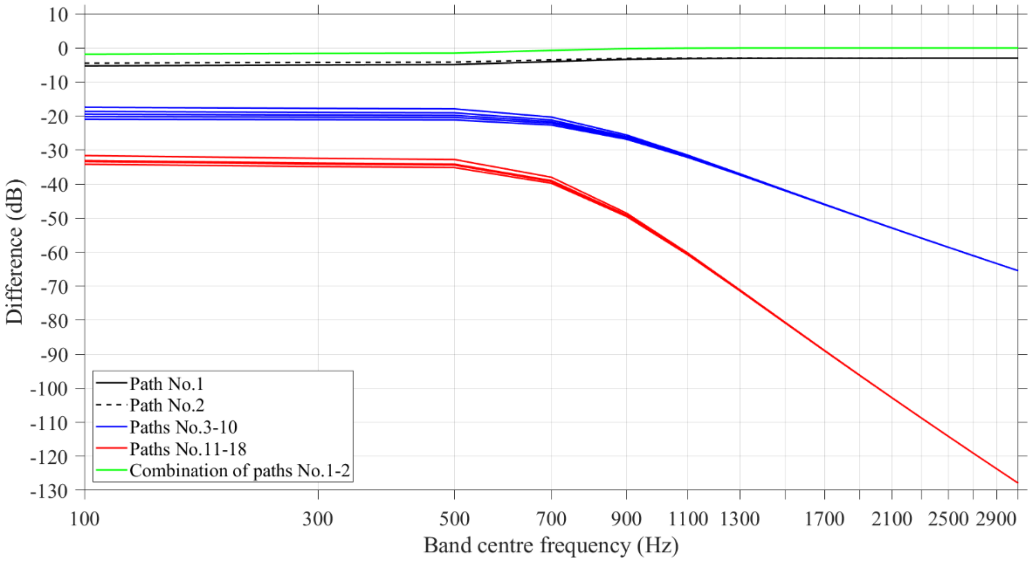

Figure C-6 Difference between the energy ratio, E_1/E_7, from the SEA matrix solution and path analysis.

Table C-7 Transmission paths to beam SS8 through pile 2 shown in Figure 3-8 for power input to beam SS1 (grey shading indicates the strongest path).

Number of intermediate subsystems	**Number of paths**	**Paths**		
0	-	-		
1	-	-		
2	5	No.1 (1→3→6→8)		
		No.2 (1→4→7→8)		
		No.3 (1→4→6→8)		
		No.4 (1→5→7→8)		
		No.5 (1→5→6→8)		
3	-	-		
4	11	No.6 (1→3→2→4→6→8)	No.10 (1→4→2→3→6→8)	No.14 (1→5→6→4→7→8)
		No.7 (1→3→2→4→7→8)	No.11 (1→4→6→5→7→8)	No.15 (1→5→7→4→6→8)
		No.8 (1→3→6→4→7→8)	No.12 (1→4→7→5→6→8)	No.16 (1→5→7→9→10→8)
		No.9 (1→3→6→5→7→8)	No.13 (1→4→7→9→10→8)	
5	-	-		

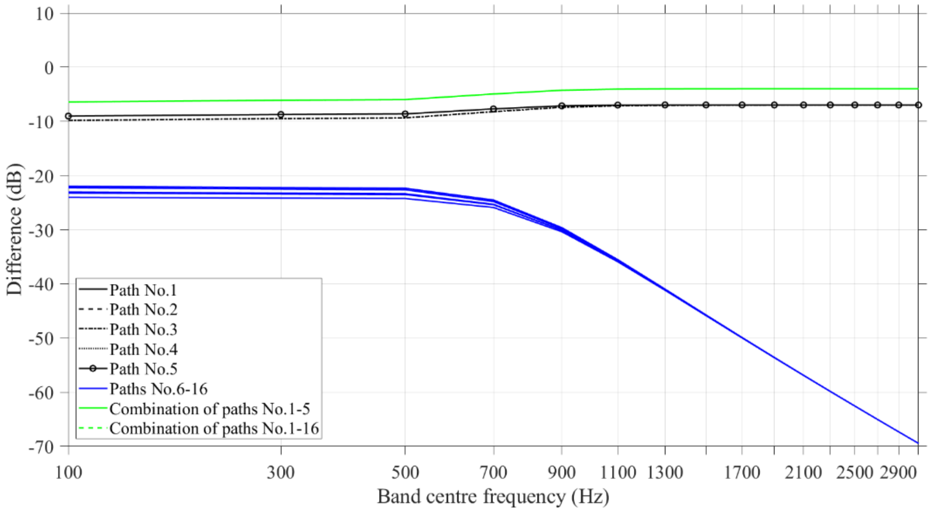

Figure C-7 Difference between the energy ratio, E_1/E_8, from the SEA matrix solution and path analysis. Combination of paths No. 1-5 and No. 1-16 result in identical curves.

Table C-8 Transmission paths to beam SS9 through pile 2 shown in Figure 3-8 for power input to beam SS1 (grey shading indicates the strongest path).

Number of intermediate subsystems	**Number of paths**	**Paths**		
0	-	-		
1	-	-		
2	2	No.1 (1→4→7→9)		
		No.2 (1→5→7→9)		
3	-	-		
4	13	No.3 (1→3→2→4→7→9)	No.8 (1→4→6→5→7→9)	No.13 (1→5→6→8→7→9)
		No.4 (1→3→6→4→7→9)	No.9 (1→4→6→8→7→9)	No.14 (1→5→6→8→10→9)
		No.5 (1→3→6→5→7→9)	No.10 (1→4→6→8→10→9)	No.15 (1→5→7→8→10→9)
		No.6 (1→3→6→8→7→9)	No.11 (1→4→7→8→10→9)	
		No.7 (1→3→6→8→10→9)	No.12 (1→5→6→4→7→9)	
5	-	-		

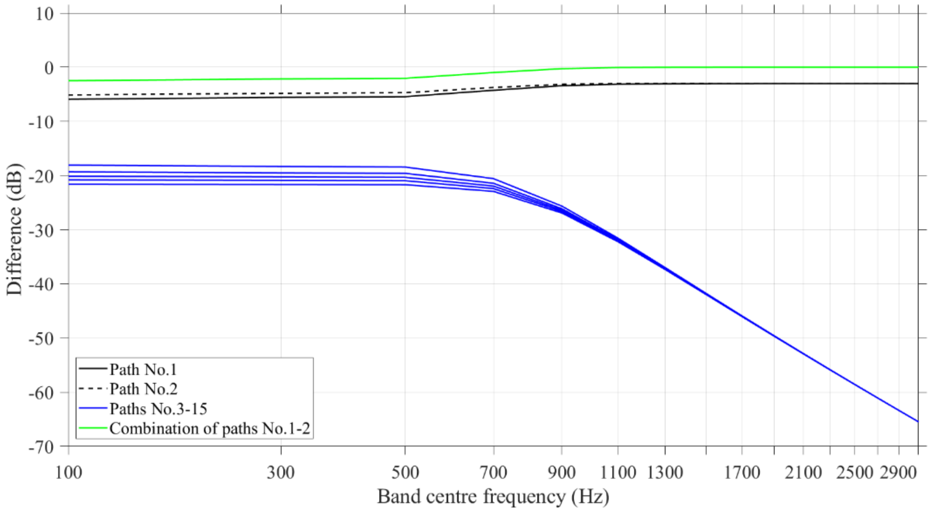

Figure C-8 Difference between the energy ratio, E_1/E_9, from the SEA matrix solution and path analysis.

Table C-9 Transmission paths to beam SS10 through pile 2 shown in Figure 3-8 for power input to beam SS1 (grey shading indicates the strongest path).

Number of intermediate subsystems	**Number of paths**	**Paths**		
0	-	-		
1	-	-		
2	-	-		
3	4	No.1 (1→3→6→8→10)		
		No.2 (1→4→6→8→10)		
		No.3 (1→4→7→8→10)		
		No.4 (1→4→7→9→10)		
4	-	-		
5	32	No.5 (1→3→2→4→6→8→10)	No.16 (1→4→2→3→6→8→10)	No.27 (1→5→6→4→7→8→10)
		No.6 (1→3→2→4→7→8→10)	No.17 (1→4→6→5→7→8→10)	No.28 (1→5→6→4→7→9→10)
		No.7 (1→3→2→4→7→9→10)	No.18 (1→4→6→5→7→9→10)	No.29 (1→5→6→8→7→9→10)
		No.8 (1→3→6→4→7→8→10)	No.19 (1→4→6→8→7→9→10)	No.30 (1→5→6→8→11→13→10)
		No.9 (1→3→6→4→7→9→10)	No.20 (1→4→6→8→11→13→10)	No.31 (1→5→6→8→11→14→10)
		No.10 (1→3→6→5→7→8→10)	No.21 (1→4→6→8→11→14→10)	No.32 (1→5→6→8→12→13→10)
		No.11 (1→3→6→5→7→9→10)	No.22 (1→4→6→8→12→13→10)	No.33 (1→5→7→4→6→8→10)

		No.12 (1→3→6→8→7→9→10)	No.23 (1→4→7→5→6→8→10)	No.34 (1→5→7→8→11→13→10)
		No.13 (1→3→6→8→11→13→10)	No.24 (1→4→7→8→11→13→10)	No.35 (1→5→7→8→11→14→10)
		No.14 (1→3→6→8→11→14→10)	No.25 (1→4→7→8→11→14→10)	No.36 (1→5→7→8→12→13→10)
		No.15 (1→3→6→8→12→13→10)	No.26 (1→4→7→8→12→13→10)	

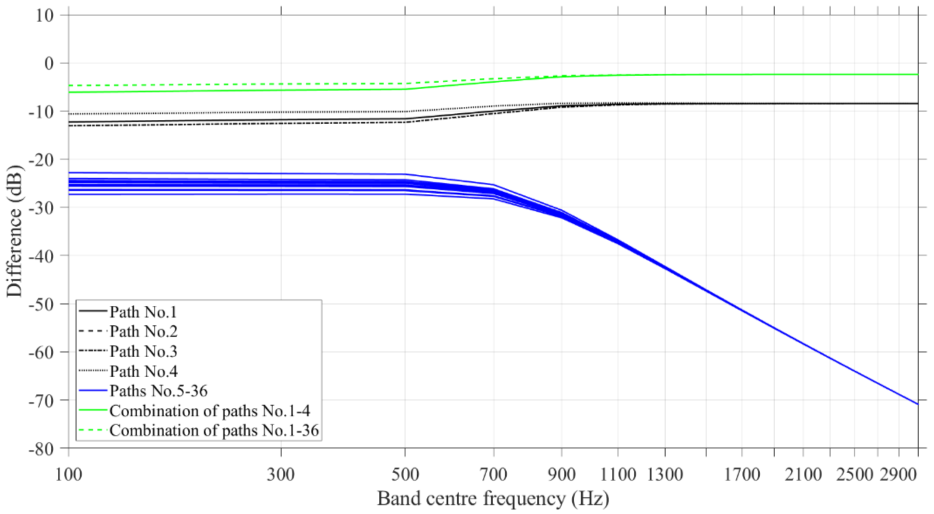

Figure C-9 Difference between the energy ratio, E_1/E_{10}, from the SEA matrix solution and path analysis.

Table C-10 Transmission paths to beam SS11 through pile 2 shown in Figure 3-8 for power input to beam SS1 (grey shading indicates the strongest path).

Number of intermediate subsystems	Number of paths	Paths		
0	-	-		
1	-	-		
2	-	-		
3	5	No.1 (1→3→6→8→11)		
		No.2 (1→4→6→8→11)		
		No.3 (1→4→7→8→11)		
		No.4 (1→5→6→8→11)		
		No.5 (1→5→7→8→11)		
4	-	-		
5	30	No.6 (1→3→2→4→6→8→11)	No.16 (1→4→6→8→10→14→11)	No.26 (1→5→6→8→10→13→11)
		No.7 (1→3→2→4→7→8→11)	No.17 (1→4→6→8→12→13→11)	No.27 (1→5→6→8→10→14→11)
		No.8 (1→3→6→4→7→8→11)	No.18 (1→4→7→5→6→8→11)	No.28 (1→5→6→8→12→13→11)
		No.9 (1→3→6→5→7→8→11)	No.19 (1→4→7→8→10→13→11)	No.29 (1→5→7→4→6→8→11)
		No.10 (1→3→6→8→10→13→11)	No.20 (1→4→7→8→10→14→11)	No.30 (1→5→7→8→10→13→11)
		No.11 (1→3→6→8→10→14→11)	No.21 (1→4→7→8→12→13→11)	No.31 (1→5→7→8→10→14→11)
		No.12 (1→3→6→8→12→13→11)	No.22 (1→4→7→9→10→8→11)	No.32 (1→5→7→8→12→13→11)
		No.13 (1→4→2→3→6→8→11)	No.23 (1→4→7→9→10→13→11)	No.33 (1→5→7→9→10→8→11)
		No.14 (1→4→6→5→7→8→11)	No.24 (1→4→7→9→10→14→11)	No.34 (1→5→7→9→10→13→11)
		No.15 (1→4→6→8→10→13→11)	No.25 (1→5→6→4→7→8→11)	No.35 (1→5→7→9→10→14→11)

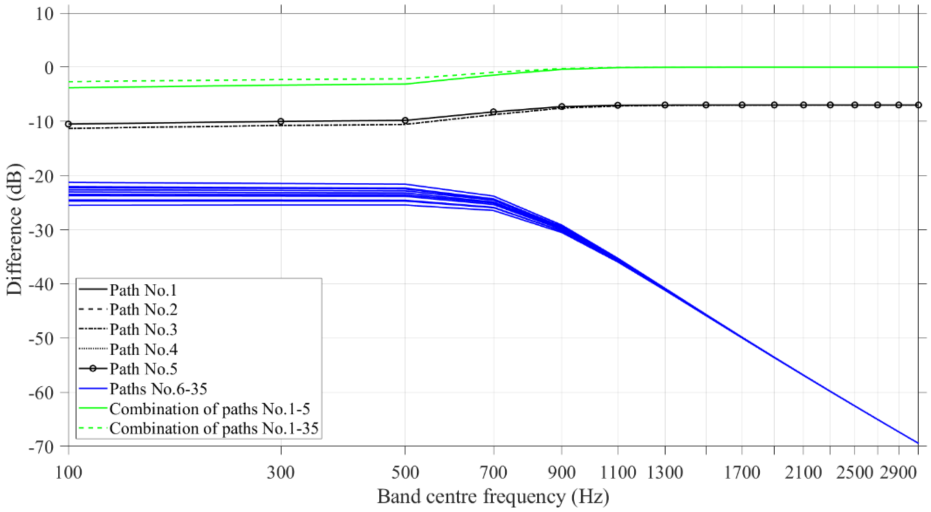

Figure C-10 Difference between the energy ratio, E_1/E_{11}, from the SEA matrix solution and path analysis.

Table C-11 Transmission paths to beam SS12 through pile 2 shown in Figure 3-8 for power input to beam SS1 (grey shading indicates the strongest path).

Number of intermediate subsystems	**Number of paths**	**Paths**		
0	-	-		
1	-	-		
2	-	-		
3	5	No.1 (1→3→6→8→12)		
		No.2 (1→4→6→8→12)		
		No.3 (1→4→7→8→12)		
		No.4 (1→5→6→8→12)		
		No.5 (1→5→7→8→12)		
4	-	-		
5	23	No.6 (1→3→2→4→6→8→12)	No.14 (1→4→6→8→10→13→12)	No.22 (1→5→6→8→10→13→12)
		No.7 (1→3→2→4→7→8→12)	No.15 (1→4→6→8→11→13→12)	No.23 (1→5→6→8→11→13→12)
		No.8 (1→3→6→4→7→8→12)	No.16 (1→4→7→5→6→8→12)	No.24 (1→5→7→4→6→8→12)
		No.9 (1→3→6→5→7→8→12)	No.17 (1→4→7→8→10→13→12)	No.25 (1→5→7→8→10→13→12)
		No.10 (1→3→6→8→10→13→12)	No.18 (1→4→7→8→11→13→12)	No.26 (1→5→7→9→10→8→12)
		No.11 (1→3→6→8→11→13→12)	No.19 (1→4→7→9→10→8→12)	No.27 (1→5→7→9→10→13→12)
		No.12 (1→4→2→3→6→8→12)	No.20 (1→4→7→9→10→13→12)	No.28 (1→5→7→8→11→13→12)
		No.13 (1→4→6→5→7→8→12)	No.21 (1→5→6→4→7→8→12)	

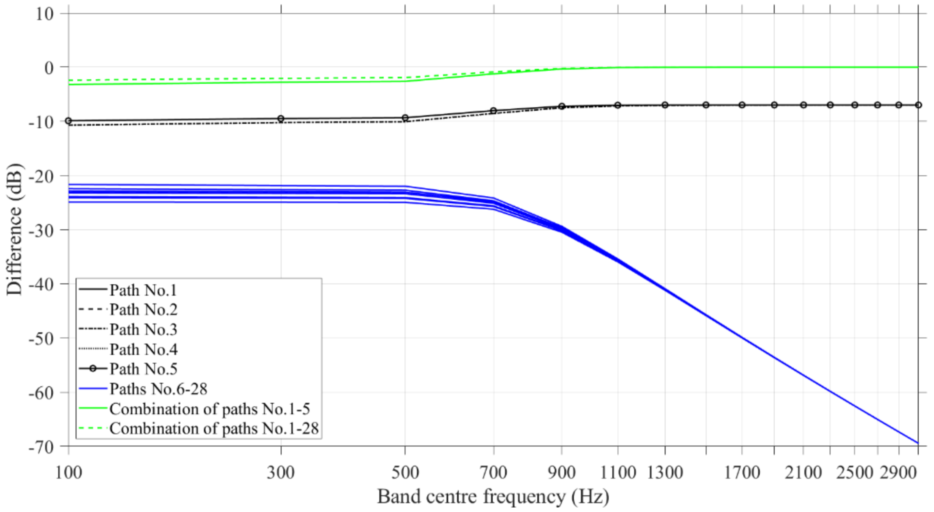

Figure C-11 Difference between the energy ratio, E_1/E_{12}, from the SEA matrix solution and path analysis.

Table C-12 Transmission paths to beam SS13 through pile 2 shown in Figure 3-8 for power input to beam SS1 (grey shading indicates the strongest path).

Number of intermediate subsystems	**Number of paths**	**Paths**		
0	-	-		
1	-	-		
2	-	-		
3	-	-		
4	17	No.1 (1→3→6→8→10→13)	No.7 (1→4→7→8→10→13)	No.13 (1→5→6→8→12→13)
		No.2 (1→3→6→8→11→13)	No.8 (1→4→7→8→11→13)	No.14 (1→5→7→8→10→13)
		No.3 (1→3→6→8→12→13)	No.9 (1→4→7→8→12→13)	No.15 (1→5→7→8→11→13)
		No.4 (1→4→6→8→10→13)	No.10 (1→4→7→9→10→13)	No.16 (1→5→7→8→12→13)
		No.5 (1→4→6→8→11→13)	No.11 (1→5→6→8→10→13)	No.6 (1→5→7→9→10→13)
		No.6 (1→4→6→8→12→13)	No.12 (1→5→6→8→11→13)	
5	-	-		

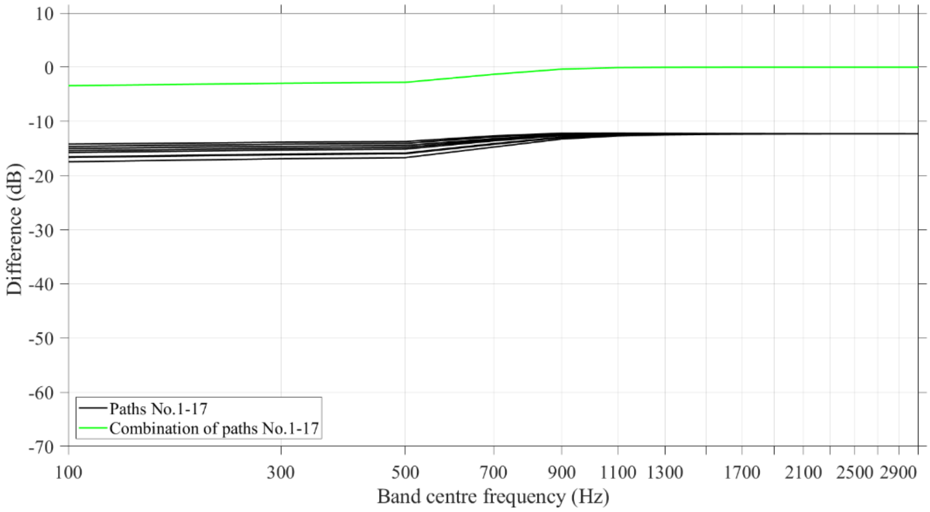

Figure C-12 Difference between the energy ratio, E_1/E_{13}, from the SEA matrix solution and path analysis.

Table C-13 Transmission paths to beam SS14 through pile 2 shown in Figure 3-8 for power input to beam SS1 (grey shading indicates the strongest path).

Number of intermediate subsystems	**Number of paths**	**Paths**	
0	-	-	
1	-	-	
2	-	-	
3	-	-	
4	12	No.1 (1→3→6→8→10→14)	No.7 (1→4→7→9→10→14
		No.2 (1→3→6→8→11→14)	No.8 (1→5→6→8→10→14
		No.3 (1→4→6→8→10→14)	No.9 (1→5→6→8→11→14
		No.4 (1→4→6→8→11→14)	No.10 (1→5→7→8→10→14
		No.5 (1→4→7→8→10→14)	No.11 (1→5→7→8→11→14
		No.6 (1→4→7→8→11→14)	No.12 (1→5→7→9→10→14)
5	-	-	

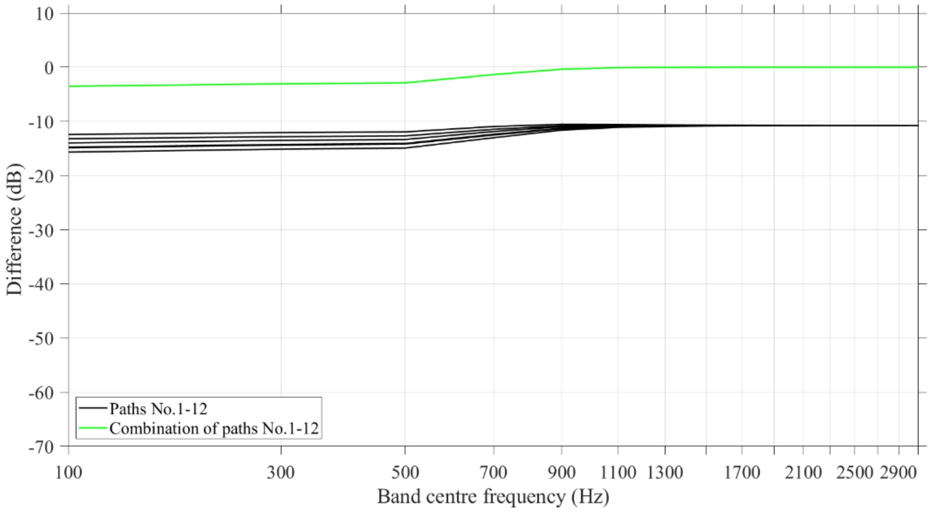

Figure C-13 Difference between the energy ratio, E_1/E_{14}, from the SEA matrix solution and path analysis.

References

[1] R. Huo , A. Agapiou, V. Bocos-Bintintant, L. J. Brown, C. Burns, C. S. Creaser, N. A. Devenport, B. Gao-Lau, C. Guallar-Hoyas, L. Hildebrand, A. Malkar, H. J. Martin, V. H. Moll, P. Patel, A. Ratiu, J. C. Reynolds, S. Sielemann, R. Slodzynski, M. Statheropoulos, M. A. Turner, V. Vautz, V. E. Wright and C. L. P. Thomas, “The trapped human experiment,” *Journal of Breath Research,* vol. 5, pp. 1-12, 2011.

[2] A. G. Macintyre, J. A. Barbera and E. R. Smith, “Surviving collapsed structure entrapment after earthquakes: A "Time-to-Rescue" analysis,” *Prehospital and Disaster Medicine,* vol. 21, no. 1, pp. 4-19, 2006.

[3] A. G. Macintyre, J. A. Barbera and B. P. Petinaux, “Survival interval in earthquake entrapments: Research findings reinforced during the 2010 Haiti earthquake Response,” *Disaster Medicine and Public Health Preparedness,* vol. 5, no. 1, pp. 13-22, 2011.

[4] C.-J. Bäckström and N. Christofferson, “Urban search and rescue - an evaluation of technical search equipment and methods,” Lund University, Lund, 2006.

[5] A. T. Güntner, N. J. Pineau, P. Mochalski, H. Wiesenhofer, A. Agapiou, C. A. Mayhew and S. E. Pratsinis, “Sniffing entrapped humans with sensor arrays,” *Analytical Chemistry,* vol. 90, pp. 4940-4945, 2018.

[6] M. van Zomeren, “Search methods in USAR,” Delft University of Technology, Delft, 2008.

[7] R. D. Cook, D. S. Malkus, M. E. Plesha and R. J. Witt, Concepts and Applications of Finite Element Analysis, 4th ed., Hoboken, NJ: John Wiley & Sons, Inc, 2001.

[8] R. H. Lyon and R. G. DeJong, Theory and application of Statistical Energy Analysis, 2nd ed., Newton: Butterworth-Heinemann, 1995.

[9] *NFPA 1670:2017 - Standard on Operations and Training for Technical Search and Rescue Incidents,* National Fire Protection Association.

[10] R. M. Downey, “Types of Collapse,” *WNYF Magazine,* pp. 10-11, 2001.

[11] L. Collins, Technical Rescue Operations, Volume II: Common Emergencies, 1st ed., Tulsa: Penn Well Corporation, 2005.

[12] J. O'Connell, Collapse operations for first responders, 1st ed., Tulsa: Penn Well Corporation, 2012.

[13] H. Sezen , A. S. Whittaker, K. J. Elwood and K. M. Mosalam, “Performance of reinforced concrete buildings during the August 17, 1999 Kocaeli, Turkey earthquake, and seismic design and construction practice in Turkey,” *Engineering Structures,* vol. 25, pp. 103-114, 2003.

[14] *National Urban Search and Rescue Response System - Structure Collapse Awareness Training,* FEMA, 2008.

[15] A. Bayraktar, A. C. Altunişik and M. Pehlivan, "Performance and damages of reinforced concrete buildings during the October 23 and November 9, 2011 Van, Turkey, earthquakes," *Soil Dynamics and Earthquake Engineering,* vol. 53, pp. 49-72, 2013.

[16] C. Schweier and M. Markus, "Classification of collapsed buildings for fast damage and loss assessment," *Bulletin of Earthquake Engineering,* vol. 4, pp. 177-192, 2006.

[17] M. N. Fardis, Seismic Design, Assessment and Retrofitting of Concrete Buildings, New York: Springer, 2009.

[18] J. . D. Marshall, A. F. Lang, S. M. Baldridge and D. R. Popp, "Recipe for disaster: Construction methods, materials, and building performance in the January 2010 Haiti earthquake," *Earthquake Spectra,* vol. 27, pp. 323-343, 2011.

[19] F. Yépez and O. Yépez, "Role of construction materials in the collapse of R/C buildingsafter Mw 7.8 Pedernales – Ecuador earthquake, April 2016," *Case Studies in Structural Engineering,* vol. 7, pp. 24-31, 2017.

[20] D. V. Hutton, Fundamentals of Finite Element Analysis, 1st ed., New York: McGraw-Hill , 2004.

[21] A. Khennane, Introduction to Finite Element Analysis Using MATLAB and Abaqus, 1st ed., Boca Raton: CRC Press, Taylor & Francis Group, 2013.

[22] S. Atamturktur and J. A. Laman, “Finite element model correlation and calibration of historic masonry monuments: review,” *The Structural Design Of Tall and Special Buildings,* vol. 21, pp. 96-113, 2012.

[23] M. Valente and G. Milani, “Seismic assessment of historical masonry towers by means of simplifiedapproaches and standard FEM,” *Construction and Building Materials,* vol. 108, pp. 74-104, 2016.

[24] R. Jankowski, “Non-linear FEM analysis of earthquake-induced pounding between the main building and the stairway tower of the Olive View Hospital,” *Engineering Structures,* vol. 31, pp. 1851-1864, 2009.

[25] S. Kokot, A. Anthoine, P. Negro and G. Solomos, “Static and dynamic analysis of a reinforced concrete flat slab frame building for progressive collapse,” *Engineering Structures,* vol. 40, pp. 205-217, 2012.

[26] G. R. Liu and S. S. Quek, The Finite Element Method: A Practical Course, Oxford: Butterworth-Heinemann, 2014.

[27] T. Łodygowski and W. Sumelka, “Limitations in application of finite element methods in acoustic numerical simulation,” *Journal of Theoretical and Applied Mechanics,* vol. 44, no. 4, pp. 849-865, 2006.

[28] N. Attala and F. Sgard, Finite element and boundary methods on structural acoustics and vibrations, Boca Raton: CRC Press, Taylor&Francis Group, 2015.

[29] P. Langer, M. Maeder, C. Guist, M. Krause and S. Marburg, “More than six elements per wavelength: The practical use of structural finite element models

and their accuracy in comparison with experimental results," *Journal of Computational Acoustics,* vol. 25, no. 4, pp. 1-23, 2017.

[30] T. Hartmann, G. Tanner, G. Xie, D. Chappell and J. Bajars, "Modelling of high-frequency structure-borne sound transmission on FEM grids using the Discrete Flow Mapping technique," *Journal of Physics: Conference Series,* vol. 744, pp. 1-10, 2016.

[31] Y. Mizushima, Y. Mukai, H. Namba, K. Taga and T. Saruwatari, "Super-detailed FEM simulations for full-scale steel structure with fatal rupture at joints between members—Shaking-table test of full-scale steel frame structure to estimate influence of cumulative damage by multiple strong motion: Part 1," *Japan Architectural Review,* vol. 1, no. 1, pp. 96-108, 2018.

[32] N. Pešić, S. Živanović, J. Dennis and J. Hargreaves, "Experimental and finite element dynamic analysis of incrementally loaded reinforced concrete structures," *Engineering Structures,* vol. 103, pp. 15-27, 2015.

[33] A. Earij, G. Alfano, K. Cashell and X. Zhou, "Nonlinear three–dimensional finite–element modelling of reinforced–concrete beams: Computational challenges and experimental validation," *Engineering Failure Analysis,* vol. 82, pp. 92-115, 2017.

[34] J. Ožbolt and A. Sharma, "Numerical simulation of reinforced concrete beams with different shearreinforcements under dynamic impact loads," *International Journal of Impact Engineering,* vol. 38, pp. 940-950, 2011.

[35] E. K. Ervin, “Vibro-impact behaviorof two orthogonal beams,” *Journal of Engineering Mechanics,* vol. 135, pp. 529-537, 2009.

[36] M. Filippoupolitis, C. Hopkins, R. Völtl, U. Schanda, J. Mahn and L. Krajči, “Structural dynamics of a dowelled-joist timber floor in the low-frequency range modelled using finite element simulation,” *Engineering Structures,* vol. 148, pp. 602-620, 2017.

[37] F. Zhou, K. M. Mosalam and M. Nakashima, “Finite-element analysis of a composite frame under large lateral cyclic loading,” *Journal of Structural Engineering,* vol. 133, pp. 1018-1026, 2007.

[38] P. Martinelli, A. Galli, L. Barazzetti, M. Colombo , R. Felicetti, M. Previtali, F. Roncoroni, M. Scola and M. Di Prisco, “Bearing capacity assessment of a 14th century arch bridge in Lecco (Italy),” *International Journal of Architectural Heritage,* vol. 12, pp. 237-256, 2018.

[39] T. Marwala, Finite-element model updating using computational intelligence techniques, 1st ed., London: Springer, 2010.

[40] J. M. Seelig and W. H. Hoppman, “Normal mode vibrations of systems of elastically connected parallel bars,” *Journal of the Acoustical Society of America,* vol. 36, pp. 93-99, 1964.

[41] S. S. Rao, “Natural vibrations of systems of elastically connected Timoshenko beams,” *The Journal of the Acoustical Society of America,* vol. 55, pp. 1232-1237, 1974.

[42] Z. Oniszczuk, “Free transverse vibrations of elastically connected simply supported double-beam complex system,” *Journal of Sound and Vibration,* vol. 232, pp. 387-403, 1999.

[43] T. Irie, G. Yamada and Y. Kobayashi, “The steady state response of an internally damped double-beam system interconnected by several springs,” *Journal of the Acoustical Society of America,* vol. 71, no. 5, pp. 1155-1162, 1982.

[44] J. Li and H. Hua, “Dynamic stiffness vibration analysis of an elastically connected three-beam system,” *Applied Acoustics,* vol. 69, pp. 591-600, 2008.

[45] Y. Gur, D. A. Wagner and K. N. Morman, “Energy finite element analysis methods for mid-frequency NVH applications,” *SAE International Journal of Passenger Cars,* vol. 108, pp. 2979-2987, 1999.

[46] C. Hopkins, Sound Insulation, Oxford: Butterworth-Heinemann, 2007.

[47] R. J. M. Craik, Sound Transmission Through Buildings: Using Statistical Energy Analysis, Hampshire: Gower Publishing Limited, 1996.

[48] C. Hopkins, “Statistical energy analysis of coupled plate systems with low modal density and low modal overlap,” *Journal of Sound and Vibration,* vol. 251, no. 2, pp. 193-214, 2002.

[49] C. Hopkins, “Experimental statistical energy analysis of coupled plateswith wave conversion at the junction,” *Journal of Sound and Vibration,* vol. 322, pp. 155-166, 2009.

[50] L. Cremer, M. Heckl and E. E. Ungar, Structure-Borne Sound, Berlin: Springer-Verlag, 1973.

[51] R. H. Lyon, Statistical energy analysis of dynamical systems theory and applications, Cambridge: MIT Press, 1975.

[52] D. A. Bies and S. Hamid, “In situ determination of loss and coupling loss factors by the power injection method,” *Journal of Sound and Vibration,* vol. 70, no. 2, pp. 187-204, 1980.

[53] B. Mosley, J. Bungey and R. Hulse, Reinforced Concrete Design to Eurocode 2, New York: Palgrave Macmillan, 2012.

[54] *ISO 9052-1:1989 Acoustics - Determination of dynamic stiffness - Part 1: Materials used under floating floors in dwellings,* International Organization for Standardization.

[55] B. J. Mac Donald, Practical Stress Analysis with Finite Elements, 2nd ed., Dublin: Glasnevin Publishing, 2013.

[56] *Abaqus 6.14 Documentation and User Manual,* Providence, Rhode Island, USA: Dassault Systèmes Simulia Corporation, 2014.

[57] A. K. Chopra, Dynamics of Structures, 3rd ed., New Jersey: Prentice Hall, 2006.

[58] C. W. de Silva, Vibration and shock handbook, 1st ed., Boca Raton: Taylor & Francis, 2005.

[59] M. Petyt, Introduction to finite element vibration analysis, 2nd ed., New York: Cambridge University Press, 2010.

[60] D. Lu, J. Meng, S. Zhang, Y. Shi, K. Dai and Z. Huang, “Damping Ratios of Reinforced Concrete Structures Under Actual Ground Motion Excitations,” in *Dynamics of Civil Structures, Volume 2: Proceedings of the 37th IMAC, A Conference and Exposition on Structural Dynamics* , Cham, Springer, 2019, pp. 259-268.

[61] H. Bachmann, W. J. Ammann, F. Deischl, J. Eisenmann, I. Floegl, G. H. Hirsch, G. K. Klein, G. J. Lande, O. Mahrenholtz, H. G. Natke, H. Nussbaumer, A. J. Pretlove, J. H. Rainer, E.-U. Saemann and L. Steinbeisser, Vibration Problems in Structures: Practical Guidelines, Boston: Birkhäuser Verlag, 1995.

[62] D. J. Ewins, Modal Testing: Theory, Practice and Application, Baldock: Research Studies Press Ltd., 2000.

[63] D. J. Ewins, “Model validation: Correlation for updating,” *Sadhana*, vol. 25, no. 3, pp. 221-234, 2000.

[64] G. Martin, E. Balmes and T. Chancelier, “Improved Modal Assurance Criterion using a quantification of identification errors per mode/sensor,” in *26th International Conference on Noise and Vibration engineering (ISMA2014)*, Leuven, 2014.

[65] J. F. Mercer, G. S. Aglietti, M. Remedia and A. M. Kiley, “Study of Correlation Criteria for Spacecraft-Launch Vehicle Coupled Loads Analysis,” in *32nd IMAC Conference and Exposition on Structural Dynamics,* Brescia, 2012.

[66] R. J. Allemang, “The modal assurance criterion - Twenty years of use and abuse,” *Sound and Vibration,* pp. 14-21, 2003.

[67] W. Heylen and T. Janter, “Extensions of the modal assurance criterion,” *Journal of Vibrations and Acoustics,* vol. 112, pp. 468-472, 1990.

[68] P. Bamforth, D. Chisholm, J. Gibbs and T. Harrison, “Properties of Concrete for use in Eurocode 2,” The Concrete Centre, Surrey, 2008.

[69] *MATLAB R2018b,* Natick, Massachusetts: The Mathworks Inc., 2018.

[70] R. J. Craik and R. S. Smith, “Sound transmission through lightweight parallel plates. Part II: structure-borne sound,” *Applied Acoustics,* vol. 61, pp. 247-269, 2000.

[71] R. J. Craik, “The effect of random errors on a large statistical energy analysis model,” *Journal of Sound and Vibration,* vol. 91, no. 1, pp. 57-64, 1983.